FINAL REPORT

to the

NATIONAL AERONAUTICS AND SPACE ADMINISTRATION

For Grant NGR 14-004-008 (041)

(Formerly NsG-694)

For the period: June 1964 to August 1974

TURBULENCE COEFFICIENTS AND STABILITY STUDIES FOR THE COAXIAL FLOW OF DISSIMILAR FLUIDS

by

Herbert Weinstein
Professor of Chemical Engineering

and

S. Levan
Associate Professor of Mechanical Engineering

Illinois Institute of Technology
Chicago, Illinois 60616

[illegible]

February, 1975

FINAL REPORT

to the

NATIONAL AERONAUTICS AND SPACE ADMINISTRATION

For Grant NGR 14-004-008 (041)

(Formerly NsG-694)

For the period: June 1964 to August 1974

TURBULENCE COEFFICIENTS AND STABILITY STUDIES FOR THE COAXIAL FLOW OR DISSIMILAR FLUIDS

By

Herbert Weinstein
Professor of Chemical Engineering

and

Z. Lavan
Associate Professor of Mechanical Engineering

Illinois Institute of Technology
Chicago, Illinois 60616

NASA Technical Officer: Harvey S. Bloomfield

February, 1975

Table of Contents

Introduction

The work performed under NASA grant #NGR 14-004-008 (originally NSG-694) and its extensions covered many aspects of the fluid dynamics of coaxial flows and of rotating flows. Previous results of this work received publication in the form of both NASA contractor reports and professional journal articles. Lists of these reports and papers are presented in an Appendix of this report. In the body of this report two different analytical investigations of fluid dynamics problems of relevance to the gaseous core nuclear reactor program are presented. Since all prior work had already been published, the results of these investigations constitute the final report of work done under the Grant.

The first of these two works, "Numerical Solutions of Driven Vortices of Binary Fluid in Cylindrical Geometry" is an analysis of the vortex type flow which appears in the nuclear "light bulb" concept. In this work, a numerical treatment is developed for the rotating flow which includes a description of the nuclear fuel addition. The problem is formulated with the complete Navier-Stokes equations in order to show the interaction between the fuel addition, the main flow and the boundary layer flow in an accurate manner. The results presented are the first to show holdup of the nuclear fuel for the case of steady fuel addition. The results for fuel holdup are discouraging and it remains to be seen whether optimization of injection location will provide substantial improvement.

The second work, "Laminar Confined Coaxial Entrance Flow

with Heat Generation," is an analysis of the fluid flow in the fuel inlet region for the coaxial flow gaseous core nuclear reactor concept. This is a region in which analysis is difficult due to the existence of very large gradients. In the analysis, the boundary layer form of the equations of motion is used because the large gradients make a more exact formulation extremely difficult to solve numerically. Results demonstrate that the large expansion due to temperature change will take place axially unless strong radial pressure gradients are developed by induced non-axial velocity components. This represents a significant difference from the present conceptual description.

These two investigations are the culmination of the NASA sponsored IIT work on gaseous core nuclear reactors. The first of the two investigations extends the development of numerical methods for the solution of the Navier-Stokes equations for appropriate geometries to the case of rotating flows and almost completes the gas core program requirements in this area. It is still necessary to extend the capability for Navier-Stokes equations integration to spherical coordinates and to increase the range of Reynolds numbers for which solutions can be found with reasonable computer time usage.

The second investigation demonstrates that even the conceptual design of the coaxial flow reactor needs further development. The extension of analytical capability to spherical coordinates will greatly aid in the further conceptual development of the reactor.

INVESTIGATION A

NUMERICAL SOLUTIONS OF DRIVEN VORTICES OF BINARY FLUID IN A CYLINDRICAL GEOMETRY

By

Yong Woo Shin

and

Zalman Lavan

ABSTRACT

The steady state laminar motion of a viscous, incompressible and binary fluid is studied for a rotating flow in a cylindrical geometry. The mathematical model employed is a cold flow simulation of the fluid mechanics of the Light-Bulb concept of the gaseous core nuclear engine. The radial inward convection of angular momentum of the coolant gas through the porous periphery drives the vortex, mixes with the fuel gas and eventually leaves the chamber as a mixture through a small exit hole on one end wall. The fuel gas addition is mathematically simulated by an interior mass source.

A new computation method is presented to account for the interior mass addition. The method uses a potential function in addition to the stream function and vorticity used in current methods for solving viscous incompressible flows. By assuming that the fluid's velocity consists of two parts, one that is the gradient of a potential function, and the other calculated by appropriate derivatives of the stream function, it was found possible to satisfy the continuity equation which contains a source term. This method can also be applied to unsteady compressible flows where the unsteady continuity term is viewed as a source term while iterating over an intermediate time level. This technique is applied to driven vortex flows of a binary system and carried through to numerical results.

The governing equations are formulated in terms of Stokes' stream function, the tangential vorticity and a potential function as a time dependent problem. Steady state solutions are then obtained as large time solutions of the time dependent problem. A numerical method by finite differences, specifically the alternating-direction-implicit method, is employed for solving the equations. Once the velocity field is solved, the pressure is obtained by solving the Poisson equation of pressure with Neumann boundary conditions that are determined by given kinematics. For purposes of computational efficiency, the solution method by Fourier analysis is based on fast Fourier transforms.

Numerical results were obtained for axial Reynolds numbers of 1 and 20, tangential Reynolds numbers up to 100 and aspect ratios of 1 and 2. Without rotation, the primary flow was found to be more or less uniform through the bulk of the chamber. However, with rotation the bulk of the fluid flows through the relatively narrow region of the boundary layers formed along the stationary end walls. Also, the flow in the main body of the chamber consists of recirculating secondary flow cells. The intensity of this flow feature increases with increasing rotation for fixed through-put and decreases with increasing through-put for fixed rotation. The results obtained for binary flows show that the hold-up of internally injected mass increases with

increasing rotation for fixed primary flow and Schmidt number. Finally, the containment factor increases with decreasing the density ratio (density of fisrionable materials to density of coolant) with other parameters kept constant.

TABLE OF CONTENTS

LIST OF TABLES

LIST OF ISLUSTRATIONS

NOMENCLATURE

In the following, symbols and abbreviations used in this thesis are listed. The symbols used only locally are explained there and hence not included here.

English letters:

a	aspect ratio
b	non-dimensional geometry parameter as defined in (59)
c	mass fraction of component A
D_{AB}	mass diffusivity in binary diffusion
D/Dt	material derivative
e(r,z)	local error function in the continuity equation
E_d	discretization error
f_{A-B}	fractional mass addition of component A relative to that of component B
h	Δr
H	vorticity-like function defined in Eq. 15
k	Δz
L	length of vortex chamber
M	number of mesh spacings in z coordinate
$\vec{n}_A$	mass flux vector of component A
$\vec{n}_B$	mass flux vector of component B
N	number of mesh spacings in r coordinate
p	static pressure

q_p	iteration parameter in elliptic ADI equation of potential function
q_s	iteration parameter in elliptic ADI equation of stream function
r	radial coordinate
r_A	interior mass source of component A
r_e	exhaust hole radius
R	chamber radius
Re	axial Reynolds number
Re_t	tangential Reynolds number
Sc	Schmidt number
t	time coordinate
u	radial component velocity
u_{inj}	radial injection velocity on periphery
v	tangential component velocity
$\vec{v}$	velocity vector
v_o	tangential velocity on periphery
w	axial component velocity
w_{ex}	axial velocity at the exhaust hole
w_m	reference velocity for flow due to interior mass addition as defined in (60)
z	axial coordinate

Greek Letters:

α	$\Delta t/hk$
β	h/k
Γ	angular momentum
Γ_o	angular momentum on periphery

δ	hk
$\Delta r, \Delta t, \Delta z$	radial mesh size, time step, axial mesh size respectively
∇	del operator
∇^2	Laplacian operator
$\nabla \cdot$	divergence operator
∇x	curl operator
ϵ	potential function parameter defined in (59)
ζ	tangential component vorticity
η	containment factor
λ	volumetric coefficient of viscosity
μ	shear coefficient of viscosity
ρ	mixture density
ρ_A	density of component A in mixture
$\rho_{A,P}$	density of pure component A
ρ_B	density of component B in mixture
$\rho_{B,P}$	density of pure component B
ϕ	potential function
ψ	Stokes' stream function
$\vec{\psi}$	vector potential
$\vec{\omega}$	vorticity vector

Subscripts:

A	refers to component A
B	refers to component B
e	refers to exhaust hole
i	mesh point in radial direction
j	mesh point in axial direction

Superscripts:

n	refers to time level
*	refers to non-dimensional variable

Abbreviations:

ADI	alternating direction implicit
FFT	fast Fourier transform
SOR	successive over relaxation

CHAPTER I

INTRODUCTION

Rotating flows have long been a subject of investigation to fluid dynamicists as applied to Ranque-Hilsch tubes,[34]* cyclone separators, heat exchangers, MHD vortex power generators,[23] and many other devices. Recently advanced concepts of gaseous core nuclear reactors have further stimulated the study of vortex flows. The subject has also been studied for purely academic purposes.[14]

The present study has directly been motivated by one of the advanced reactor concepts, i.e. the Light-Bulb concept, and is concerned with containment of fissionable material and how the phenomena involved in vortex flows influence containment.

Definition of the Problem

In the Light-Bulb reactor[19] the fissionable material is kept inside a cylindrical container and the propellant flows outside of the cylinder through an annular space. A transparent cylindrical shell separates the propellant from the fissionable material. The fuel is maintained in a vapor state at very high temperature, and transfers heat to the propellant through the transparent separating shell by radiation. To maintain the integrity of the shell which partitions the fissionable material and the propellant, it

---

* For all numbered references, see bibliography.

is necessary to inject coolant gas at the shell. The coolant gas is intended to play another important role. Since the coolant is injected with rotation, a vortex is formed which then causes the formation of boundary layers on the end walls of the chamber. The flow of fluid in and out of the boundary layers induces recirculating secondary flow cells in the main body and fluid dynamically retains the fissionable material in this region of closed flow cells. The coolant gas fed to the vortex chamber is withdrawn through an end wall, cooled and then recirculated. Fuel entrained by the coolant is separated before recirculation.

In actual operations, a required amount of fissionable material called the critical mass has to be maintained in the reactor chamber. This necessitates an attainment of a certain fuel concentration. The coolant gas that is injected to cool the wall separating the propellant gas and fissionable material entrains some of the fissionable material while passing through the chamber. Although the required concentration level of the fissionable material can be maintained by replacing the amount entrained by the coolant gas it is very desirable to keep this as small as possible. By forming a vortex and therefore inducing recirculating flows, the critical fuel mass may be held in the closed flow region with a minimum loss. Because of the particular features of the confined vortex flow, the manner in which the fissionable material is introduced is important. It has

been suggested that the fissionable material be injected from an end wall in the form of small pellets so that it can reach the retention region without being swept out of the chamber by the boundary layer flows.

The present study consists of a numerical solution of a binary fluid system in a cylindrical container of finite length as shown in Fig. 1. One of the components can be the fissionable material and the other coolant. Addition of fissionable material is simulated by an interior mass source in the annular containment region. The coolant fluid enters through a rotating porous periphery and leaves axially through a small exhaust hole on one end wall.

Because of the particular manner in which the fissionable material is introduced, the continuity equation contains a source term. For this reason the conventional computational scheme for obtaining numerical solutions in terms of the stream function and the vorticity fails.

A new computational method is developed here to treat this problem of interior mass addition by means of a convenient formulation which consists of the stream function, the vorticity and one other function. This function is a potential function which is introduced into the formulation so that the continuity equation that contains a source term is satisfied. It may be mentioned that the same technique can be applied to time dependent compressible flow problems. In such problems the unsteady term in the continuity

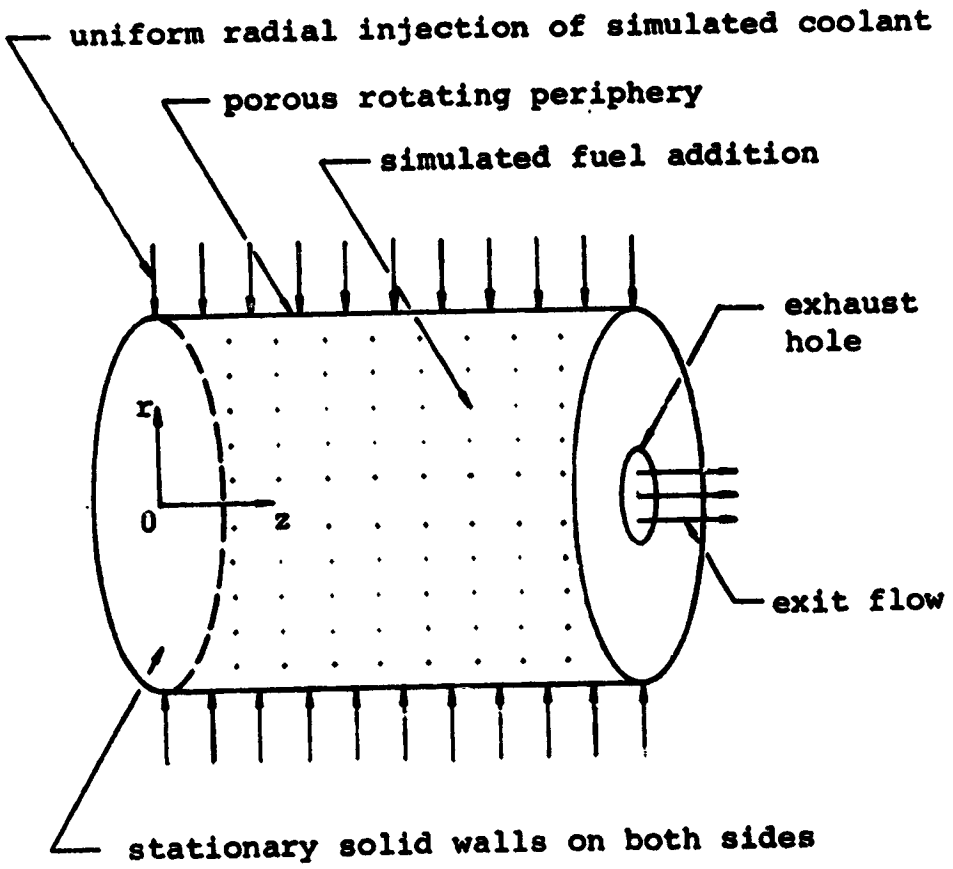

Fig. 1. The Flow Configuration and the Adopted Coordinate System.

equation is treated as a source term in the iteration process over the time step. The method is used in this study to obtain numerical solutions for binary driven vortex flows.

The basic differential equations are written in unsteady form in terms of the stream function, the vorticity and the newly introduced potential function. A numerical method by finite differences has been employed as the solution method. The alternating-direction-implicit method is used for both the parabolic and elliptic equations. After the kinematics are solved, the pressure is obtained by solving the Poisson equation of pressure. The method of Fourier analysis is used for this purpose in which the fast Fourier transforms have been employed to obtain an efficient computational procedure.

Literature Review

Rather than attempt to give an elaborate historical survey of vortex flow investigations the discussion here is limited only to those that are directly related to the present problem. Earlier analytical approaches to vortex flow problems assumed the flow to be one-dimensional.[11] There have been other investigations which considered the boundary layer flow formed over a finite disk with some specified outer velocity distribution.[10],[12] These studies have not considered the influence of one part of the flow on the other, i.e. the bulk flow affecting the boundary layer flow and vice versa. Accordingly, results of these studies do

not render sufficient information to describe the confined vortex flow problem. The importance of the interaction between the two flow regions was first noted by Anderson,[2] who considered the laminar boundary layer over the stationary end wall. More recently, Rosenzweig, Lewellen and Ross[31] studied the interaction problem analytically, in which the flow was divided into three subregions, the end-wall boundary layer, the primary flow and the central vortex core. For high rotation rates, they obtained a similarity solution for an assumed turbulent boundary layer. A comprehensive review on confined vortex flows can be found in Lewellen[22],[24] and Rott and Lewellen.[33]

Experimental work on confined vortex flows includes the flow visualization studies of Roschke[30] and Ross.[32] In both of these the secondary flow pattern shown in the visualization results was obtained for jet-driven vortices. Roschke studied also the effects of aspect ratio and the end-wall geometry on resulting flow configuration.

However, no numerical work can be found in the literature that considers the driven vortex flows in the configuration which simulates the Light-Bulb reactor concept. A numerical method applied to the flow configuration which is probably closest to that of the present study is given by Hornbeck.[17] He only considered the limiting case of small aspect ratio in which the recirculating flow could not occur. Nevertheless, the literature of rotating flows

in a system completely enclosed by solid boundaries or in a semi-infinite or infinite region is large. Equations of hydrodynamics may be written in terms of velocity and pressure or in stream function and vorticity. Of the many studies that employed the stream function-vorticity formulation, the important ones include the work of Pao,[25] Briley,[9] Lavan,[20] and Aziz.[4] Pao considered the secondary flows in a finite length cylinder with solid boundaries. One end wall was stationary and the other wall rotated with the periphery. Briley investigated the time dependent motion of spin-up, spin-down and reverse-rotations. Lavan examined the development of swirling flows in a circular duct. On the other hand, in a few cases the velocity-pressure formulation has also been used for numerical solutions of rotating flows. Williams[35] considered a three-dimensional thermal convection problem with rotation in an annular region. It is the author's belief that the work of Williams is the only published one that uses successfully the velocity-pressure formulation in rotating flows. Finally, it may be mentioned that no publications can be found that consider the rotating flow of a binary fluid system. It is the belief of the author of this thesis that the method developed here is the one most suitable for obtaining numerical results for confined vortex flow problems of binary fluids.

CHAPTER II
MATHEMATICAL FORMULATION

In this chapter a set of differential equations is written for a binary fluid system. One species of the system is introduced into the chamber as an interior mass source, whereas the second component enters through the porous periphery. The equations are obtained from the conservation laws of species, momentum, energy and the constitutive laws. The result thus obtained yields a set of equations in terms of velocity and pressure. By eliminating pressure from above velocity-pressure formulation, a second formulation is derived in which the equations are expressed in terms of stream function, vorticity and potential function. The merit of the stream function-vorticity formulation in numerical integration schemes is discussed in this chapter.

Underlying Assumptions

The important assumptions made in this study are listed below. The basic differential equations are derived under these conditions.

(1) Steady, isothermal, incompressible and axi-symmetric flow.

(2) Binary fluid system.

(3) The first species enters the chamber as an interior mass source with negligible momentum.

(4) Density varies with composition only.

(5) Constant viscosity.

(6) Mass diffusion is assumed to take place solely by concentration gradients.

The compressibility effect is neglected because the variation of pressure in the system is small when compared to the high absolute pressure. Constant viscosity is assumed because the objective of this study is to model a cold flow simulation of the Light Bulb reactor. And the effects of concentration variations on the viscosity are small. The viscosity would of course not be constant in the reactor itself because of the large temperature variations that exist there. Other assumptions that are considered minor will be discussed in the specific places where they occur.

Governing Equations

Diffusion and Continuity. The continuity equations for components A and B are obtained respectively by taking the mass balances of individual components:[7]

$$\frac{\partial \rho_A}{\partial t} + \nabla \cdot \vec{n}_A = r_A \qquad (1)$$

$$\frac{\partial \rho_B}{\partial t} + \nabla \cdot \vec{n}_B = 0 \qquad (2)$$

Adding these two equations yields the continuity equation of the mixture:

$$\frac{\partial \rho}{\partial t} + \nabla \cdot (\rho \vec{v}) = r_A \qquad (3)$$

The mass diffusion equation is derived taking into account the effect of the concentration gradient only. By substituting Fick's law of binary diffusion into the equation for species A, Eq. 1, and making use of the mixture continuity, Eq. 3, the species A equation can be expressed as follows when the mass diffusivity is constant:

$$\rho \frac{DC_A}{Dt} = D_{AB} \nabla \cdot (\rho \nabla c_A) + r_A (1 - c_A) \qquad (4)$$

Momentum Equation. The momentum equation with constant viscosity in the absence of body forces and for Newtonian fluids is:[3]

$$\rho \frac{D\vec{v}}{Dt} = -\nabla p + \mu \nabla^2 \vec{v} + (\lambda + \mu) \nabla (\nabla \cdot \vec{v}) \qquad (5)$$

With Stokes' hypothesis, $3\lambda + 2\mu = 0$, the momentum equation reduces to:

$$\rho \frac{D\vec{v}}{Dt} = -\nabla p + \mu \nabla^2 \vec{v} + \frac{1}{3} \mu \nabla (\nabla \cdot \vec{v}) \qquad (6)$$

The tangential component of this vector equation for an axi-symmetric flow is:

$$\rho\left[\frac{Dv}{Dt} + \frac{uv}{r}\right] = \mu\left[\nabla^2 v - \frac{v}{r^2}\right] \qquad (7)$$

where the operator $\frac{D}{Dt}$ under axial symmetry is:

$$\frac{D}{Dt} = \frac{\partial}{\partial t} + u\frac{\partial}{\partial r} + w\frac{\partial}{\partial z}$$

This tangential component velocity equation is expressed in terms of the angular momentum by the variable change $\Gamma = rv$:

$$\rho\frac{D\Gamma}{Dt} = \mu\left[\Gamma_{rr} - \frac{1}{r}\Gamma_r + \Gamma_{zz}\right]^* \qquad (8)$$

The equations given above constitute the velocity-pressure formulation and numerical solutions for the velocity components, density and pressure can be obtained from their finite difference analogue without further modification. However, difficulties have been reported in the literature[5] in solving the hydrodynamic equations when the pressure is included. Therefore in the formulation used here, the pressure is first eliminated by introducing the vorticity and the vorticity is then expressed in terms of the stream function. In this manner the same problem

---

* The subscripts in the equation represent differentiations. This convention is extensively used throughout this thesis.

is reformulated in terms of the stream function and vorticity. Since this formulation can be solved without much difficulties it is adopted in this study and will be developed in the following.

Vorticity Transport Equation. The vorticity transport equation is obtained by taking a curl of the momentum equation which for constant viscosity and no body forces is expressed as:

$$\rho\left[\frac{D\vec{\omega}}{Dt} + (\nabla\cdot\vec{v})\vec{\omega} - (\vec{\omega}\cdot\nabla)\vec{v}\right] + \nabla\rho \times \frac{D\vec{v}}{Dt} = \mu\nabla^2\vec{\omega} \qquad (9)$$

For axi-symmetric flow it is sufficient to consider only the tangential component of the vorticity vector:

$$\rho\left[\frac{D\zeta}{Dt} + (u_r + w_z)\zeta - \frac{1}{r}(v^2)_z\right] + \rho_z\left(\frac{Du}{Dt} - \frac{v^2}{r}\right) - \rho_r\frac{Dw}{Dt}$$

$$= \mu\left(\nabla^2\zeta - \frac{\zeta}{r^2}\right) \qquad (10)$$

A new function is introduced next by a change of variables:

$$H = \frac{\zeta}{r} \qquad (11)$$

This changes the anti-symmetric function ζ to a symmetric function H with respect to r, and upon substitution Eq. 10 reduces to a simpler equation that is especially convenient for numerical integration.

$$\rho\left[\frac{DH}{Dt} + (\nabla\cdot\vec{v})H - \frac{1}{r^2}(v^2)_z\right] + \frac{\rho_z}{r}\left(\frac{Du}{Dt} - \frac{v^2}{r}\right)$$

$$- \frac{\rho_r}{r}\frac{Dw}{Dt} = \mu\left(\nabla^2 H + \frac{2}{r}H_r\right) \qquad (12)^*$$

An important simplification that results from this change of variables is that the term, ζ/r^2 no longer appears in the equation.

Potential Function Equation. A potential function of an auxiliary nature is introduced in such a way that it identically satisfies the continuity equation which has a source term. In more conventional problems of incompressible flows or compressible steady flows, the Stokes' stream function satisfies the continuity equation which in that case has no source term.

In order to make the discussion general, a vector potential is used, which for an axi-symmetric flow reduces to a single non-vanishing component, i.e. the tangential component. Let

$$\rho\vec{v} = \nabla \times \vec{\psi} - \rho\nabla\phi \qquad (13)$$

With this definition of the mass average velocity, the continuity equation for steady flow becomes:

---

* Eq. 12 is called the vorticity equation hereafter.

$$\nabla\cdot(\nabla \times \vec{\psi} - \rho\nabla\phi) = r_A$$

Since $\nabla\cdot(\nabla \times \vec{\psi}) = 0$:

$$\nabla\cdot(\rho\nabla\phi) = -r_A \tag{14}$$

This is the equation that the potential function must satisfy which together with the vector potential $\vec{\psi}$ yields the velocity vector through Eq. 13. When an unsteady flow of variable density is considered, the term $\partial\rho/\partial t$ can be treated as part of the source term r_A.
The potential function Eq. 14 and the expression for the velocity vector Eq. 13 are expanded as in the following for axi-symmetric flow:

$$\phi_{rr} + (\frac{1}{r} + \frac{\rho_r}{\rho})\phi_r + \phi_{zz} + \frac{\rho_z}{\rho}\phi_z + \frac{r_A}{\rho} = 0 \tag{15}$$

and

$$u = -\frac{1}{\rho r}\psi_z - \phi_r; \quad w = \frac{1}{\rho r}\psi_r - \phi_z \tag{16}$$

Stream Function Equation. The defining equation of vorticity is:

$$\vec{\omega} = \nabla \times \vec{v}$$

Upon substitution for $\vec{v}$ from Eq. 13 and using the vector identity, $\nabla \times (\nabla\phi) = 0$, the vorticity is expressed as:

$$\vec{\omega} = \nabla \times (\frac{1}{\rho}\nabla \times \vec{\psi}) \tag{17}$$

The tangential component of Eq. 17 is after change of variables:

$$(\frac{1}{\rho r}\psi_r)_r + (\frac{1}{\rho r}\psi_z)_z + rH = 0 \tag{18}$$

Mixture Density. The mixture density neglecting effects of pressure changes is a function of composition (mass fraction) only:

$$\rho = \frac{\rho_{A,P}}{\frac{\rho_{A,P}}{\rho_{B,P}} + c_A(1 - \frac{\rho_{A,P}}{\rho_{B,P}})} \tag{19}$$

Pressure Equation. Two different solution methods are considered for the pressure. First, the pressure can be obtained by integrating the momentum equations. A second method is to solve the Poisson equation obtained by taking the divergence of the momentum equation. Both of these methods are used in the work reported here.

In the stream function-vorticity formulation which is used throughout this work, the kinematics are solved first independently of pressure. Therefore, the pressure

may be calculated from known kinematics by either method.

The momentum equation is rewritten in a form convenient for the line integration of pressure:

$$\nabla p = -\rho\frac{D\vec{v}}{Dt} + \mu\nabla^2\vec{v} + \frac{1}{3}\mu\nabla(\nabla\cdot\vec{v}) \tag{20}$$

Also the Poisson equation of pressure obtained as indicated above is:

$$\nabla^2 p = \nabla\cdot\left[-\rho\frac{D\vec{v}}{Dt} + \mu\nabla^2\vec{v} + \frac{1}{3}\mu\nabla(\nabla\cdot\vec{v})\right] \tag{21}$$

It may be mentioned that when the governing equations are formulated in terms of the stream function and vorticity, the error in pressure calculation does not affect the solution of the kinematics. Primarily this is the reason why the stream function-vorticity formulation has been more extensively used than the velocity-pressure formulation. Aziz[4] in his studies with both formulations found the one using the stream function and vorticity advantageous even for three dimensional problems in which he had to calculate all three components of both the vorticity and vector potential (stream function).

Transport Equations in a Conservation Form. In obtaining numerical solutions by finite differences, it is preferable to express the convective terms in a conservation form. The basic idea, as can be found in Emmons,[13]

is to conserve the transport quantity even with finite differences. The convective terms expressed in terms of a general transport quantity, q, have the form:

$$(\rho\vec{v}\cdot\nabla)q = \nabla\cdot(\rho\vec{v}q) - q(\nabla\cdot\rho\vec{v})$$

Using continuity, Eq. 3, under steady ..tate conditions the above equation can be expressed in the following conservative form:

$$(\rho\vec{v}\cdot\nabla)q = \nabla\cdot(\rho\vec{v}q) - r_A q \tag{22}$$

This equation in cylindrical coordinates under axi-symmetry reads:

$$\rho(uq_r + wq_z) = \frac{1}{r}(r\rho uq)_r + (\rho wq)_z - r_A q \tag{23}$$

Boundary Conditions

Since all of the differential equations are elliptic in the spatial variables, boundary conditions on the entire boundary are required. Along the center line the condition of symmetry is prescribed, whereas on solid boundaries the no slip condition on velocities and a vanishing concentration gradient are imposed. On the porous peripheral wall, a uniform injection velocity and zero flux of species A are assumed. And at the exhaust hole a porous plug condition and zero concentration gradient are

specified. Under these conditions, the total mass flow rate through the exhaust hole is not known a priori. Therefore, at each time step of the numerical computation the total mass flow is computed from the available solution, and from the overall mass balance the injection velocity at the periphery is determined for the boundary conditions of the · · · time step solution.

Th. oundary conditions for the stream function are:

$$\psi(0,z) = 0 \tag{24}$$

$$\psi(r,0) = 0 \tag{25}$$

On the periphery, $u = -u_{inj}$ = constant, and hence from Eq. 16:

$$\psi_z = -\rho R(-u_{inj} + \phi_r)$$

And upon integration:

$$\psi(R,z) = -R \int_0^z \rho(-u_{inj} + \phi_r)\,dz \tag{26}$$

Also

$$\psi(r,L) = \psi(R,L) \qquad \text{for } r \geq r_e \tag{27}$$

At the exhaust hole, from Eq. 16:

$$\psi(r,L) = \int_0^r \rho r(w_{ex} + \phi_z)dz \qquad \text{for } r \leq r_e \tag{28}$$

The boundary conditions for vorticity are obtained by evaluating the stream function equation on the boundary for no slip conditions. Especially with the introduction of the potential function which by nature allows slip velocities, the no slip conditions are attained through the boundary conditions on the vorticity.

With respect to the axis, r = 0, the axial velocity is symmetric whereas the radial velocity is anti-symmetric, and hence this vorticity like function H is symmetric.

$$H_r(0,z) = 0 \tag{29}$$

At the solid boundary, z = 0, w = 0 and u = 0. Hence

$$H(r,0) = -\frac{1}{r}\left(\frac{1}{\rho r}\psi_z\right)_z \tag{30a}$$

in which the no slip condition, u = 0 is satisfied by:

$$\psi_z = -\rho r \phi_r \tag{30b}$$

On the periphery, r = R, $u = -u_{inj}$, w = 0 and $\phi = 0$. Hence

$$H(R,z) = -\frac{1}{r}\left(\frac{1}{\rho r}\psi_r\right)_r$$

Expanding this and applying the no slip condition, w = 0 results in:

$$H(R,z) = -\frac{1}{\rho r^2}\psi_{rr} \tag{31a}$$

where the no slip condition, w = 0 is ensured by an additional condition:

$$\psi_r = 0 \tag{31b}$$

At z = L, u = 0 and hence

$$H(r,L) = -\frac{1}{r}\left[\left(\frac{1}{\rho r}\psi_r\right)_r + \left(\frac{1}{\rho r}\psi_z\right)_z\right]$$

subject to the condition $\psi_z = -\rho r\phi_r$.

Expanding the above expression gives:

$$H(r,L) = -\frac{1}{r}\left[\left(\frac{1}{\rho r}\psi_r\right)_r + \frac{1}{\rho r}\left(-\frac{\rho z}{\rho}\psi_z + \psi_{zz}\right)\right] \tag{32a}$$

which is subject to the following condition to satisfy u = 0:

$$\psi_z = -\rho r\phi_r \tag{32b}$$

Boundary conditions for the angular momentum are:

$$\Gamma(0,z) = 0 \tag{33}$$

$$\Gamma(r,0) = 0 \tag{34}$$

$$\Gamma(R,z) = \Gamma_o \tag{35}$$

$$\Gamma(r,L) = 0 \tag{36}$$

No mass flux of component A across the periphery and zero concentration gradient at the exhaust hole are assumed. Along the center line the condition of symmetry gives:*

$$c_r(0,z) = 0 \tag{37}$$

Across solid boundaries the total mass transfer as well as the velocity vanishes. Hence from the expression for the mass flux,

$$\vec{n}_A = \rho\vec{v}c - \rho D_{AB}\nabla c$$

the following boundary conditions result:

$$c_z(r,0) = 0 \tag{38}$$

$$c_z(r,L) = 0 \tag{39}$$

At the periphery the condition of no flux of component A yields:

$$D_{AB}c_r(R,z) + u_{inj}c(R,z) = 0 \tag{40}$$

The boundary conditions on component B can be deduced from those on component A. The mass fluxes of each component are:

---

* The subscript A is suppressed hereafter in the mass fraction of component A.

$$\vec{n}_A = \rho\vec{v}c_B - D_{AB}\frac{\partial c_B}{\partial n}$$

$$\vec{n}_B = \rho\vec{v}c_A - D_{AB}\frac{\partial c_A}{\partial n}$$

where n represents a local coordinate normal to the boundary. Adding both equations yields:

$$\vec{n}_A + \vec{n}_B = \rho\vec{v}$$

At the periphery, where $\vec{n}_A = 0$:

$$\vec{n}_B = \rho\vec{v}$$

The boundary conditions for the potential function are the symmetric condition on the axis and zero normal gradient on solid boundaries. However, at the periphery and exhaust hole an arbitrary functional value, $\phi = 0$ is assigned. In this manner, the conditions on velocity are satisfied by assigning appropriate values to the stream function on these boundaries.

$$\phi_r(0,z) = 0 \qquad (41)$$

$$\phi_z(r,0) = 0 \qquad (42)$$

$$\phi(R,z) = 0 \tag{43}$$

$$\phi_z(r,L) = 0 \quad \text{for } r_e \leq r \leq R \tag{44a}$$

$$\phi(r,L) = 0 \quad \text{for } 0 \leq r \leq r_e \tag{44b}$$

Non-dimensional Formulation

In this section the system of equations and boundary conditions in the stream function-vorticity formulation as obtained in previous sections are non-dimensionalized with properly chosen reference quantities. The characteristic reference values are chosen such that the normalized variables remain of order one. This is important since only then are the non-dimensional governing parameters meaningful as they appear in the non-dimensionalized governing differential equations.[22] The non-dimensional variables are written with a superscript (*), whereas the reference quantities are written with a subscript (ref) unless already specified. Let

$$r^* = r/R,\ z^* = z/L,\ t^* = t/t_{ref}$$

$$u^* = u/w_{ex},\ v^* = v/v_o,\ w^* = w/w_{ex}$$

$$\rho^* = \rho/\rho_{B,p},\ \psi^* = \psi/\psi_{ref},\ H^* = H/H_{ref} \tag{45}$$

$$\Gamma^* = \Gamma/\Gamma_o,\ \phi^* = \phi/\phi_{ref},\ r^*_A = r_A/r_{A,ref}$$

$$p^* = p/p_{ref} \tag{45}$$

Substitute the above relations into Eq. 16 and obtain:

$$u^* = -\frac{b^2}{2a\rho^* r^*}\psi^*_{z^*} - \varepsilon\phi^*_{r^*} \tag{46a}$$

$$w^* = \frac{b^2}{2\rho^* r^*}\psi^*_{r^*} - \frac{\varepsilon}{a}\phi^*_{z^*} \tag{46b}$$

In above equations two reference quantities are determined and three non-dimensional parameters are introduced:

$$\psi_{ref} = \tfrac{1}{2}\rho_{B,P} r_e^2 w_{ex};\quad \phi_{ref} = w_m R$$

$$b = r_e/R;\quad a = L/R;\quad \varepsilon = w_m/w_{ex}$$

where w_m represents the reference velocity for interior mass addition as the total mass addition averaged over the entire periphery.

Substituting (45) into the stream function Eq. 18:

$$\left(\frac{1}{\rho^* r^*}\psi^*_{r^*}\right)_{r^*} + \frac{1}{a^2}\left(\frac{1}{\rho^* r^*}\psi^*_{z^*}\right)_{z^*} = -\frac{1}{b^4} r^* H^* \tag{47}$$

where $H_{ref} = \psi_{ref}/\rho_{B,P} r_e^4$ is used.

The potential function Eq. 15 is normalized using (45):

$$\phi^*_{r^*r^*} + \left(\frac{1}{r^*} + \frac{\rho^*_{r^*}}{\rho^*}\right)\phi^*_{r^*} + \frac{1}{a^2}\phi^*_{z^*z^*} + \frac{1}{a^2}\frac{\rho^*_{z^*}}{\rho^*}\phi^*_{z^*} + \frac{r^*_A}{\rho^*} = 0 \qquad (48)$$

where $r_{A,ref} = \rho_{B,P}\phi_{ref}/R^2$.

Now the vorticity Eq. 12 is normalized to:

$$H^*_{t^*} = \frac{1}{\rho^*}\left[H^*_{r^*r^*} + \frac{3}{r^*}H^*_{r^*} + \frac{1}{a^2}H^*_{z^*z^*} - \frac{Re}{br^*}(r^*\rho^*u^*H^*)_{r^*}\right.$$

$$\left. - \frac{Re}{ba}(\rho^*w^*H^*)_{z^*}\right] + \frac{Re}{b}\left[\varepsilon\frac{r^*_A}{\rho^*} - \left(u^*_{r^*} + \frac{u^*}{r^*} + \frac{1}{a}w^*_{z^*}\right)\right]H^*$$

$$+ \frac{2b}{Rer^*}\left[\frac{Re_t^2}{ar^{*3}}(\Gamma^{*2})_{z^*} - \frac{Re^2\rho^*_{z^*}}{a\rho^*}(u^*u^*_{r^*} + \frac{1}{a}w^*u^*_{z^*}\right.$$

$$\left. - \frac{Re_t^2}{Re^2}\frac{\Gamma^{*2}}{r^{*3}}) + \frac{Re^2\rho^*_{r^*}}{\rho^*}(u^*w^*_{r^*} + \frac{1}{a}w^*w^*_{z^*})\right] \qquad (49)$$

where $Re = \rho_{B,P}w_{ex}r_e/\mu$, $Re_t = \rho_{B,P}v_o r_e/\mu$ and

$t_{ref} = \rho_{B,P}R^2/\mu$.

The angular momentum Eq. 8 after non-dimensionalization reduces to:

$$\Gamma^*_{t^*} = \frac{1}{\rho^*}\left[\Gamma^*_{r^*r^*} - \frac{1}{r^*}\Gamma^*_{r^*} + \frac{1}{a^2}\Gamma^*_{z^*z^*} - \frac{Re}{br^*}(r^*\rho^*u^*\Gamma^*)_{r^*}\right.$$

$$\left. - \frac{Re}{ba}(\rho^*w^*\Gamma^*)_{z^*}\right] + \frac{Re\varepsilon r^*_A}{b\rho^*}\Gamma^* \qquad (50)$$

The equation for diffusion, Eq. 4, is normalized to:

$$c_{t^*} = \frac{1}{S_c}\left[c_{r^*r^*} + \left(\frac{1}{r^*} + \frac{\rho^*_{r^*}}{\rho^*}\right)c_{r^*} + \frac{1}{a^2}\frac{\rho^*_{z^*}}{\rho^*}c_{z^*}\right]$$

$$- \frac{Re}{b\rho^* r^*}(r^*\rho^* u^* c^*)_{r^*} - \frac{Re}{ba\rho^*}(\rho^* w^* c)_{z^*} + \frac{Re\varepsilon r^*_A}{b\rho^*} \qquad (51)$$

where $S_c = \frac{\mu}{\rho_{B,P} D_{AB}}$.

The mixture density, Eq. 19, is non-dimensionalized to:

$$\rho^* = \frac{\rho_{A,P}/\rho_{B,P}}{\rho_{A,P}/\rho_{B,P} + c(1 - \rho_{A,P}/\rho_{B,P})} \qquad (52)$$

Finally, Eq. 20 and 21 involved in pressure calculations are non-dimensionalized to:

$$p^*_{r^*} = -\rho^*\left(u^* u^*_r + \frac{w^*}{a} u^*_{z^*} - \frac{Re_t^2}{Re^2}\frac{v^{*2}}{r^*}\right) + \frac{b}{Re}\left(\nabla^{*2} u^* - \frac{u^*}{r^{*2}}\right)$$

$$+ \frac{b}{3Re}\left(u^*_{r^*} + \frac{u^*}{r^*} + \frac{1}{a}w^*_{z^*}\right)_{r^*} \qquad (53a)$$

$$\frac{1}{a}p^*_{z^*} = -\rho^*\left(u^* w^*_{r^*} + \frac{w^*}{a}w^*_{z^*}\right) + \frac{b}{Re}\nabla^{*2} w^* + \frac{b}{3aRe}\left(u^*_{r^*}\right.$$

$$\left. + \frac{u^*}{r^*} + \frac{1}{a}w^*_{z^*}\right)_{z^*} \qquad (53b)$$

and,

$$\nabla^{*2} p^* = -S^*, \text{ where} \tag{54a}$$

$$S^* = \frac{1}{r^*}(r(F_1^*)_{r^*} + \frac{1}{a}(F_2^*)_{z^*} \tag{54b}$$

where the reference pressure is determined:

$$p_{ref} = \rho_{B,P} w_{ex}^2$$

Non-dimensional governing parameters and reference quantities determined above are summarized below:

Non-dimensional governing parameters:

Geometry parameters;

$$a = L/R, \; b = r_e/R$$

Potential function parameter,

$$\varepsilon = w_m/w_{ex}$$

and

$$\begin{aligned} Re &= \rho_{B,P} w_{ex} r_e/\mu \\ Re_t &= \rho_{B,P} v_o r_e/\mu \\ S_c &= \frac{\mu}{\rho_{B,P} D_{AB}} \end{aligned} \tag{55}$$

Reference quantities:

$$t_{ref} = \rho_{B,P} R^2/\mu, \; \psi_{ref} = \frac{1}{2}\rho_{B,P} r_e^2 w_{ex},$$

$$H_{ref} = \psi_{ref}/\rho_{B,P}r_e^4,$$

$$\phi_{ref} = w_m R, \; r_{A,ref} = \rho_{B,P}\phi_{ref}/R^2, \tag{56}$$

$$w_m = f_{A-B}u_{inj}, \quad \Gamma_o = Rv_o$$

The boundary conditions are non-dimensionalized in the same way and presented in the summary section of the differential equations and the boundary conditions in Chapter III.

CHAPTER III

METHOD OF SOLUTION

Due to the extreme complexity and added difficulties arising from the non-linearities of the equations, any hope for an exact analytical solution is remote. Therefore, it was decided to seek approximate numerical solutions by finite differences. The governing equations are formulated in terms of the stream function, the vorticity and the potential function. The system of equations consists of two elliptic, three parabolic and an algebraic equation. The steady state solution is obtained by a large time solution of an unsteady problem. When a time dependent solution is sought, the solution procedure requires the solution of two elliptic equations after every time step. Since the solution of elliptic equations is the most time consuming, it is important to select an efficient numerical scheme for elliptic equations. Both the successive-over-relaxation (SOR) and the alternating-direction-implicit (ADI) method are known to be efficient. However, ADI method of Peaceman and Rachford[26] has been chosen because of its relatively high convergence rate compared to SOR as the number of nodes in the mesh becomes large. This has been shown in the numerical experiments of Birkhoff, Varga and Young.[8]

ADI is also used for the parabolic equations. The stationary ADI (fixed parameter) which is used throughout this study is proven unconditionally stable for a simple

diffusion equation by Peaceman and Rachford. Later this property of unconditional stability is shown by Pearson[27] to apply to the diffusion equation with first order derivatives included. Various numerical schemes used in various hydrodynamic problems are reviewed by Ames.[1]

Once the steady state solution is obtained for the set of equations, the pressure is calculated either by line integration of the momentum equation or by solving the Poisson equation obtained by taking the divergence of the momentum equation. The Poisson equation was solved by the method of Fourier analysis,[18] in which a computational algorithm known as fast Fourier transforms was employed.

Summary of Differential Equations and Boundary Conditions

The set of governing equations and boundary conditions given in Ch. II are summarized and rewritten below in a non-dimensional form*

The stream function equation:

$$\left(\frac{1}{\rho r}\psi_r\right)_r + \frac{1}{a^2}\left(\frac{1}{\rho r}\psi_z\right)_z = -\frac{1}{b^4} rH \qquad (47)$$

The vorticity equation:

$$H_t = \frac{1}{\rho}\left[H_{rr} + \frac{3}{r}H_r + \frac{1}{a^2}H_{zz} - \frac{Re}{br}(r\rho uH)_r - \frac{Re}{ba}(\rho wH)_z\right]$$

(continued)

* The superscript (*) for the non-dimensional variables is suppressed from here on.

$$+ \frac{Re}{b}\left[\epsilon\frac{r_A}{\rho} - (u_r + \frac{u}{r} + \frac{1}{a}w_z)\right] H + \frac{2b}{Rer}\left[\frac{Re_t^2}{ar^3}(\Gamma^2)_z\right.$$

$$\left. - \frac{Re^2\rho_z}{a\rho}(uu_r + \frac{1}{a}wu_z - \frac{Re_t^2}{Re^2}\frac{\Gamma^2}{r^3}) + \frac{Re^2\rho_r}{\rho}(uw_r + \frac{1}{a}ww_z)\right]$$

(49)

The angular momentum equation:

$$\Gamma_t = \frac{1}{\rho}\left[\Gamma_{rr} - \frac{1}{r}\Gamma_r + \frac{1}{a^2}\Gamma_{zz} - \frac{Re}{br}(r\rho u\Gamma)_r\right.$$

$$\left. - \frac{Re}{ba}(\rho w\Gamma)_z\right] + \frac{Re\epsilon r_A}{b}\Gamma \qquad (50)$$

The mass diffusion equation:

$$c_t = \frac{1}{s_c}\left[c_{rr} + (\frac{1}{r} + \frac{\rho_r}{\rho})c_r + \frac{1}{a^2}c_{zz} + \frac{1}{a^2}\frac{\rho_z}{\rho}c_z\right]$$

$$-\frac{Re}{b\rho r}(r\rho uc)_r - \frac{Re}{ba\rho}(\rho wc)_z + \frac{Re\epsilon r_A}{b\rho} \qquad (51)$$

The potential function equation:

$$\phi_{rr} + (\frac{1}{r} + \frac{\rho_r}{\rho})\phi_r + \frac{1}{a^2}\phi_{zz} + \frac{1}{a^2}\frac{\rho_z}{\rho}\phi_z + \frac{r_A}{\rho} = 0 \qquad (48)$$

The density equation:

$$\rho = \frac{\rho_{A,P}/\rho_{B,P}}{\rho_{A,P}/\rho_{B,P} + c(1 - \rho_{A,P}/\rho_{B,P})} \tag{52}$$

The velocity equations:

$$u = -\frac{b^2}{2a\rho r}\psi_z - \varepsilon\phi_r \tag{46a}$$

$$w = \frac{b^2}{2\rho r}\psi_r - \frac{\varepsilon}{a}\phi_z \tag{46b}$$

The pressure equations:

$$p_r = -F_1 \tag{53a}$$

$$\frac{1}{a}p_z = -F_2 \tag{53b}$$

$$\nabla^2 p = -S \tag{54a}$$

where

$$F_1 = \rho(uu_r + \frac{w}{a}u_z - \frac{Re_t^2}{Re^2}\frac{v^2}{r}) - \frac{b}{Re}(\nabla^2 u - \frac{u}{r^2})$$

$$- \frac{b}{3Re}(u_r + \frac{u}{r} + \frac{1}{a}w_z)_r \tag{53c}$$

$$F_2 = \rho(uw_r + \frac{w}{a}w_z) - \frac{b}{Re}\nabla^2 w - \frac{b}{3aRe}(u_r + \frac{u}{r} + \frac{1}{a}w_z)_z$$

(53d)

$$S = \frac{1}{r}(rF_1)_r + \frac{1}{a}(F_2)_z \qquad (54b)$$

And the boundary conditions:

$$\psi(0,z) = 0 \qquad (57)$$

$$\psi(r,0) = 0 \qquad (58)$$

$$\psi(1,z) = -\frac{2a}{b^2}\int_0^z \rho(1,z)\left[-u_{inj} + \phi_r(1,z)\right]dz \qquad (59)$$

$$\psi(r,1) = \psi(1,1) \qquad \text{for } b < r < 1 \qquad (60a)$$

$$\psi(r,1) = \frac{2}{b^2}\int_0^r \rho(r,1)r\left[1 + \frac{\varepsilon}{a}\phi_z(r,1)\right]dr$$

$$\text{for } 0 < r < b \qquad (60b)$$

$$H_r(0,z) = 0 \qquad (61)$$

$$H(r,0) = -\left[\frac{b^4}{a^2\rho r}(-\frac{\rho_z}{\rho}\psi_z + \psi_{zz})\right]_{(r,0)}$$

$$\text{subject to } \psi_z = -\left[\frac{2\varepsilon a}{b^2}\rho r\phi_r\right]_{(r,0)} \qquad (62)$$

$$H(1,z) = -\left[\frac{b^4}{\rho r^2}\psi_{rr}\right](1,z)$$

$$\text{subject to } \psi_r\Big|_{(1,z)} = 0 \tag{63}$$

$$H(r,1) = -\frac{b^4}{r}\left[\left(\frac{1}{\rho r}\psi_r\right)_r + \frac{1}{a^2\rho r}\left(-\frac{\rho_z}{\rho}\psi_z + \psi_{zz}\right)\right](r,1)$$

$$\text{subject to } \psi_z = -\left[\frac{2\varepsilon a}{b^2}\rho r\phi_r\right](r,1) \tag{64}$$

$$\Gamma(0,z) = 0 \tag{65}$$

$$\Gamma(r,0) = 0 \tag{66}$$

$$\Gamma(1,z) = 1 \tag{67}$$

$$\Gamma(r,1) = 0 \tag{68}$$

$$c_r(0,z) = 0 \tag{69}$$

$$c_z(r,0) = 0 \tag{70}$$

$$c_r(1,z) + \frac{ReS_c}{b}u_{inj}c(1,z) = 0 \tag{71}$$

$$c_z(r,1) = 0 \tag{72}$$

$$\phi_r(0,z) = 0 \tag{73}$$

$$\phi_z(r,0) = 0 \tag{74}$$

$$\phi(1,z) = 0 \tag{75}$$

$$\phi_z(r,1) = 0 \quad \text{for } b < r < 1 \tag{76a}$$

$$\phi(r,1) = 0 \text{ for } 0 < r < b \tag{76b}$$

Now that the parabolic equations are expressed in a general form the finite difference equations can also be expressed in a general manner.

The parabolic equations in a conservation form can be written as:

$$f_t = Af_{rr} + Bf_r + Cf_{zz} + Df_z + E(r\rho uf)_r + F(\rho wf)_z + Gf + H \tag{77}$$

The coefficients A through H appearing in this equation can be obtained by comparison with individual equations.

The Numerical Method by Finite Differences

In order to apply the finite difference approximations to the set of governing equations, the region of interest is divided into a finite number of subregions with

equal spacings. Since in the numerical computation the desired steady state solution is obtained by a large time solution of unsteady state problem, the time coordinate is also divided into a finite number of steps. With this grid system a differential equation of a continuous function is transformed into a system of finite difference equations of discrete mesh functions. The relationship between the continuous function f(r,z,t) and the mesh function $f^n_{i,j}$ is

$$f^n_{i,j} \stackrel{\sim}{=} f(i\Delta r,\ j\Delta z,\ n\Delta t)$$

since

$$r_i = i\Delta r, \quad i = 0,1,2.....,N$$

$$z_j = j\Delta z, \quad j = 0,1,2,.....,M$$

$$t_n = n\Delta t, \quad n = 0,1,2,.....,L$$

Finite Difference Approximations of Parabolic Equations. The non-iterative implicit numerical scheme, the alternating-direction-implicit procedure of Peaceman and Rachford[26] is employed for the finite difference approximation. In this method, each equation is written in a sequence of two difference equations each of which is implicit in only one space coordinate involving only a half time step. Now the finite difference equations obtained after applying ADI to the general form of parabolic equations,

Eq. 77 are:

for the first time step,

$$\frac{2}{\alpha}(f_{i,j}^{n+1/2} - f_{i,j}^{n}) = \frac{A}{\beta}(f_{i-1,j}^{n+1/2} - 2f_{i,j}^{n+1/2} + f_{i+1,j}^{n+1/2})$$

$$+ \frac{kB}{2}(f_{i+1,j}^{n+1/2} - f_{i-1,j}^{n+1/2}) + \beta C(f_{i,j-1}^{n} - 2f_{i,j}^{n} + f_{i,j+1}^{n})$$

$$+ \frac{hD}{2}(f_{i,j+1}^{n} - f_{i,j-1}^{n}) + \frac{kE}{2}(r_{i+1}\rho_{i+1,j}^{n+1/2}u_{i+1,j}^{n+1/2}f_{i+1,j}^{n+1/2}$$

$$- r_{i-1}\rho_{i-1,j}^{n+1/2}u_{i-1,j}^{n+1/2}f_{i-1,j}^{n+1/2}) + \frac{hF}{2}(\rho_{i,j+1}^{n}w_{i,j+1}^{n}f_{i,j+1}^{n}$$

$$-\rho_{i,j-1}^{n}w_{i,j-1}^{n}f_{i,j-1}^{n}) + \frac{\delta G}{2}(f_{i,j}^{n+1/2} + f_{i,j}^{n}) + \delta H \qquad (78a)$$

and for the second half step,

$$\frac{2}{\alpha}(f_{i,j}^{n+1} - f_{i,j}^{n+1/2}) = \frac{A}{\beta}(f_{i-1,j}^{n+1/2} - 2f_{i,j}^{n+1/2} + f_{i+1,j}^{n+1/2}$$

$$+ \frac{kB}{2}(f_{i+1,j}^{n+1/2} - f_{i-1,j}^{n+1/2}) + \beta C(f_{i,j-1}^{n+1} - 2f_{i,j}^{n+1} + f_{i,j+1}^{n+1})$$

$$+ \frac{hD}{2}(f_{i,j+1}^{n+1} - f_{i,j-1}^{n+1}) + \frac{kE}{2}(r_{i+1}\rho_{i+1,j}^{n+1/2}u_{i+1,j}^{n+1/2}f_{i+1,j}^{n+1/2}$$

$$-r_{i-1}\rho_{i-1,j}^{n+1/2}u_{i-1,j}^{n+1/2}f_{i-1,j}^{n+1/2}) + \frac{hF}{2}(\rho_{i,j+1}^{n+1}w_{i,j+1}^{n+1}f_{i,j+1}^{n+1}$$

$$- \rho_{i,j-1}^{n+1}w_{i,j-1}^{n+1}f_{i,j-1}^{n+1}) + \frac{\delta G}{2}(f_{i,j}^{n+1} + f_{i,j}^{n+1/2}) + \delta H \qquad (78b)$$

where $h = \Delta r$, $k = \Delta z$, $\alpha = \Delta t/hk$, $\beta = h/k$ and $\delta = hk$. Above equations are rearranged and given in a form convenient for numerical computation:

$$a^*_{i,j} f^{n+1/2}_{i-1,j} + b^*_{i,j} f^{n+1/2}_{i,j} + c^*_{i,j} f^{n+1/2}_{i+1,j} = d^*_{i,j} \tag{79a}$$

$$a^{**}_{i,j} f^{n+1}_{i,j-1} + b^{**}_{i,j} f^{n+1}_{i,j} + c^{**}_{i,j} f^{n+1}_{i,j+1} = d^{**}_{i,j} \tag{79b}$$

where

$$a^*_{i,j} = \frac{1}{\beta}A - \frac{k}{2}B - \frac{k}{2}E\, r_{i-1}\rho^{n+1/2}_{i-i,j}u^{n+1/2}_{i-1,j}$$

$$b^*_{i,j} = -\frac{2}{\alpha} - \frac{2}{\beta}A + \frac{\delta}{2}G$$

$$c^*_{i,j} = \frac{1}{\beta}A + \frac{k}{2}B + \frac{k}{2}E\, r_{i+1}\rho^{n+1/2}_{i+1,j}u^{n+1/2}_{i+1,j} \tag{80a}$$

$$d^*_{i,j} = -\frac{2}{\alpha}f^n_{i,j} - (f^n_{i,j-1} - 2f^n_{i,j} + f^n_{i,j+1})\beta C$$

$$-\frac{h}{2}(f^n_{i,j+1} - f^n_{i,j-1})D - \frac{h}{2}(\rho^n_{i,j+1}w^n_{i,j+1}f^n_{i,j+1}$$

$$- \rho^n_{i,j-1}w^n_{i,j-1}f^n_{i,j-1})F - \frac{\delta}{2}Gf^n_{i,j} - \delta H$$

$$a^{**}_{i,j} = \beta C - \frac{h}{2}D - \frac{h}{2}F\rho^{n+1}_{i,j-1}w^{n+1}_{i,j-1}$$

(continued)

$$b^{**}_{i,j} = -\frac{2}{\alpha} - 2\beta C + \frac{\delta}{2}G$$

$$c^{**}_{i,j} = \beta C + \frac{h}{2}D + \frac{h}{2}F\rho^{n+1}_{i,j+1}w^{n+1}_{i,j+1} \qquad (80b)$$

$$d^{**}_{i,j} = -\frac{2}{\alpha}f^{n+1/2}_{i,j} - \frac{1}{\beta}(f^{n+1/2}_{i-1,j} - 2f^{n+1/2}_{i,j} + f^{n+1/2}_{i+1,j})A$$

$$- \frac{k}{2}(f^{n+1/2}_{i+1,j} - f^{n+1/2}_{i-1,j})B - \frac{k}{2}(r_{i+1}\rho^{n+1/2}_{i+1,j}u^{n+1/2}_{i+1,j}f^{n+1/2}_{i+1,j}$$

$$- r_{i-1}\rho^{n+1/2}_{i-1,j}u^{n+1/2}_{i-1,j}f^{n+1/2}_{i-1,j})E - \frac{\delta}{2}Gf^{n+1/2}_{i,j} - \delta H$$

Finite Difference Approximations of Elliptic Equations. The ADI of Peaceman and Rachford is also used for the elliptic equations. Iterations are carried out first implicitly in r coordinate and next in z coordinate in an alternating manner. Following Birkhoff, Varga and Young[8] for the case of a single iteration parameter, the finite difference equations can be expressed as the following.

The finite difference equations of the stream function:

for the first iterate,

$$-\frac{2}{\beta(\rho_{i,j}r_i - \rho_{i-1,j}r_{i-1})}\psi^{*}_{i-1,j} + \left[\frac{2}{\beta}\left(\frac{1}{\rho_{i+1,j}r_{i+1} + \rho_{i,j}r_i}\right.\right.$$

$$\left.\left. + \frac{1}{\rho_{i,j}r_i + \rho_{i-1,j}r_{i-1}}\right) + q_s\right]\psi^{*}_{i,j} - \frac{2}{\beta(\rho_{i+1,j}r_{i+1} + \rho_{i,j}r_i)}$$

$$\psi^{*}_{i+1,j} = q_s\psi_{i,j} + \frac{2\beta}{a^2 r_i}\left[\frac{1}{\rho_{i,j+1} + \rho_{i,j}}(\psi_{i,j+1} - \psi_{i,j})\right.$$

$$\left. - \frac{1}{\rho_{i,j} + \rho_{i,j-1}}(\psi_{i,j} - \psi_{i,j-1})\right] + \frac{\delta}{b^4} r_i H_{i,j} \qquad (81a)$$

and for the second iterate,

$$- \frac{2\beta}{a^2 r_i(\rho_{i,j} + \rho_{i,j-1})}\psi^{**}_{i,j-1} + \left[\frac{2\beta}{a^2 r_i}\left(\frac{1}{\rho_{i,j+1} + \rho_{i,j}}\right.\right.$$

$$\left.\left. + \frac{1}{\rho_{i,j} + \rho_{i,j-1}}\right) + q_s\right]\psi^{**}_{i,j} - \frac{2\beta}{a^2 r_i(\rho_{i,j+1} + \rho_{i,j})}\psi^{**}_{i,j+1}$$

$$= q_s\psi^{*}_{i,j} + \frac{2}{\beta}\left[\frac{1}{\rho_{i+1,j}r_{i+1} + \rho_{i,j}r_i}(\psi^{*}_{i+1,j} - \psi^{*}_{i,j})\right.$$

$$\left. - \frac{1}{\rho_{i,j}r_i + \rho_{i-1,j}r_{i-1}}(\psi^{*}_{i,j} - \psi^{*}_{i-1,j})\right] + \frac{\delta}{b^4} r_i H_{i,j} \qquad (81b)$$

The finite difference equations of the potential function: for the first iterate,

$$\left[-\frac{1}{\beta} + \frac{k}{2}\left(\frac{1}{r_i} + \frac{\rho_{i+1,j} - \rho_{i-1,j}}{2h\rho_{i,j}}\right)\right]\phi^{*}_{i-1,j} + \left(\frac{2}{\beta} + q_p\right)\phi^{*}_{i,j}$$

$$- \left[\frac{1}{\beta} + \frac{k}{2}\left(\frac{1}{r_i} + \frac{\rho_{i+1,j} - \rho_{i-1,j}}{2h\rho_{i,j}}\right)\right]\phi^{*}_{i+1,j} = q_p\phi_{i,j} + \frac{\beta}{a^2}(\phi_{i,j-1}$$

$$- 2\phi_{i,j} + \phi_{i,j+1}) + \frac{\beta}{4a^2\rho_{i,j}}(\rho_{i,j+1} - \rho_{i,j-1})(\phi_{i,j+1} - \phi_{i,j-1})$$

$$+ \frac{\delta(r_A)_{i,j}}{\rho_{i,j}} \qquad (82a)$$

and for the second iterate,

$$\frac{\beta}{a^2}(-1 + \frac{\rho_{i,j+1} - \rho_{i,j-1}}{4\rho_{i,j}})\phi^{**}_{i,j-1} + (\frac{2\beta}{a^2} + q_p)\phi^{**}_{i,j} - \frac{\beta}{a^2}(1$$

$$+ \frac{\rho_{i,j+1} - \rho_{i,j-1}}{4\rho_{i,j}})\phi^{**}_{i,j+1} = q_p\phi^{*}_{i,j} + \frac{1}{\beta}(\phi^{*}_{i-1,j} - 2\phi^{*}_{i,j}$$

$$+ \phi^{*}_{i+1,j}) + \frac{k}{2}(\frac{1}{r_i} + \frac{\rho_{i+1,j} - \rho_{i-1,j}}{2h\rho_{i,j}})(\phi^{*}_{i+1,j} - \phi^{*}_{i-1,j})$$

$$+ \frac{\delta(r_A)_{i,j}}{\rho_{i,j}} \qquad (82b)$$

In above equations the functions with superscripts (*) and (**) represent the first and the second iterate respectively.

The Numerical Method and the Finite Difference Approximations of the Boundary Conditions. The finite difference equations obtained by ADI method as given above result in a tridiagonal system of algebraic equations since each equation is implicit in only one direction. The solution of the tridiagonal system is obtained by an efficient matrix inversion

known as the Thomas method described by Lee.[21] In general, non-linear problems can be treated as a set of linear problems. In the present problem non-linearities exist in the equations as well as in the boundary conditions, i.e., the boundary conditions for the vorticity. When it is necessary to account for non-linearities, the equations and the boundary conditions are iterated over the same time step until a predetermined convergence criterion is satisfied before advancing to a new time level.

The boundary conditions are all approximated by finite differences with second order accuracy to be consistent with the accuracy associated with the finite difference equations. The first and second order derivatives for boundary points are expressed in finite differences as in the following.
The first order derivative:

$$f_x(x_o^+) = \frac{1}{2\Delta x}\left[-3f(x_o) + 4f(x_o + \Delta x) - f(x_o + 2\Delta x)\right] + O(\Delta x^2)$$

$$f_x(x_o^-) = \frac{1}{2\Delta x}\left[3f(x_o) - 4f(x_o - \Delta x) + f(x_o - 2\Delta x)\right] + O(\Delta x^2)$$

The second order derivative with a specified value of first order derivative:

$$f_{xx}(x_o^+) = \frac{1}{2\Delta x^2}\left[-6f'(x_o)\Delta x - 7f(x_o) + 8f(x_o + \Delta x) - f(x_o + 2\Delta x)\right] + 0(\Delta x^2)$$

$$f_{xx}(x_o^-) = \frac{1}{2\Delta x^2}\left[6x'(x_o)\Delta x - 7f(x_o) + 8f(x_o - \Delta x) - f(x_o - 2\Delta x)\right] + 0(\Delta x^2)$$

Finally, the second order derivative with no restriction on the first order derivative:

$$f_{xx}(x_o^+) = \frac{1}{\Delta x^2}\left[2f(x_o) - 5f(x_o + \Delta x) + 4f(x_o + 2\Delta x) - f(x_o + 3\Delta x)\right] + 0(\Delta x^2)$$

$$f_{xx}(x_o^-) = \frac{1}{\Delta x^2}\left[2f(x_o) - 5f(x_o - \Delta x) + 4f(x_o - 2\Delta x) - f(x_o - 3\Delta x)\right] + 0(\Delta x^2)$$

In the following, the computational procedure is described to obtain the near-steady-state solution by the time dependent formulation. At a certain time level, n, all the functional values are known from which functional values at a new time level, n+1, are to be obtained. This procedure is repeated until a predetermined criterion is met for the

steady state solution.

(1) Compute Γ^{n+1} solving the ADI equation of Γ using the functional values known at time level n.

(2) Compute H^{n+1} solving the ADI equation of H with boundary conditions based on current value of ψ and ρ.

(3) Using the elliptic ADI equation of ψ compute ψ^{n+1} by repeating the iterations* until the following convergence criterion is satisfied:

$$\text{Max.} \quad \left|\psi_{i,j}^{n+1} - \psi^{n}\right| \leq \varepsilon_1 \psi_{ref}$$

where ε_1 is some small positive number and ψ_{ref} is some reference value of ~~the stream function~~.

(4) Improve u^{n+1} and w^{n+1} using current value of ψ computed in step (3).

~~(5) Co~~mpute c^{n+1} solving the ADI equation of c using the currently available values of other functions involved.

(6) Update ρ^{n+1} using recent value of c obtained in step (5).

(7) Using the elliptic ADI equation of ϕ, compute ϕ^{n+1} by repeating the iterations* until the following

---

* If only the steady state solution is needed, the iteration is terminated after one cycle, which yields a meaningless intermediate solution. However, it results in an appreciable reduction in computation time.

criterion is met:

$$\text{Max.} \quad \left|\psi_{i,j}^{n+1} - \psi_{i,j}^{n}\right| \leq \varepsilon_2 \phi_{ref}$$

where ε_2 is some small positive number and ϕ_{ref} is some reference value of the potential function.

(8) Update u^{n+1} and w^{n+1} using current values of ψ, ρ and ϕ obtained in steps (3), (6) and (7) respectively.

(9) Evaluate the boundary values of H based on current values of ψ, ρ and ϕ.

(10) Return to step (1) and repeat the cycle without advancing the time step*. With these non-linear time iterations the solution approaches that of the time dependent problem. The iteration is terminated when the following convergence criterion is satisfied.

$$\text{Max.} \quad \left|\psi_{i,j}^{k+1} - \psi_{i,j}^{k}\right| \leq \varepsilon_3 \psi_{ref}$$

where k is the iteration counter and ε_3 is some small positive number. This completes the computational procedure for one time step advancing.

(11) For a steady state solution, above procedures are repeated until the time dependent solution converges

---

* If interested in large time solution only, this iteration is not necessary except in the first few time steps.

to the steady state solution. The convergence criterion is again:

$$\text{Max.} \quad \left|\psi_{i,j}^{n+1} - \psi_{i,j}^{n}\right| \leq \varepsilon_4 \psi_{ref}$$

where ε_4 is some small positive number.

Pressure Calculation

Once the steady state solution is obtained from the set of governing equations formulated in the stream function, vorticity and potential function, the pressure is obtained either by a line integration or solving the Poisson equation of pressure.

Pressure by Line Integration. This method involves evaluation of pressure gradients at every grid point in the region and numerical integration along conveniently chosen paths. In this study, pressure is first integrated axially along $r^* = 0.5$ from $z^* = 0$ to $z^* = 1$, and next radially inward and outward to cover the entire region. Pressure gradients are obtained using Eq. 53 for known velocity field. This equation is rewritten below:

$$p_r = -\rho\left(uu_r + \frac{w}{a}u_z - \frac{Re_t^2}{Re^2}\frac{v^2}{r}\right) + \frac{b}{Re}\left(\nabla^2 u - \frac{u}{r^2}\right) + \frac{b}{3Re}$$

$$\left(u_r + \frac{u}{r} + \frac{1}{a}w_z\right)_r \qquad (53a)$$

$$p_z = -\rho(uw_r + \frac{w}{a}w_z) + \frac{b}{Re}\nabla^2 w + \frac{b}{3aRe}(u_r + \frac{u}{r} + \frac{1}{a}w_z)_z \tag{53b}$$

The integration formula used here is known as Euler's polygonal curves:

$$f(x_o - \Delta x) = f(x_o) + \frac{\Delta x}{12}\left[-5f_x(x_o - \Delta x) - 8f_x(x_o) + f_x(x_o + \Delta x)\right]$$

$$f(x_o) = f(x_o - \Delta x) + \frac{\Delta x}{12}\left[5f_x(x_o - \Delta x) + 8f_x(x_o) - f_x(x_o + \Delta x)\right] \tag{83}$$

$$f(x_o + \Delta x) = f(x_o) + \frac{\Delta x}{12}\left[-f_x(x_o - \Delta x) + 8f_x(x_o) + 5f_x(x_o + \Delta x)\right]$$

Pressure by Solution of Poisson Equation. The pressure can also be obtained by solving the Poisson equation of pressure Eq. 54. This equation is rewritten below:

$$\nabla^2 p = -S(r,z) \tag{54a}$$

where the source function S is a known function when the

velocity field is obtained. The boundary conditions are obtained from the known velocity field by Eq. 53a and 53b. Since it is difficult to solve a Poisson equation with Neumann boundary conditions all around, it was decided to obtain solutions by a series expansion in eigenfunctions. This method is similar to that of Green's function and is chosen because of its computational efficiency.

The Poisson equation with inhomogeneous boundary conditions is first converted into one with homogeneous boundary conditions. This is accomplished by constructing a simple function p_o such that it satisfies the original inhomogeneous boundary conditions.[18] Then the solution to the homogeneous problem $\bar{p}$ is related with that of the original inhomogeneous problem p by:

$$\bar{p} = p - p_o \tag{84}$$

The resulting Poisson equation with homogeneous Neumann boundary conditions is:

$$\nabla^2\bar{p} = -\bar{S} \tag{85a}$$

where

$$\bar{S} = S + \nabla^2 p_o \tag{85b}$$

Now assume a form of the solution as a finite sum of Fourier cosine functions of z and at the same time expand the source function in a finite cosine series:

$$\bar{p} = \frac{1}{2}c_o(r) + \sum_{n=1}^{N} c_n(r)\cos n\pi z \tag{86}$$

$$-\bar{S} = \frac{1}{2}d_o(r) + \sum_{n=1}^{N} d_n(r)\cos n\pi z \tag{87}$$

The number of terms in the series is taken same as that of the mesh points in z coordinates.[15][16] Substituting these equations into Eq. 85a yields a set of ordinary differential equations for the Fourier amplitudes:

$$c_n''(r) + \frac{1}{r}c_n'(r) - \frac{n^2\pi^2}{a^2}c_n(r) = d_n(r), \quad n = 0,1,\ldots,N \tag{88}$$

with homogeneous Neumann boundary conditions:

$$c_n'(r) = 0 \text{ at } r = 0 \text{ and } r = 1 \tag{89}$$

This set of ordinary differential equations was solved numerically by finite differences, in which the Thomas method is used for the resulting tri-diagonal system. A matter deserving a comment here is that the fundamental Fourier amplitude $c_o(r)$ can best be determined within an additive constant. This is the reason why the pressure can only be determined within some constant. Once $\bar{p}$ is obtained, p is determined by Eq. 84.

For purposes of computational efficiency, a simple version of the fast Fourier transforms (FFT) is used. The reduction in computation time is accomplished by using the symmetry property of cosine functions to minimize the multiplicative operations. The reduction in computation time realized is approximately by a factor of 4. The method of performing the fast Fourier cosine transforms is given in Appendix A.

CHAPTER IV

ERROR ANALYSIS

In this chapter, various errors involved in the numerical computation are discussed. Efforts are made to check the solutions obtained internally as well as externally by way of comparisons with other related studies. Unfortunately, a solution to the present problem in its full complexity does not exist in the published literature. However, results of visualization experiments and numerical studies of similar rotating flows are found and they are used for both qualitative and quantitative verifications.

There are two major sources of error in solutions obtained by numerical methods. The discretization error is the difference between the exact solutions of the finite difference equations and those of the differential equations. In addition, actual numerical solutions include another error called the round-off error since the computing machine uses only a finite number of digits.

In this work, equations are posed as an initial value problem and steady state solutions are obtained by continuing the computation until the solution no longer changes. The solutions thus obtained contain both discretization and round-off errors. If, in the solution procedures, these errors remain bounded as time increases, the numerical scheme is said to be stable. As the mesh size decreases,

the finite difference equations approach the differential equations since truncated Taylor series expansions are used for the finite difference representation. The consistency condition[29] is thus satisfied. For certain simple linear problems, the consistency and stability are shown by Lax's Theorem[29] to imply convergence. Hence for simple problems, it is proved that stable numerical solutions converge to the solutions of differential equations when the mesh size approaches zero. However, the theorem does not extend in general to apply to more complex and non-linear equations. Therefore, the result of Lax's Theorem can only be used as guides for non-linear problems and the numerical solutions obtained in this work are subject to verification as to their validity as solutions to the differential equations.

In order to answer the question of how closely the numerical results obtained approximate the true solutions of the differential equations, a series of checks are made. They are briefly listed below and described in the remainder of this chapter.

(1) Verify how well the numerical solution satisfies the constraint of the continuity equation on a discrete basis.

(2) Check how closely the compatibility condition* is satisfied by individual species (the over-all

---

* The surface integral of flux on boundary being compatible with the volume integral of source in the interior.

species balance).

(3) Check how well the numerical solution satisfies the compatibility condition for the Poisson equation of pressure.

(4) Establish the uniqueness of the steady state solution by using different initial conditions.

(5) Compare the numerical results of the present study with reported visualization experiments for a qualitative verification.

(6) Use the computer program of this study to solve the rotating flow problem of Pao[25] and compare the results for a quantitative verification.

(7) Estimate the discretization error by an extrapolation using different grid sizes.

(8) Calculate the pressure by both line integration of the momentum equation and by the solution of the Poisson equation for the pressure and compare the results.

The first three of these checks are considered to be weak internal checks. Whereas the next four are strong positive checks. Finally, item (8) is believed sufficient for the verification of the pressure results.

Internal Checks

The checks mentioned in this section are simple internal checks which partially contribute to the verification of the numerical solutions reported in this work. The first

verification is of the continuity equation in the finite difference approximation. The error in the continuity equation is:

$$e(r,z) = \frac{1}{r}(r\rho u)_r + \frac{1}{a}w_z - \varepsilon r_A \qquad (90)$$

where e(r,z) represents the error in a non-dimensional form. The relative local error, i.e. the absolute error e(r,z) divided by the largest of the three terms involved, are computed at every interior grid point for four selected runs. These four runs were selected in such a way that they are representative of all the cases considered in this study and also they are expected to have the maximum error. The results show that the relative errors are less than 10^{-5} at all interior node points except at the two nodes adjacent to the boundary point at which the exit hole terminates. At these two interior nodes the errors are found to be as large as 50 percent. It indicates that the violation of the continuity constraint is localized very close to a point which is nearly a singular point and does not extend into the interior.

The second check made is on the over-all balance of species. For every computer run, the total amount of interior mass injection and the sum of mass transfer across the boundary are computed for the component A. This checks the compatibility condition for the mass diffusion equation

as well as the general validity of the numerical solution. The results of this check shows that the condition is satisfied to within less than 5 percent error.

The third simple check carried out is on the compatibility condition of the Poisson equation of pressure. The source term and the boundary conditions are evaluated from known solutions of kinematics. If the numerical solution obtained for the kinematics is valid, the boundary conditions are expected to be compatible with the differential equation. This is the reason why the verification of the compatibility condition serves as a check for a valid solution of kinematics. The result shows that this condition is met within less than 10 percent deviation for all rotating flows considered. For non-rotating flows, however, the error is found to be as large as 50 percent. For this reason, the line integration method was adopted for pressure calculations of all non-rotating flows.

Finally, the uniqueness of the steady state solution is established since identical results are obtained from three different initial conditions for two chosen flow cases. The initial conditions considered are those of solid body rotation, those in which the interior values are interpolated from boundary conditions, and finally initial values of zero everywhere in the region. Single component flows of $Re = 20$, $Re_t = 0$ and $Re = 20$, $Re_t = 50$ were used for this part of the analysis.

Comparison with Results of Prior Works

In this section comparisons are made of the results of the present work with those of prior studies of other investigators. The first comparison is made with the experimental visualization results by Roschke[30] and Ross.[32] These studies were concerned with the secondary flow patterns obtained in jet-driven vortices which had a small exit hole on one end. Schematic sketches of the over-all flow pattern were drawn from the visualization results. These sketches showed features such as boundary layer flows on stationary end walls and vortex core flows along the cylinder axis toward the exhaust hole. This over-all secondary flow pattern is consistent with the numerical results of the present study as given in the next chapter. And this is considered to be a global, qualitative verification.

The second check made is with the numerical solution of Pao[25] who considered the steady motion of an incompressible flow in a finite cylindrical container. In this problem one end wall was stationary and the other rotated with the periphery. The governing equations of this problem are identical to those of the present study for the special case of single component flow. Furthermore, this problem is considered to possess the same mathematical complexity as well as the flow features of the present problem. the boundary conditions of Pao's problem are:

$$r = 0;\ u = 0,\ v = 0,\ w_r = 0$$

$r = 1;\ u = 0,\ v = 1,\ w = 0$

$z = 0;\ u = 0,\ v = 0,\ w = 0$

$z = 1;\ u = 0,\ v = r,\ w = 0$

The computer program written for the present problem was modified to meet the above boundary conditions. This modified program was used to solve Pao's problem for the case of $Re_t = 100$* and the result obtained was compared with that given by Pao. In Figure 2 the stream function is compared for a fixed axial location, $z^* = 0.5$. The axial velocity along the cylinder axis is compared in Fig. 3. Finally, a comparison is made in Fig. 4 of the radial velocity along three different radial distances, r^*=0.2,0.4 and0.6.

The comparison is excellent as shown. It may be mentioned that in both Pao's and the present work, the finite difference approximations were of second order accuracy although different numerical schemes were used. Pao's numerical results are supported by his visualization experiments. The comparison with Pao's solution is considered to serve as a strong quantitative verification on the validity of the numerical results reported in this work.

Estimate of Discretization Error

In this section, discretization error is estimated based on a quadratic extrapolation which is similar to Richardson's extrapolation.[28] The method involves

---

* The characteristic velocity and the length used in the tangential Reynolds number are v_o and R respectively.

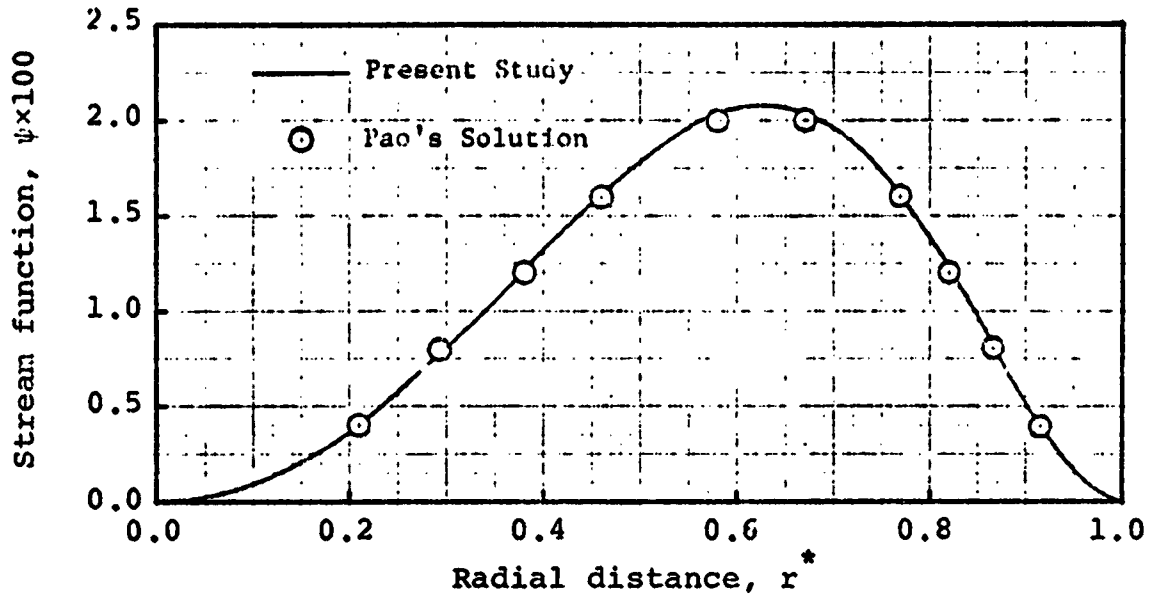

Fig. 2. Comparison of the Stream Function along $z^* = 0.5$ of the Present Study with That of Pao's for $Re_t = 100$.

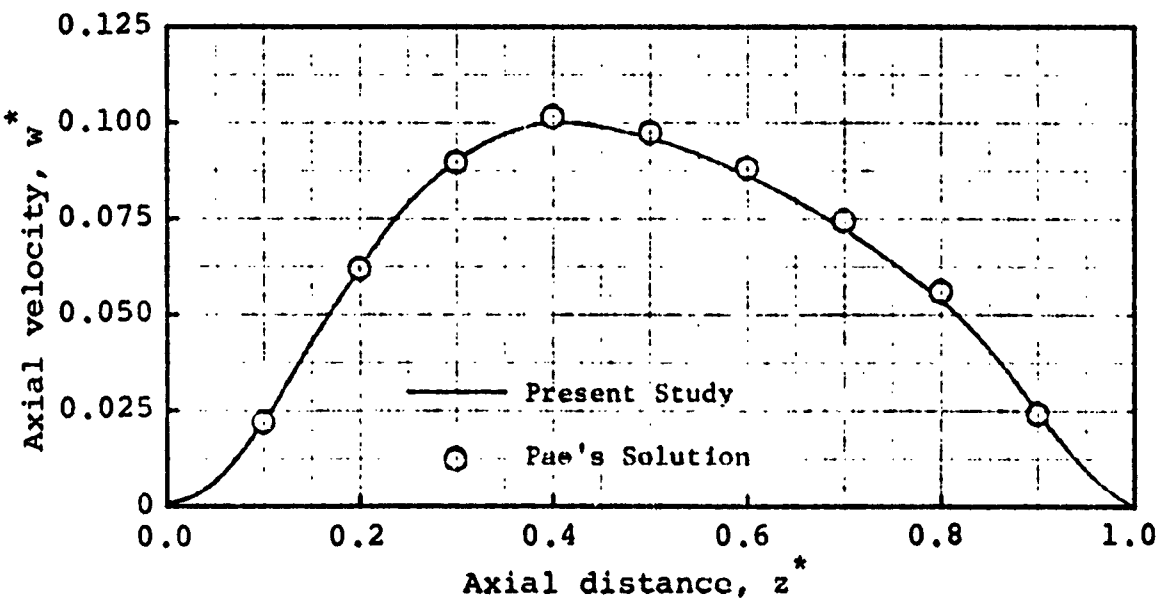

Fig. 3. Comparison of the Axial Velocity along the Center Line of the Present Study with That of Pao's for $Re_t = 100$.

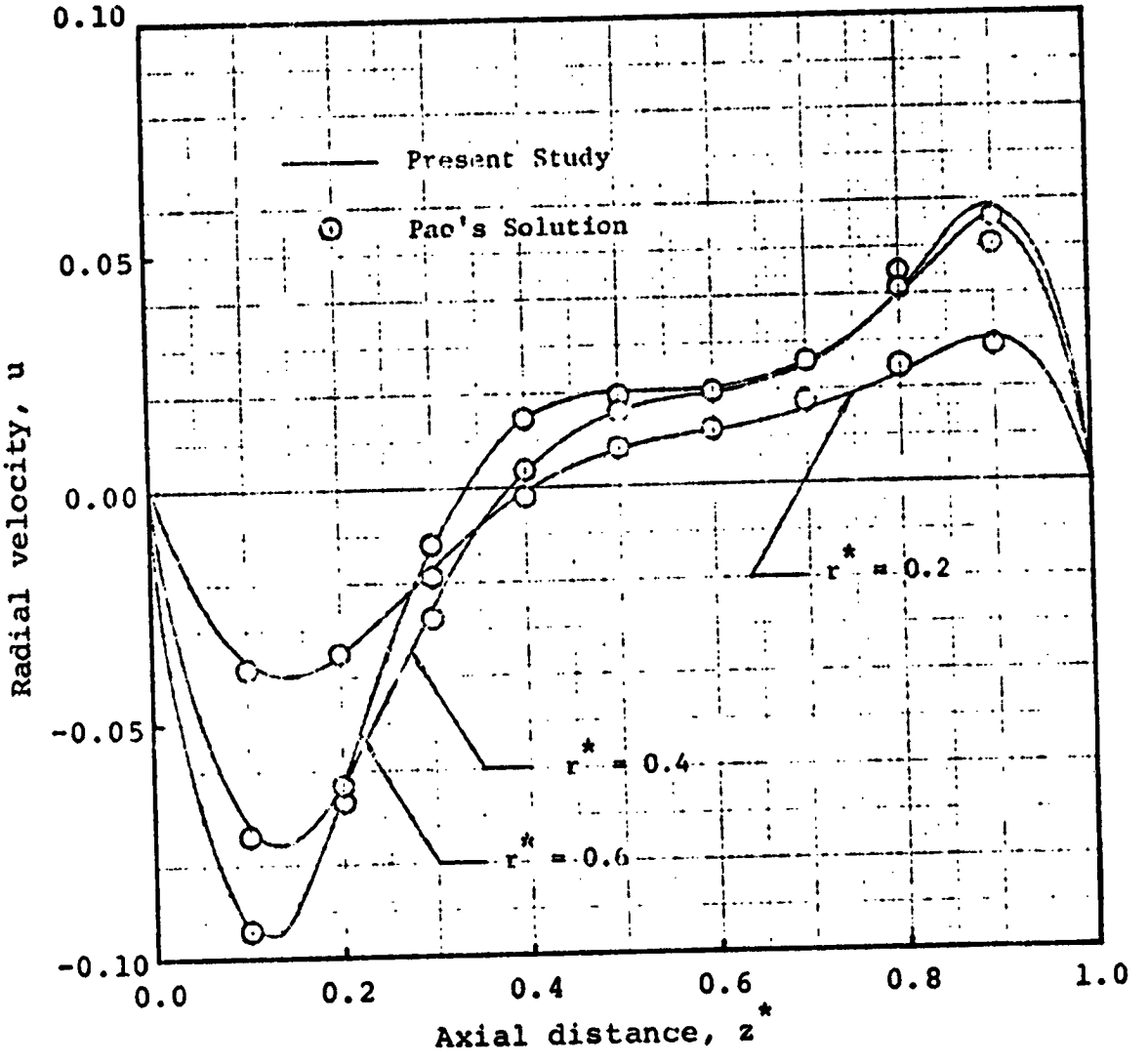

Fig. 4. Comparison of the Radial Velocity of the Present Study with That of Pao's[25] for $Re_t = 100$.

calculating the approximate mesh function f(h) for three different mesh sizes. From these calculations the exact solution f(0) corresponding to zero mesh size and also the discretization error E_d can be evaluated. Suppose the mesh function f which depends on grid size is calculated for three different grid sizes, h, εh and δh where $0 < \delta < \varepsilon < 1$. Then from Taylor series expansion,

$$\begin{aligned} f(h) &= f(0) + ah + bh^2 + 0(h^3) \\ f(\varepsilon h) &= f(0) + a\varepsilon h + b\varepsilon^2 h^2 + 0(h^3) \\ f(\delta h) &= f(0) + a\delta h + b\delta^2 h^2 + 0(h^3) \end{aligned} \tag{91}$$

where a and b are constants which depend on the first and second order derivations of f respectively. But in this analysis the order of approximation in all the finite difference equations is of $0(h^2)$ and hence a = 0. Therefore the ratio,

$$\frac{f(h) - f(\varepsilon h)}{f(\varepsilon h) - f(\delta h)} = \frac{(1 - \varepsilon^2)bh^2 + 0(h^3)}{(\varepsilon^2 - \delta^2)bh^2 + 0(h^3)} \tag{92}$$

approaches the limit as the mesh size h tends to zero:

$$\frac{f(h) - f(\varepsilon h)}{f(\varepsilon h) - f(\delta h)} = \frac{1 - \varepsilon^2}{\varepsilon^2 - \delta^2} \tag{93}$$

The error E_d is obtained from Eq. 91 and 92:

$$E_d = f(h) - f(0) = \frac{f(\varepsilon h) - f(\delta h)}{\varepsilon^2 - \delta^2} \qquad (94)$$

This method of error analysis is applied to a non-rotating flow of Re = 20 using four different grid sizes, 1/20, 1/28, 1/36, 1/44. From the results then the errors are estimated for grid sizes of 1/20 and 1/28. The errors were calculated based on the computed values of circulation along six chosen paths as in the following:

$\int_0^1 w^* dz^*$ along $r^* = 0.25$, 0.50 and 0.75

$-\int_0^1 u^* dr^*$ along $z^* = 0.25$, 0.50 and 0.75

The integral quantities were chosen rather than local quantities since they reflect errors associated with a group of mesh points along the path of integration.

The results show that the relative discretization errors associated with grid sizes of 1/20 and 1/28 are 12 and 4% respectively. For rotating flows, however, the errors are expected to be higher because of the induced secondary flows and thin boundary layers which have steep gradients of velocity. Nevertheless, for the range of flow parameters considered in this study it is believed that the errors are not much affected by the wall rotation.

The calculated circulations along the chosen paths and their variation with mesh spacing are shown in Fig. 5 and 6.

Check on Pressure Calculation

Pressure is calculated both by line integration using the integration formula, Eq. 83, and by solving the Poisson equation of pressure. A comparison of the results is given in Fig. 7 for the case of Re = 1 and Re_t = 50 of the single component flow. In this figure the pressure is plotted against radial distance for three chosen axial locations. The results show good agreement between the two methods and this is considered sufficient to establish the validity of the results for the pressure calculations.

Concluding Remarks

In light of the results of the error analysis that are discussed in this chapter, the numerical results reported in the next chapter can be viewed with confidence. As pointed out in the earlier section of this chapter, the details of flow solutions in the vicinity of the exhaust hole are not considered to be accurately discerned. However, the associated inaccuracy is very much localized and limited to the immediate vicinity of the exit port. This was brought out by the result of the check on continuity in the previous section. Finally, it is shown by the results of the compatibility check for the Poisson equation of pressure that the line integration method should be used for all non-rotating flows, whereas for rotating flows, that

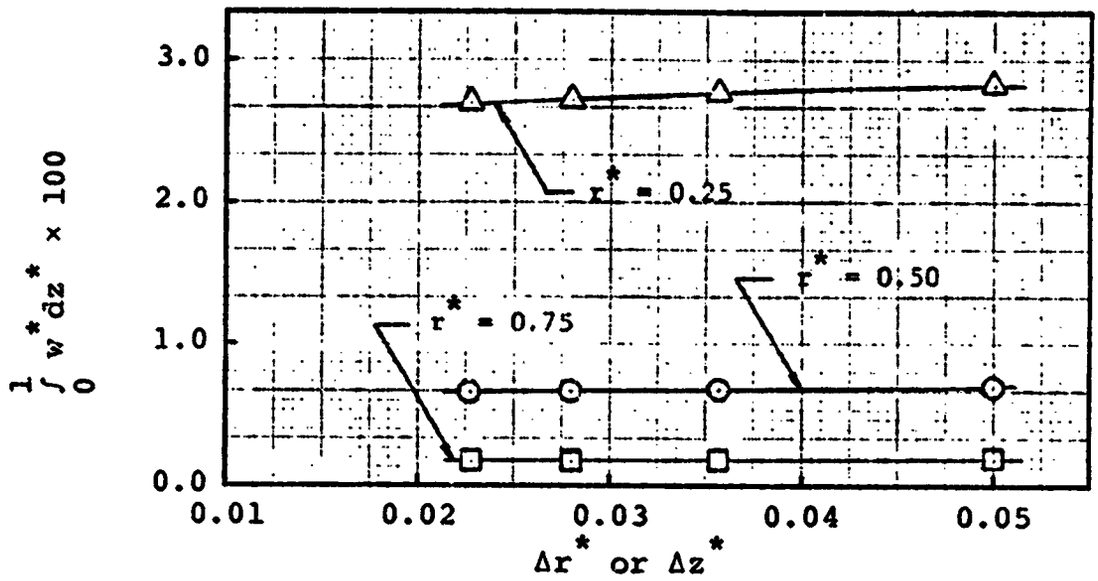

Fig. 5. Calculated Circulation along Three Axial Paths vs. Grid Spacing.

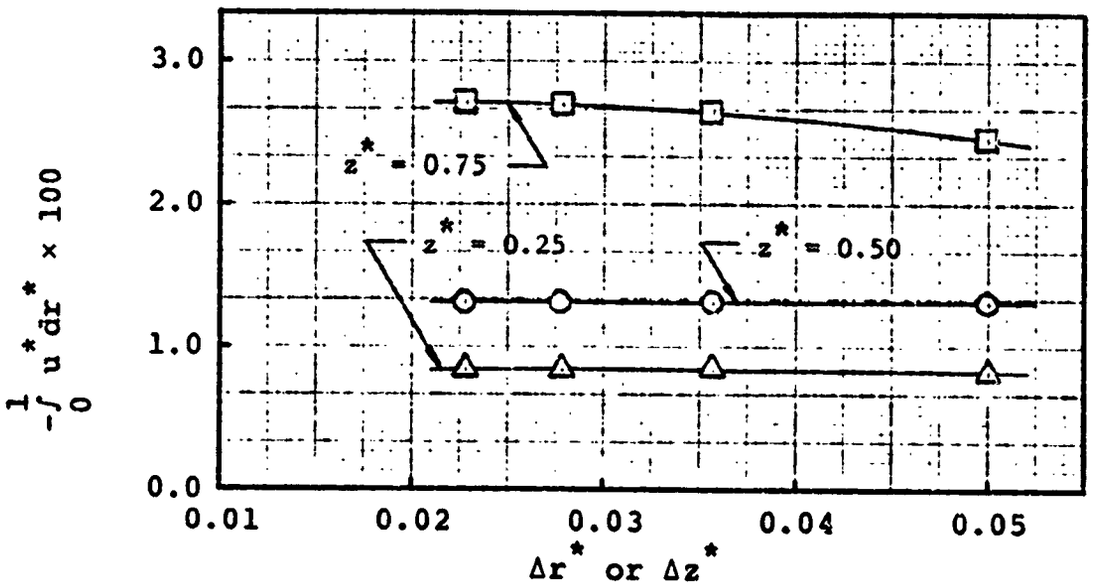

Fig. 6. Calculated Circulation along Three Radial Paths vs. Grid Spacings.

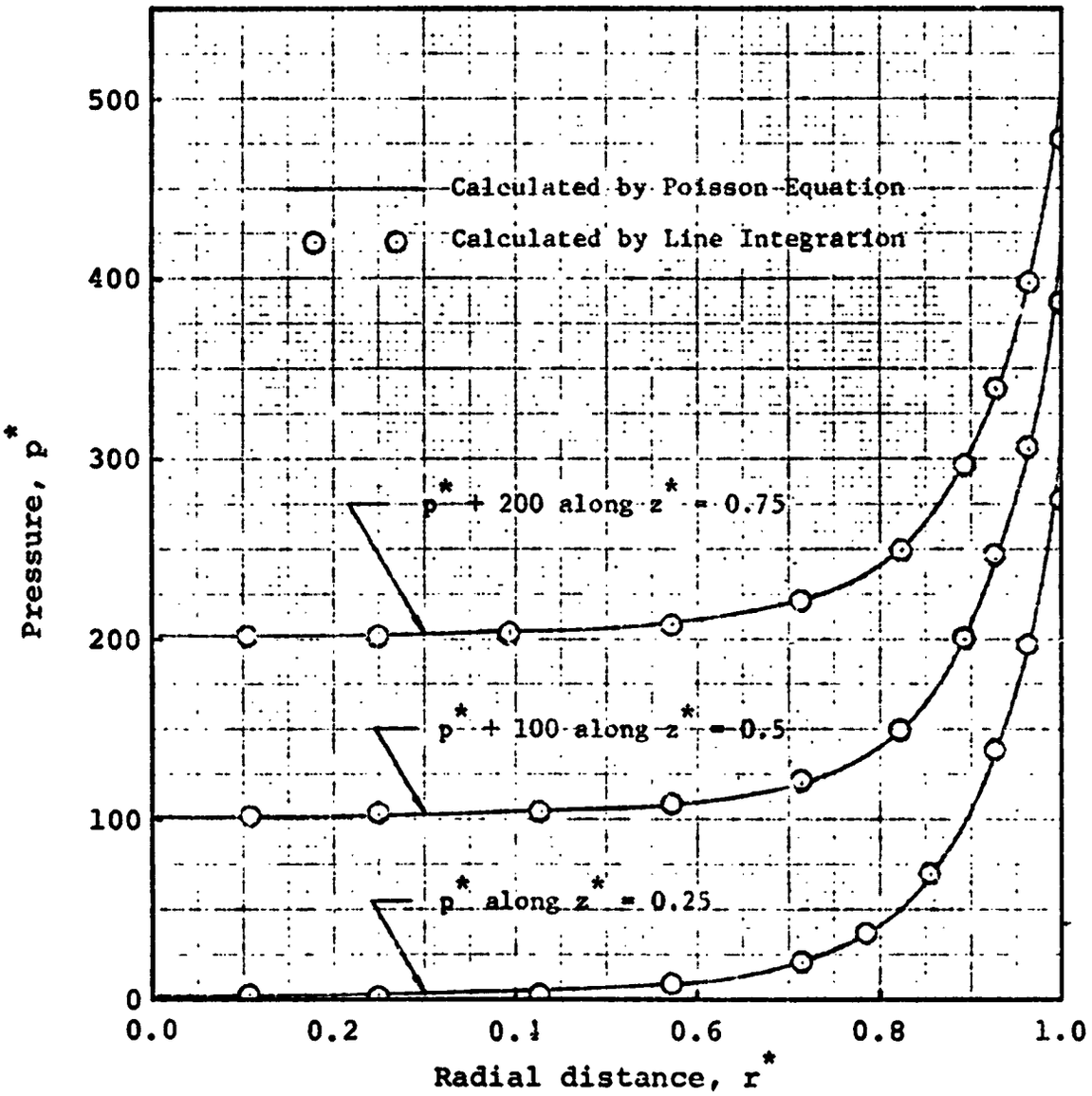

Fig. 7. Comparison of the Pressure Calculations for Three Chosen Axial Locations for Re = 1 and Re_t = 50.

pressure can be obtained by solving the Poisson equation.

CHAPTER V

NUMERICAL RESULTS

Results of the numerical calculations are presented in this chapter. The computer program that was used to produce them was written in Fortran V for the UNIVAC 1108 and included in Appendix B. In early stages of data acquisition, the limits of stable solutions were explored for the governing parameters, particularly the axial and tangential Reynolds numbers. The result showed that stable solutions were obtainable without excessive machine time for Reynolds numbers upto 20 for rotating flows with tangential Reynolds numbers as large as 100. Whereas for non-rotating flows stable solutions were obtainable for Reynolds numbers as high as 2000.

The maximum time step and the optimum iteration parameters for given flow cases are determined by numerical experiments for the parabolic and elliptic equations respectively. The exhaust hole radius is kept constant $r_e = 0.125R$ for all the flow cases considered. Aspect ratios considered are 1 and 2 and the Schmidt number is fixed, i.e. $S_c = 1$ for all binary flows studied.

Although it is possible in principle to compute the required mass addition rate of component A that is necessary to maintain a predetermined critical mass in the chamber, the computation procedure required to do this is difficult.

Therefore, for purposes of simplicity the containment of component A is calculated for given values of the mass addition rate. Since it is desirable to keep the mass addition of simulated fissionable material as small as possible, relatively small values, 0.01 and 0.05, are considered for the injection rates of component A(f_{A-B}).

Grid systems of 29 x 29 and 21 x 41 are used for flows of aspect ratio of 1 and 2 respectively. In Table 1, single component flows that were considered in this study are summarized. Whereas Table 2 lists the binary fluid flow cases studied. The component simulating fissionable material is introduced by a uniform interior source distributed over an annular containment region, $0.125 < r^* < 0.875$ and $0.125\ z^* < 0.875$ for all binary flow cases. This choice of mass injection schedule is made in order to reflect local effects of secondary flows on the resulting containment factor. Although the assumed uniform source distribution may not be an efficient one for achieving high containment, it is considered most suitable for studying the effects of local secondary flows on the retention of fissionable material.

Because only the steady state solution is of interest it was necessary to iterate the elliptic equations only once for each time step. Final steady state solutions are obtained with a minimum of computer time in this way, but the results produced before convergence is reached does not represent the true transient behavior of the flow.

Table 1. Summary of Numerical Results for Single Component Flows.

Item	Re	Re_t	N x M	Δt	q_s	a	b
1	1	0	29 x 29	0.001	0.25	1	0.125
2	1	25	29 x 29	0.001	0.25	1	0.125
3	1	50	29 x 29	0.001	0.25	1	0.125
4	1	100	29 x 29	0.001	0.25	1	0.125
5	20	0	29 x 29	0.001	2.5	1	0.125
6	20	50	29 x 29	0.001	2.5	1	0.125
7	20	100	29 x 29	0.001	2.5	1	0.125
8	1	0	21 x 41	0.002	0.125	2	0.125
9	1	15	21 x 41	0.002	0.125	2	0.125
10	20	0	21 x 41	0.002	1.25	2	0.125
11	20	15	21 x 41	0.002	1.25	2	0.125

Table 2. Summary of Numerical Results for Binary Fluid Flows.

Item	Re	Re_t	S_c	N x M	Δt	q_s	q_p	a	b	ρ_A/ρ_B	f_{A-B}
1	20	0	1	29 x 29	0.001	2.5	0.6	1	0.125	0.5	0.01
2	20	50	1	29 x 29	0.001	2.5	0.6	1	0.125	0.5	0.01
3	20	100	1	29 x 29	0.001	2.5	0.6	1	0.125	0.5	0.01
4	20	0	1	29 x 29	0.001	2.5	0.6	1	0.125	1.0	0.01
5	20	50	1	29 x 29	0.001	2.5	0.6	1	0.125	1.0	0.01
6	20	100	1	29 x 29	0.001	2.5	0.6	1	0.125	1.0	0.01
7	20	0	1	29 x 29	0.001	2.5	0.6	1	0.125	2.0	0.01
8	20	50	1	29 x 29	0.001	2.5	0.6	1	0.125	2.0	0.01
9	20	100	1	29 x 29	0.001	2.5	0.6	1	0.125	2.0	0.01
10	20	0	1	29 x 29	0.001	2.5	0.6	1	0.125	0.5	0.05
11	20	50	1	29 x 29	0.001	2.5	0.6	1	0.125	0.5	0.05

Results are presented in the following three sections separately for single component flows, binary fluid flows and for the pressure respectively. Calculated values are plotted along selected r* and/or z* values whichever is deemed appropriate for the particular case under consideration. Results are given in a manner that they show parametrically the effects of rotation on the resulting secondary flow, concentration field and finally the containment factor.

Single Component Flows

Flows with an aspect ratio of 1 are taken up first for discussion. Streamlines for flows of Re = 1 and for Re_t = 0 and 50, are presented in Fig. 8 and 9 in which the overall flow configurations can be seen. With no rotation, i.e. Re_t = 0, the fluid enters at the porous wall at the periphery and flows more or less uniformly through the bulk of the chamber. However, with rotation, Re_t = 50, a pair of recirculating closed flow cells are formed in the main body of the chamber. The primary fluid injected at the periphery flows in the boundary layers on the stationary end walls and around the recirculating closed cells. The mass flow rate in the secondary recirculating cells is measured by the quantity, $|\psi|_{max}$ in the closed cells. This quantity increases from 0 to 45.9 as the wall rotation, Re_t varies from 0 to 100 for fixed primary flow rate of Re = 1. This is shown in Fig. 13.

It is to be noted that for a particular ratio of

wall rotation to primary flow, i.e. $Re_t/R_e = 50$, a closed streamline appears, which contains the chamber center line. The appearance of this particular streamline brings about a new flow feature worthy of discussion. Half of the primary flow that flows through the left end wall boundary layer, changes direction, passes through the central bulk region and joins with the remaining half to finally exit through the exhaust hole. This flow configuration is not a desirable one for fluid dynamic containment. It may also be mentioned that this flow can not be studied by the simple analytical model of Rosenzweig, Lewellen and Ross[31] since they assumed the axial velocity to be uniform in the region of the central vortex core.

Streamline patterns for a higher primary flow rate, $R_e = 20$, for wall rotations of $Re_t=0$, 50 and 100 are given in Fig. 10, 11 and 12 respectively. In this case a similar partern of vortex motion is set up by the wall rotation. The primary flow is through the end wall boundary layers and around the outside of the induced recirculating flow cells. The secondary flow rate, $|\psi|_{max}$ of the closed cells varied from 0 to 2.64 as the tangential Reynolds number increased from 0 to 100. This is shown in Fig. 13. A comparison of this result with that of $R_e = 1$ indicates that the secondary flow rate decreases for a fixed rate of wall rotation as the axial Reynolds number increases. The streamline patterns show that the fraction of primary

flow that passes through the central bulk region decreases when the tangential Reynolds number increases from 50 to 100. It may be stated from the streamline patterns for both R_e = 1 and 20 that increasing the tangential Reynolds number will at first decrease the fractional primary flow turning to the main body when the axial Reynolds number is fixed. This tendency persists until a minimum is reached. Further increase in rotation will increase the fractional primary flow until a flow condition develops where the closed streamline appears as given in Fig. 9. This suggests the existence of an optimum rotation rate for a given primary flow that yields the most favorable flow structure for containment.

In the case of an axial Reynolds number of 20, a small closed flow cell that contains the chamber axis is formed in front of the exit port. This has not been observed in the case of Re = 1. A close examination of the pressure distribution along the axis revealed a high pressure point immediately downstream from the cell. It is thought that the porous plug conditions imposed on the primary flow at the exhaust hole causes a region of local high pressure on the center line so that the primary flow can adjust within a short distance to comply with the boundary conditions. The local high pressure induced by the exit port boundary conditions then causes a local reverse flow to form a closed flow cell. In the case of

Re = 1, however, the pressure level required for the necessary adjustment was not high enough to cause a back flow. However, the detailed flow configuration as given in the vicinity of the exahust hole should be viewed with reservations. The grid system used in the numerical computation yields only three and a half nodes across the exit port and thus the rapid changes in the primary flow in this local region have to be approximated by only a few points. A local high value of the error in the continuity constraint was also observed in this region as discussed in Ch. IV.

Radial and axial velocity components are plotted for Re = 1 in Fig. 14 and 15 for Re_t = 0 and 50 respectively. These figures support the discussions given above in regard to the streamline patterns. With no rotation, an asymmetry in the veloicty distributions about the mid-plane, z* = 0.5 is shown. At Re_t = 50, the relative effect of the primary flow is low and as a result velocity distributions are nearly symmetric about the mid-plane. The radial velocity distribution shown in Fig. 15 reveals that the end wall boundary layer thickness grows rapidly as the flow approaches the chamber axis. The results of Re_t = 100 with Re = 1 are not given here since they are similar to the case of Re_t = 50 but with an increased intensity of the recirculating flow features described above.

The distribution of angular momentum is shown for Re = 1 and Re_t = 50 in Fig. 16. It indicates a radial

distribution which does not vary axially in the main body of the chamber. Hence a steep axial gradient exists near the end walls. This supports the $\Gamma(r)$ assumption made by Rosenzweig, Lewellen and Ross[31] in their analytical model of driven vortex flows. The observed high axial gradient of angular momentum near the end walls provides a large source term in the vorticity equation. Through the stream function equation, this leads in turn to a large variation in the vorticity and results in boundary layers in this region. The distribution of angular momentum also is shown to be symmetric about the mid-plane.

Plots of radial and axial velocities for Re = 20 are given for Re_t = 0, 50 and 100 in Fig. 17, 18 and 19. The velocity distributions are similar to those for the case of Re = 1. But the distribution is less symmetric about the mid-plane because of the higher primary flow rate. This effect is more pronounced for lower tangential Reynolds numbers and in the region close to the axis. The angular momentum is given in Fig. 20 and 21 for Re_t = 50 and 100 respectively. These figures show distributions similar to the case of Re = 1. The symmetric distribution of angular momentum about the mid-plane is not altered by the increased primary flow rate.

In the rest of this section results for an aspect ratio of 2 are discussed. Only a few runs are made for this case. The streamline patterns of Re=1 are shown in Fig. 22 and 23 for tangential Reynolds

numbers of 0 and 15 respectively. For the particular value of the ratio, $Re_t/Re = 15$, the pattern of a closed streamline that joins with the chamber axis is again formed and it causes a large fraction of the primary flow to pass through the central region of the chamber. The streamlines for $Re = 20$ are given in Fig. 24 and 25 for cases of $Re_t = 0$ and 15 respectively. For these values of parameters, the fractional primary flow turning to the central region is reduced because of the increased axial Reynolds number for the fixed tengential Reynolds number of 15. The secondary flow rate for this case in which the aspect ratio is 2 is also plotted in Fig. 13. From this figure, it may be seen that the secondary flow rate increases as the aspect ratio increases for fixed axial and tengential Reynolds numbers.

Velocities are plotted for $Re = 1$ in Fig. 26 and 27 for $Re_t = 0$ and 15. The velocities for $Re = 20$ are given in Fig. 28 and 29 respectively for $Re_t = 0$ and 15. The velocity distribution is similar to the case with an aspect ratio of 1. The asymmetrical distribution of radial and axial velocities can be seen for the case of $Re = 20$ and $Re_t = 15$. It appears that thinner boundary layers are formed on the end walls. Angular momentum is given in Fig. 30 and 31 for $Re = 1$ and 20 respectively. The region in which the axial gradient of angular momentum is steep also seems narrower than that for the case of aspect ratio of 1. This results in a higher axial gradient of angular momentum

and hence a higher secondary flow rate. This is in agreement with the result given in Fig. 13. Finally, the general distribution of angular momentum is similar to the case with an aspect ratio of 1.

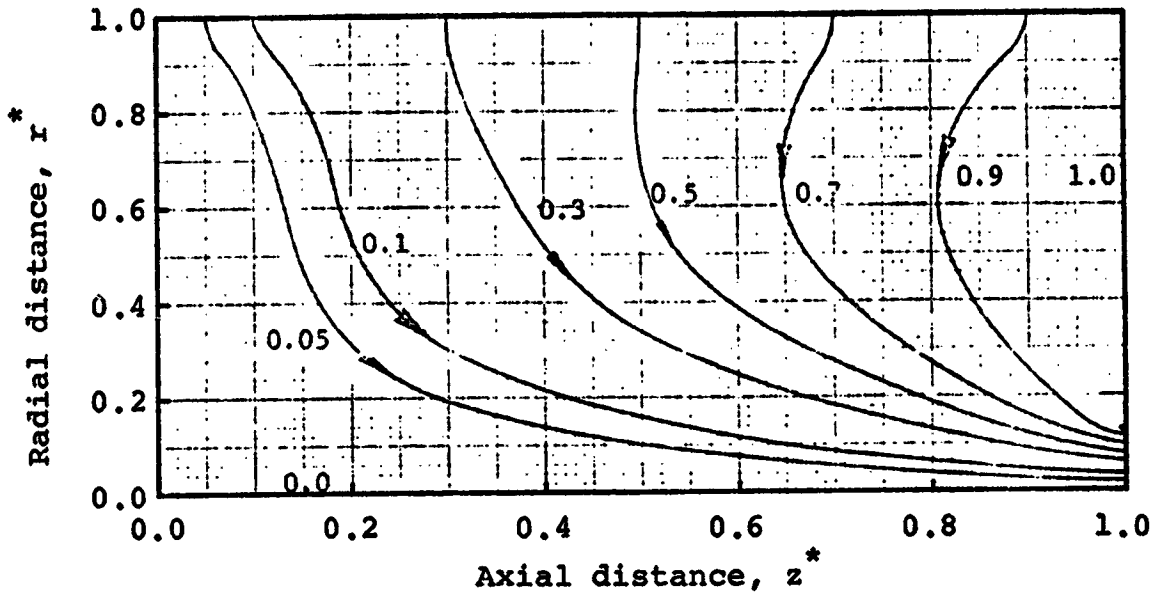

Fig. 8. Streamline Pattern for Re = 1, Re_t = 0 and a = 1.

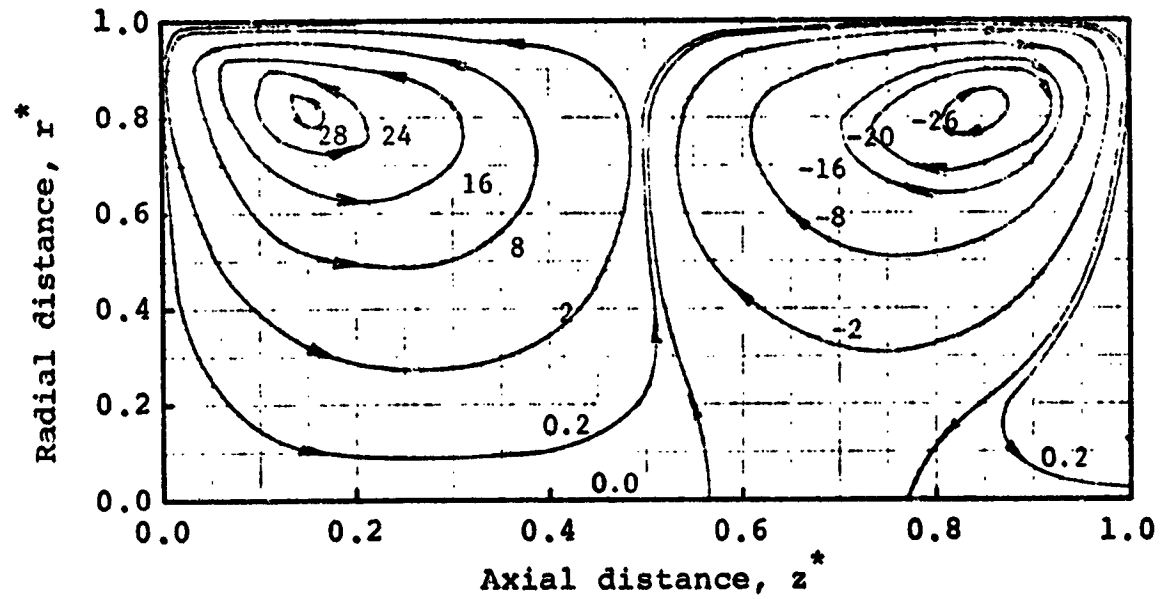

Fig. 9. Streamline Pattern for Re = 1, Re_t = 50 and a = 1.

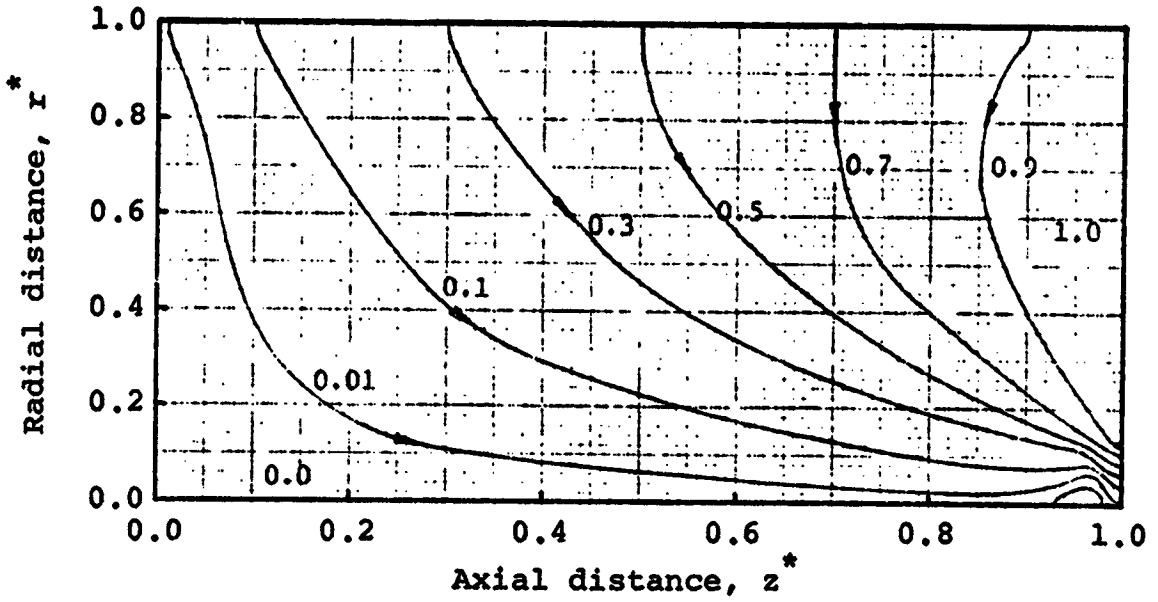

Fig. 10. Streamline Pattern for Re = 20, Re_t = 0 and a = 1.

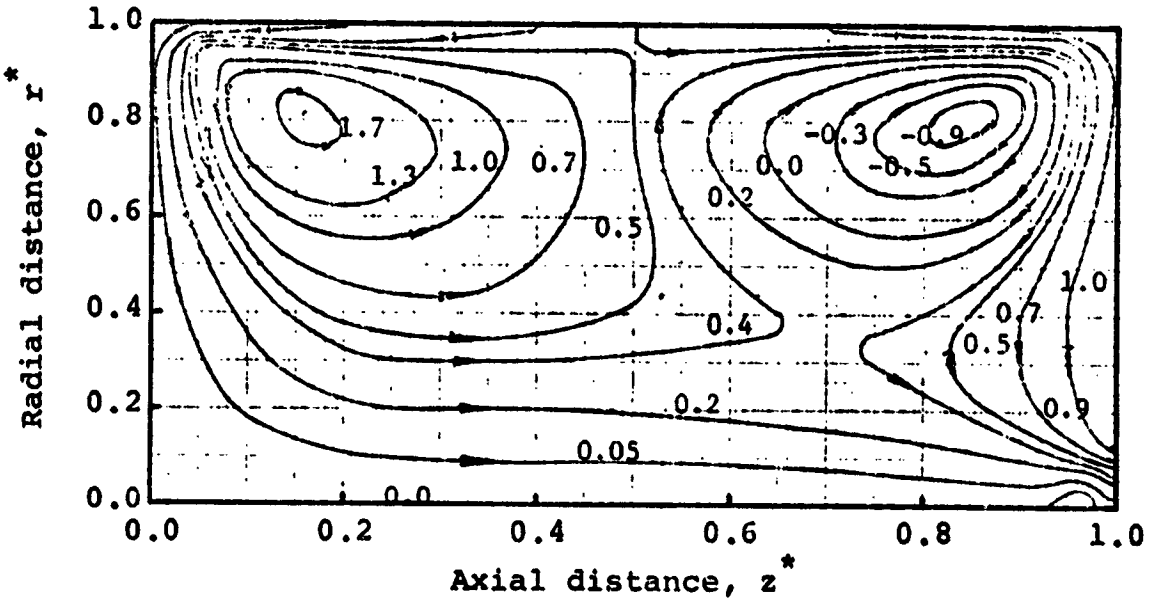

Fig. 11. Streamline Pattern for Re = 20, Re_t = 50 and a = 1.

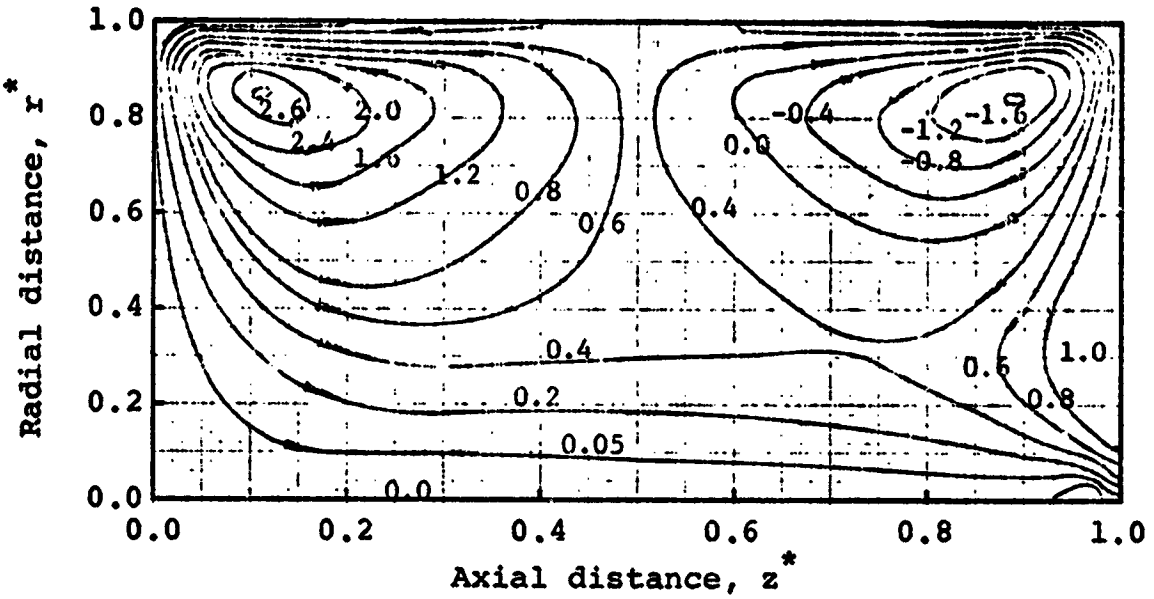

Fig. 12. Streamline Pattern for Re = 20, Re_t = 100 and a = 1.

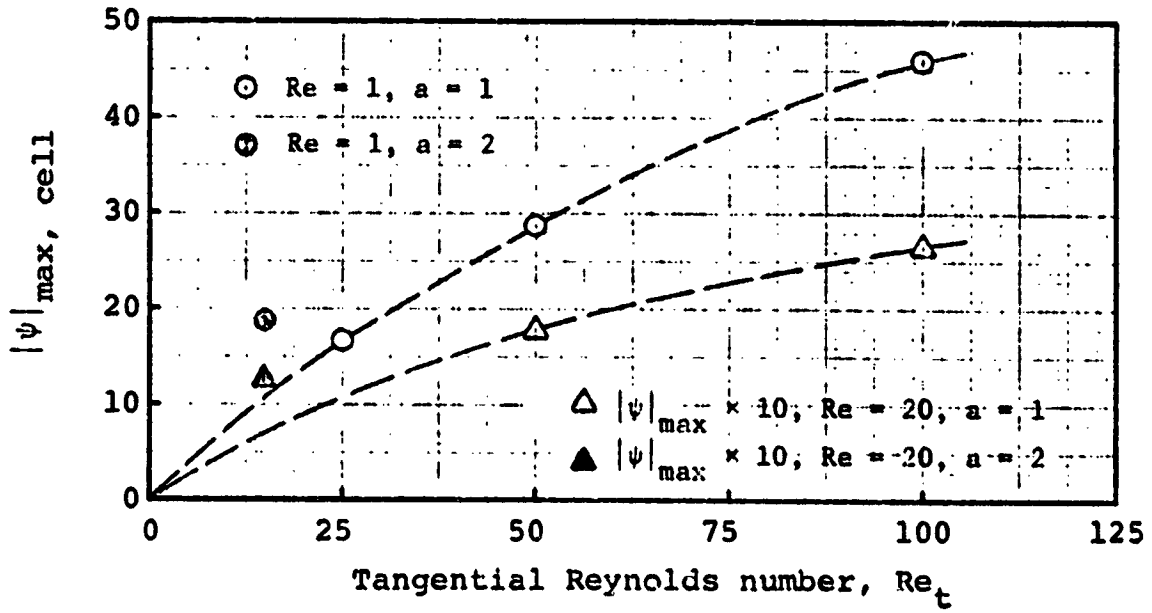

Fig. 13. Secondary Flow Rate vs. Tangential Reynolds Number.

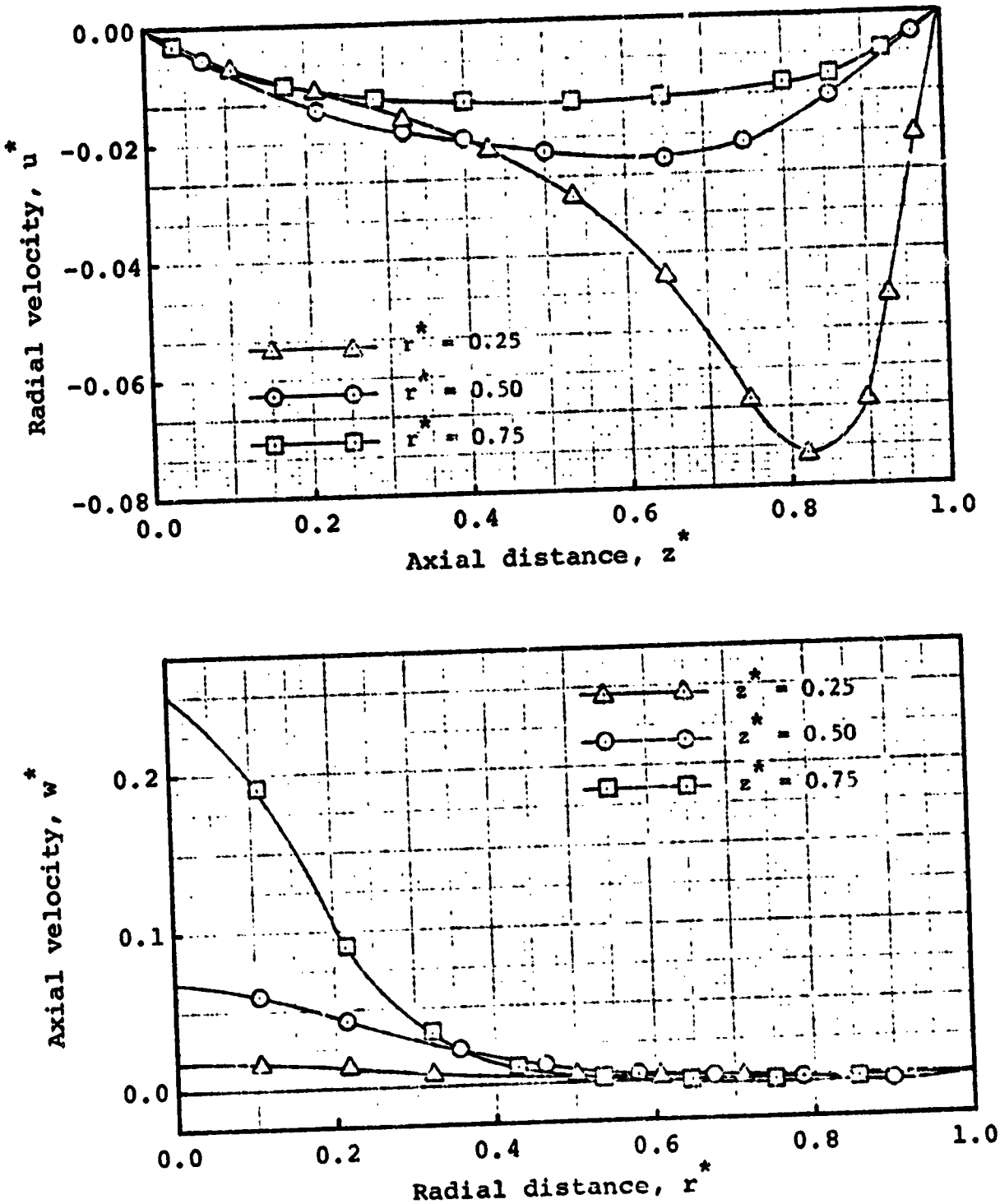

Fig. 14. (a) Radial Velocity vs. Axial Distance for Three Selected Radial Locations, (b) Axial Velocity vs. Radial Distance for Three Selected Axial Locations, for Re = 1, Re_t = 0 and a = 1.

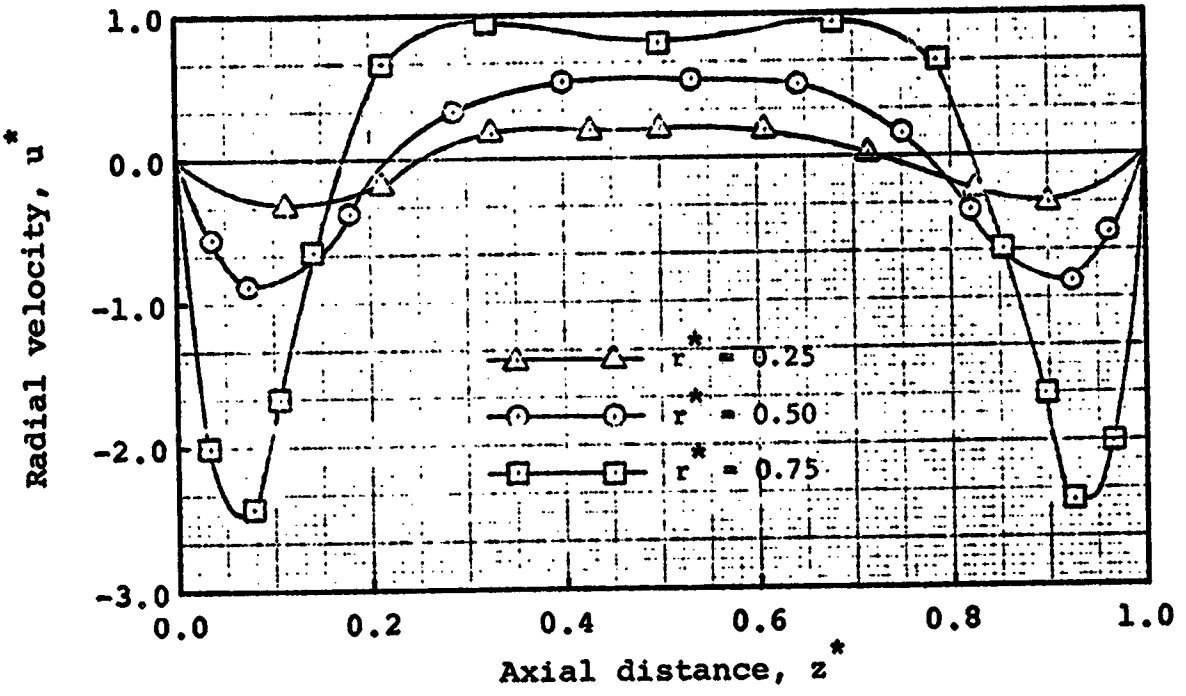

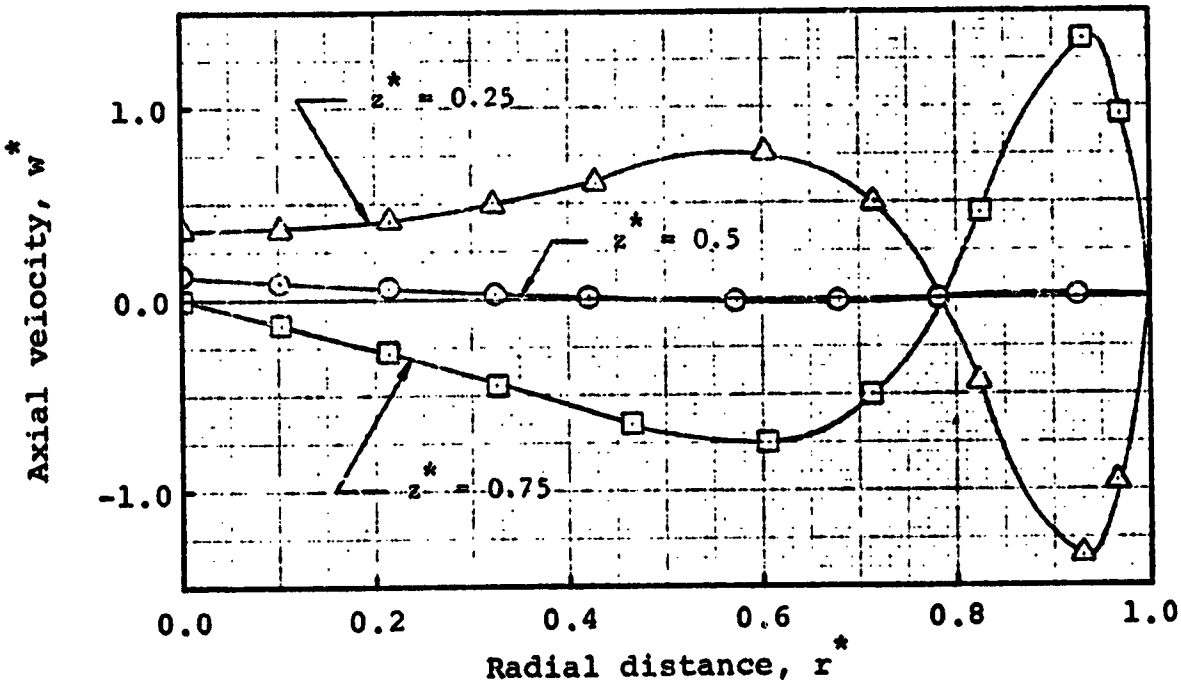

Fig. 15. (a) Radial Velocity vs. Axial Distance for Three Selected Radial Locations, (b) Axial Velocity vs. Radial Distance for Three Selected Axial Locations, for Re = 1, Re_t = 50 and a = 1.

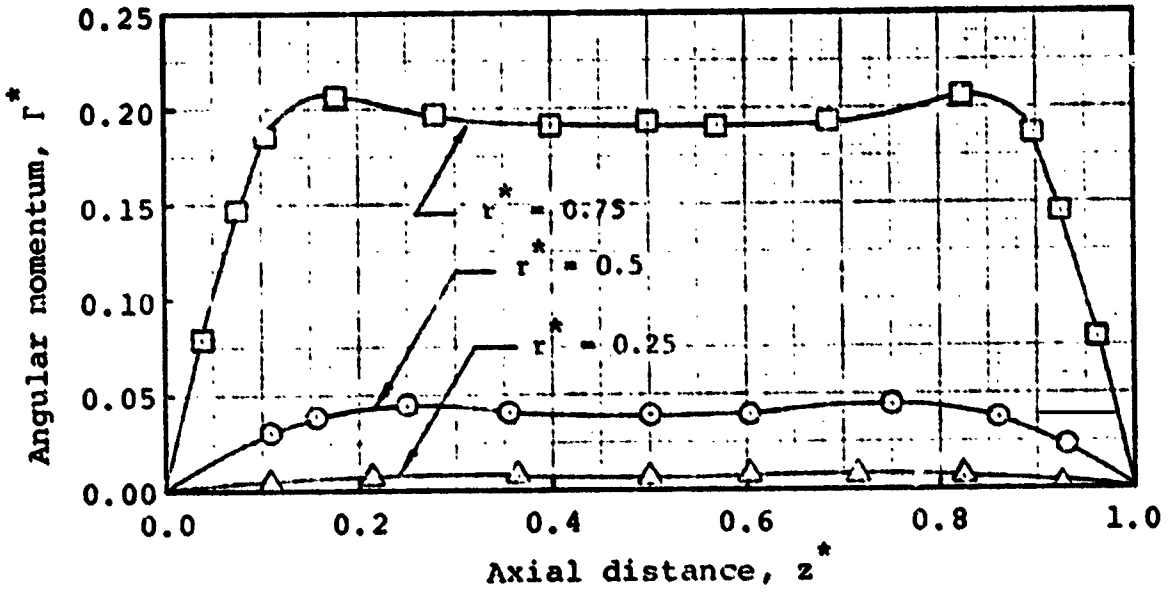

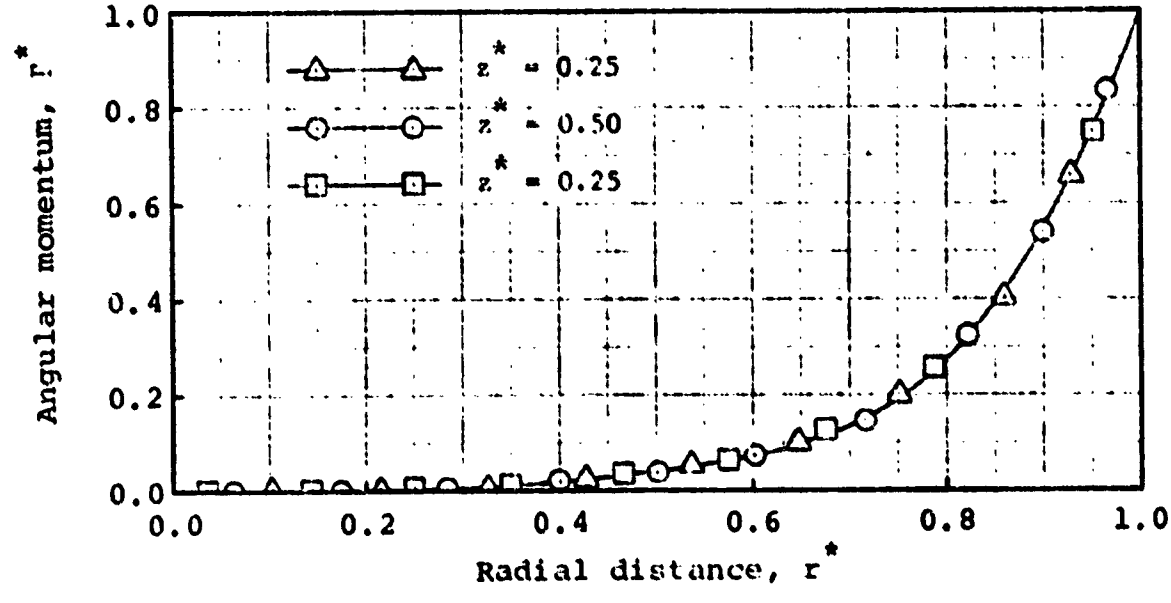

Fig. 16. Distribution of Angular Momentum for Re = 1, Re_t = 50 and a = 1.

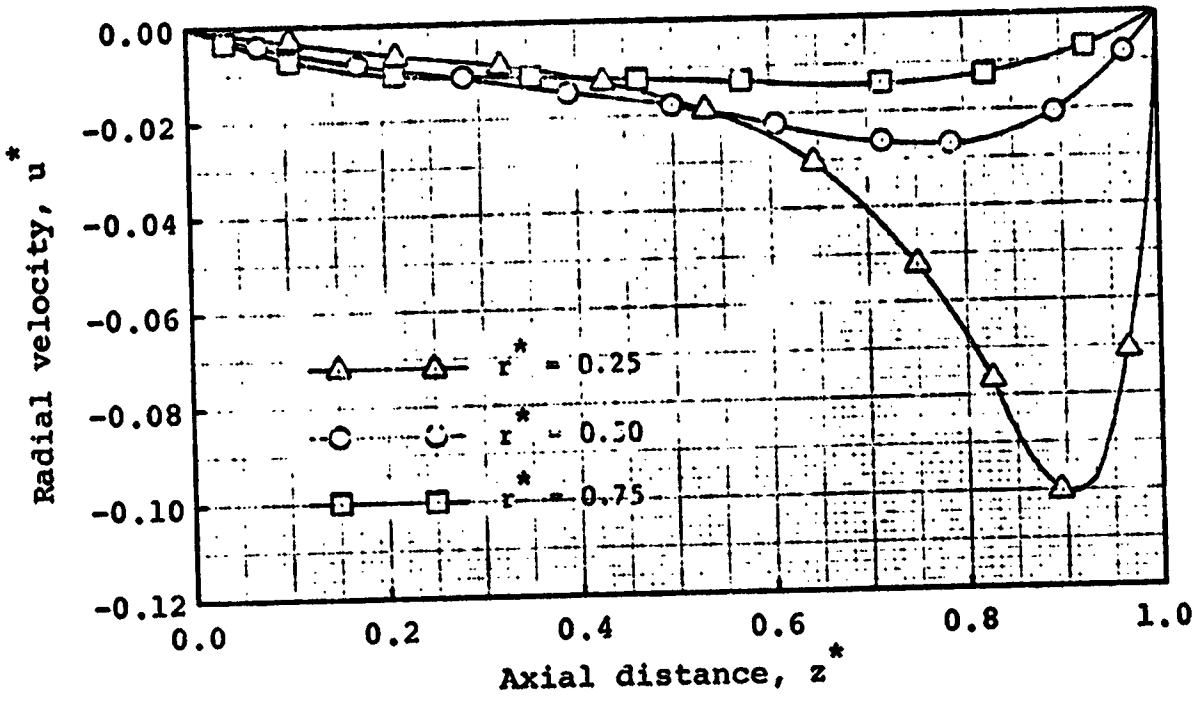

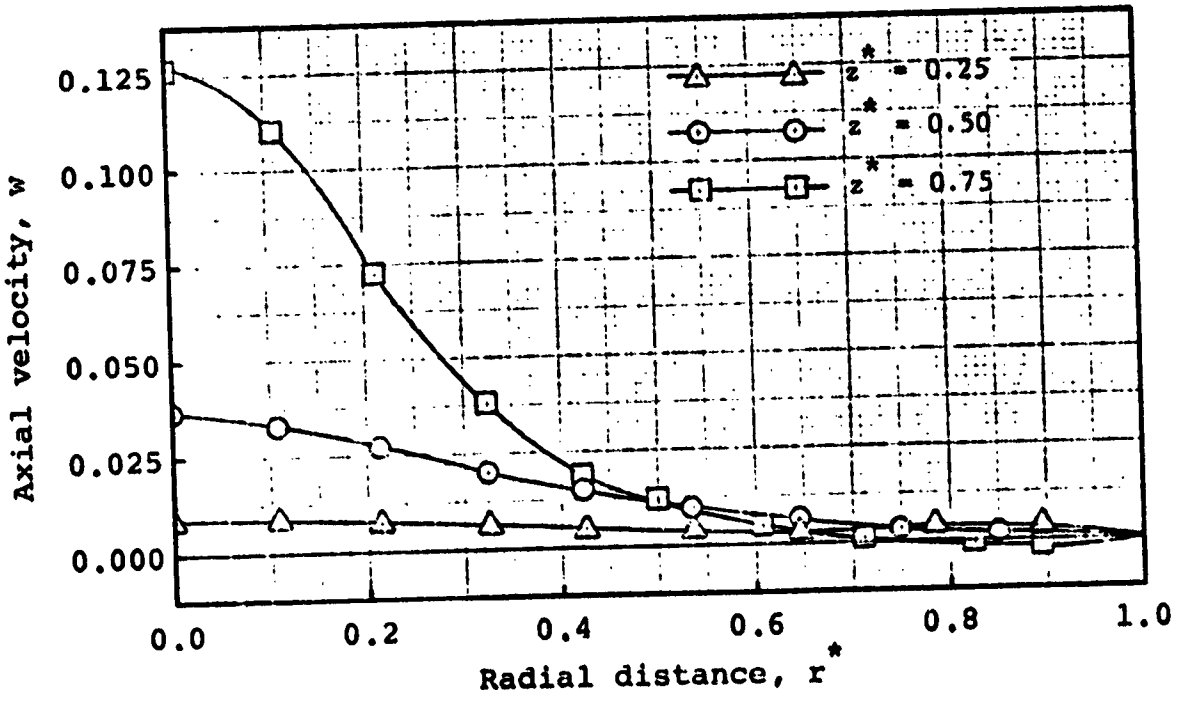

Fig. 17. (a) Radial Velocity vs. Axial Distance for Three Selected Radial Locations, (b) Axial Velocity vs. Radial Distance for Three Selected Axial Locations, for Re = 20, Re_t = 0 and a = 1.

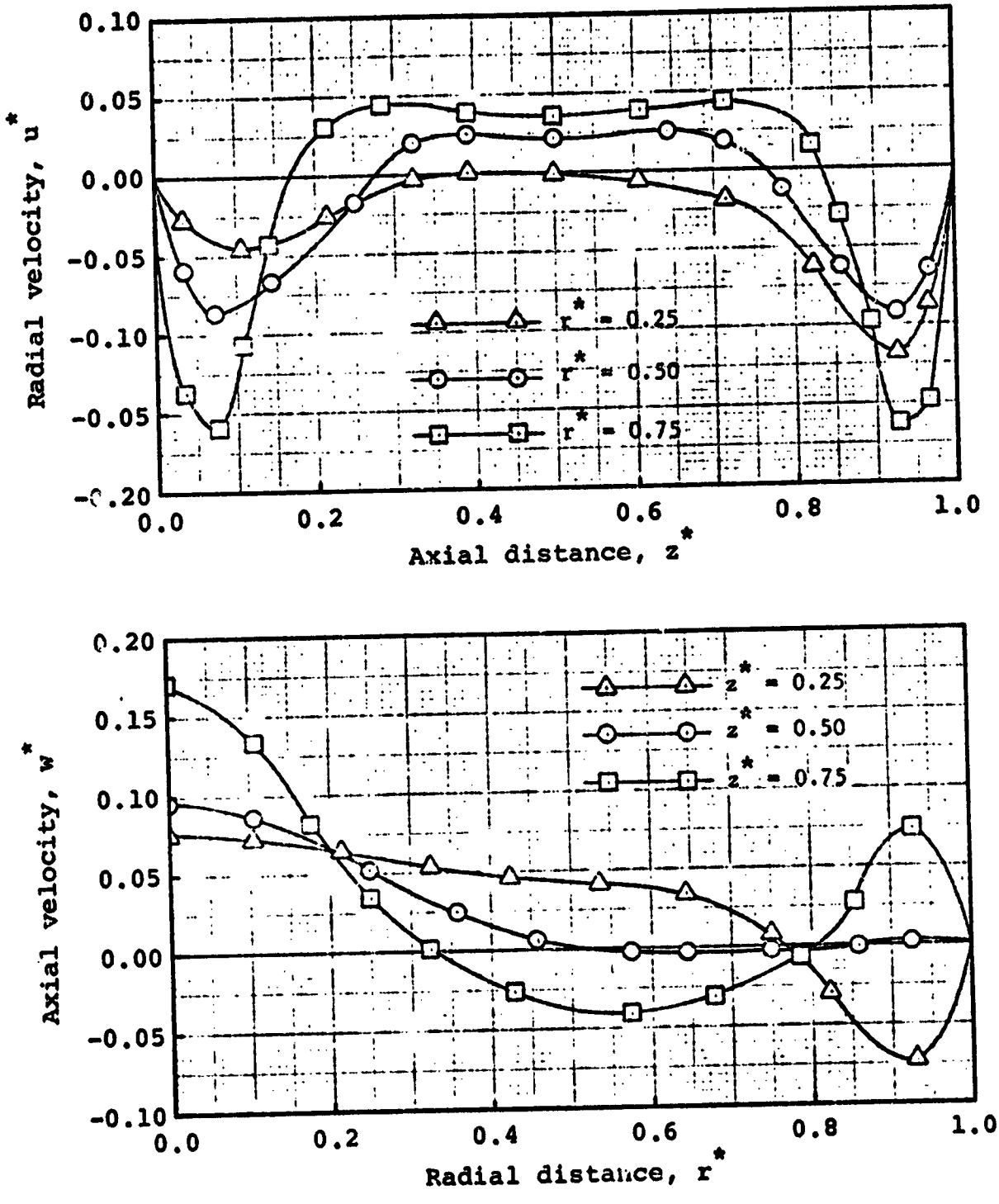

Fig. 18. (a) Radial Velocity vs. Axial Distance for Three Selected Radial Locations, (b) Axial Velocity vs. Radial Distance for Three Selected Axial Locations, for Re = 20, Re_t = 50 and a = 1.

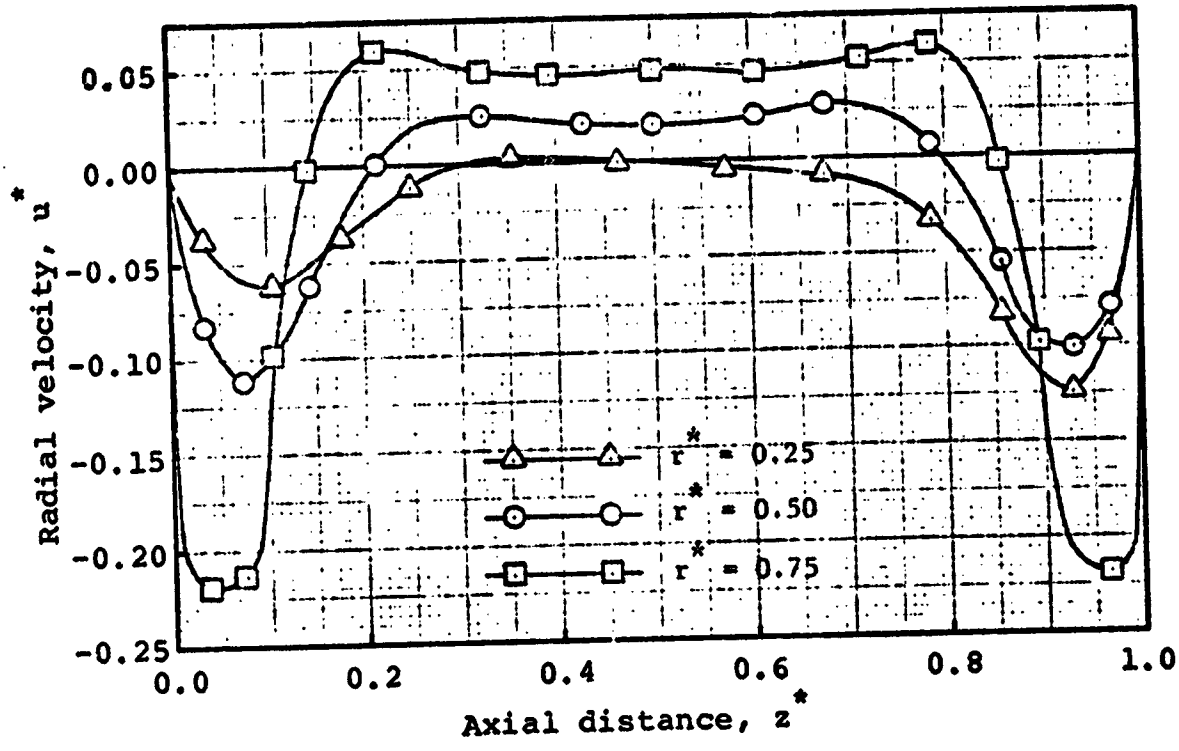

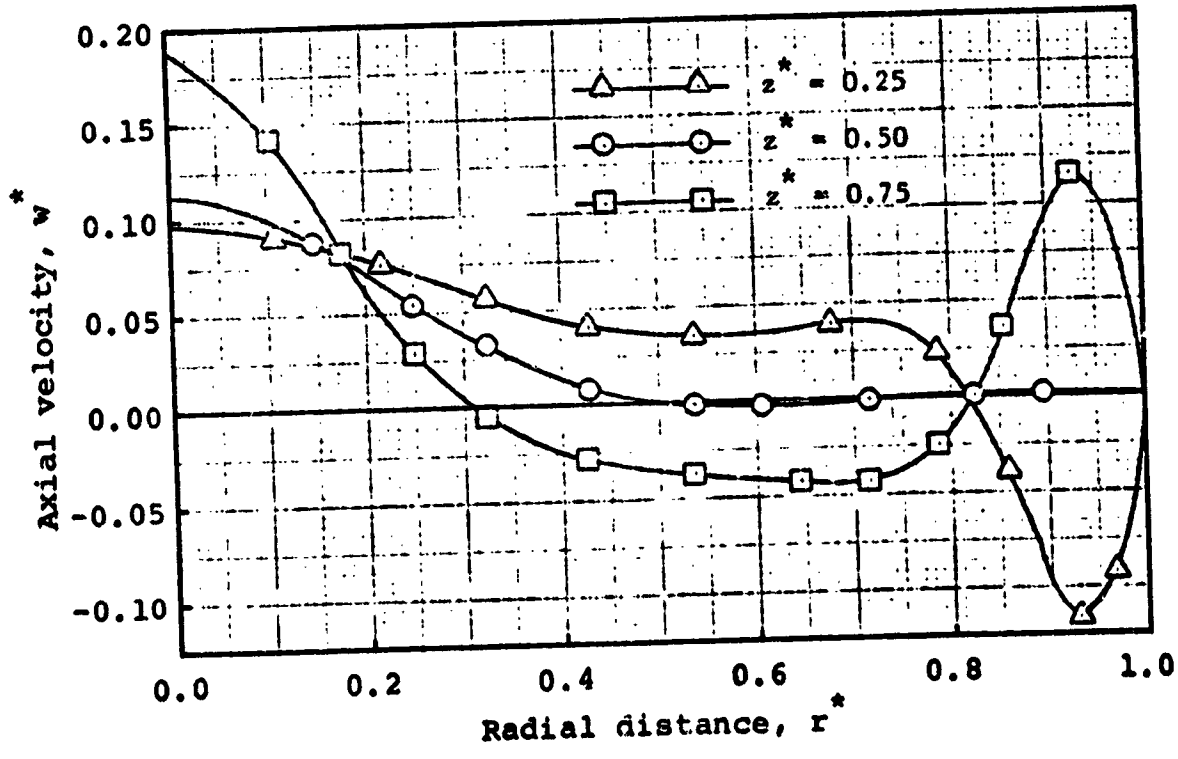

Fig. 19. (a) Radial Velocity vs. Axial Distance for Three Selected Radial Locations, (b) Axial Velocity vs. Radial Distance for Three Selected Axial Locations, for Re = 20, Re_t = 100 and a = 1.

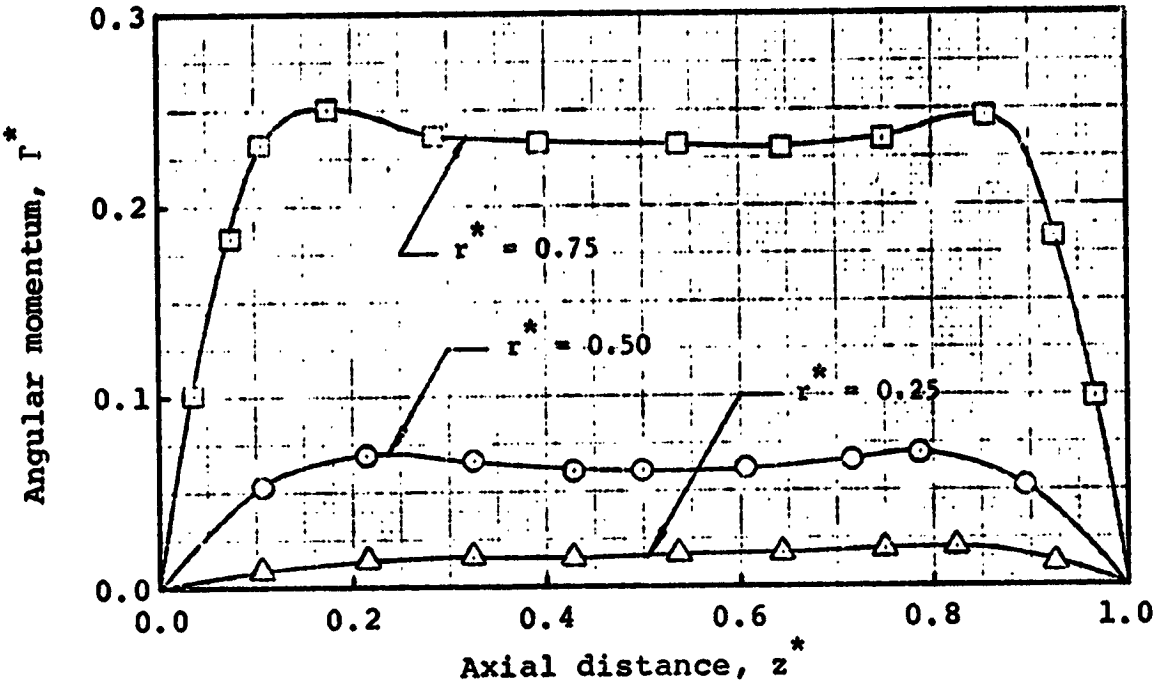

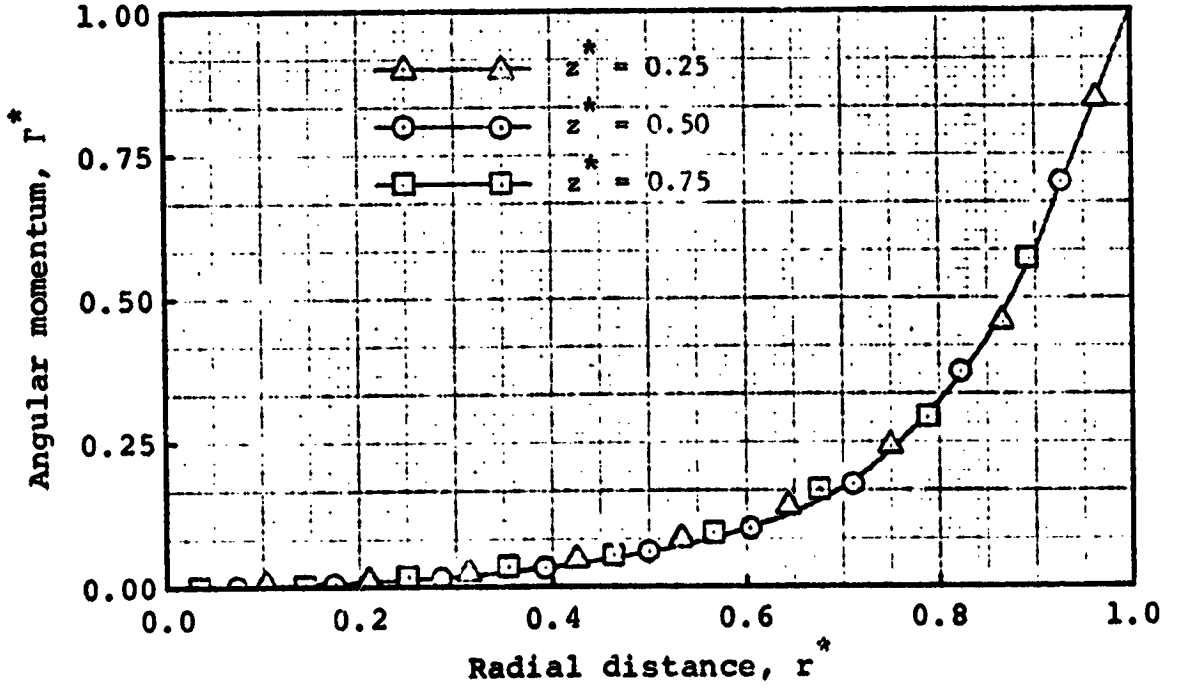

Fig. 20. Distribution of Angular Momentum for Re = 20, Re_t = 50 and a = 1.

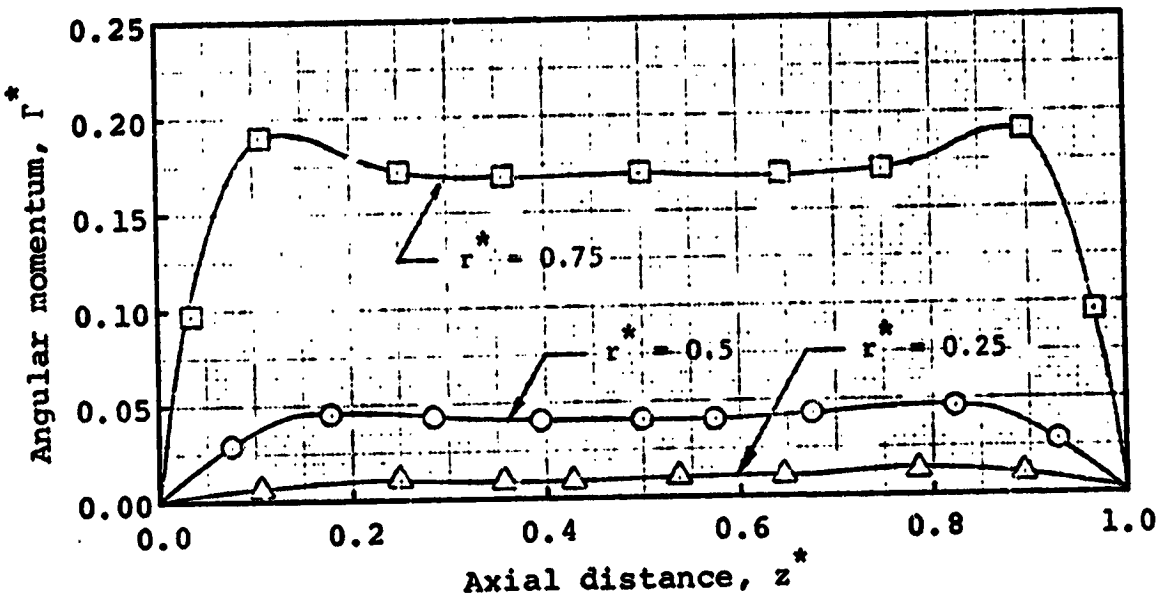

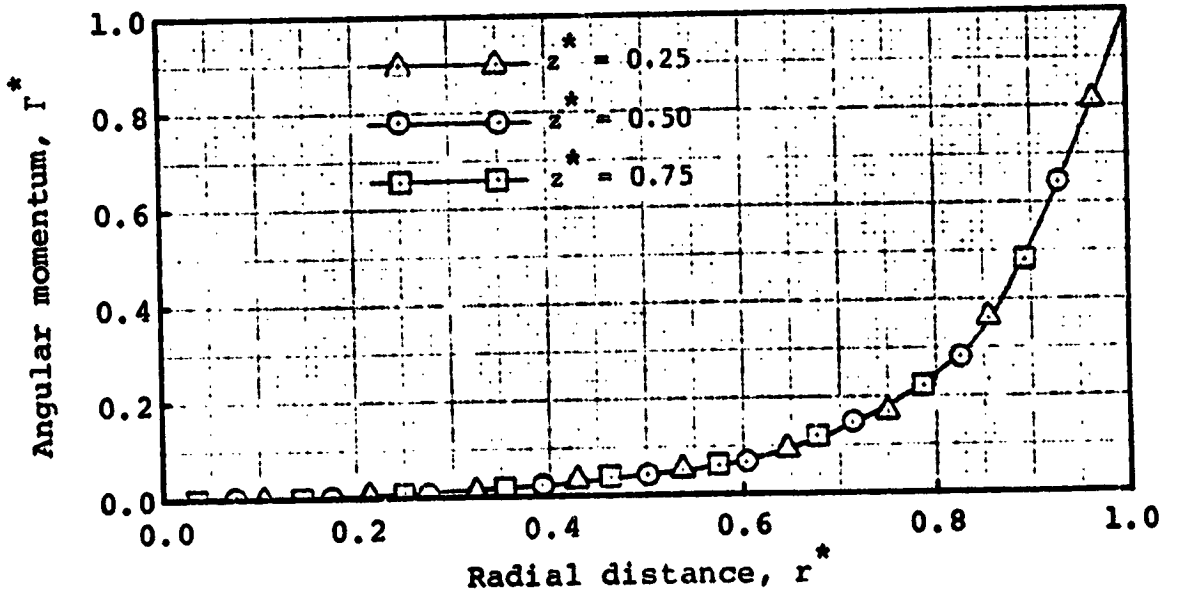

Fig. 21. Distribution of Angular Momentum for Re = 20, Re_t = 100 and a = 1.

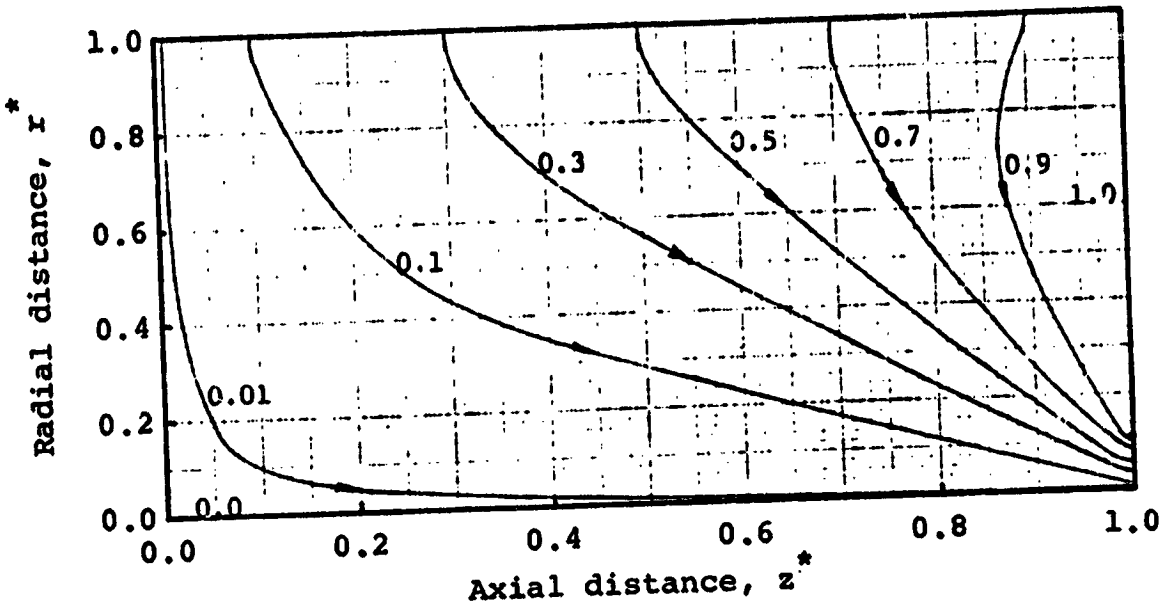

Fig. 22. Streamline Pattern for Re = 1, Re_t = 0 and a = 2.

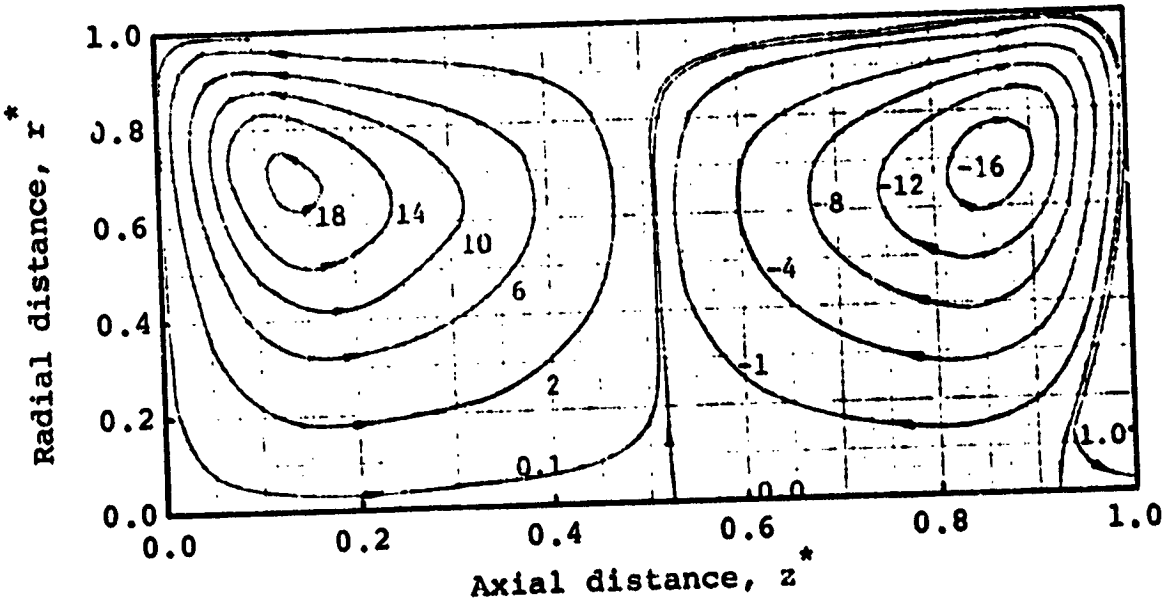

Fig. 23. Streamline Pattern for Re = 1, Re_t = 15 and a = 2.

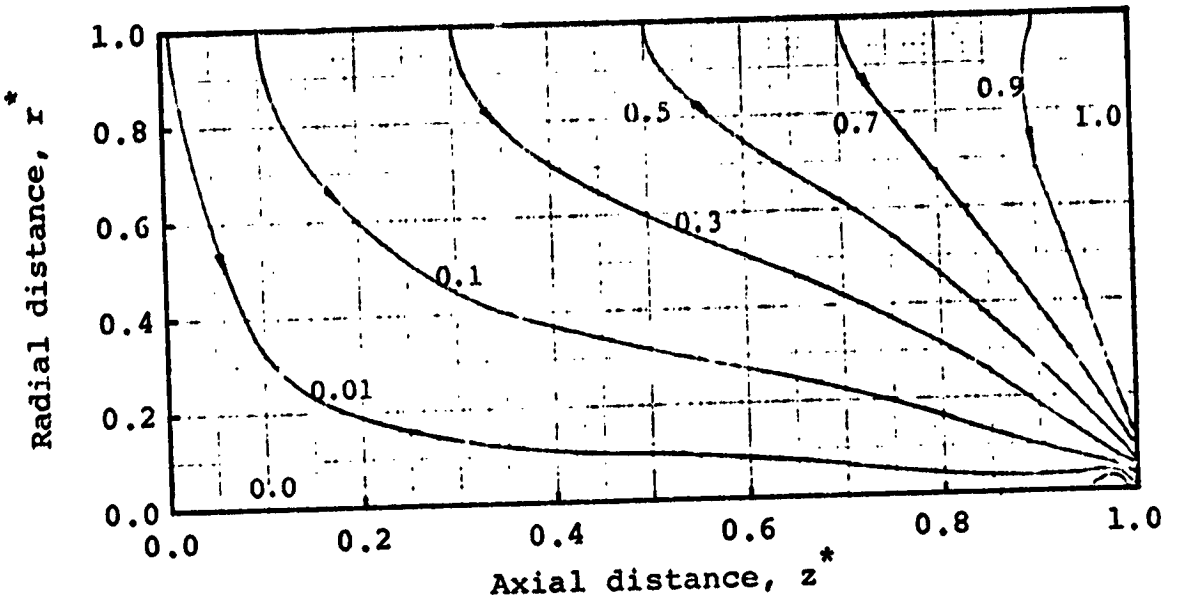

Fig. 24. Streamline Pattern for Re = 20, Re_t = 0 and a = 2.

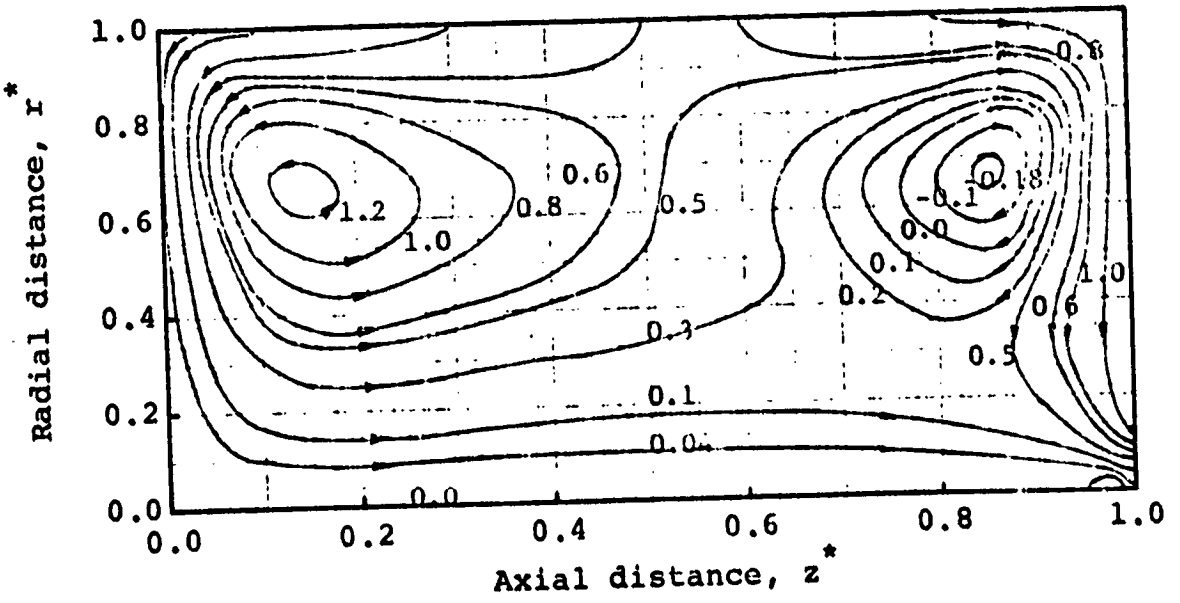

Fig. 25. Streamline Pattern for Re = 20, Re_t = 15 and a = 2.

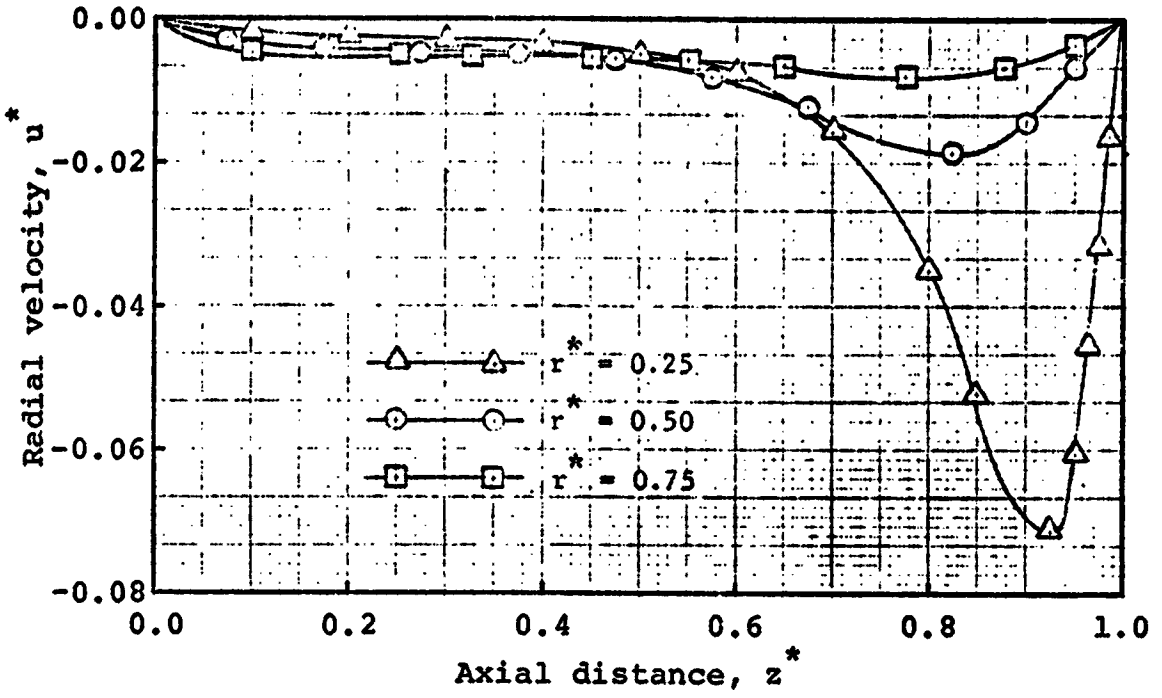

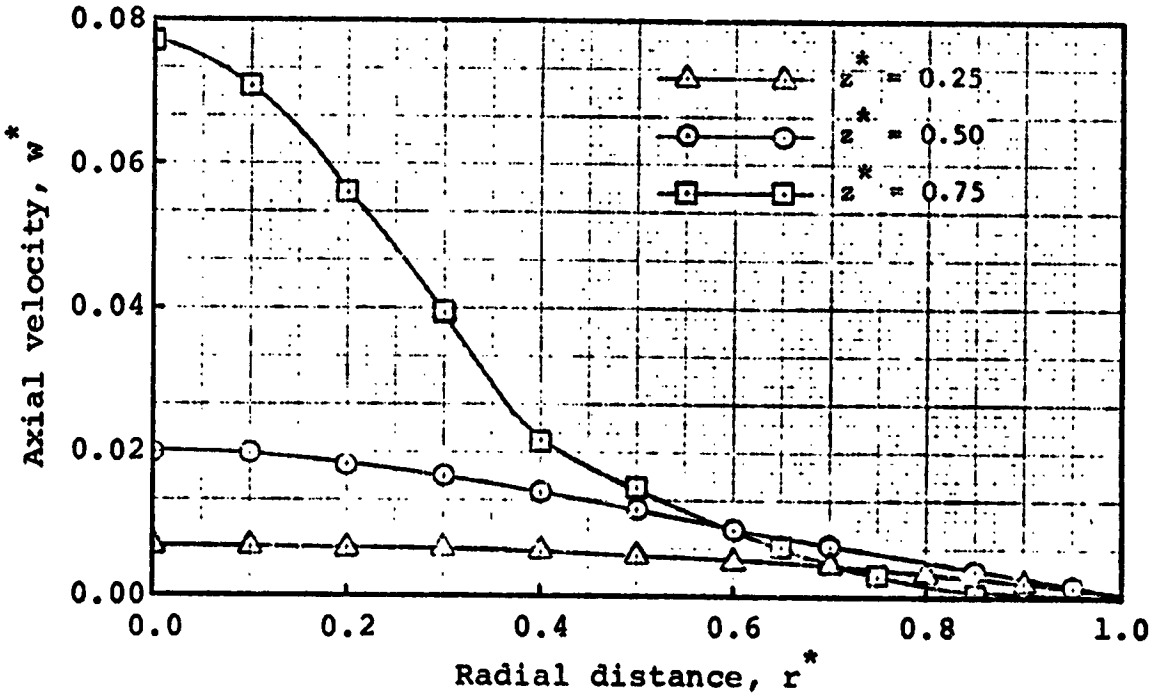

Fig. 26. (a) Radial Velocity vs. Axial Distance for Three Selected Radial Locations, (b) Axial Velocity vs. Radial Distance for Three Selected Axial Locations, for Re = 1, Re_t = 0 and a = 2.

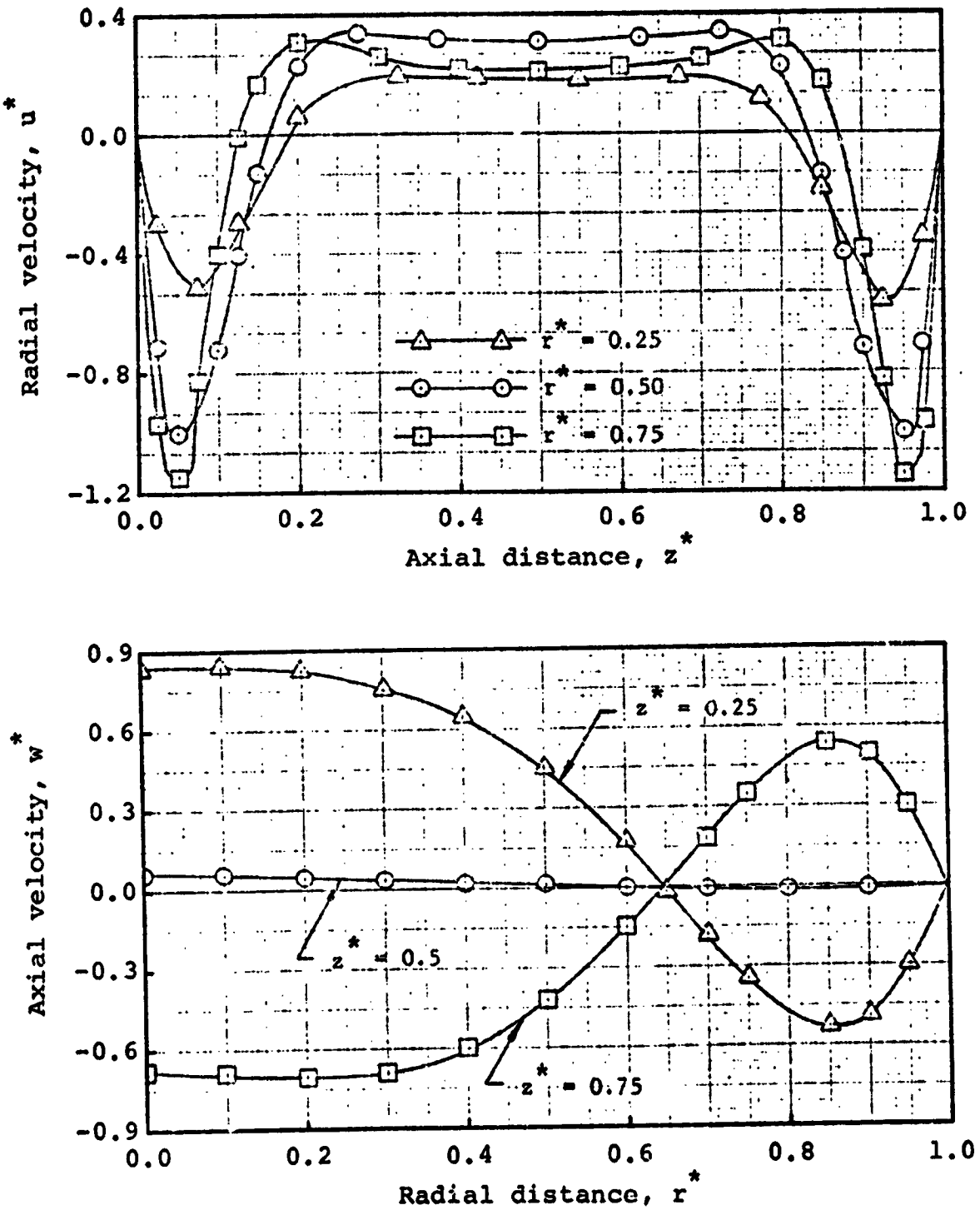

Fig. 27. (a) Radial Velocity vs. Axial Distance for Three Selected Radial Locations, (b) Axial Velocity vs. Radial Distance for Three Selected Axial Locations, for Re = 1, Re_t = 15 and a = 2.

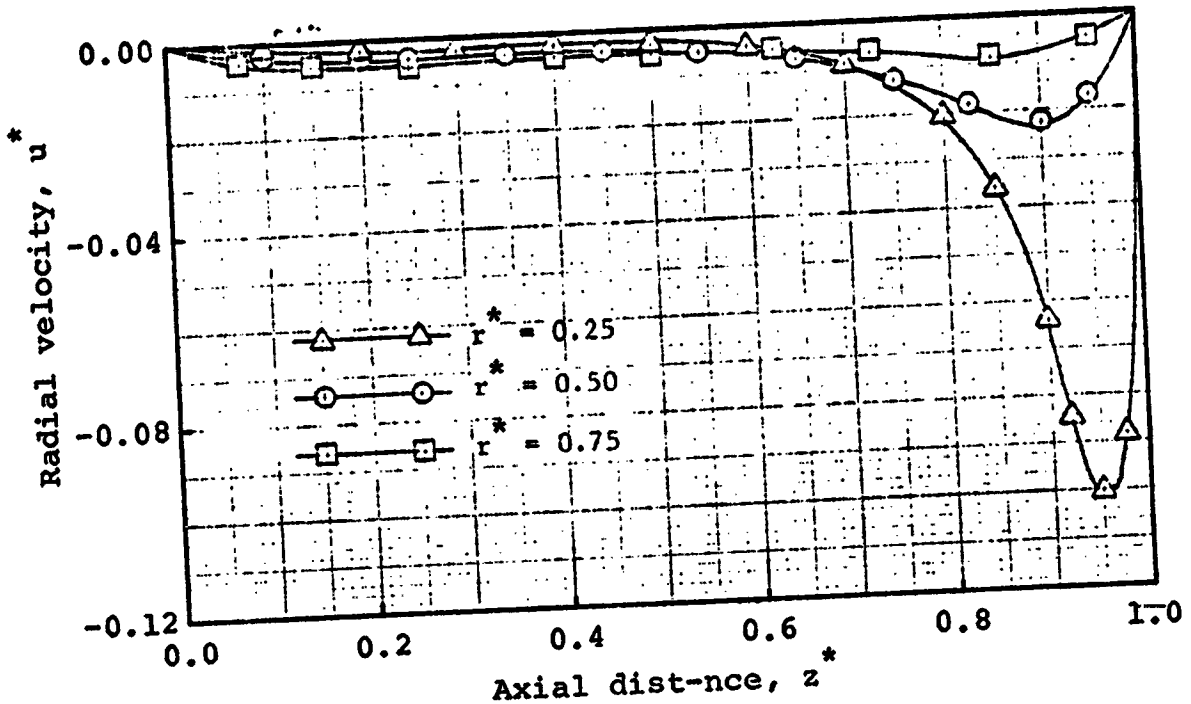

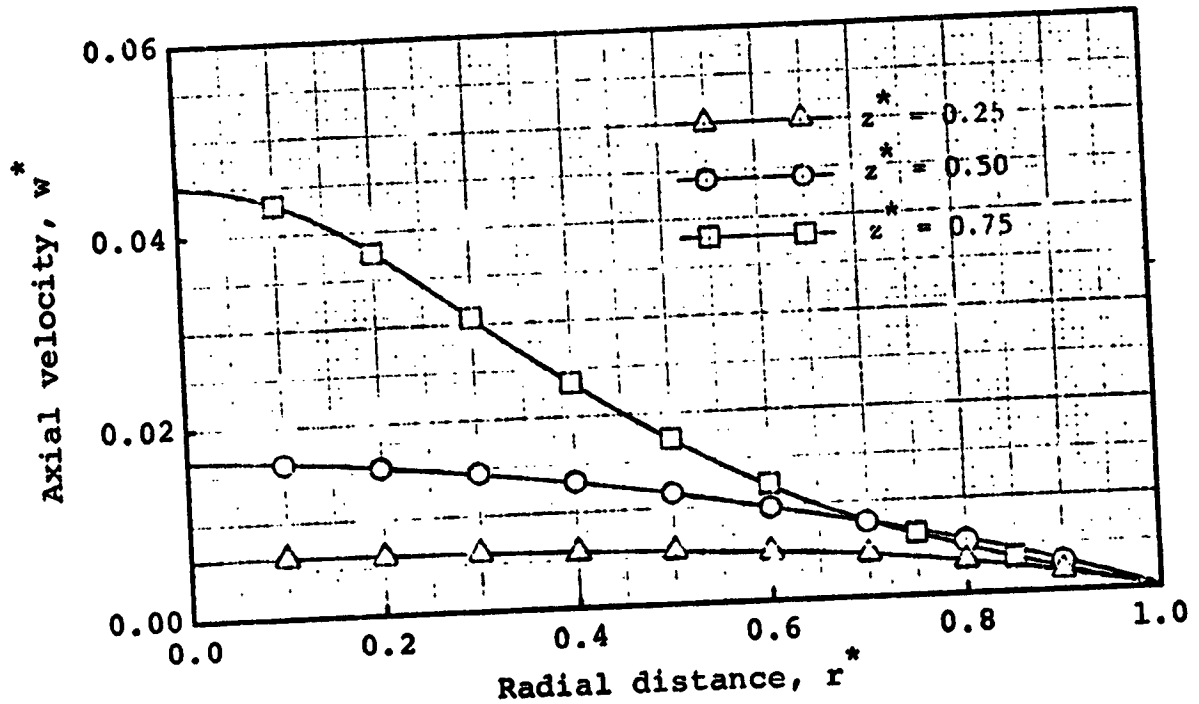

Fig. 28. (a) Radial Velocity vs. Axial Distance for Three Selected Radial Locations, (b) Axial Velocity vs. Radial Distance for Three Selected Axial Locations, for Re = 20, Re_t = 0 and a = 2.

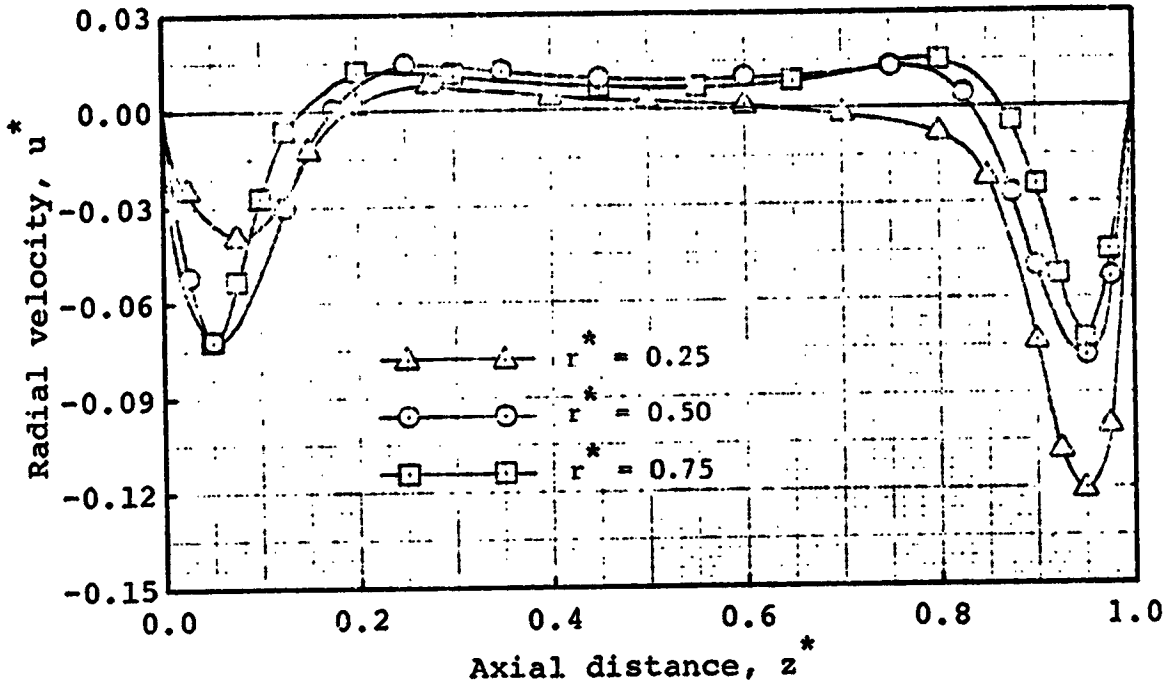

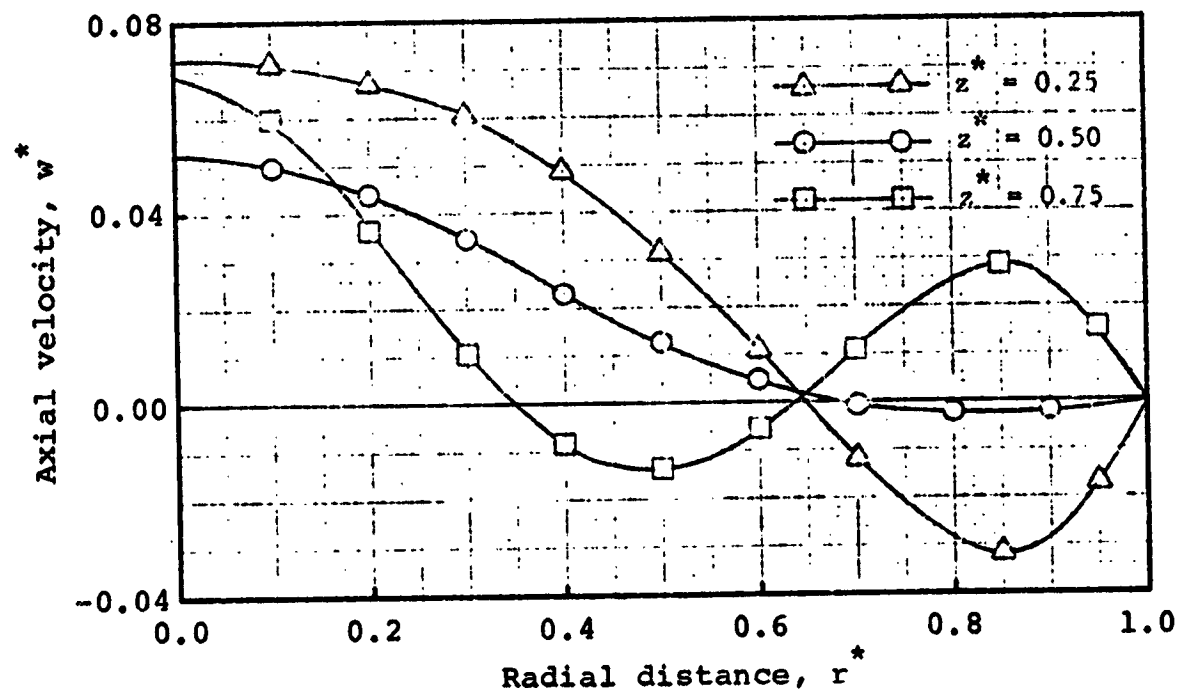

Fig. 29. (a) Radial Velocity vs. Axial Distance for Three Selected Radial Locations, (b) Axial Velocity vs. Radial Distance for Three Selected Axial Locations, for Re = 20, Re_t = 15 and a = 2.

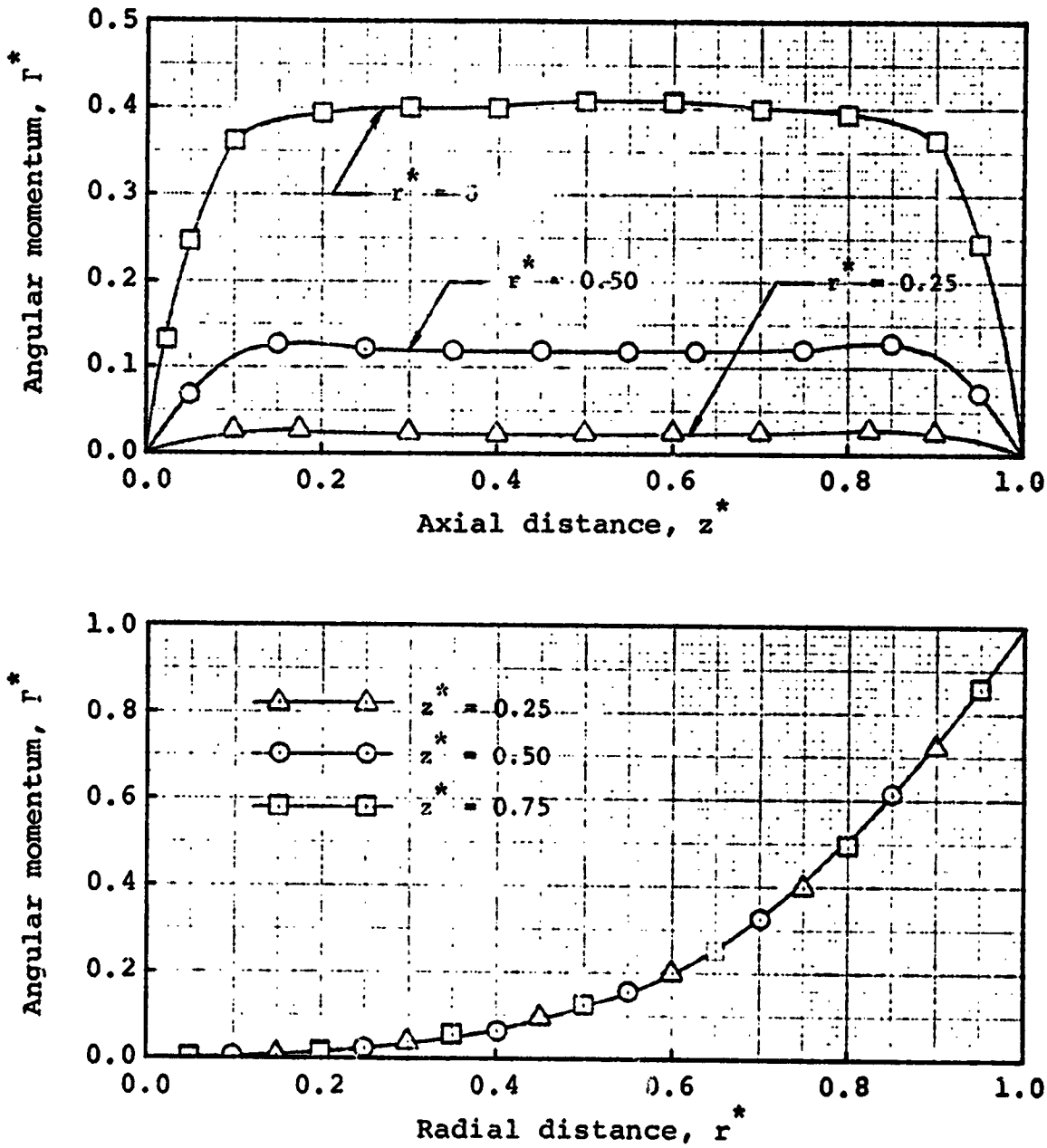

Fig. 30. Distribution of Angular Momentum for Re = 1, Re_t = 15 and a = 2.

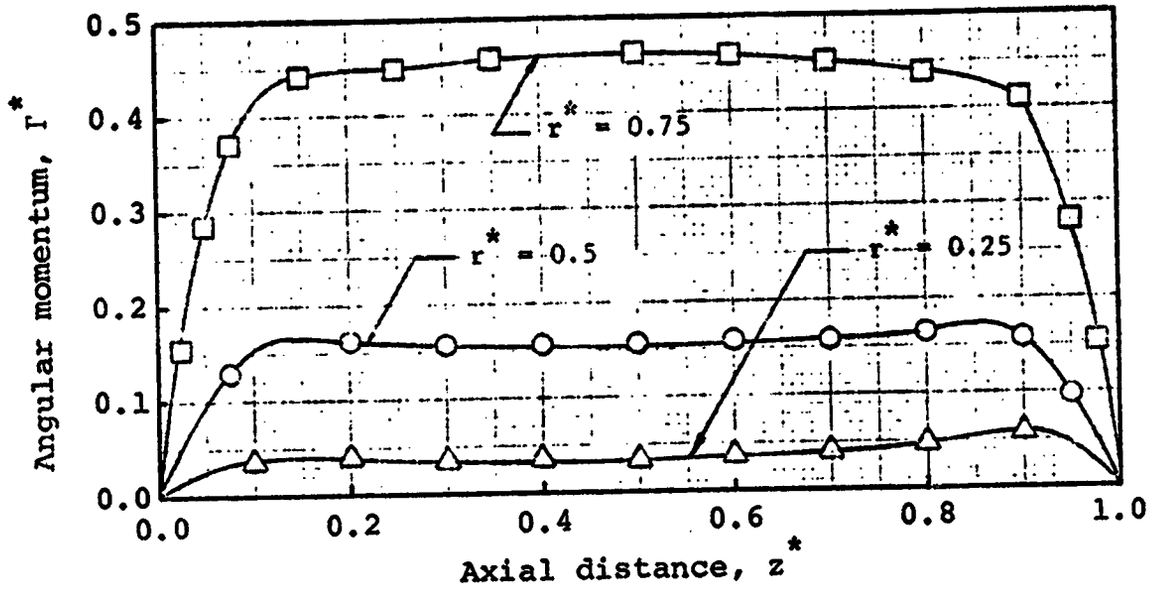

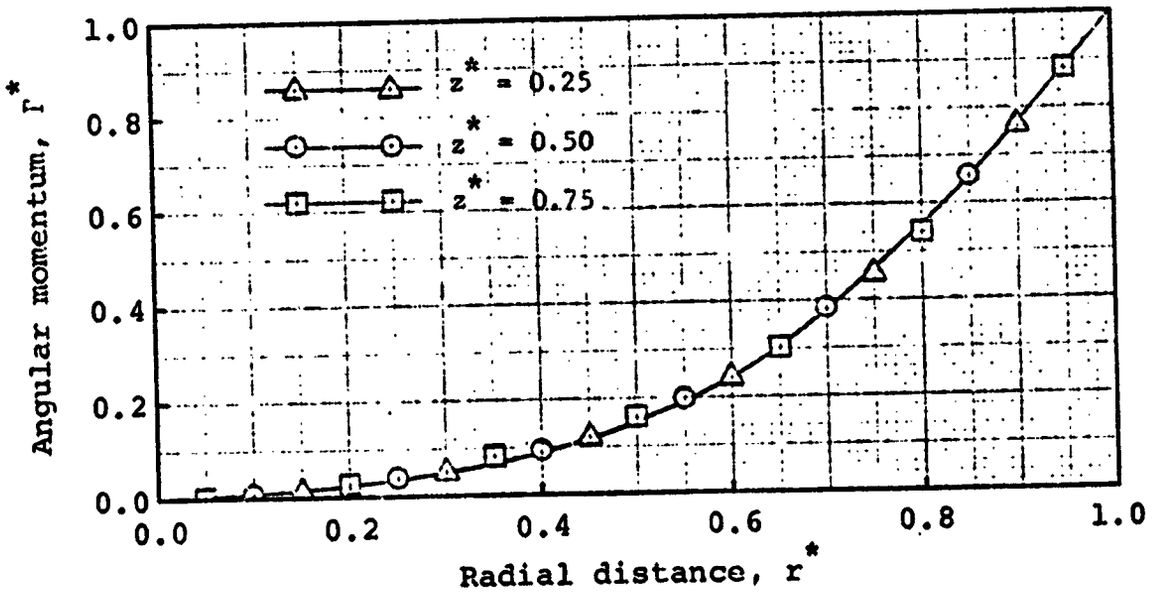

Fig. 31. Distribution of Angular Momentum for Re = 20, Re_t = 15 and a = 2.

Binary Fluid Flows

Results for binary fluid flows are presented and discussed in this section. The relative interior mass addition values of component A, f_{A-B} equal to 0.01 and 0.05 are considered. For these low values of f_{A-B}, the result shows that the velocity field does not deviate much from the single component flows (without interior mass addition). Moreover, the characterisitc flow features of driven vortices remain unaltered. Therefore, only the values of the potential function and mass concentration are presented and discussed. Results of mass diffusion are given in such a manner that they show the effect of the tangential Reynolds number on the concentration distribution for a fixed axial Reynolds number using the pure density ratio as a parameter. Only the axial Reynolds number of 20 is considered for binary flows since high axial Reynolds numbers are desirable to achieve convection dominated mass transfer which is required for fluid dynamic containment.

It may be seen from the equation that the potential function is insensitive to both the pure density ratio and the tangential Reynolds number. This is because the potential function is affected by the tangential Reynolds number only to the extent that it affects the density field. And the influence of the density field on the potential function is mild for the relatively low values of f_{A-B} considered. This has also been shown by the results.

For this reason, the potential function is presented only for a single value of the pure density ratio, 0.5, and a tangential Reynolds number of 100. It is given in Fig. 32 as representative for a family of such figures. It is to be noted that the potential function equation is decoupled from the rest of the equations of the system when the pure density ratio is unity. In this case the potential function is determined once in the beginning for a specified mass addition schedule and the result is used for subsequent calculations of the remaining variables. Results given in this section are all for a fixed value of aspect ratio of 1.

Results for concentrations of fissionable material component A, are plotted in Fig. 33, 34 and 35 for tangential Reynolds numbers of 0, 50 and 100 respectively for the case of a fixed Schmidt number of 1, f_{A-B}=0.01 and pure density ratio of 0.5. It is seen in these figures that as the tangential Reynolds number increases the over-all level of concentration increases and also its gradient becomes steeper. The mass fraction is also plotted in Fig. 36 through 41 for pure density ratios of 1 and 2 each for tangential Reynolds numbers of 0, 50 and 100. These are also for a Schmidt number of 1 and a mass addition rate, f_{A-B} of 0.01. The figures show little variation in concentration distribution due to the variation in the pure density ratios from 0.5 to 2.0. It may be stated that the effect of the pure density ratio on the resulting density

field is mild and hence the concentration equation is only weakly affected by the variation in the pure density ratio. The effect of rotation on concentration in these cases is similar to the case of the pure density ratio of 0.5. Both the over-all level and the gradient of concentration are shown to increase with increasing tangential Reynolds number.

Next, the case with interior mass addition, f_{A-B}, of 0.05 is considered. The potential function for a pure density ratio of 0.5 and a tangential Reynolds number of 50 is plotted in Fig. 42. The distribution of the potential function obtained is similar to the case with an interior mass source of 0.01 since the function has been normalized by appropriate reference quantity. The mass fraction of component A is given in Fig. 43 and 44 for the tangential Reynolds number of 0 and 50 both for the case of Schmidt number of 1 and pure density ratio of 0.5. The figures show that the distribution is similar to that obtained with a mass addition rate, f_{A-B}, of 0.01 discussed above. But the over-all concentration is increased by a factor approximately equal to the ratio of the mass addition rates. It is also seen in this case that the vortex motion increases the over-all concentration as well as its gradient, which indicates the fluid dynamic containment property of driven vortices.

Finally, the containment factor is calculated according to the following expression:

$$\eta = \frac{\text{Total Mass of Fuel (Component A) in the Chamber}}{\text{Total Fuel Mass if 100\% Fuel in the Mass Addition Region}}$$

$$= \frac{\rho_{B,P} \int_0^1 \int_0^1 \rho^*(r^*,z^*)c(r^*,z^*)r^*dr^*dz^*}{\rho_{A,P} \int_{r_1^*}^{r_2^*} \int_{z_1^*}^{z_2^*} r^*dr^*dz^*} \qquad (95)$$

The containment factor as expressed above represents a ratio of an actual average residence time of fissionable material based on steady operating conditions to that of an ideal reference time. This reference time is chosen as the residence time of fissionable material for an ideal case of 100% fissionable material in the assumed containment region. The containment region here is the region in which the fissionable material source is uniform.

The containment factor is computed numerically by a double integration using a trapezoidal rule after the steady state solution is obtained. The results for pure density ratios, $\rho_{A,P}/\rho_{B,P}$ of 0.5, 1.0 and 2.0 are plotted against tangential Reynolds numbers in Fig. 45 for a mass addition rate, of 0.01. The figure indicates that the containment factor increases with increasing tangential Reynolds number for a fixed axial Reynolds number, Schmidt number and pure density ratio. The containment factor calculated for a mass addition rate, $f_{A-B'}$ of 0.05 and pure density ratio of 0.5 is also included in this figure. The figure shows that it

nearly follows the curve of $f_{A-B}=0.01$ when the value is scaled by the ratio of the two mass addition rates. This indicates that the over-all concentration of fissionable material and hence the containment increases more or less linearly with the fuel mass injection rate. As may be seen from the mass diffusion equation, a further increase in containment factor can be realized by an increase in either the axial Reynolds number or Schmidt number. Finally, it is seen that decreasing the pure density ratio increases the containment for fixed rotation.

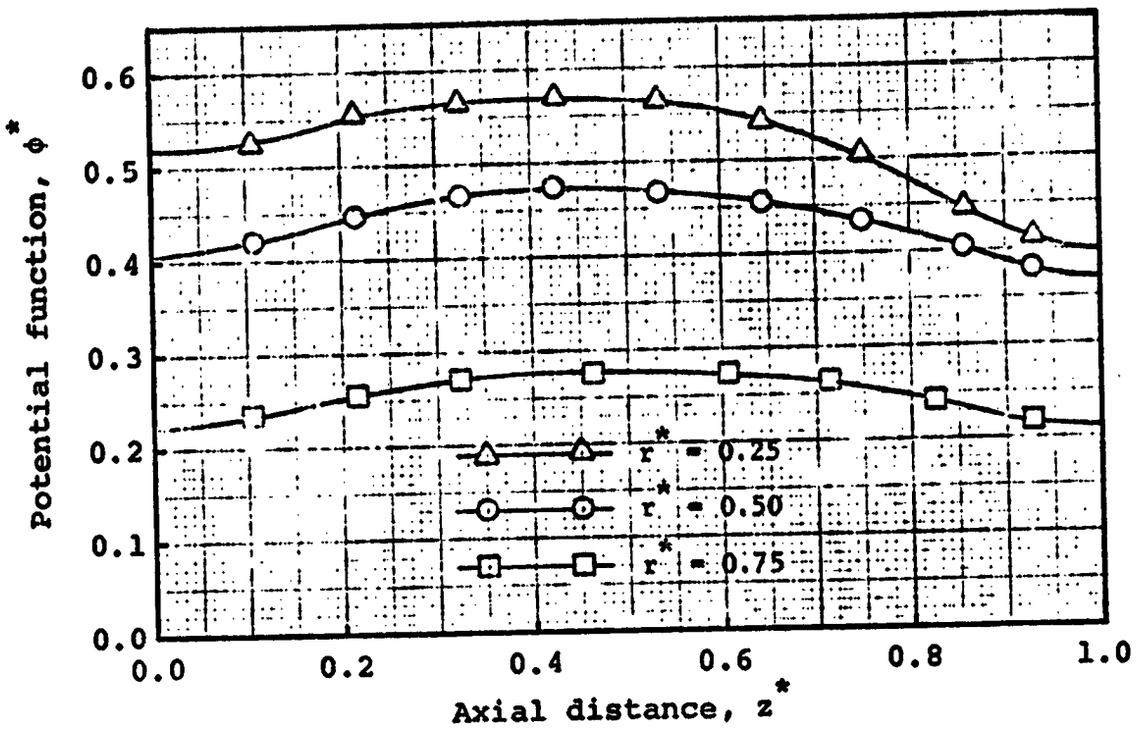

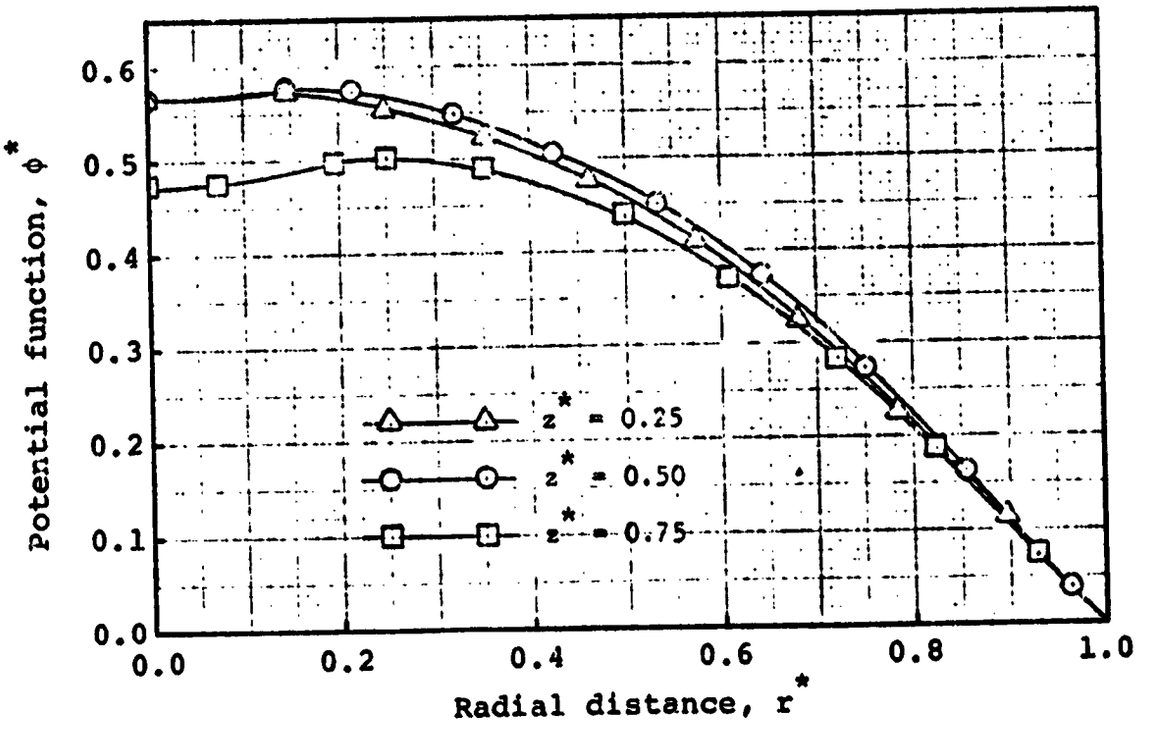

Fig. 32. Potential Function for Re = 20, Re_t = 100, $\rho_{A,P}/\rho_{B,P}$ = 0.5, f_{A-B} = 0.01 and a = 1.

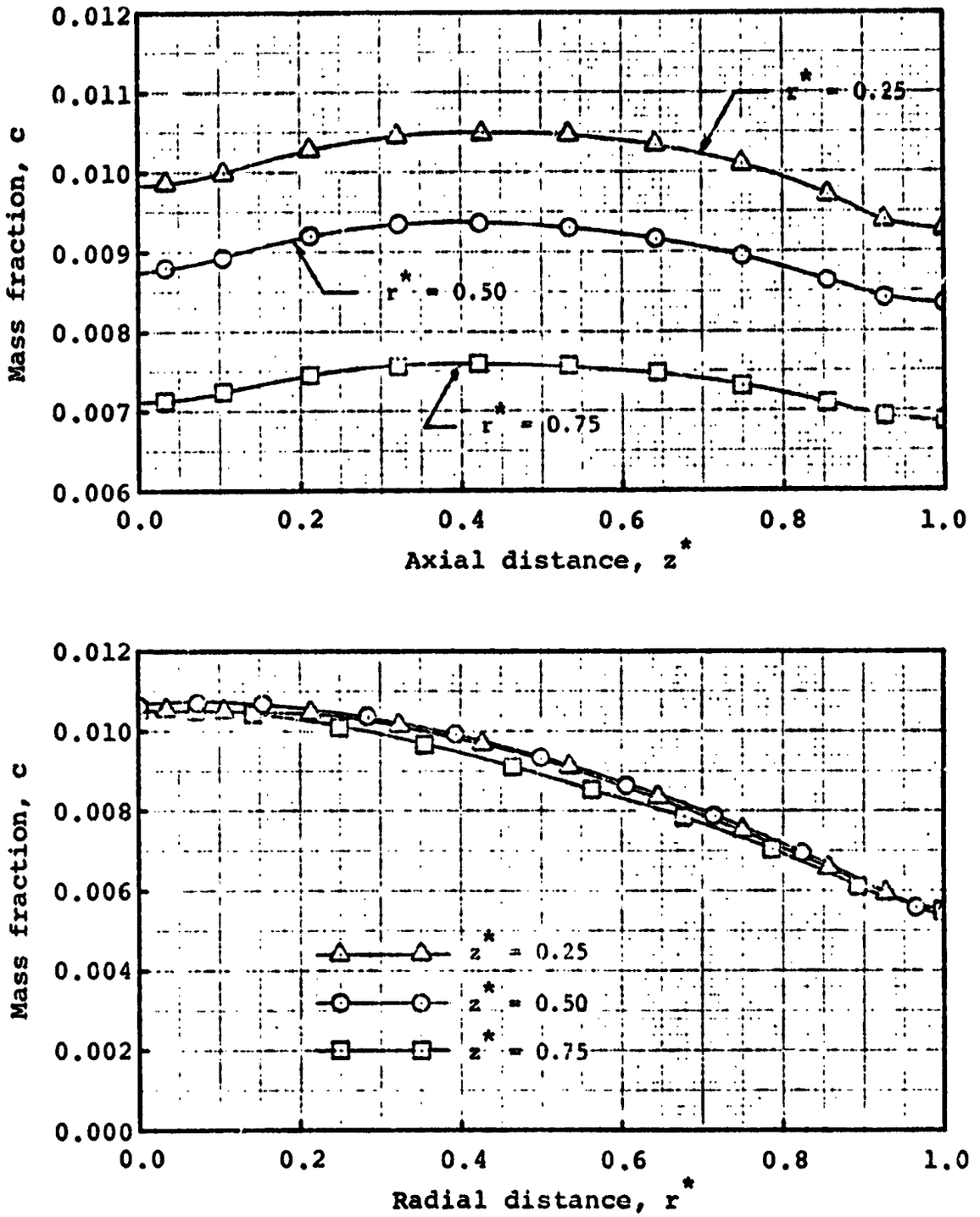

Fig. 33. Mass Fraction of Component A (Simulated Fuel) for Re = 20, Re_t = 0, Sc = 1, $\rho_{A,P}/\rho_{B,P}$ = 0.5, f_{A-B} = 0.01 and a = 1.

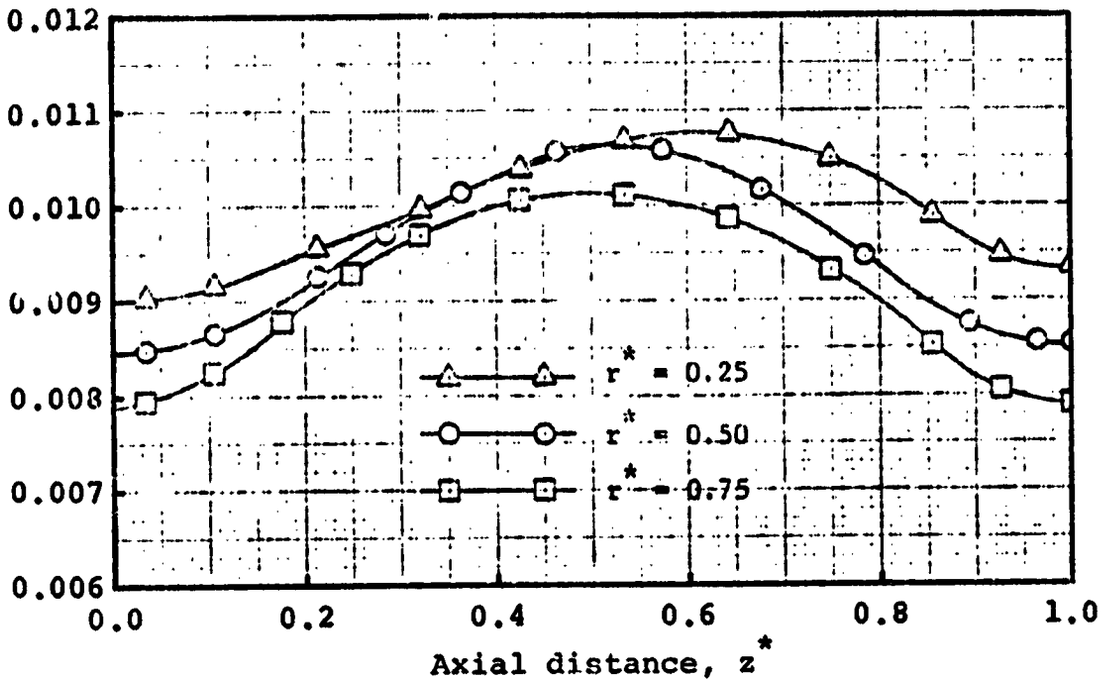

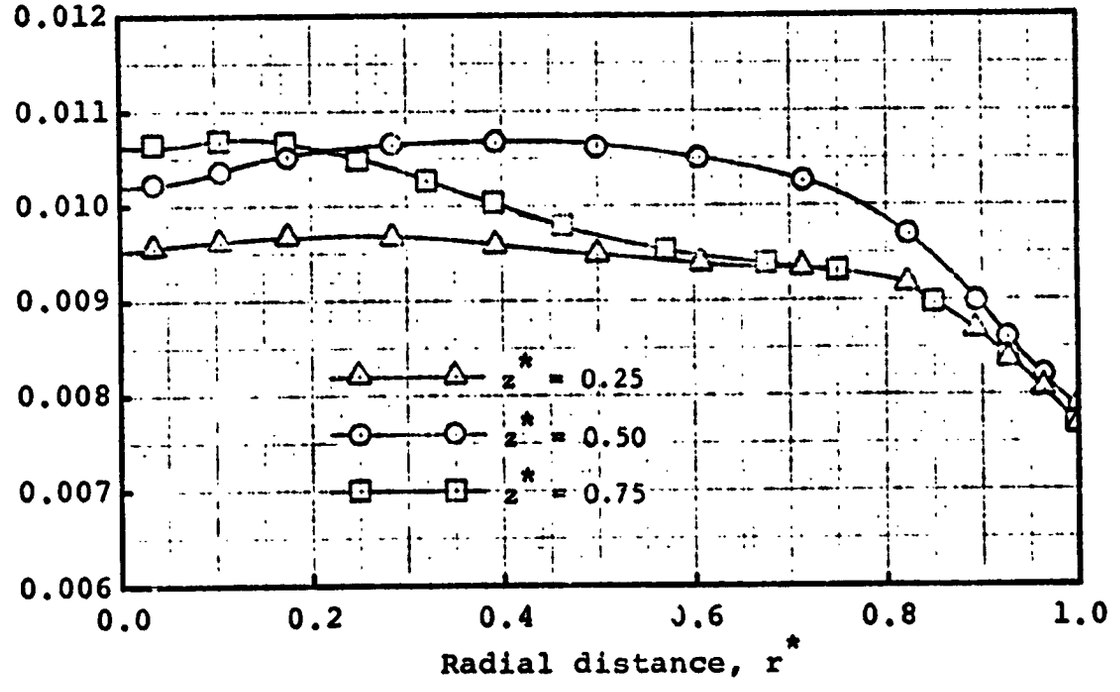

Fig. 34. Mass Fraction of Component A (Simulated Fuel) for Re = 20, Re_t = 50, Sc = 1, $\rho_{A,P}/\rho_{B,P}$ = 0.5, f_{A-B} = 0.01 and a = 1.

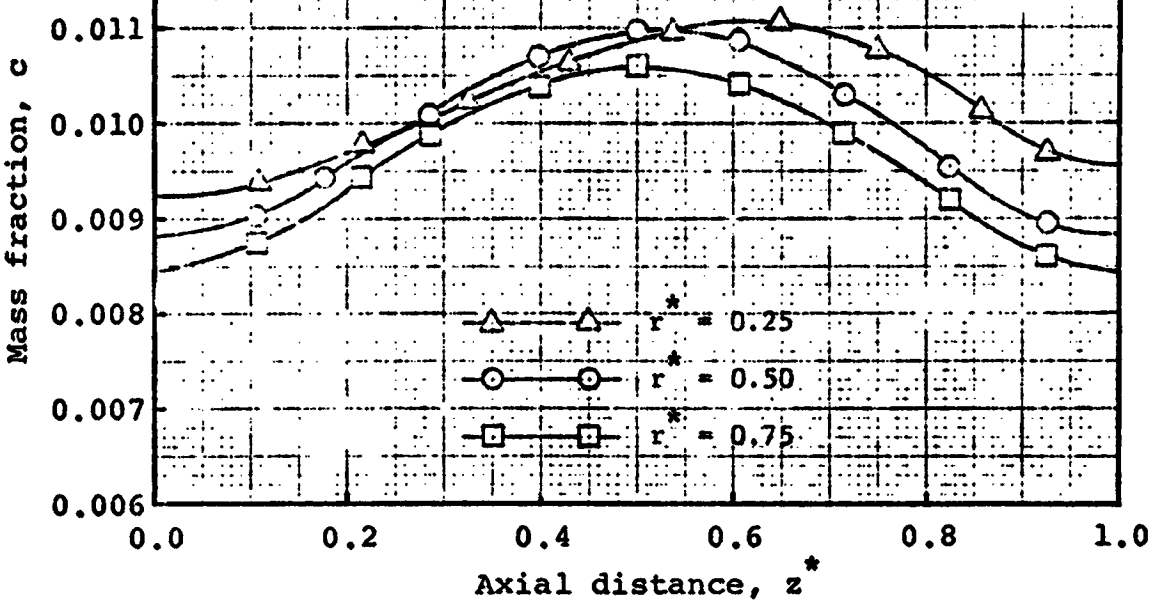

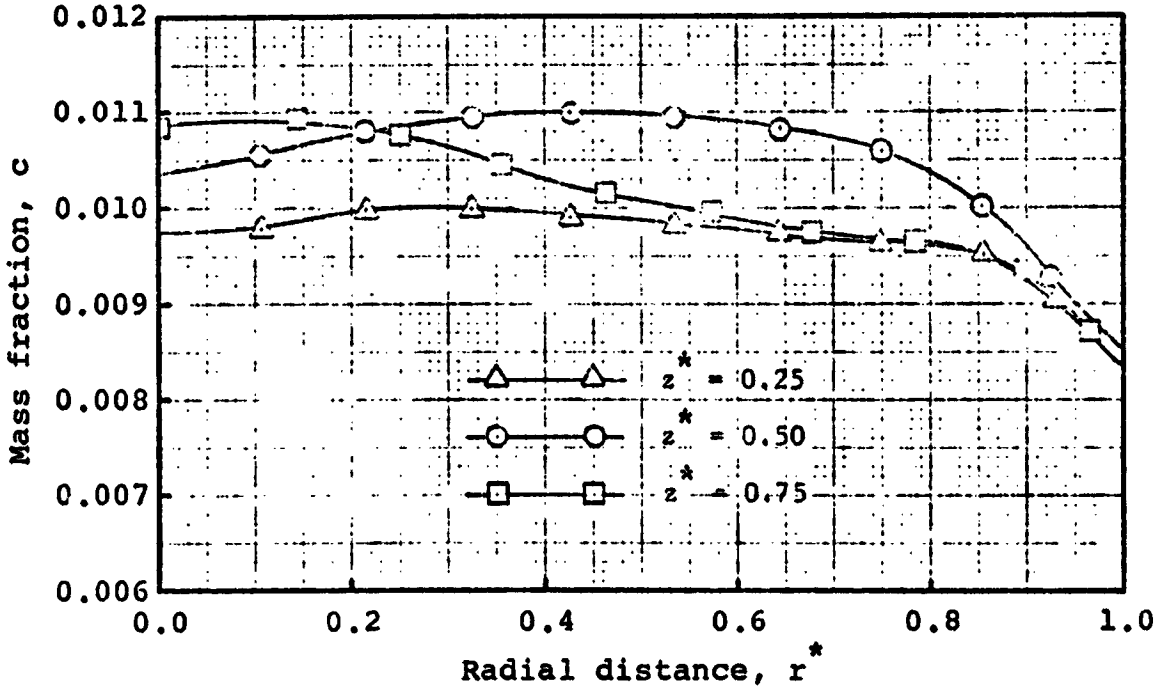

Fig. 35. Mass Fraction of Component A (Simulated Fuel) for Re = 20, Re_t = 100, Sc = 1, $\rho_{A,P}/\rho_{B,P}$ = 0.5, f_{A-B} = 0.01 and a = 1.

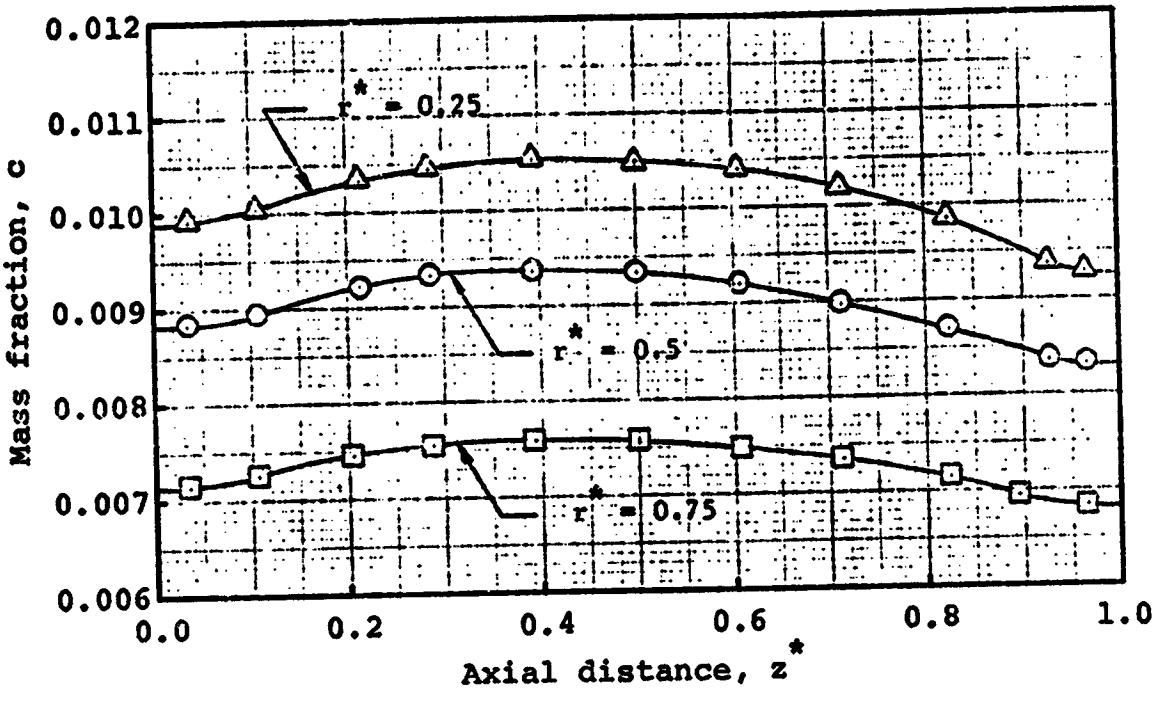

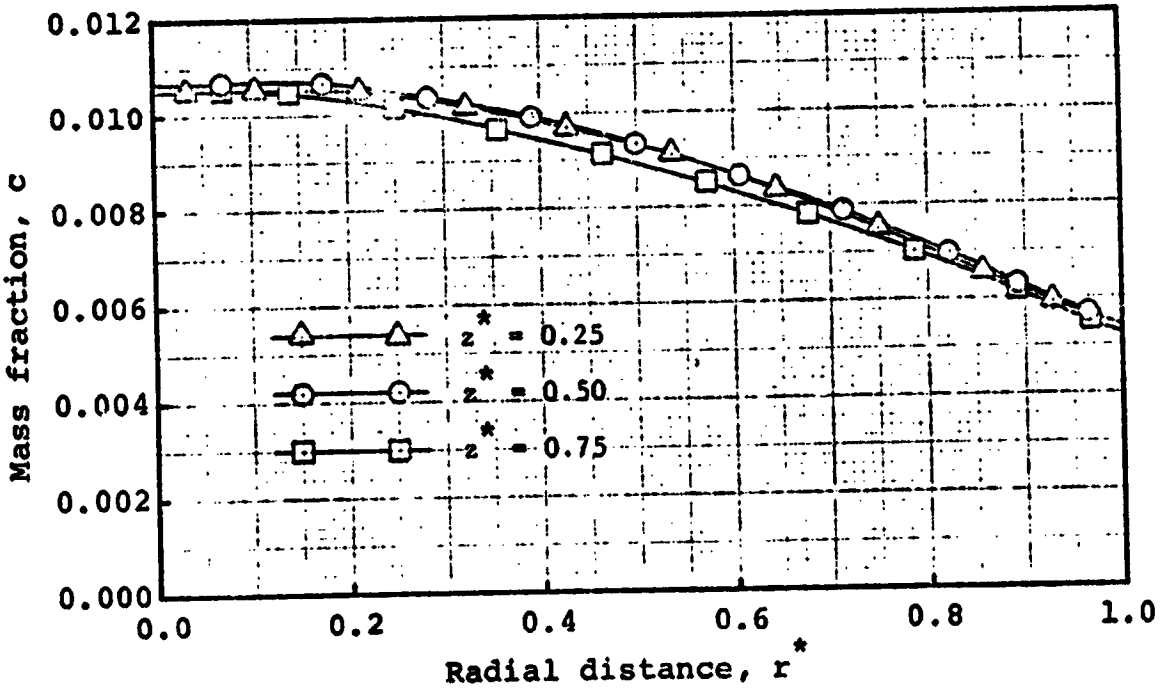

Fig. 36. Mass Fraction of Component A (Simulated Fuel) for Re = 20, Re_t = 0, Sc = 1, $\rho_{A,P}/\rho_{B,P}$ = 1, f_{A-B} = 0.01 and a = 1.

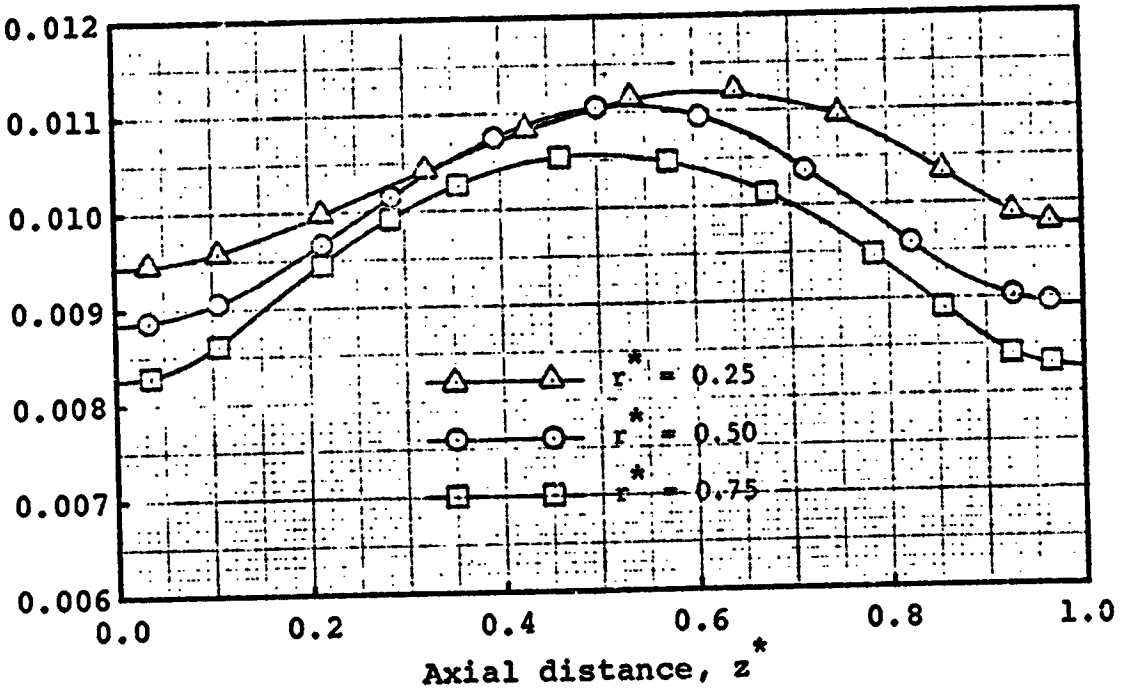

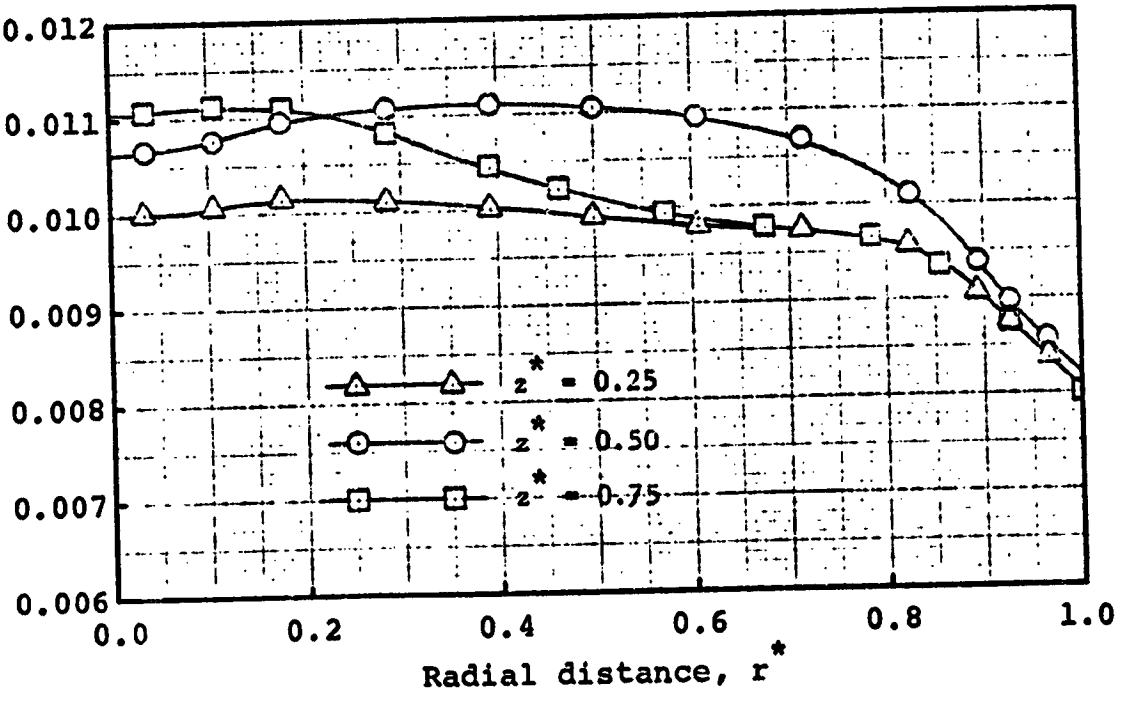

Fig. 37. Mass Fraction of Component A (Simulated Fuel) for Rc = 20, Re_t = 50, Sc = 1, $\rho_{A,P}/\rho_{B,P}$ = 1, f_{A-B} = 0.01 and a = 1.

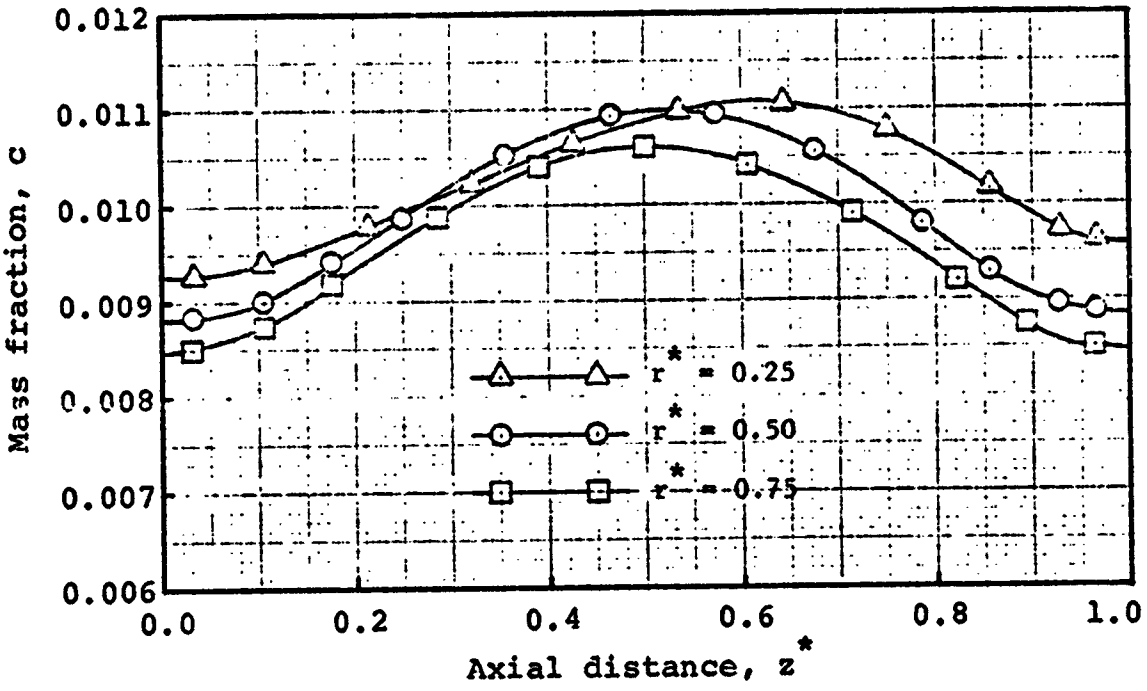

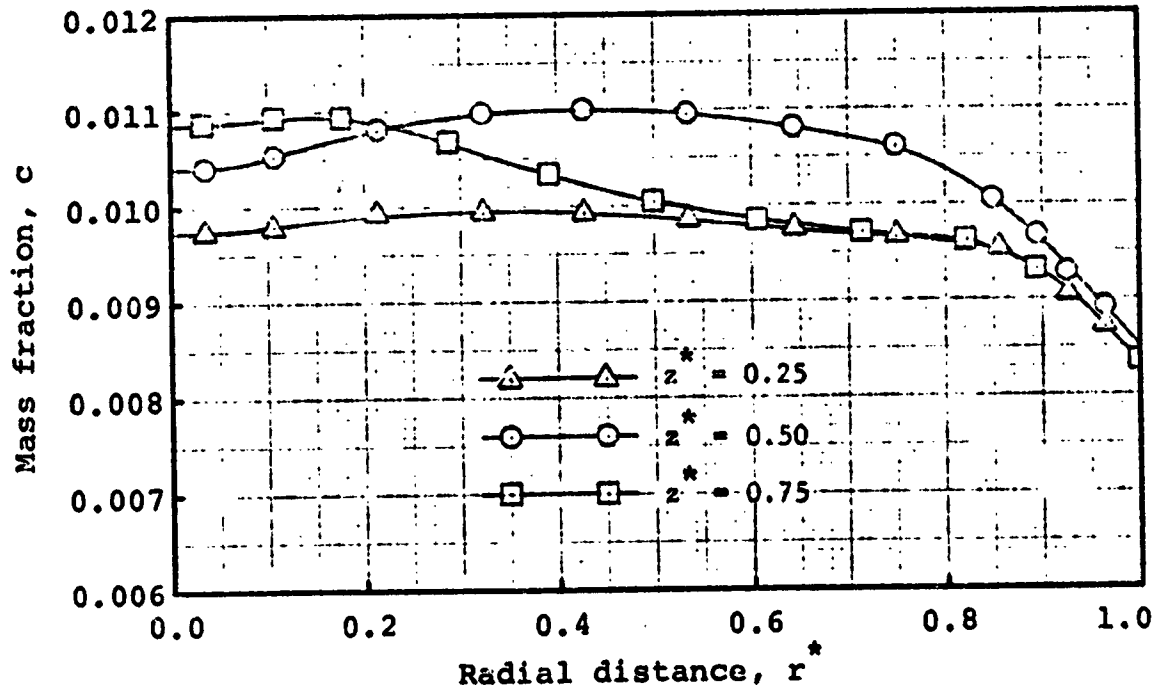

Fig. 30. Mass Fraction of Component A (Simulated Fuel) for Re = 20, Re_t = 100, Sc = 1, $\rho_{A,P}/\rho_{B,P}$ = 1, f_{A-B} = 0.01 and a = 1.

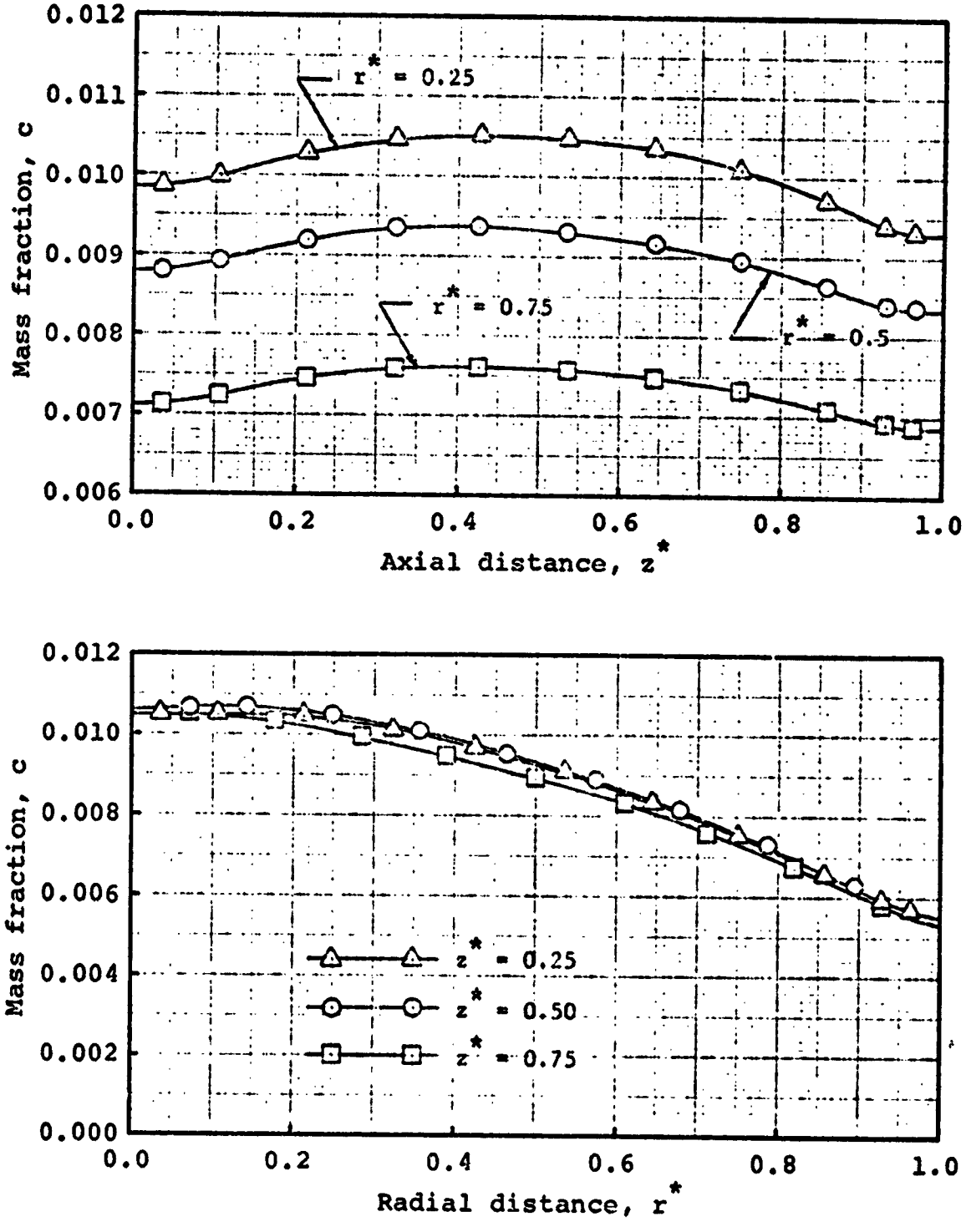

Fig. 39. Mass Fraction of Component A (Simulated Fuel) for Re = 20, Re_t = 0, Sc = 1, $\rho_{A,P}/\rho_{B,P}$ = 2.0, f_{A-B} = 0.01 and a = 1.

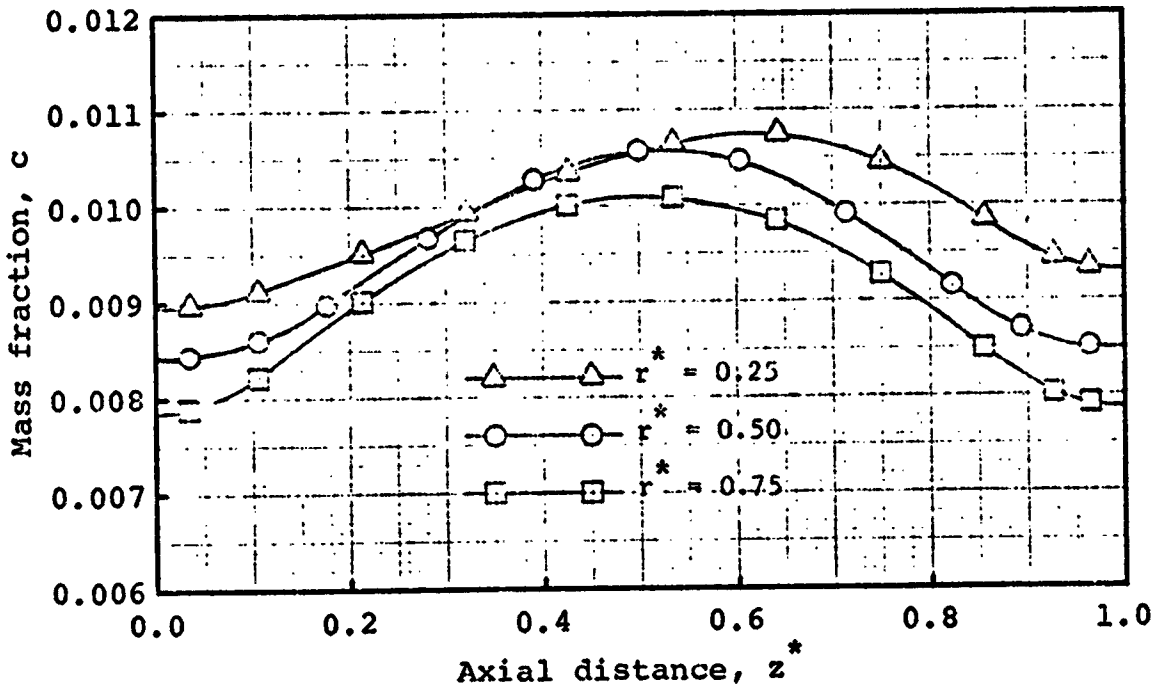

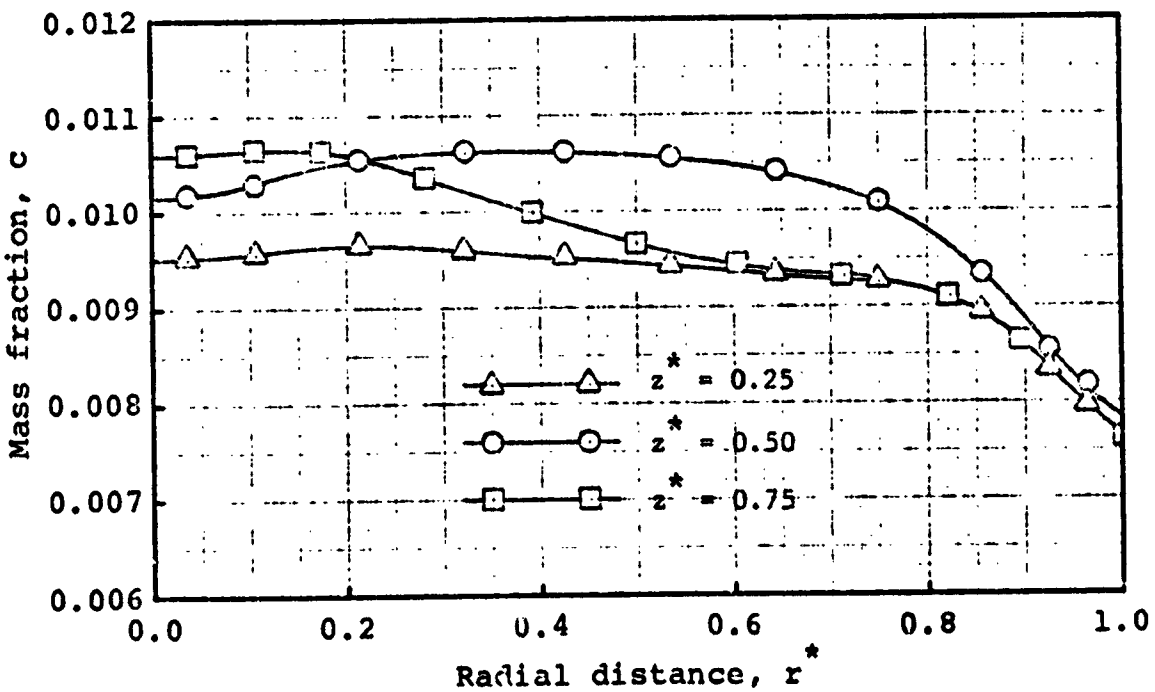

Fig. 40. Mass Fraction of Component A (Simulated Fuel) for Re = 20, Re_t = 50, Sc = 1, $\rho_{A,P}/\rho_{B,P}$ = 2, f_{A-B} = 0.01 and a = 1.

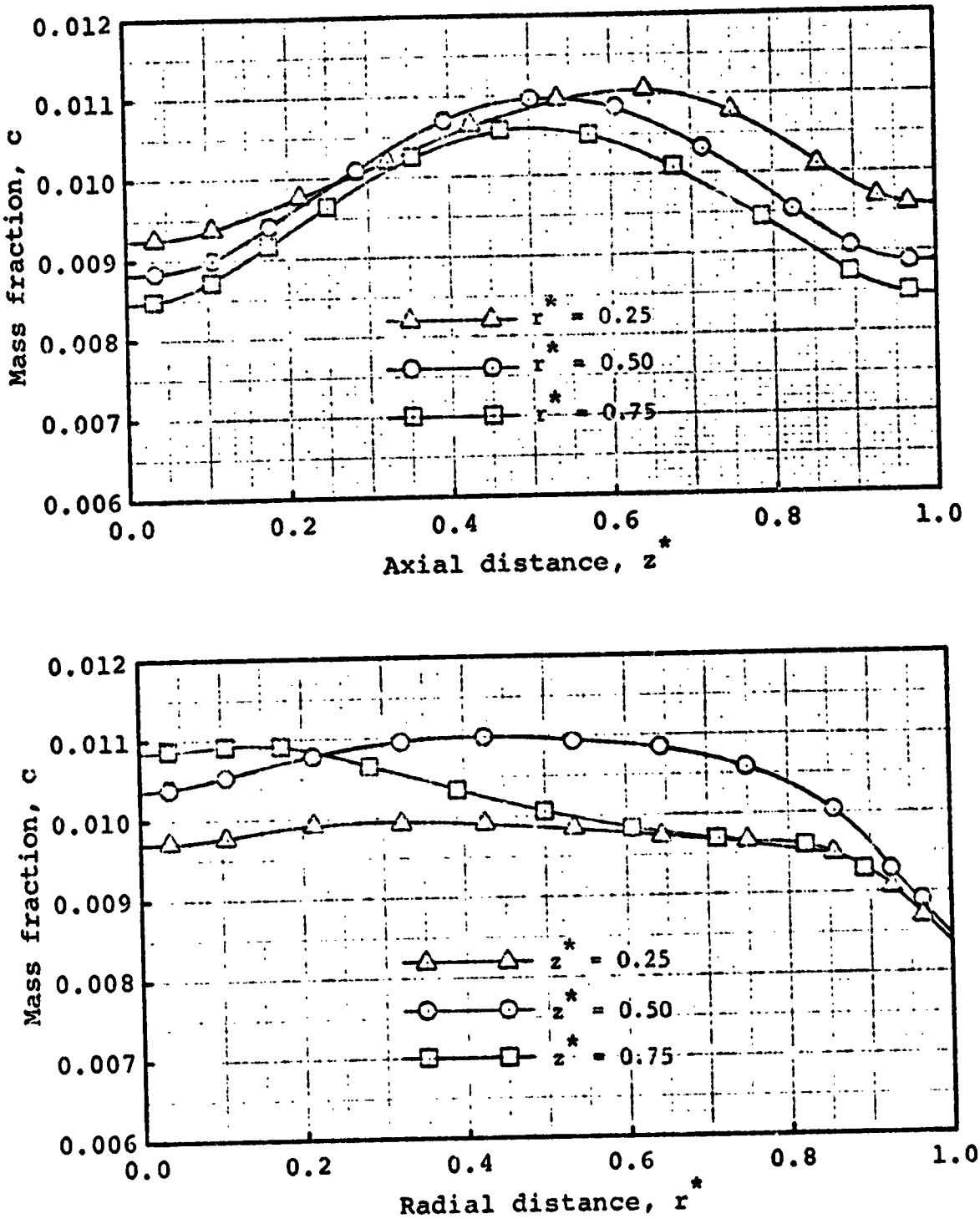

Fig. 41. Mass Fraction of Component A (Simulated Fuel) for Re = 20, Re_t = 100, Sc = 1, $\rho_{A,P}/\rho_{B,P}$ = 2, f_{A-B} = 0.01 and a = 1.

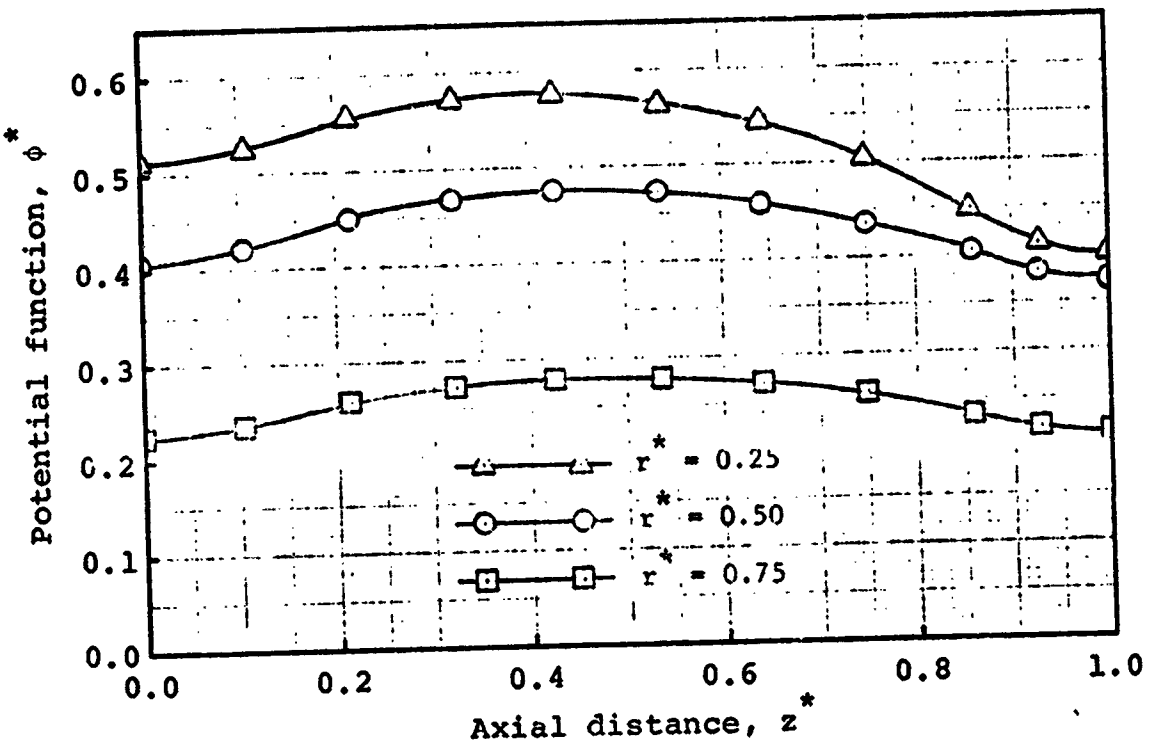

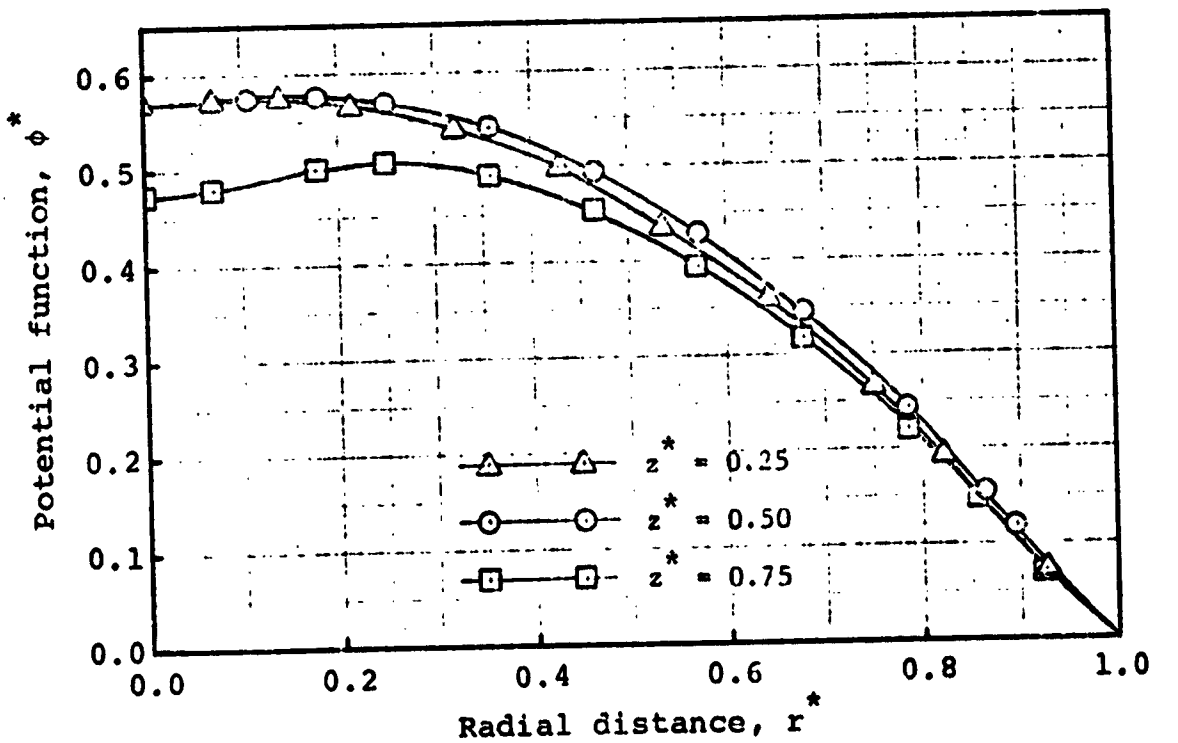

Fig. 42. Potential Function for Re = 20, Re_t = 50, $\rho_{A,P}/\rho_{B,P}$ = 0.5, f_{A-B} = 0.05 and a = 1.

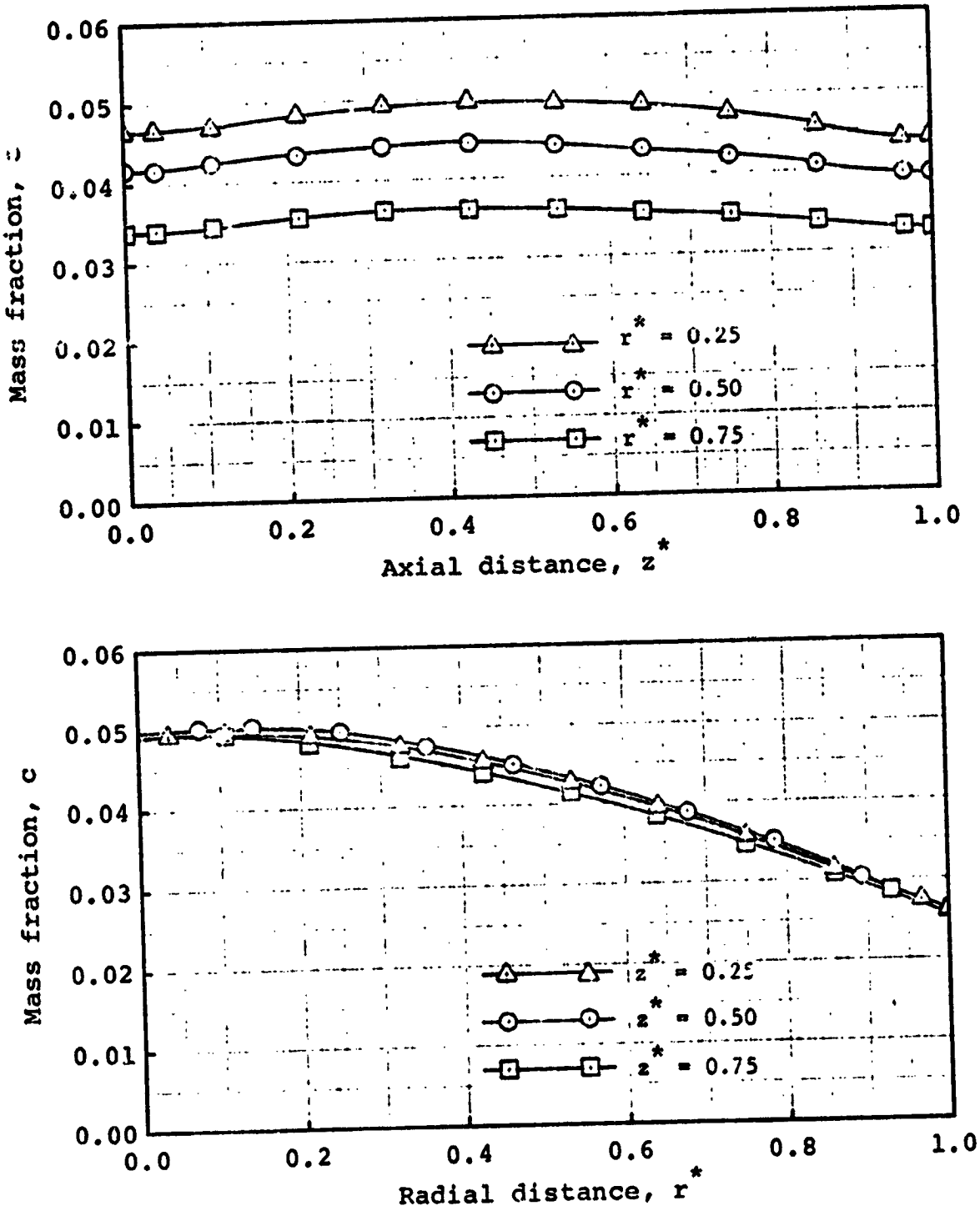

Fig. 43. Mass Fraction of Component A (Simulated Fuel) for Re = 20, Re_t = 0, Sc = 1, $\rho_{A,P}/\rho_{B,P}$ = 0.5, f_{A-B} = 0.05 and a = 1.

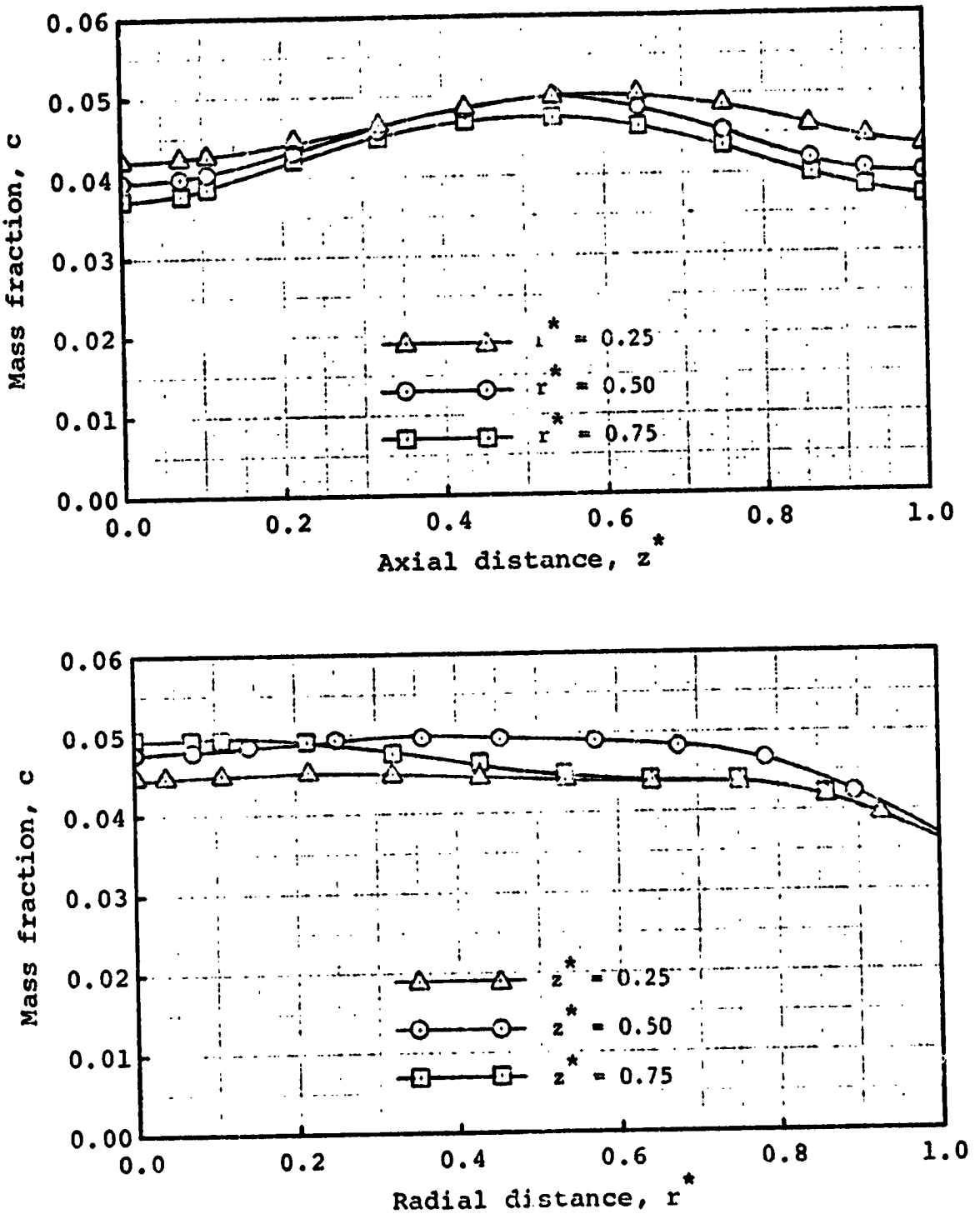

Fig. 44. Mass Fraction of Component A (Simulated Fuel) for Re = 20, Re_t = 50, Sc = 1, $\rho_{A,P}/\rho_{B,P}$ = 0.5, f_{A-B} = 0.05 and a = 1.

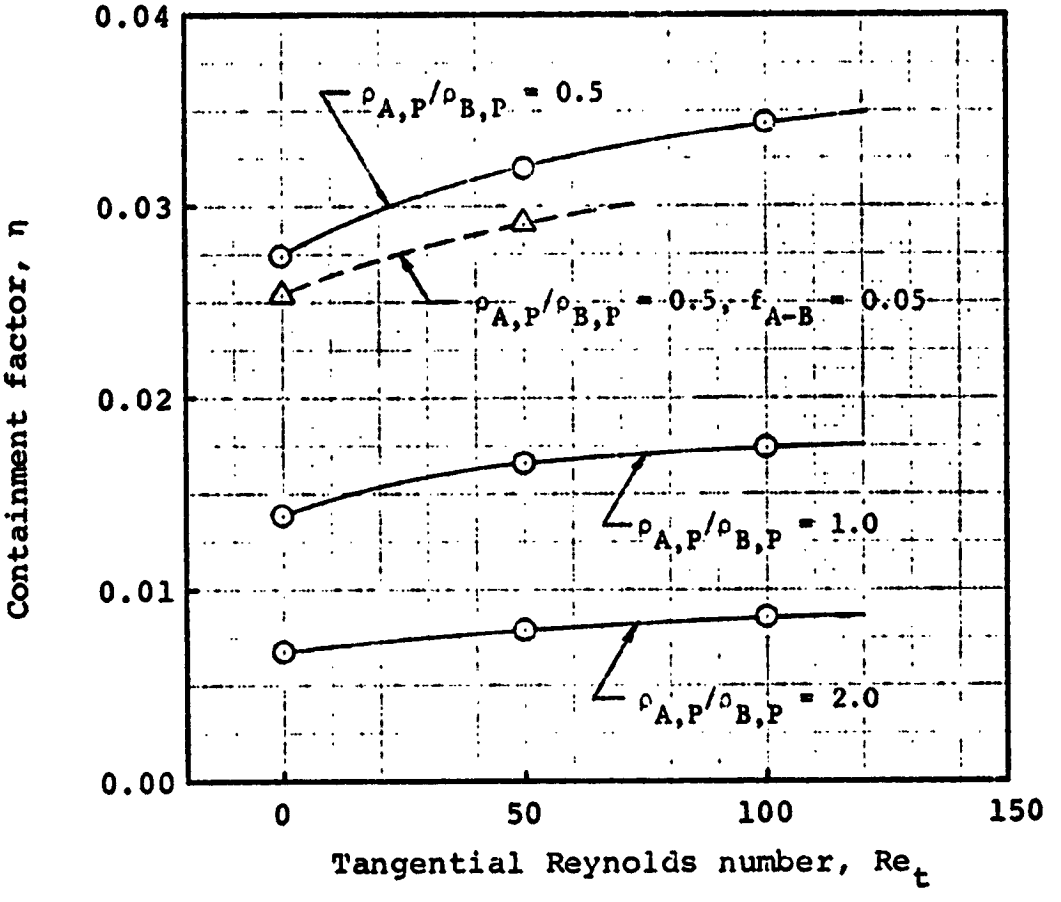

Fig. 45. Containment Factor vs. Tangential Reynolds Number for $\rho_{A,P}/\rho_{B,P}$ = 0.5, 1.0, 2.0 and f_{A-B} = 0.01, 0.05 (The Case of f_{A-B} = 0.05 is Divided by 5)

Pressure Calculation

Pressure calculations are made only for single component flows and they are presented in this section. As mentioned in Ch. IV, the pressure is calculated by the method of line integration for non-rotating flows. For rotating flows it is calculated by solving the Poisson equation of pressure, in which the Fourier analysis is used and 1 Fourier cosine transforms are employed as an effici. omputational algorithm.

The esult for an axial Reynolds number of 1 is presented in Fig. 46 and 47 for tangential Reynolds numbers of 0 and 50 respectively. In the absence of rotating motion, the variation in the pressure is small except in the region near the exhaust hole where the primary flow is accelerating. A decrease in pressure is shown toward the chamber axis near the exit hole. When rotation is present, however, a high radial pressure gradient is formed in the bulk region to balance the large centrifugal force field caused by the angular momentum distribution induced by wall rotation. The uniform radial distribution of pressure shown in Fig. 47 is in agreement with the uniform radial distribution of angular momentum given in Fig. 16. Near the end walls, the rotating motion is retarded by viscosity and hence the local centrifugal force is decreased. However, the pressure in this region is nearly equal to the imposed pressure. The unbalance between the pressure and the centrifugal force

in this region results in a large radial inward flow toward the axis. The mild axial pressure gradient observed in the end wall boundary layer and near the periphery is thought to be a result of the continuity constraint interacting with the momentum field. The symmetry of the pressure profile about the mid-plane, $z^*=0.5$ is shown for the value of the ratio, $Re_t/Re=50$.

Results of the pressure calculation for an axial Reynolds number of 20 are given in Fig. 48 and 49 for $Re_t=50$ and 100 respectively. These figures indicate that the pressure as well as its radial gradient increase as the tangential Reynolds number increases. The radial pressure gradient is seen to increase with radial distance from the axis. A comparison of Fig. 47 with 48 reveals a flatter axial distribution of pressure with lower primary flow rate for a fixed rate of rotation. The discussion given for axial Reynolds number of 1 also applies in general to this case of Re=20. Finally, the pressure calculation for an aspect ratio of 2 is shown for axial Reynolds numbers of 1 and 20, each with a tangential Reynolds number of 15. The result for Re=1 is given in Fig. 50 and that for Re = 20 in Fig. 51. The pressure profile in general is similar to those for the aspect ratio of 1. The only noticeable difference is the asymmetry in the distribution about the mid-plane. The asymmetry in the pressure profile becomes more pronounced as the axial Reynolds number increases for a fixed tangential Reynolds number.

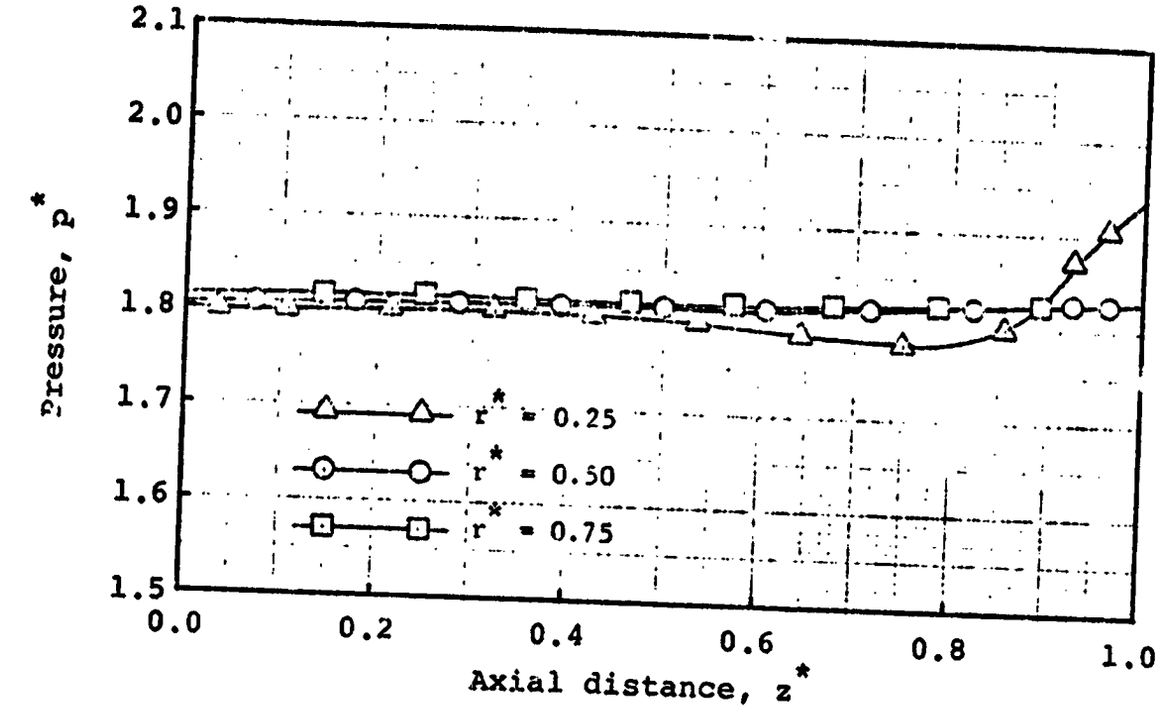

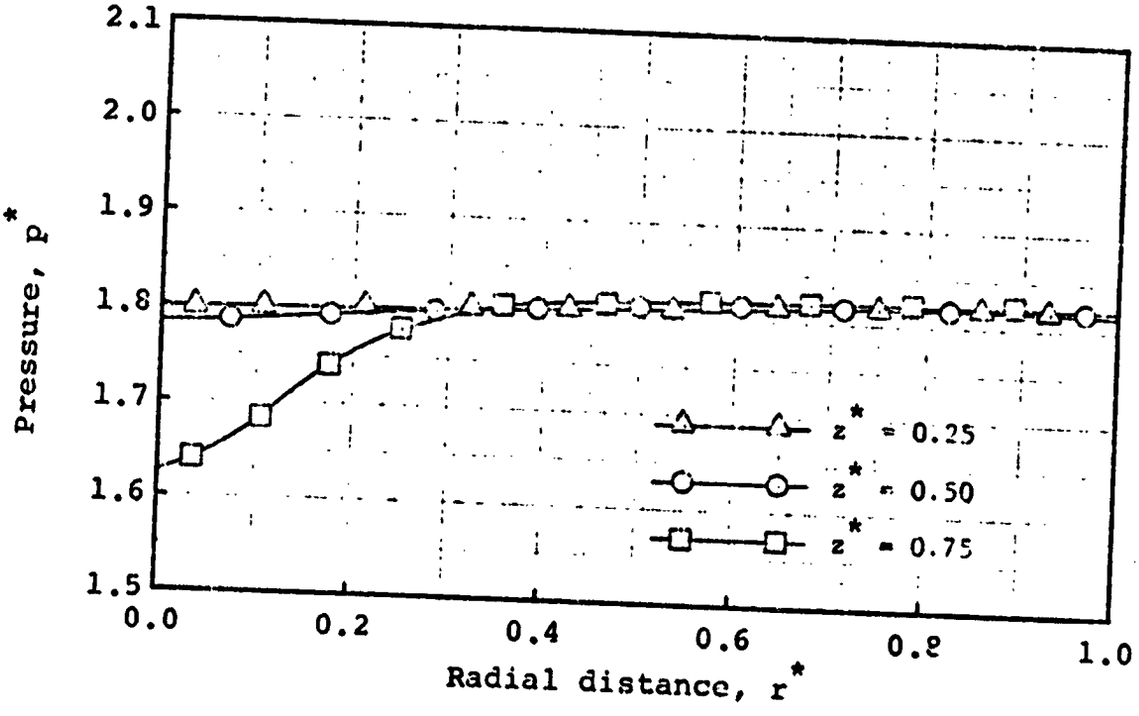

Fig. 46. Pressure Distribution for Re = 1, Re_t = 0 and a = 1.

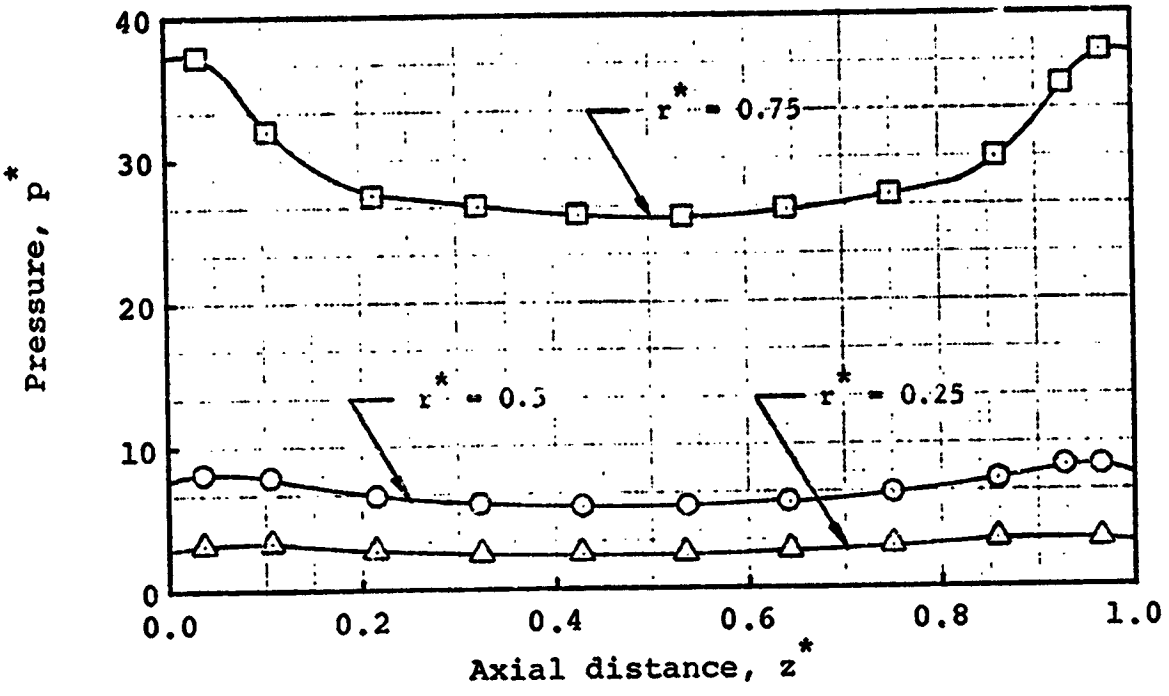

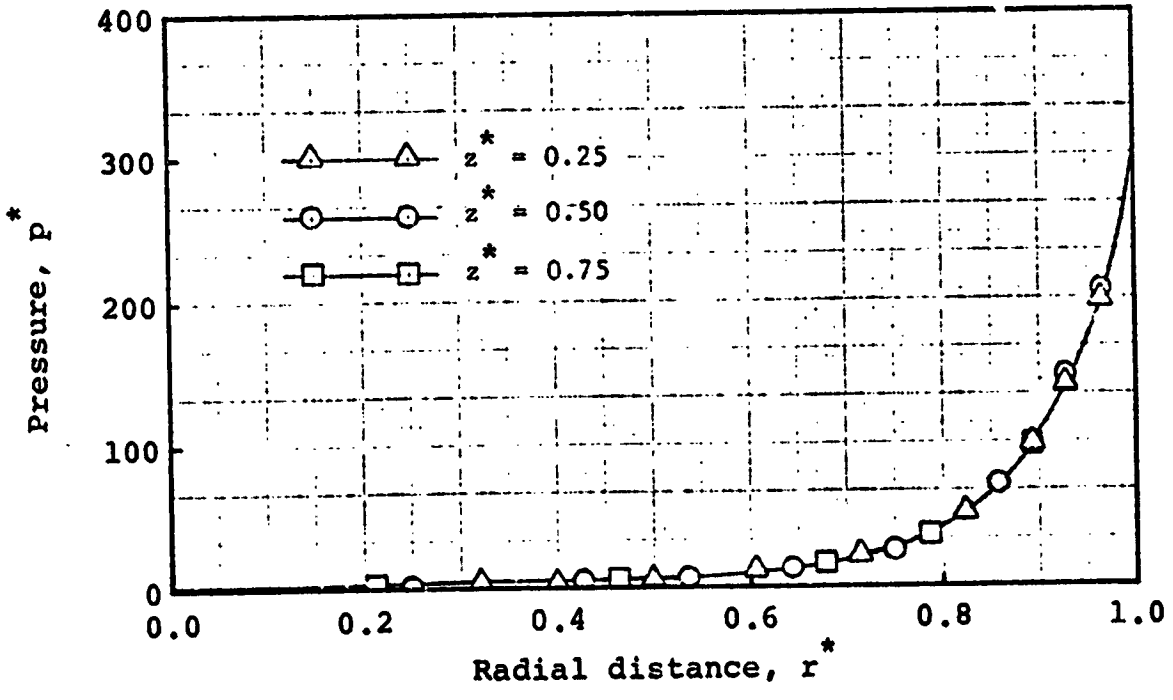

Fig. 47. Pressure Distribution for Re = 1, Re_t = 50 and a = 1.

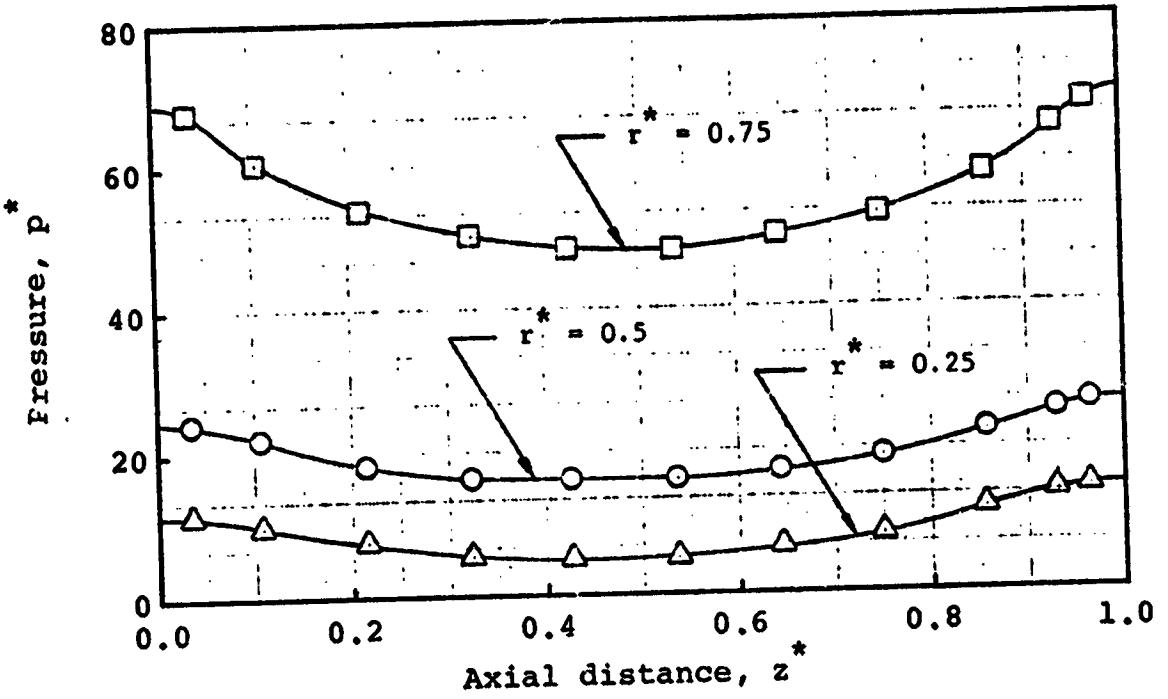

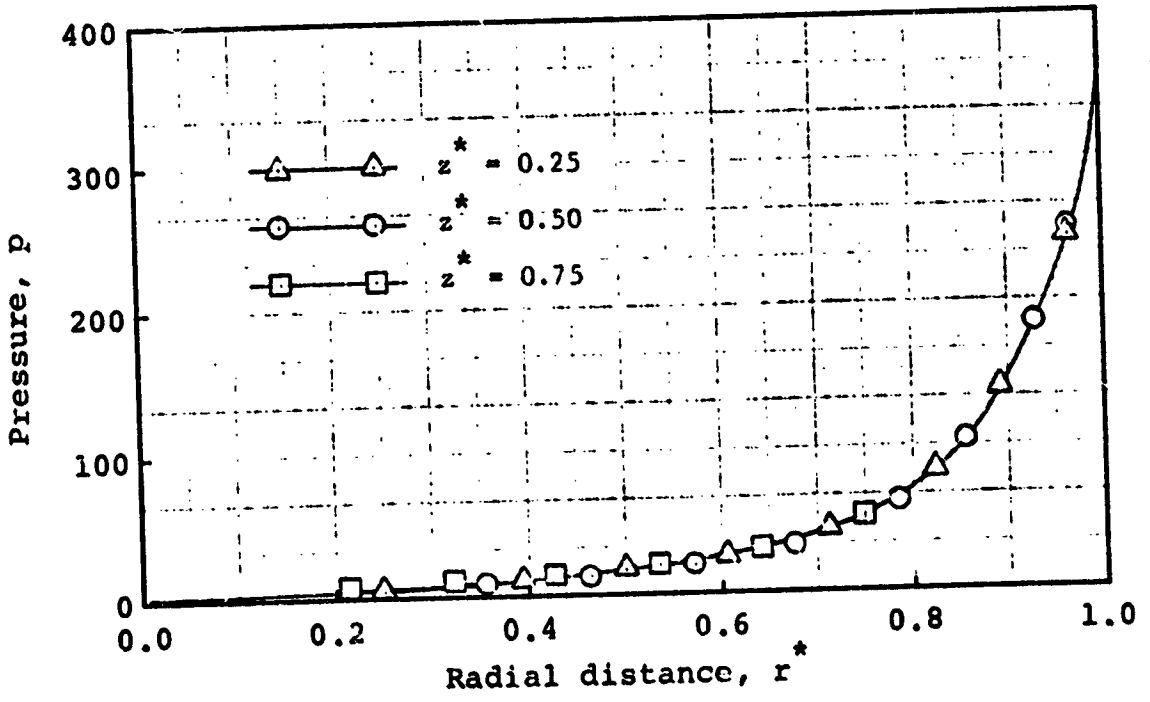

Fig. 48. Pressure Distribution for Re = 20, Re_t = 50 and a = 1.

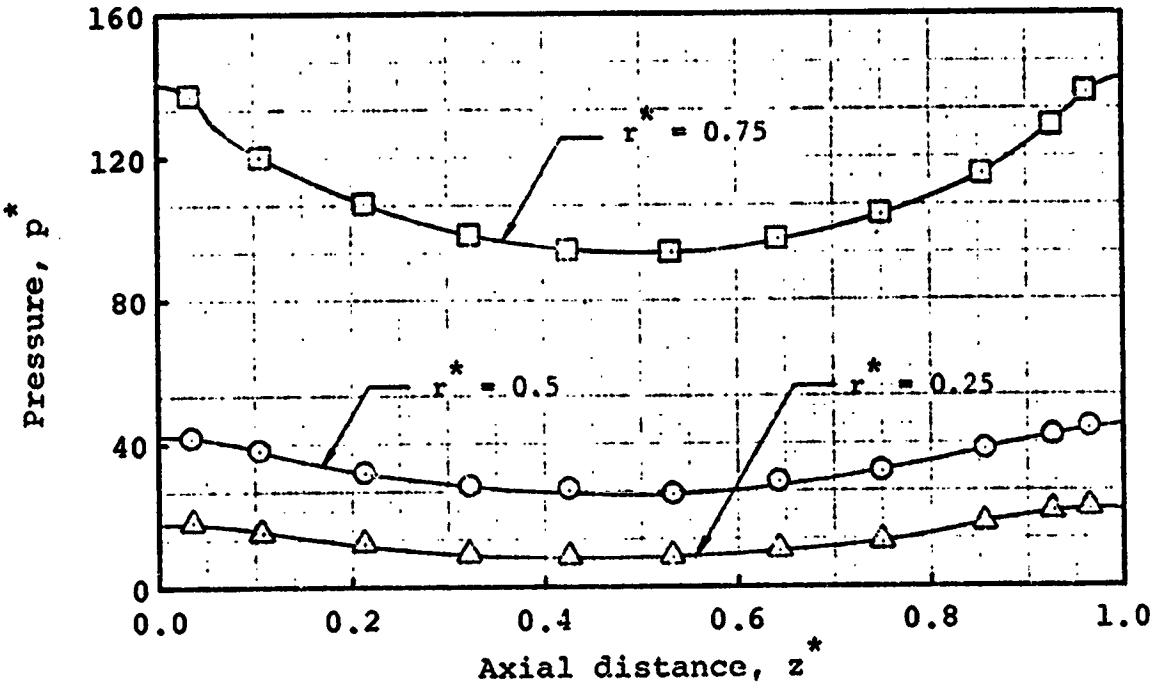

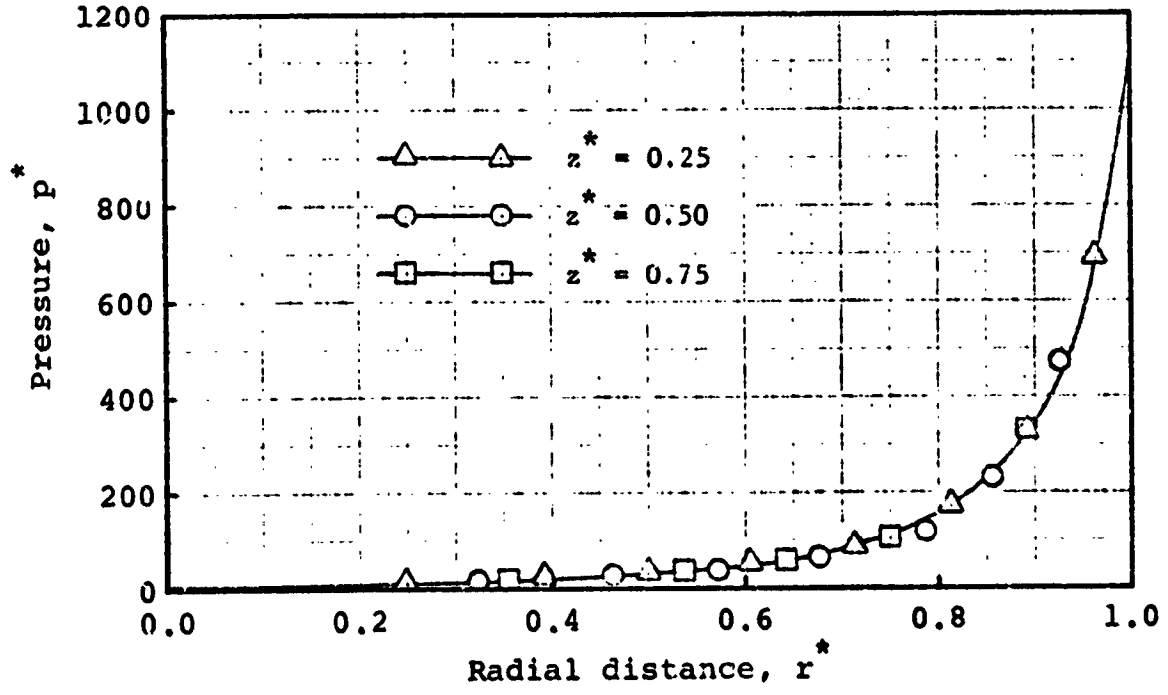

Fig. 49. Pressure Distribution for Re = 20, Re_t = 100 and a = 1.

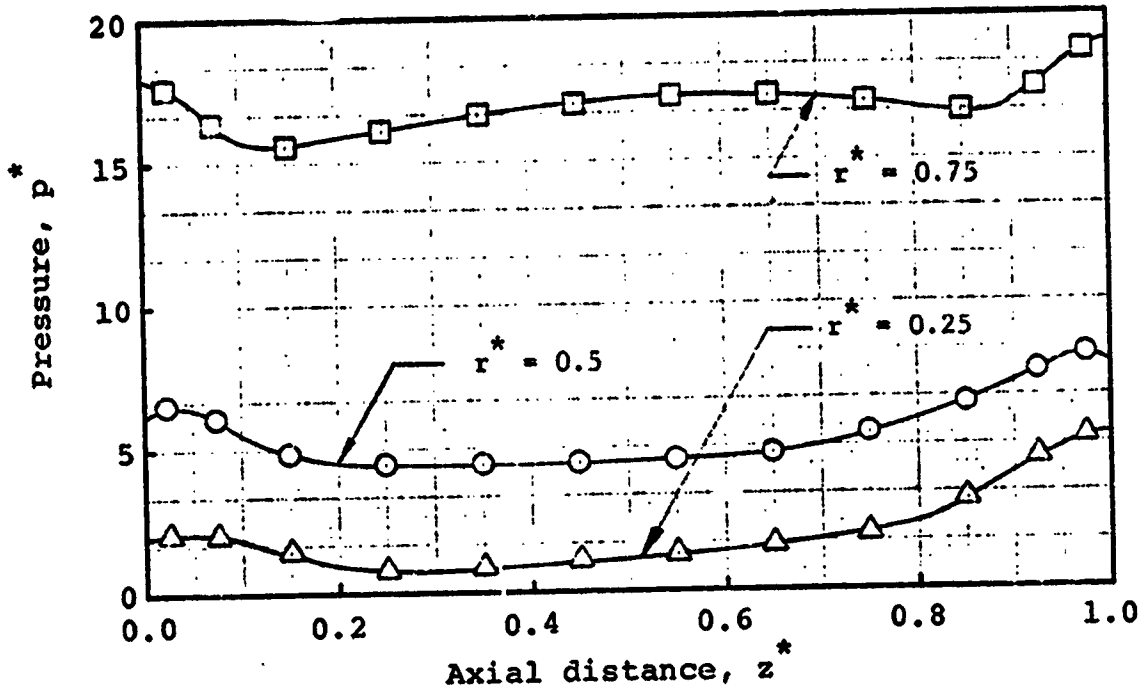

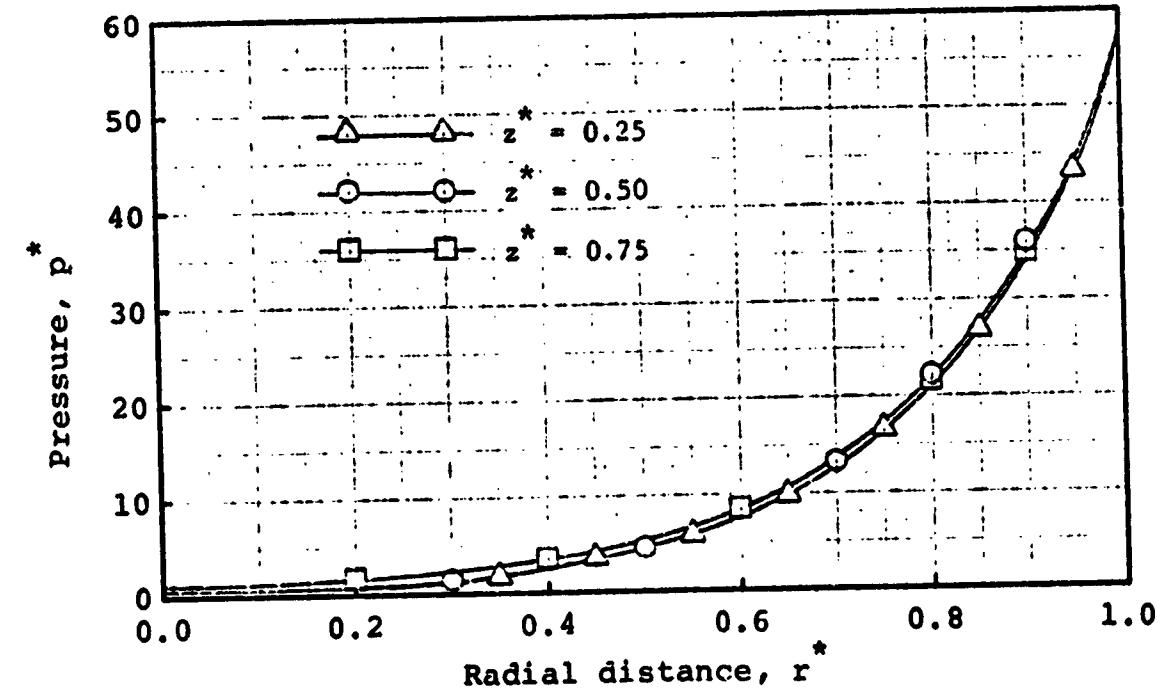

Fig. 50. Pressure Distribution for Re = 1, Re_t = 15 and a = 2.

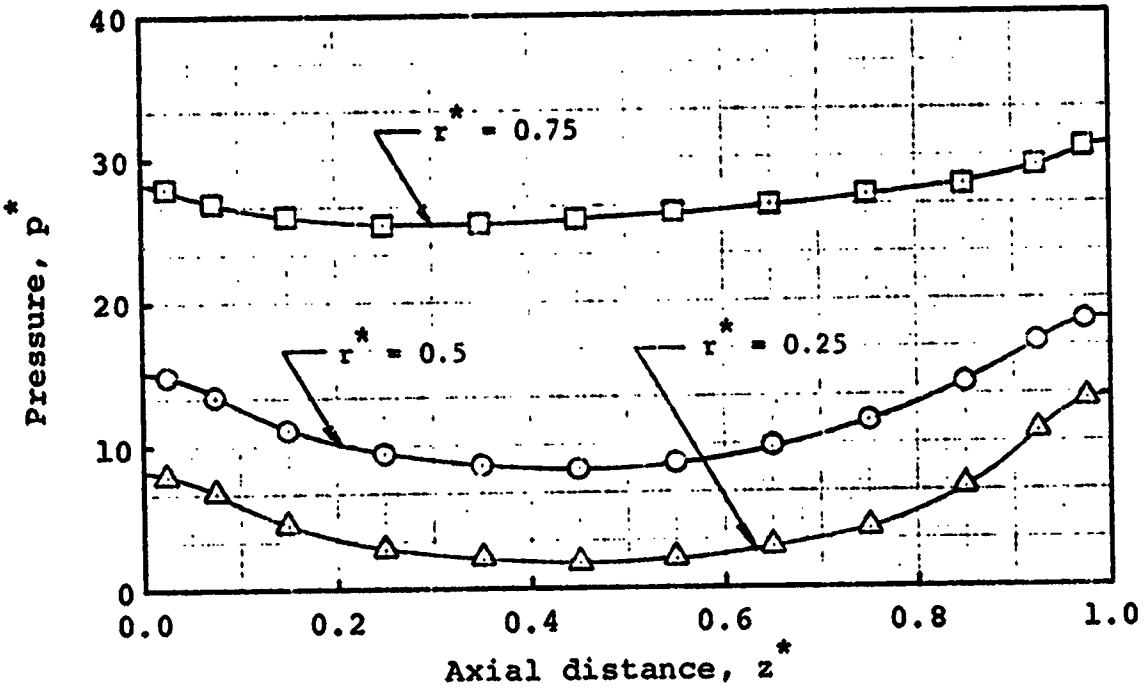

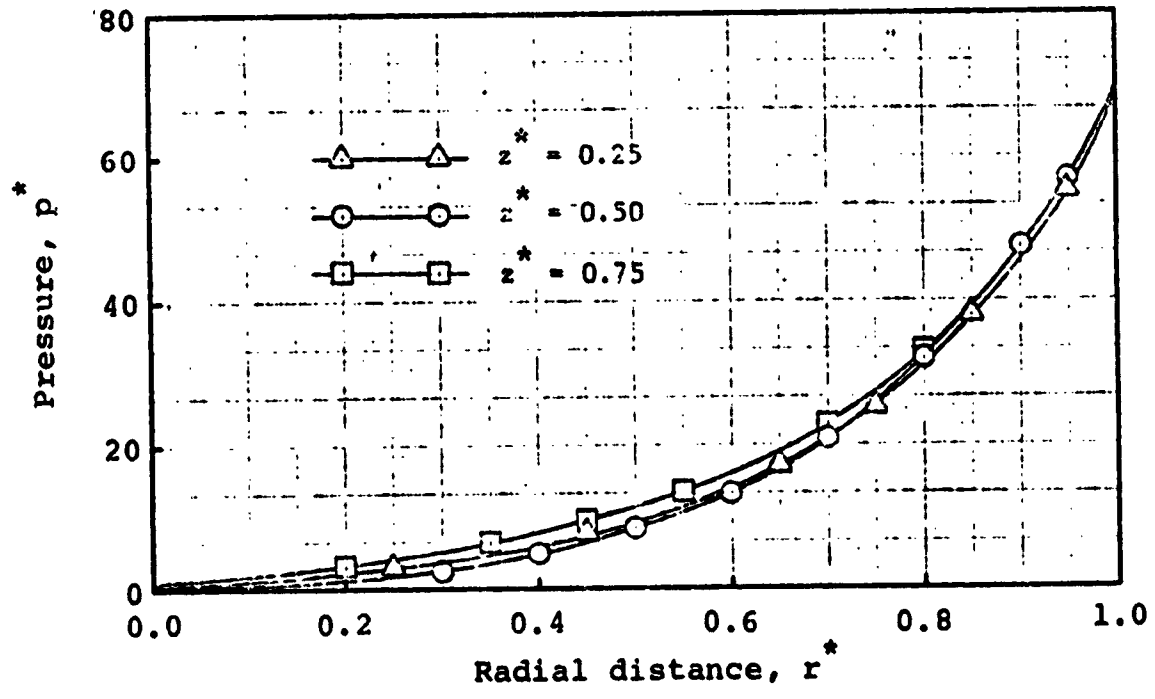

Fig. 51. Pressure Distribution for Re = 20, Re_t = 15 and a = 2.

CHAPTER VI

SUMMARY AND CONCLUSIONS

In the preceding chapters, a numerical study of driven vortices of single component and binary fluids in a cylindrical container is described. The complete axi-symmetric equations of motion and mass diffusion are solved numerically by finite difference techniques. The basic differential equations modeling the cold flow simulation of the advanced Light-Bulb reactor concept includes the continuity equation that contains a source term. Because of the source term in the continuity equation, the simple conventional scheme of formulating the problem in terms of the stream function and vorticity fails. Therefore, a method is developed in this study that enables the solution of this problem by a formulation in terms of the stream function, vorticity and one other function. This additional function is a potential function, and is introduced so that it identically satisfies the continuity equation that has a source term. Another possible application of this technique is to unsteady compressible flow problems in which the transient term in the continuity equation can be regarded as the source term.

The governing equations are written with the unsteady term included in terms of the stream function, vorticity and the potential function. The steady state solutions are obtained by large time solutions of time dependent problems.

The implicit numerical scheme of the ADI method is used. After the kinematics are solved, the pressure is obtained either by line integration or by solving the Poisson equation of pressure. Fourier analysis has been applied to the Poisson equation as the solution method, in which fast Fourier transforms are employed as an efficient computational algorithm. An extensive study is undertaken of the error analysis for the numerical results obtained in this study. This includes the estimate of the discretization error and a comparison with prior studies of other investigators.

Numerical results are obtained to show the effects of various parameters, in particular the axial and tangential Reynolds numbers on the secondary flow pattern and the resulting containment property. Results show that in the absence of rotation the flow is largely through the central region. When rotation is present, however, a high radial pressure gradient is formed in the main body to balance the centrifugal force. Near the stationary end walls, the viscosity retards the rotational motion and the imposed radial pressure gradient creates a large radial inward flow. These end wall boundary layers interacting with the vortex motion formed in the bulk region, induce recirculating secondary closed flow cells in the central region of the chamber. The secondary mass flow rate increases with increase in tangential Reynolds number for a

fixed primary flow rate and aspect ratio. It appears that the secondary flow rate also increases as the aspect ratio increases for fixed axial and tangential Reynolds numbers.

Fluid dynamic containment of the component A (simulated fissionable material) is realized when the convection effect dominates the diffusion in the mass transport process and the mass is held within the recirculating flow cells by the convection currents. For a fixed axial Reynolds number of 20, the results show that the secondary flow rate increases with the tangential Reynolds number. This enhances the relative dominance of the convection effects over diffusion in the mass transport process. Moreover, the fraction of primary flow that passes through the bulk region of closed flow cells decreases as the tangential Reynolds number increases. As a result of these flow features, the containment factor increases as the tangential Reynolds number increases for a fixed axial Reynolds number, Schmidt number and aspect ratio. For a given secondary flow rate, the containment factor also increases when either the axial Reynolds number or the Schmidt number increases since it also increases the convection effect relative to the diffusion. It appears that an increase in the aspect ratio also increases the containment factor. Finally, the containment factor increases as the pure density ratio decreases for a

fixed Schmidt number, axial and tangential Reynolds numbers.

The method developed in this thesis seems to be most suitable and efficient for obtaining numerical solutions of binary flows with interior mass source. The method has been applied successfully to the driven vortex flow problems of binary fluids, in which one of the fluid components is introduced by an interior mass source. The numerical results showed that the fluid dynamic containment of the simulated fuel component, introduced as an interior mass source, can be achieved by the convection currents of recirculating closed flow cells formed by the rotating periphery. The containment property is shown to increase with increasing the rotation for fixed primary flow rate.

BIBLIOGRAPHY

1. Ames, W. F. Numerical Methods for Partial Differential Equations. Barnes and Noble, Inc., New York, 1969.
2. Anderson, O. L. "Theoretical Solutions for the Secondary Flow on the End Wall of a Vortex Tube." UAC Research Labs. Report R-2494-1 (1961), United Aircraft Corp.
3. Aris, R. Vectors, Tensors, and the Basic Equations of Fluid Mechanics. Prentice-Hall, Inc., New Jersey, 1962.
4. Aziz, K. A Numerical Study of Cellular Convection. Ph.D. Thesis, Rice University, Houston, Texas, 1965.
5. Aziz, K. and Hellums, J. D. "Numerical Solution of the Three Dimensional Equations of Motion for Laminar Natural Convection". Physics of Fluids, 10 (1967), 2, 314-324.
6. Bertram, S. "On the Derivation of the Fast Fourier Transform." IEEE Transactions on Audio and Electroacoustics, AU-18 (1970), 1, 55-58.
7. Bird, R. B., Stewart, W. E. and Lightfoot, E. N. Transport Phenomena. John Wiley and Sons, Inc., New York, 1966.
8. Birkhoff, G., Varga, R. S. and Young, D. "Alternating Direction Implicit Methods." Advances in Computers, 3 (1962), 189-273.
9. Briley, W. R. Time-Dependent Rotating Flow in a Cylindrical Container. Ph.D. Thesis, University of Texas, Austin, Texas, 1968.

10. Deissler, R. G. and Perlmutter, M. "An Analysis of the Energy Separation in Laminar and Turbulent Compressible Vortex Flows." Proceedings of the Heat Transfer and Fluid Mechanics Institute, Stanford University Press, Stanford, Calif., 1958, 40-53.

11. Donaldson, C. dup. and Sullivan, R. D. "Behavior of Solutions of the Navier-Stokes Equations for a Complete Class of Viscous Vortices." Proceedings of the Heat Transfer and Fluid Mechanics Institute, Stanford University Press, Stanford, Calif., 1960, 16-30.

12. Einstein, H. A. and Li, H. "Steady Vortex Flow in a Real Fluid." Proceedings of the Heat Transfer and Fluid Mechanics Institute, Stanford University Press, Stanford, Calif., 1951, 33-43.

13. Emmons, H. W. "Critique of Numerical Modeling of Fluid-Mechanics Phenomena." Annual Review of Fluid Mechanics, 2 (1970), 15-36.

14. Greenspan, H. P. The Theory of Rotating Fluids. Cambridge University Press, Cambridge, 1968.

15. Haming, R. W. Numerical Methods for Scientists and Engineers. McGraw-Hill Book Co., Inc., 1962.

16. Hockney, R. W. "A Fast Direct Solution of Poisson's Equation Using Fourier Analysis." J. Assoc. Comp. Mach. 12 (1965), 1, 95-113.

17. Hornbeck, R. W. "Viscous Flow in a Short Cylindrical Vortex Chamber with a Finite Swirl Ratio." NASA TN D-5132 (1969).

18. Lanczos, C. Linear Differential Operators. Van Nostrand, London, 1961.

19. Latham, T. S. "Nuclear Studies of the Nuclear Light Bulb Rocket Engine." UAC Research Labs. Report G-910375-3 (1968), United Aircraft Corp.

20. Lavan, Z. Investigation of Swirling Flows in Ducts. Ph.D. Thesis, Illinois Institute of Technology, Chicago, Illinois, 1966.

21. Lee, E. S. Quasilinearization and Invariant Imbedding, with Applications to Chemical Engineering and Adaptive Control. Academic Press, 1968.

22. Lewellen, W. S. "A Review of Confined Vortex Flows." NASA CR 1772 (1971), National Aeronautics and Space Administration, Washington, D.C.

23. Lewellen, W. S. "Magnetohydrodynamically Driven Vortices." Proceedings of the Heat Transfer and Fluid Mechanics Institute, Stanford University Press, 1960, 1-15.

24. Lewellen, W. S. Three-Dimensional Viscous Vortices in Incompressible Flow. Ph.D. Thesis, University of California, Los Angeles, Calif., 1964.

25. Pao, H. "A Numerical Computation of a Confined Rotating Flow." J. Applied Mechanics, Transactions of the ASME, 37 (1970), 2, 480-487.

26. Peaceman, D. W. and Rachford, H. H., Jr. "The Numerical Solution of Parabolic and Elliptic Differential Equations." J. Soc. Indust. Appl. Math., 3(1955),1,28-41.

27. Pearson, C. E. "A Computational Method for Time-Dependent Two-Dimensional Incompressible Viscous Flow Problems." Sperry Rand Research Center Report RR-64-17, 1964.

28. Ralston, A. A First Course in Numerical Analysis. McGraw-Hill Book Co., New York, 1965.

29. Richtmyer, R. D. and Morton, K. W. Difference Methods for Initial-Value Problems. Interscience Publishers, 2nd ed., New York, 1967.

30. Roschke, E. J. "Flow-Visualization Studies of a Confined Jet-Driven Water Vortex." JPL Technical Report 32-1004, Jet Propulsion Lab., California Institute of Technology Pasadena, Calif. 1966.

31. Rosenzweig, M. L., Lewellen, W. S. and Ross, D. H. "Confined Vortex Flows with Boundary-Layer Interaction." AIAA J., 2 (1964), 12, 2127-2134.

32. Ross, D. H. "An Experimental Study of Secondary Flow in Jet-Driven Vortex Chambers." Aerospace Corporation Report ATN-64(9227)-1, Aerospace Corp., El Segundo, Calif., 1964.

33. Rott, N. and Lewellen, W. S. "Boundary Layers and Their Interactions in Rotating Flows." Progress in Aeronautical Sciences, 7 (1966), Pergamon Press, London, 111-144.

34. Westly, R. "A Bibliography and Survey of the Vortex Tube." College Aeronautics (Cranfield) Note No. 9, 1954.

35. Williams, G. P. "Numerical Integration of the Three-Dimensional Navier-Stokes Equations for Incompressible Flow." J. Fluid Mechanics, 37 (1969), 4, 727-750.

INVESTIGATION B

LAMINAR CONFINED COAXIAL ENTRANCE FLOW WITH HEAT GENERATION

By

Gopala Krishna Murty Bobba

and

Herbert Weinstein

ABSTRACT

The gas core nuclear reactor concept was introduced fifteen years ago because of a possible application as an engine for space vehicles. Recently, interest has grown in applying this concept for ground based power generation. In this thesis the results of a parametric study on the entrance flow region in a gas core nuclear reactor are presented. The physical system is modeled as laminar confined, coaxial flow with heat generation in the inner fluid. The governing equations include the boundary layer approximations and the assumptions of only radial radiative transport of energy represented as an energy diffusion term.

The Von Mises transformation and a ζ transformation are used to transform the equations into nonlinear nonhomogeneous convective-diffusion equations. A unique combination of forward and backward difference equations which yields accurate results at moderate computational times, is used in the numerical method.

Results show that the rapidly accelerating, heat generating inner stream actually shrinks in radius as it expands axially. This conclusion is in opposition to that assumed in previous analyses of the flow region downstream of the entrance region.

TABLE OF CONTENTS

LIST OF TABLES

LIST OF FIGURES

TABLE OF NOMENCLATURE

Symbol	Definition
c	Specific heat
C	Excess pressure drop
C_1, C_2	Constants defined by equation 37
DP	Total pressure drop
E	Function defined by equation 25
F	Function defined by equation 25
g_c	Conversion factor
G	Dimensionless gas constant
H	Function defined by equation 25
k	Thermal conductivity
K	Ratio of inner stream to outer stream thermal conductivities
L	Scale factor
M	Ratio of inner stream to outer stream viscosities Number of grid points in the outer stream
N	Number of grid points in the inner stream
P	Dimensionless pressure
Pr	Prandtl number
r	Dimensionless radial coordinate
R	Tube radius
Re	Reynolds number
S	Ratio of inner to outer stream specific heats
T	Dimensionless temperature
T_e	Dimensionless wall temperature
T_w	Wall temperature
u_f	Function defined by equation 45
u	Dimensionless axial velocity

Symbol	Definition
v	Dimensionless radial velocity
W	Function defined by equation 20
z	Dimensionless axial coordinate

Greek Symbols

α	Dimensionless inner stream radius
β	Function defined by equation 30
γ	Function defined by equation 25
δ	Function defined by equation 25
ΔP	Change in pressure
Δx	Finite difference grid size in axial direction
$\Delta \zeta$	Finite difference grid size in radial direction
ζ	Function defined by equation 22
Θ	Function defined by equation 21
Θ_e	Constant defined by equation 26
μ	Viscosity
π	Gas constant
ρ	Dimensionless density
σ	Function defined by equation 25
ϕ	Generation function
Φ	Dimensionless generation function
ψ	Stream function defined by equation 17
ψ_w	Value of stream function at the wall
ω	Function defined by equation 25

Superscripts

-	Denotes dimensional variables
i	Finite difference grid index in axial direction

Subscripts	Definition
i	Denotes initial values
j=1	Denotes inner stream variables
j=2	Denotes outer stream variables
n	Finite difference grid index in radial direction
R	Denotes ratio of inner to outer stream initial entrance variable values

CHAPTER I

INTRODUCTION

Fluid mechanics problems associated with the concept of a gas core nuclear reactor have been studied for many years. Most of the theoretical work has been limited to the main portion of the cavity where severe gradients of velocity, temperature, and pressure do not exist. The reasons for this limitation are obvious. There is also a general lack of understanding about the behavior of the transport mechanisms in entrance flows. Because of these problems, the highly complex entrance flow problem of gas core reactors has been essentially ignored. Only one previous attempt has been made to solve the complex entrance flow problem and that analysis used inviscid flow equations.

The object of the present work effort is to formulate a realistic model of the entrance region flow in the reactor and to study the effects of various parameters on the flow field. A new transformation is developed to solve not only this problem but entrance flow problems in general, since simple solution methods to this problem are not generally available. A unique combination of forward and backward difference equations is used in the numerical method, which yields accurate results at moderate computational times.

In an open cycle gas core nuclear reactor concept, it is presently proposed that a solid uranium rod be continuously fed into the reactor cavity to produce makeup fuel for that lost through the nozzle and to maintain a critical mass.

The fuel rod enters the cavity on the axis of the working fluid flow. It is exposed to the high neutron flux and is very rapidly vaporized. The temperature of the uranium vapor increases by an order of magnitude in a very short distance downstream of the entrance point. The interaction of the rapidly expanding uranium stream with the surrounding working fluid stream is difficult to predict. It has an important influence on the mixing of the two streams, as well as on the critical mass requirements in the cavity, since the fuel stream must expand to a radius many times that of its inlet radius to keep critical mass requirements reasonable. It is also the object of this work to analyze the flow in the region of the fuel injection point where temperature changes, and hence velocity and density changes, are extremely large. This study will provide input for an analysis of the main portion of the reactor cavity where gradients of the flow variables are less severe.

The analysis presented here is an approximate one and attempts to consider only those phenomena which are of fundamental importance in the region of interest. The flow is considered to be coaxial, with the two streams immiscible. Thus, the diffusion equation can be discarded, and the problem can be treated as a two region problem. Radial body forces are neglected. Axial body forces can be incorporated in the pressure term. Thermal diffusion terms, except for Rosseland's approximation for radiative energy transport, are neglected. Internal heat generation occurs in the fuel

stream to represent the fission process. A single equation of state is used for the whole region. Initial velocities are very small, and velocities throughout the cavity are very low subsonic. Physical properties are assumed to be uniform.

CHAPTER II

BACKGROUND

This thesis is concerned with the analysis of flow in the entrance region of a gas core nuclear reactor. Previous work relevant to this thesis work can be separated into two categories. The first of these is the literature on modeling of flows in reactors and the second is the literature concerned with entrance region flows in general.

Reactor Modeling

Ever since the concept of gas core reactors for nuclear rocket engines was proposed in 1953, its development has been the basis for several experimental and theoretical investigations. The feasibility of a gas core reactor has been studied in detail[12,13,23]. A status of the art report by Rom[15] refers to the basic work completed in the fields of hydrodynamics, gaseous radiant heat transfer, neutronics and system studies.

The exchange of energy from the fissioning fuel to the propellant stream by thermal radiation has been treated by Kascak[10] using a diffusion (Rosseland's) approximation to the radiant heat flux, which is valid for optically thick fluids[2]. This treatment is adopted for the present analysis.

The analytical work on the fluid mechanics problems of gas core reactor has been limited to the main portion of the reactor cavity where gradients are not extreme. These treatments were numerical integration of the boundary layer equations, or full Navier Stokes equations for coaxial flow

of dissimilar fluids. They were concerned mainly with the mixing of the two fluid streams and hence concentrated on the diffusive terms rather than on the effects of the large internal heat generation. References 6, 7, 18 and 24 are examples of this approach.

Ghia[7] et al. studied isothermal, confined laminar mixing of dissimilar (binary and nonreacting) circular axisymmetric jets. Their results clearly indicate that the diffusion is negligible for at least one characteristic length.

Only one previous attempt[22] was made to simulate the flow field near the fuel injection location. Using inviscid equations this analysis showed the effects of large energy release and the concurrent high acceleration of inner stream fluid on the coaxial flow field. Results of this study indicated that the rapidly accelerating, heat generating, inner stream actually shrinks in radius as it expands axially. Even though inviscid analysis yielded certain useful results, it can not simulate a flow with interfacial shear and the effects of solid wall on the flow field realistically due to the degenerate nature of the equations. Also, in the inviscid analysis, stability problems were experienced and artificial viscosity type terms were added to the governing equations to overcome these difficulties. Based on this previous experience the present analysis is performed using the boundary layer equations.

General Entrance Flows

There has been an enormous amount of published literature on a variety of entrance flow studies. Unfortunately, none of these is directly applicable to the present analysis. A general description of this literature is, however, given to justify the methodology used in formulating and solving the present problem. It is impractical to cite all the published work on entrance flows; therefore, only recent papers dealing with circular conduits which contain new ideas and/or a review of previous work are cited.

The reason entrance region flows have been studied so intensively is because of their practical importance in the investigation of excess pressure drop, flow stability, and flow separation phenomena. Most of the studies involve solution of simplified Navier Stokes equations using boundary layer approximations. However, there has been some controversy over neglecting the axial diffusion terms in the governing equations for small z[5,8]. Van Dyke[20] showed rigorously in the case of entry flow in a channel that the full Navier Stokes equations reduce to boundary layer equations for the infinite Reynolds number flow. (Solutions of the full Navier Stokes equations[21] indicate that the boundary layer approximations are valid only for Reynolds numbers greater than 250.) In conclusion the flow field description obtained by using boundary layer equations is reasonably accurate for the asymptote of large distance from the entrance when Reynolds number is large. Boundary layer

equations are preferred for the present analysis because general flow features are the main concern. Also, the methods of solution for the full Navier Stokes equations become cumbersome and/or have stability problems for large Reynolds number flows.

Four basic methods of solution for the boundary layer equations are encountered in the literature:

1. Finite differences of the complete set of equations[3,9];
2. Linearization of inertial terms[11,19];
3. Method of weighted residuals[1];

and 4. Patching of solutions[4,17].

Most of these methods are numerical and all have their own merits and drawbacks. Even though analytical solutions are preferred, numerical techniques are widely used in engineering practice because they have the capability of handling more comprehensive cases with variable fluid properties and variety of boundary conditions. The simpler numerical schemes, even though they are easy to set up, usually become unattractive because large numbers of grid points are required to resolve the flow characteristics near solid boundaries and in regions of large gradients. Also, the simpler methods have stability and convergence problems when derivatives are large. This problem can sometimes be overcome, however, by judiciously introducing transformations into the basic set of equations, which results in new independent and dependent variables before using the numerical technique. Obviously,

this procedure will work when derivatives of the new dependent variables are much smaller than those of the original dependent variables.

In this thesis a series of transformations are used before solving the partial differential equations. A combination of explicit and implicit finite difference methods is also utilized with the transformed variables to obtain the largest possible grid size consistent with stability and convergence criteria.

CHAPTER III

MATHEMATICAL MODEL

The geometric model for the analysis consists of two fluids flowing coaxially within a bounding stream tube of constant radius (See Fig 1). Radial body forces are neglected to preserve axial symmetry in the flow system. Under these assumptions the steady flow situation is represented mathematically by boundary layer equations with appropriate boundary conditions. The inner stream has a large internal heat generation rate and transfers heat to the outer stream by radiation. The radial conductive transport of energy is negligible compared to the radial radiative transport. A diffusion approximation is used for the radiation equations[2]. The fluids are considered to be immiscible and no mass transfer occurs across the interface between the two streams. The interface is a stream line of both fluids. Since the velocities, temperature and pressure keep changing as the fluids travel through the tube, the radius of the interface does not remain constant. The equations are written for both fluids separately and tied together with the interface equation.

The following are the governing differential equations:

Fluid I: $0 \leq \bar{r} \leq \alpha R.$ $j = 1$

Fluid II: $\alpha R \leq \bar{r} \leq R.$ $j = 2$

State: $$\bar{P}_j = \pi_j \bar{\rho}_j \bar{T}_j \qquad (1)$$

Continuity: $$\frac{\partial}{\partial \bar{z}} (\bar{\rho}_j \bar{u}_j \bar{r}) + \frac{\partial}{\partial \bar{r}} (\bar{\rho}_j \bar{v}_j \bar{r}) = 0 \qquad (2)$$

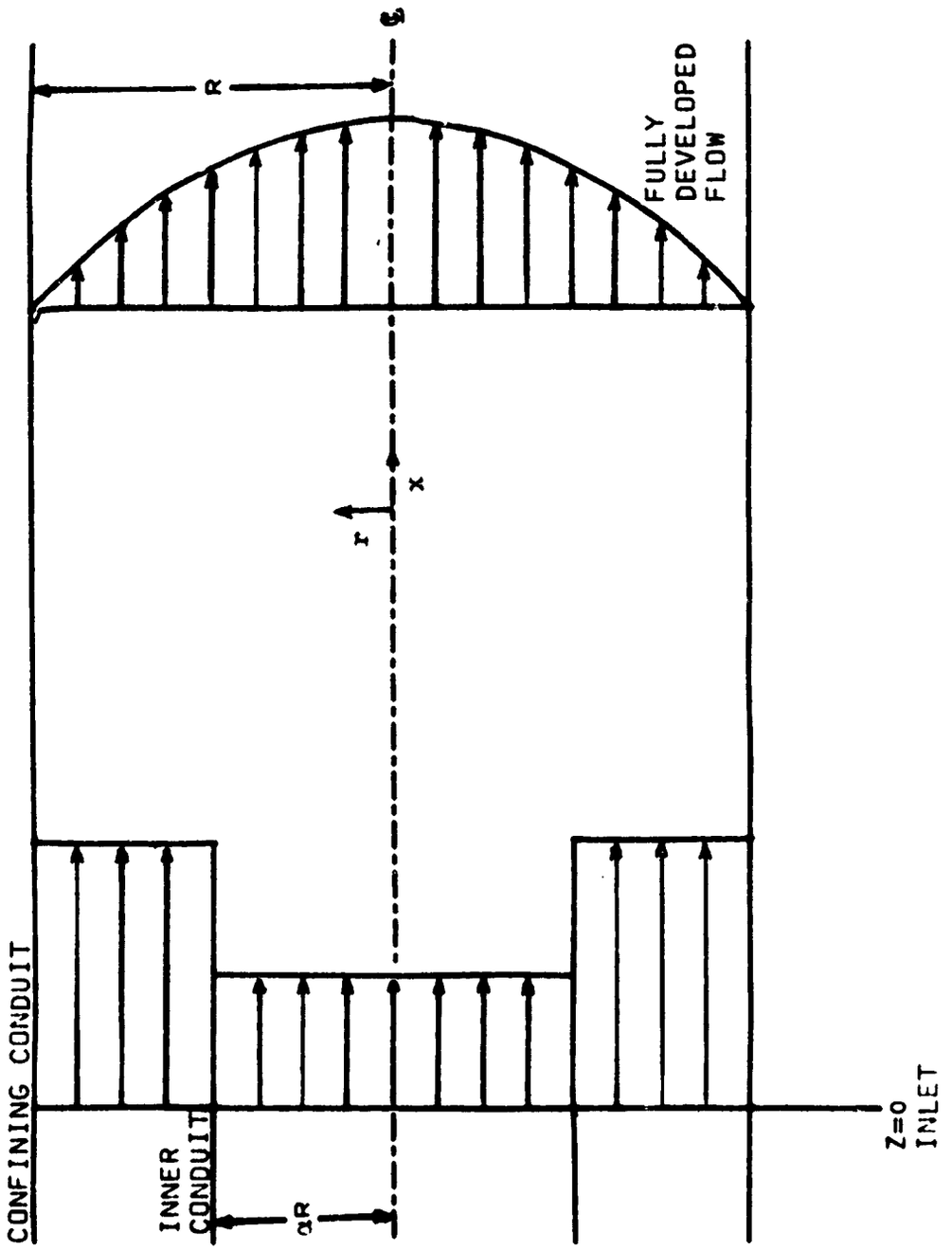

Figure 1. System for Coaxial Entrance Flow Study

Momentum: $$\bar{\rho}_j \left(\bar{u}_j \frac{\partial \bar{u}_j}{\partial \bar{z}} + \bar{v}_j \frac{\partial \bar{u}_j}{\partial \bar{r}}\right) = - \frac{d\bar{P}_j}{d\bar{z}} g_c + \frac{\mu_j}{\bar{r}} \frac{\partial}{\partial \bar{r}} \left(\bar{r} \frac{\partial \bar{u}_j}{\partial \bar{r}}\right) \quad (3)$$

Energy: $$\bar{\rho}_j \bar{c}_j \left(\bar{u}_j \frac{\partial \bar{T}_j}{\partial \bar{z}} + \bar{v}_j \frac{\partial \bar{T}_j}{\partial \bar{r}}\right) = \bar{\rho}_j \bar{u}_j \phi_j + \frac{k_j}{\bar{r}} \frac{\partial}{\partial \bar{r}} \left(\bar{r} \bar{T}_j^3 \frac{\partial \bar{T}_j}{\partial \bar{r}}\right) \quad (4)$$

Here the inner stream is assumed to generate heat at a constant rate per unit mass. For the case when the inner stream generates heat at a constant rate per unit volume, equation (4) can be written as:

$$\bar{\rho}_j \bar{c}_j \left(\bar{u}_j \frac{\partial \bar{T}_j}{\partial \bar{z}} + \bar{v}_j \frac{\partial \bar{T}_j}{\partial \bar{r}}\right) = \phi_j + \frac{k_j}{\bar{r}} \frac{\partial}{\partial \bar{r}} \left(\bar{r} \bar{T}_j^3 \frac{\partial \bar{T}_j}{\partial \bar{r}}\right)$$

From now on the subscript j, indicating either the inner fluid or the outer fluid, will be omitted for simplicity.

The following are the boundary conditions at the wall of the tube:

$$\bar{u} = 0$$
$$\bar{v} = 0 \text{ and} \quad (5)$$
$$\bar{T} = T_w.$$

Due to the axial symmetry of the problem, the conditions at the center line can be written as:

$$\frac{\partial \bar{u}}{\partial \bar{r}} = 0$$
$$\bar{v} = 0$$

$$\frac{\partial \bar{T}}{\partial \bar{r}} = 0 \tag{6}$$

The location of the interface can be calculated from the fact that it is the bounding stream line for both the fluids:

$$\frac{d(\alpha R)}{d\bar{z}} = \left.\frac{\bar{v}_1}{\bar{u}_1}\right|_{\bar{r} = \alpha R} = \left.\frac{\bar{v}_2}{\bar{u}_2}\right|_{\bar{r} = \alpha R} \tag{7}$$

Continuity of pressure, temperature, velocities, shear stress and heat flux lead to the following interface conditions:

$$\bar{P}_1 (\alpha R) = \bar{P}_2 (\alpha R)$$

$$\bar{T}_1 (\alpha R) = \bar{T}_2 (\alpha R)$$

$$\bar{u}_1 (\alpha R) = \bar{u}_2 (\alpha R)$$

$$\mu_1 \left.\frac{\partial \bar{u}_1}{\partial \bar{r}}\right|_{\bar{r} = \alpha R} = \mu_2 \left.\frac{\partial \bar{u}_2}{\partial \bar{r}}\right|_{\bar{r} = \alpha R}$$

$$k_1 \bar{T}_1^3 \left.\frac{\partial \bar{T}_1}{\partial \bar{r}}\right|_{\bar{r} = \alpha R} = k_2 \bar{T}_2^3 \left.\frac{\partial \bar{T}_2}{\partial \bar{r}}\right|_{\bar{r} = \alpha R} \tag{8}$$

The initial conditions are specific to a given calculation.

To nondimensionalize the equations, the following dimensionless variables and groups are introduced:

$$r = \frac{\bar{r}}{R} \qquad z = \frac{\bar{z}}{R\ Re}$$

$$u_j = \frac{\bar{u}_j}{u_{21}} \qquad v_j = \frac{\bar{v}_j\ Re}{u_{21}}$$

$$\rho_j = \frac{\bar{\rho}_j}{\rho_{21}} \qquad T_j = \frac{\bar{T}_j}{T_{21}} \, Pr^{1/3}$$

$$P_j = \frac{\bar{P}_j \; g_c}{\rho_{21} \; u_{21}^2} \qquad Re = \frac{R \; u_{21} \; \rho_{21}}{\mu_2}$$

$$Pr = \frac{k_2 \; T_{21}^3}{c_2 \; \mu_2} \qquad \Phi_j = \frac{\phi_j \; R}{c_2 \; T_{21}} \, Re \; Pr^{1/3}$$

$$M_j = \frac{\mu_j}{\mu_2} \qquad S_j = \frac{c_j}{c_2}$$

$$K_j = \frac{k_j}{k_2} \qquad G_j = \frac{\pi_j \; g_c \; T_{21}}{u_{21}^2 \; Pr^{1/3}}$$

Substituting the above into the dimensional equations we obtain:

Fluid I: $0 \leq r \leq \alpha, \qquad j = 1$

Fluid II: $\alpha \leq r \leq 1, \qquad j = 2$

State: $P = G \rho T$ (9)

Continuity: $\frac{\partial}{\partial z} (\rho \; u \; r) + \frac{\partial}{\partial r} (\rho \; v \; r) = 0$ (10)

Momentum: $\rho \; u \; \frac{\partial u}{\partial z} + \rho \; v \; \frac{\partial u}{\partial r} = - \frac{dP}{dz} + M \; \frac{1}{r} \; \frac{\partial}{\partial r} \; .$

$(r \; \frac{\partial u}{\partial r})$ (11)

Energy: $\rho \; u \; \frac{\partial T}{\partial z} + \rho \; v \; \frac{\partial T}{\partial r} = \rho \; u \; \Phi +$

$\frac{K}{S} \; \frac{1}{r} \; \frac{\partial}{\partial r} \; (r \; T^3 \; \frac{\partial T}{\partial r})$ (12)

The boundary conditions are:

$$u(1) = 0$$
$$v(1) = 0 \qquad (13)$$
$$T(1) = T_e$$

$$\frac{\partial u(0)}{\partial r} = 0$$
$$v(0) = 0 \qquad (14)$$
$$\frac{\partial T(0)}{\partial r} = 0$$

and the interface conditions are:

$$\frac{d\alpha}{dz} = \frac{v_1}{u_1}\bigg|_{r=\alpha} = \frac{v_2}{u_2}\bigg|_{r=\alpha} \qquad (15)$$

$$P_1(\alpha) = P_2(\alpha)$$
$$T_1(\alpha) = T_2(\alpha)$$
$$u_1(\alpha) = u_2(\alpha) \qquad (16)$$
$$M_1 \frac{\partial u_1(\alpha)}{\partial r} = \frac{\partial u_2(\alpha)}{\partial r}$$
$$K_1 \frac{\partial T_1(\alpha)}{\partial r} = \frac{\partial T_2(\alpha)}{\partial r}$$

The equation set (9)-(12) and (15), with boundary conditions (13) and (14), and interface conditions (16), is well defined with a proper set of initial conditions.

The Von Mises transformation relationships

$$\frac{\partial \psi}{\partial r} = \rho u r$$

$$\frac{\partial \psi}{\partial z} = -\rho v r \tag{17}$$

$$\frac{\partial}{\partial z}(\ ) = \frac{\partial}{\partial z}(\ ) - \rho v r \frac{\partial}{\partial \psi}(\ )$$

and

$$\frac{\partial}{\partial r}(\ ) = \rho u r \frac{\partial}{\partial \psi}(\ )$$

are introduced to reduce the equations in number by eliminating the continuity equation and the radial velocity component, v, to the following equations in (z,ψ) coordinates:

$$\rho u \frac{\partial u}{\partial z} + \frac{dP}{dz} = M \rho u \frac{\partial}{\partial \psi}(\rho u r^2 \frac{\partial u}{\partial \psi}) \tag{18}$$

$$\frac{\partial T}{\partial z} = \frac{K}{S} \frac{\partial}{\partial \psi}(\rho u r^2 T^3 \frac{\partial T}{\partial \psi}) + \Phi \tag{19}$$

The equation of state is unchanged under the transformation. It is interesting to note the equation (15) represents a line in the (z,ψ) plane.

Though the equations become simpler in Protean coordinates, three serious difficulties come into focus:

i) The boundary condition at the center line in (z,ψ) plane is

$$\left.\frac{\partial u}{\partial \psi}\right|_{r=0} = \frac{1}{\rho u r}\frac{\partial u}{\partial r} = \frac{0}{0}$$

Using L'Hospital's rule this may be evaluated as

$$\left.\rho u \frac{\partial u}{\partial \psi}\right|_{r=0} = \left.\frac{\partial^2 u}{\partial r^2}\right|_{r=0} = \text{finite}$$

Similarly, $\left.\frac{\partial T}{\partial \psi}\right|_{r=0}$ can also be shown to be bounded

and nonzero. Notice that symmetry is lost with respect to ψ at $\psi = 0$.

ii) The first and higher derivatives of u with respect to ψ at the wall are infinite. This means that wall is a singular line. Hence Taylor Series expansions cannot be written at the wall. Moreover, the truncation errors in finite difference molecules will be rather large near the vicinity of the wall.

iii) If a uniform finite difference grid is used in the (z,ψ) plane, this would amount to having a fine grid near the center line and a relatively coarse grid near the wall in the (z,r) plane. Hence, a large amount of points are needed to simulate the flow situation with reasonable accuracy.

To overcome these difficulties, the following transformations are introduced:

$$W = \frac{u^2}{2} \tag{20}$$

$$\Theta = \frac{T^4}{4} \tag{21}$$

$$\psi = (\zeta^2 - \frac{1}{2}\zeta^4)\, L \tag{22}$$

$$L = \frac{\int_o^\alpha u_{1i}\, \rho_{1i}\, rdr + \int_\alpha^1 u_{2i}\, \rho_{2i}\, rdr}{2 \int_o^1 (1-r^2)\, rdr}$$

L is the ratio of total mass of both fluids to the mass of an incompressible fluid entering with a uniform dimensionless inlet velocity of 1 and a dimensionless inlet density

of 1. The use of a scale factor, L, is convenient, when simulating coaxial flow of two incompressible fluids. The methodology used in arriving at the ζ transformation is outlined in Appendix A.

Equations (18) and (19) transform into the following equations with some manipulation:

$$\frac{\partial W}{\partial z} + \frac{1}{\rho}\frac{dP}{dz} = \frac{1}{E}\left\{\gamma \frac{\partial^2 W}{\partial \zeta^2} + \delta \frac{\partial W}{\partial \zeta}\right\} \tag{23}$$

$$\frac{\partial \Theta}{\partial z} - H = \frac{1}{F}\left\{\sigma \frac{\partial^2 \theta}{\partial \zeta^2} + \omega \frac{\partial \theta}{\partial \zeta}\right\} \tag{24}$$

where

$$E = \frac{u_f \zeta}{\mu u}$$

$$\gamma = \frac{\rho}{u_f}\frac{r^2}{\zeta}$$

$$\delta = \frac{\partial \gamma}{\partial \zeta}$$

$$H = \frac{\Phi T^3}{S}$$

$$F = \frac{S}{K}\frac{u_f}{T^3}\zeta$$

$$\sigma = \gamma u$$

$$\omega = u\delta + \frac{\gamma}{u}\frac{\partial \omega}{\partial \zeta}$$

and

$$u_f = 2(1-\zeta^2)\,L \tag{25}$$

It should be noted that equations (23) and (24) are analogous to a pair of coupled unsteady nonlinear nonhomogeneous diffusion equations. Also, u_f is the solution to the equations describing fully developed flow of two coaxial streams of incompressible fluids with no generation.

The scaling factor, L, accounts for the effect of different entrance velocities and densities of the streams on the magnitude of the fully developed velocities. The use of L results in mapping of the region $0 \leq r \leq 1$ into $0 \leq \zeta \leq 1$.

The boundary conditions for the above set of equations transform into:

$$W(1) = 0 \tag{26}$$

$$\theta(1) = \theta_e = \frac{T_e^4}{4}$$

$$\frac{dP_2}{dz} = \rho(1) \left\{\frac{\partial^2 u}{\partial r^2} + \frac{\partial u}{\partial r}\right\}\Bigg|_{r=1} \tag{27}$$

$$\frac{\partial W(0)}{\partial \zeta} = 0$$

$$\frac{\partial \Theta(0)}{\partial \zeta} = 0 \tag{28}$$

$$P_1(\beta) = P_2(\beta)$$

$$\Theta_1(\beta) = \Theta_2(\beta)$$

$$W_1(\beta) = W_2(\beta)$$

$$M_1 \frac{\partial W_1}{\partial \zeta}(\beta) = \frac{G_1}{G_2} \frac{\partial W_2}{\partial \zeta}(\beta)$$

$$K_1 \frac{\partial \theta_1}{\partial \zeta}(\beta) = \frac{G_1}{G_2} \frac{\partial \theta_2}{\partial \zeta}(\beta) \qquad (29)$$

where β is evaluated from the following equation:

$$\int_0^{\beta} u_f \, \zeta \, d\zeta = \int_0^{\beta} \rho_1 \, u_1 \, r \, dr \qquad (30)$$

Notice that symmetry at the center is preserved under the transformation and $\zeta = 1$ is not a singular line in (z,ζ) plane. The condition on P [equation (27)] is arrived at by using the momentum equation at the wall with the boundary condition (13) and applying L'Hospital's rule to evaluate the limit of $\frac{\partial u}{\partial r}$ at the wall.

Obtaining an analytical solution to the above system of equations is not possible due to the highly nonlinear nature of the problem. Hence, the solution is obtained using numerical methods.

The fully developed solution for the entrance flow problem is obtained by solving the equations resulting from dropping the terms $\frac{\partial u}{\partial z}$ and $\frac{\partial T}{\partial z}$ from equation set (9) through (16). The fully developed velocity profile is given by

$$u = -\frac{dP}{dz} \frac{1}{M_1} \frac{\alpha^2 + M_1 (1-\alpha^2) - r^2}{4} \qquad 0 \le r \le \alpha$$

$$= -\frac{dP}{dz} \frac{1-r^2}{4} \qquad \alpha \le r \le 1$$

The fully developed temperature profile cannot be obtained analytically for the case where the inner fluid

generates heat at constant rate per unit mass; but for the case where the inner fluid generates heat at a constant rate per unit volume it is given by

$$T^4 = T_e^4 + \phi S \left[(\alpha^2 - r^2) - \frac{\alpha^2}{2} \ln \alpha\right] \qquad 0 \leq r \leq \alpha$$

$$= T_e^4 - \phi S \frac{\alpha^2}{2} \ln r \qquad \alpha \leq r \leq 1$$

In either case the values of $\frac{dP}{dz}$ and radius of inner stream for fully developed flow cannot be obtained analytically. However, in the incompressible isothermal case with two fluids of the same viscosity the following relationships can be derived:

$$\frac{dP}{dz} = -8 \left(u_R \alpha^2 + 1 - \alpha^2\right)$$

and $$\alpha_f^2 = 1 \pm \sqrt{1 - \frac{\alpha^2 u_R}{u_R \alpha^2 + 1 - \alpha^2}}$$

When $\rho_R = 1$ and $u_R = 1$ these relationships agree with those for the classical entrance flow through a circular conduit.

CHAPTER IV

NUMERICAL METHOD

Several numerical methods are available for the solution of a parabolic system of coupled nonlinear partial differential equations. The finite difference methods were used because of their simplicity. Also, the stability, convergence and consistency for these methods have been very well established. In the finite difference technique two procedures exist, the explicit and the implicit. In the explicit methods, forward differences are used to approximate the derivatives in the axial direction, which lead to linear, explicit finite difference equations that can each be solved independently. The implicit methods, however, use backward differences to approximate the axial derivatives, resulting in a system of simultaneous, nonlinear equations. In general, the implicit methods are unconditionally stable, whereas the simple explicit methods are inherently unstable. In order to obtain stable, accurate solutions by using the explicit methods, restrictions on the step sizes are necessary. The proper choice of a computational method depends on the nature of the problem at hand.

The application of a purely explicit or a purely implicit method to the system of equations describing the entrance flow was not satisfactory. Due to the nonlinear nature of the problem, the restriction on maximum allowable step size to ensure stability in the case of an explicit method became progressively worse and the computational time

became prohibitive as the temperatures of the fluids started increasing. On the other hand, convergence problems were experienced in the solutions of simultaneous nonlinear equations near the entrance region in the case of implicit methods. Hence it was decided to use the explicit method near the entrance region and change to the implicit method after the gradients become less severe. This approach yields highly accurate results over the whole region at moderate computational times.

The flow region is descretized by grid points having equal spacings $\Delta\zeta_1$ $(o \leq \zeta \leq \beta)$ and $\Delta\zeta_2$ $(\beta \leq \zeta \leq 1)$ in the ζ direction and an arbitrary axial step size Δz. The discretized rectangular grid and the coordinate system used to solve the problem are shown in Figure 2. The subscript n and the superscript i are grid point indices associated with ζ and z respectively. The radial subscript n takes integer values between 1 and (M+N+2) and the axial subscript i ranges from i = 0 to any desired value. The interface is labeled by n = N+1 for the inner fluid and n = N+2 for the outer fluid.

Finite Difference Equations - Explicit Method

Substitution of three point central difference approximations for the radial derivatives and of two point forward difference approximations for the first derivatives in the axial direction into Equations (23) and (24), results in the following two finite difference equations for every interior point (i, n) of the finite difference network:

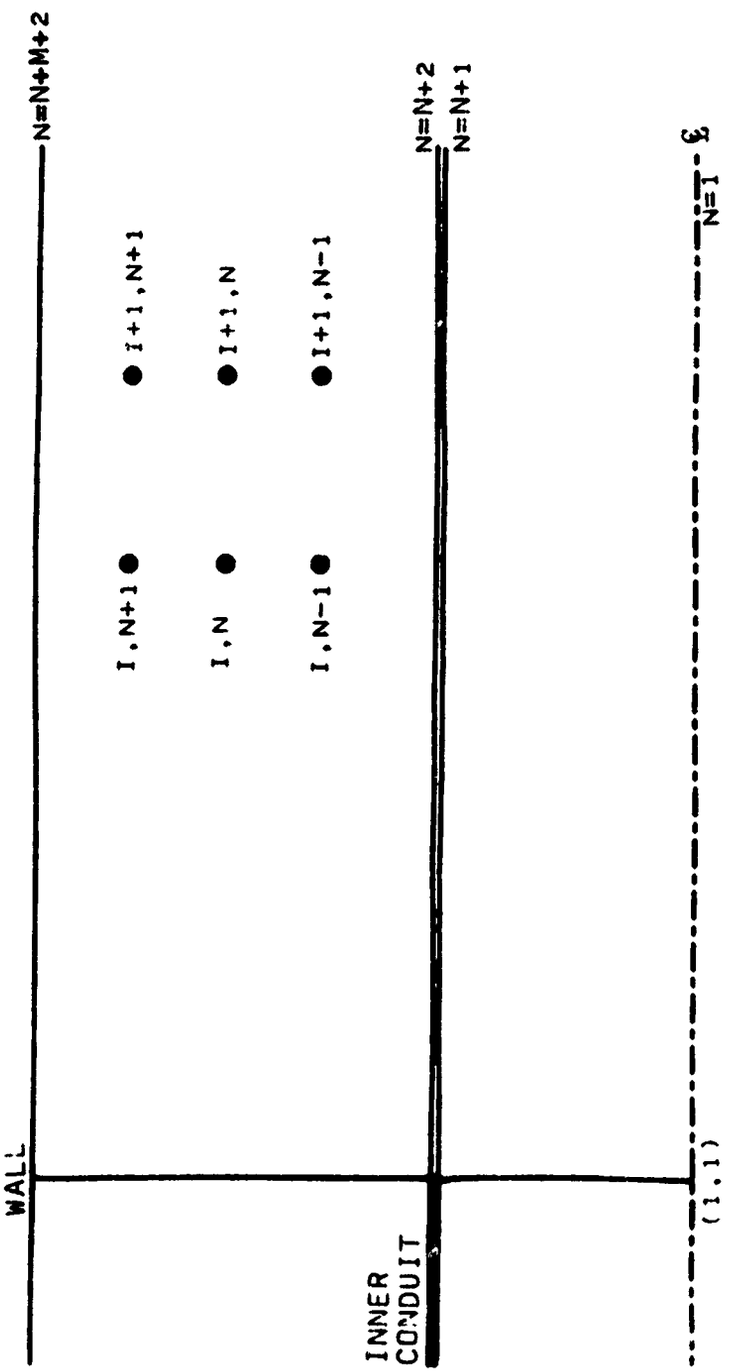

Figure 2. Finite Difference Grid System

$$W_n^{i+1} = W_n^i - \frac{\Delta P}{\rho_n^I} + \frac{\Delta z}{E_n^I} \left\{ \gamma_n^i \frac{W_{n+1}^i - 2W_n^i + W_{n-1}^i}{\Delta\zeta^2} + \delta_n^i \frac{W_{n+1}^i - W_{n-1}^i}{2\Delta\zeta} \right\} \tag{31}$$

$$\Theta_n^{i+1} = \Theta_n^i + H\,\Delta x + \frac{\Delta z}{F_n^I} \left\{ \sigma_n^i \frac{\Theta_{n+1}^i - 2\Theta_n^i + \Theta_{n-1}^i}{\Delta\zeta^2} + \omega_n^i \frac{\Theta_{n+1}^i - \Theta_{n-1}^i}{2\Delta\zeta} \right\} \tag{32}$$

The subscript j, denoting the first or the second fluid, has been omitted for simplicity.

The numerical stability considerations impose the following restriction on the largest value of Δz that can be used in the above scheme for the known $\Delta\zeta$[14].

$$\Delta z < \text{Min} \left\{ \frac{1}{2} \frac{\gamma}{E} \Delta\zeta^2 \Big|_{\text{all } n}, \frac{1}{2} \frac{\sigma}{F} \Delta\zeta^2 \Big|_{\text{all } n} \right\} \tag{33}$$

The value of $\Delta\zeta$ is not limited from stability considerations and is selected from the required resolution and the accuracy of the flow problem.

The boundary conditions, given by equations (26) through (29), have the following finite difference representations:

$$\left.\begin{aligned} W\,(M+N+2) &= 0 \\ \Theta\,(M+N+2) &= \Theta_e \end{aligned}\right\} \tag{34}$$

$$\Delta P_2 = \rho_{M+N+2}\,\Delta z \left\{ \frac{\partial u}{\partial r}^2 + \frac{\partial u}{\partial r} \Big|_{r=1} \right\} \tag{35}$$

$$\left.\begin{aligned} W_1 &= \frac{4}{3} W_2 - \frac{1}{3} W_3 \\ \Theta_1 &= \frac{4}{3} \Theta_2 - \frac{1}{3} \Theta_3 \\ P\ (N+1) &= P\ (N+2) \end{aligned}\right\} \qquad (36)$$

$$\Theta\ (N+2) = \Theta\ (N+1)$$

$$W\ (N+2) = W\ (N+1)$$

$$W\ (N+1) = \frac{C_1\ \{\ 4\ W\ (N+3) - W\ (N+4)\ \} + 4\ W\ (N) - W\ (N-1)}{3\ (1+C_1)} \qquad (37)$$

$$\Theta\ (N+1) = \frac{C_1\ \{\ 4\ \Theta\ (N+3) - \Theta\ (N+4)\ \} + 4\ \Theta\ (N) - \Theta\ (N-1)}{3\ (1+C_2)}$$

where

$$C_1 = \frac{1}{M_1} \frac{G_1}{G_2} \frac{\Delta\zeta_1}{\Delta\zeta_2}$$

and

$$C_2 = \frac{1}{K_1} \frac{G_1}{G_2} \frac{\Delta\zeta_1}{\Delta\zeta_2}$$

In obtaining finite difference representation for the derivatives at the center line, the interface, and the wall, one sided differences of second order accuracy have been used.

After prescribing a set of initial conditions, the following sequence of operations is performed to obtain the solution in the entire region of interest:

1. Compute Δz for all n from the stability condition (33). Use the smallest value of all these values for further computations.

2. Compute the value of ΔP from equation (35).

3. Compute the new values of W and 0 from equations (31), (32), (33), (35) and (36).

4. Evaluate the location of stream lines and values of radial velocities by solving the following equations:

$$\frac{r^2}{2} = \int_o^r r dr = \int_o^{\psi} \frac{d\psi}{\rho u} = 2L \int_o^{\zeta} \frac{\zeta(1-\zeta^2)d\zeta}{\rho u} \tag{38}$$

$$v = u \frac{\partial r}{\partial z})_{\zeta} \tag{39}$$

5. Proceed to next axial step. Repeat steps 1, 2, 3 and 4.

Finite Difference Equations - Implicit Method

The finite difference equations resulting from the substitution of central difference approximations of fourth order accuracy for ζ derivatives and of two point backward difference approximations for the first derivatives in the z direction are:

$$\begin{aligned}
&(16R\gamma_n^{i+1} - 8T_n^{i+1})\, W_{n-1}^{i+1} - (30R\gamma_n^{i+1} + E_n^{i+1})\, W_n^{i+1} \\
&\quad + (16R\gamma_n^{i+1} + 8T\delta_n^{i+1})\, W_{n+1}^{i+1} \\
&\quad = E_n^{i+1} \left(\frac{\Delta P}{\rho_n^{i+1}} - W_n^i\right) + (R\gamma_n^{i+1} - T\delta_n^{i+1})\, W_{n-2}^{i+1} \\
&\quad + (R\gamma_n^{i+1} + T\delta_n^{i+1})\, W_{n+2}^{i+1}
\end{aligned} \tag{40}$$

$$(16R\sigma_n^{i+1} - 8T\omega_n^{i+1})\ \theta_{n-1}^{i+1} - (30R\sigma_n^{i+1} + F_n^{i+1})\ \theta_n^{i+1}$$

$$+ (16R\sigma_n^{i+1} + 8T\omega_n^{i+1})\ \theta_{n+1}^{i+1} \qquad (41)$$

$$= -(\theta_n^i + H_n^{i+1}\Delta z)\ F_n^{i+1} + (R\sigma_n^{i+1} - T\omega_n^{i+1})\ \theta_{n-2}^{i+1}$$

$$+ (R\sigma_n^{i+1} + T\omega_n^{i+1})\ \theta_{n+2}^{i+1}$$

$$R = \frac{\Delta z}{12(\Delta \zeta)^2} \qquad (42)$$

$$T = \frac{\Delta z}{12(\Delta \zeta)} \qquad (43)$$

The finite difference representations for the boundary conditions are given by equations (34) through (37). Equations (36) and (37) take a slightly different form because of higher order approximations. For any grid size, the use of five point finite difference approximations for derivatives results in improved accuracy, compared to three point finite difference approximations.

The following procedure is used to advance the solution from the i^{th} row (where W and 0 distributions are known) to the $i+1^{th}$ row:

1. Assume a value for ΔP.

2. Assume (N+M) values of W and (N+M) values of 0 for the $i+1^{th}$ row.

3. Compute new values of W and Θ by solving N+M equations of the form of Equation (40) and of Equation (41) by tridiagonal matrix inversion.

4. Use the newly generated values of W and Θ and modified form of Equation (36) to evaluate new values for W_1^{i+1} and Θ_1^{i+1}; also compute new values for location of stream lines from Equation (38) and a new value for ΔP from Equation (35).

5. Test ΔP, W and Θ for convergence of the iteration scheme.

6. If the convergence requirements are not met, repeat steps 3, 4 and 5. If the convergence criteria are satisfied, compute the values of v and proceed to the next axial step in the marching procedure.

With this computational scheme the solution is initiated at the tube entrance, $z = 0$, where the flow field is prescribed through the initial conditions, and is then obtained at each successive axial position marching down the tube. Though there is no restriction on the maximum value of Δz used in the computation from numerical stability considerations, the set of initial conditions prescribed and the accuracy required in the final values dictate the practical value to be used. In step 4 of the implicit method computational scheme, to obtain an improved estimate of the value of ΔP, the use of relaxation and gradient techniques was proven to accelerate the convergence of the iterative scheme.

CHAPTER V

RESULTS AND DISCUSSION

The results of a parametric study of the coaxial entrance flow with heat generation are illustrated in Figures 3 through 22. The values of various system parameters choosen for run No. 1 are listed in Table 1. For this run, heat generation was prescribed as constant per unit mass. Initial velocity and temperature profiles were assumed to be flat. The base run has an axial velocity ratio of inner to outer streams of 0.1, and a density ratio of 10. Both streams have the same initial temperature. The values of specific heat, thermal conductivity, and gas constant for uranium and hydrogen were used in evaluating other dimensionless groups.

Table 1. System Parameters

Parameter	Value
Φ	8.333
k	0.01
S	0.01
G_1	1.776 (10^7)
G_2	1.776 (10^8)
α	0.7
Pr	1.0
T_e	1.0

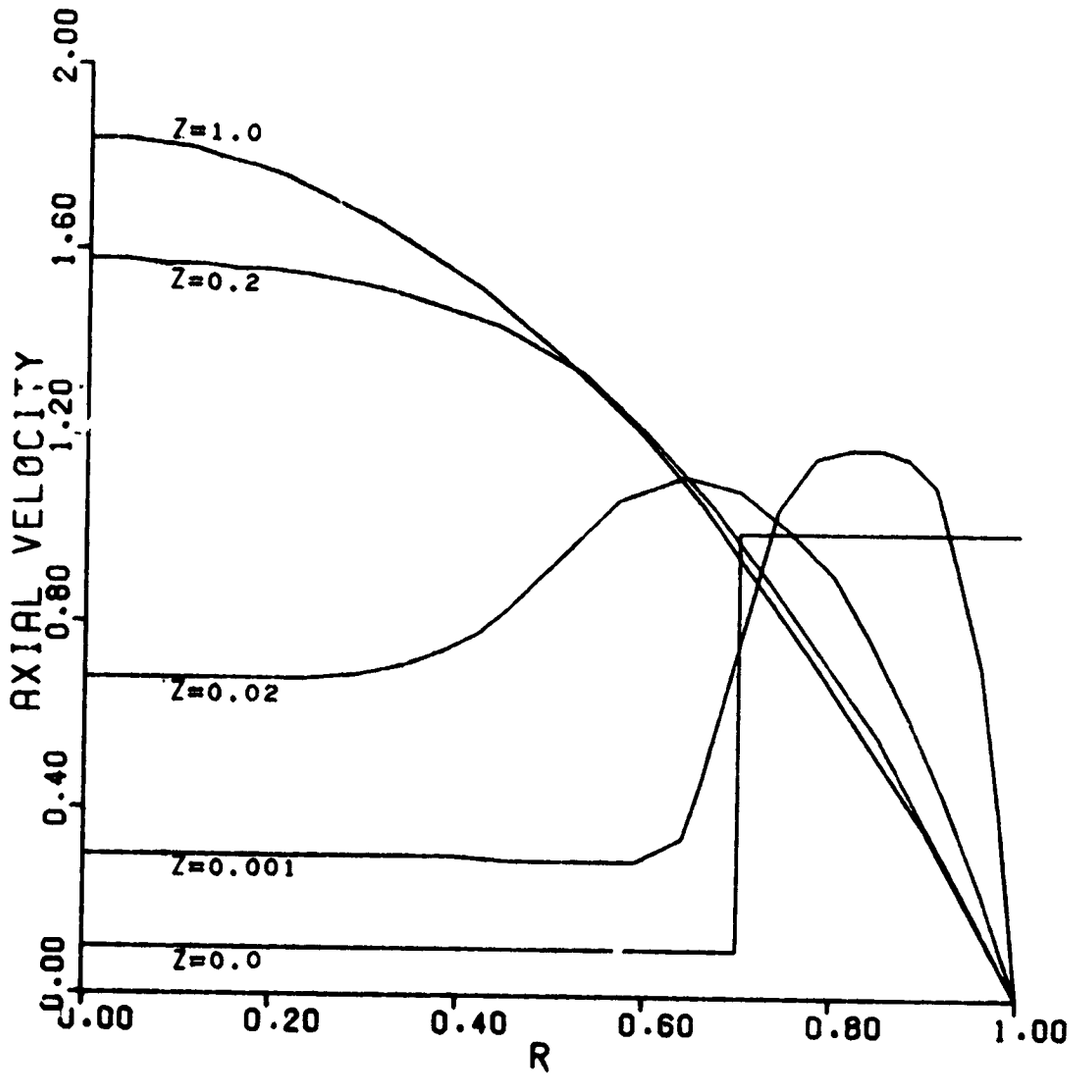

Figure 3. Axial Velocity Profiles - Constant Generation per Unit Mass Case - Parameter Set No. 1

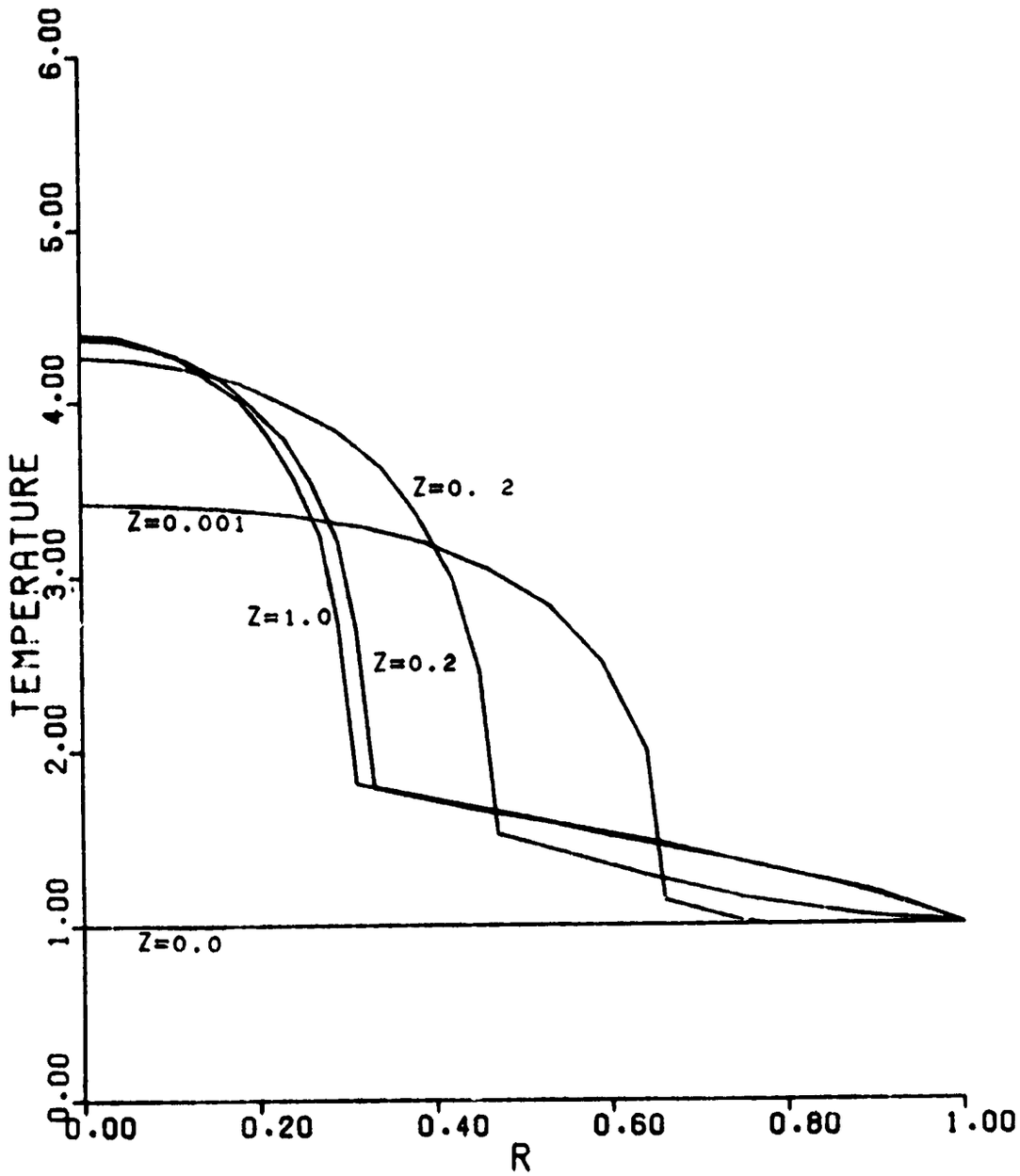

Figure 4. Temperature Profiles - Constant Generation per Unit Mass Case - Parameter Set No. 1

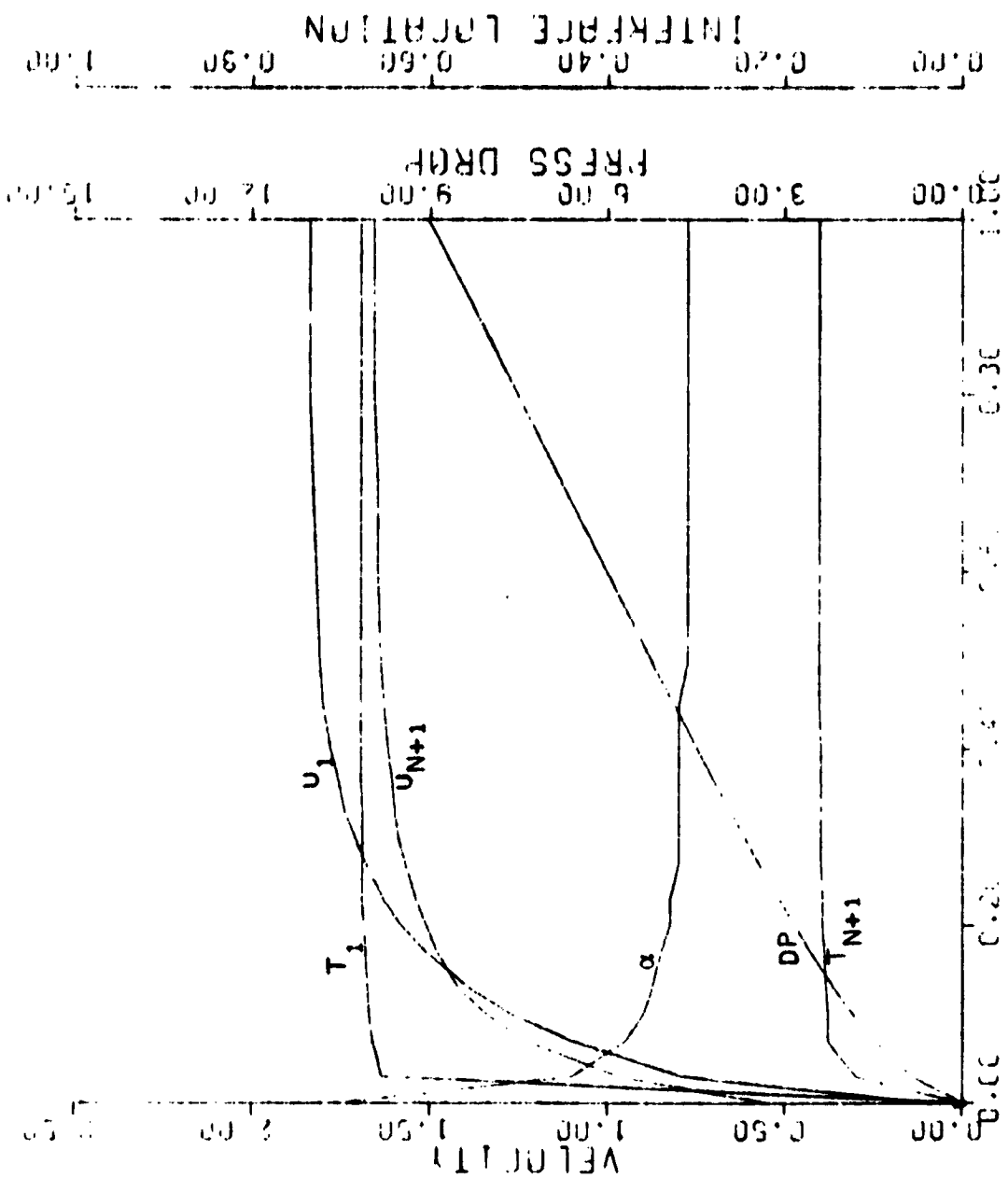

Figure 5. Axial Development of Central and Interfacial Axial Velocities and Temperatures, Pressure Drop and Location of Interface - Constant Generation per Unit Mass Case - Parameter Set No. 1

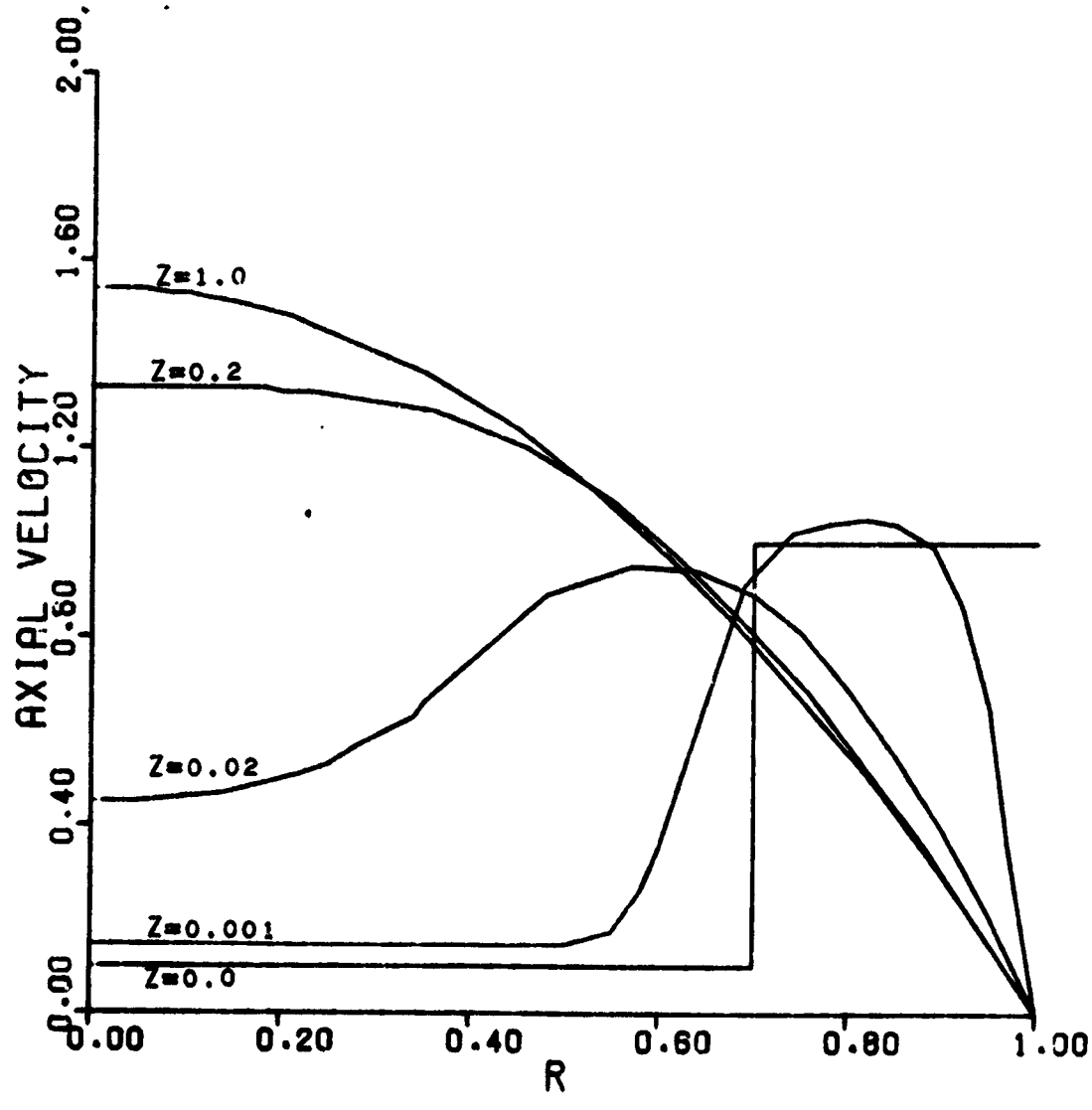

Figure 6. Axial Velocity Profiles - Constant Generation per Unit Mass Case - Parameter Set No. 2

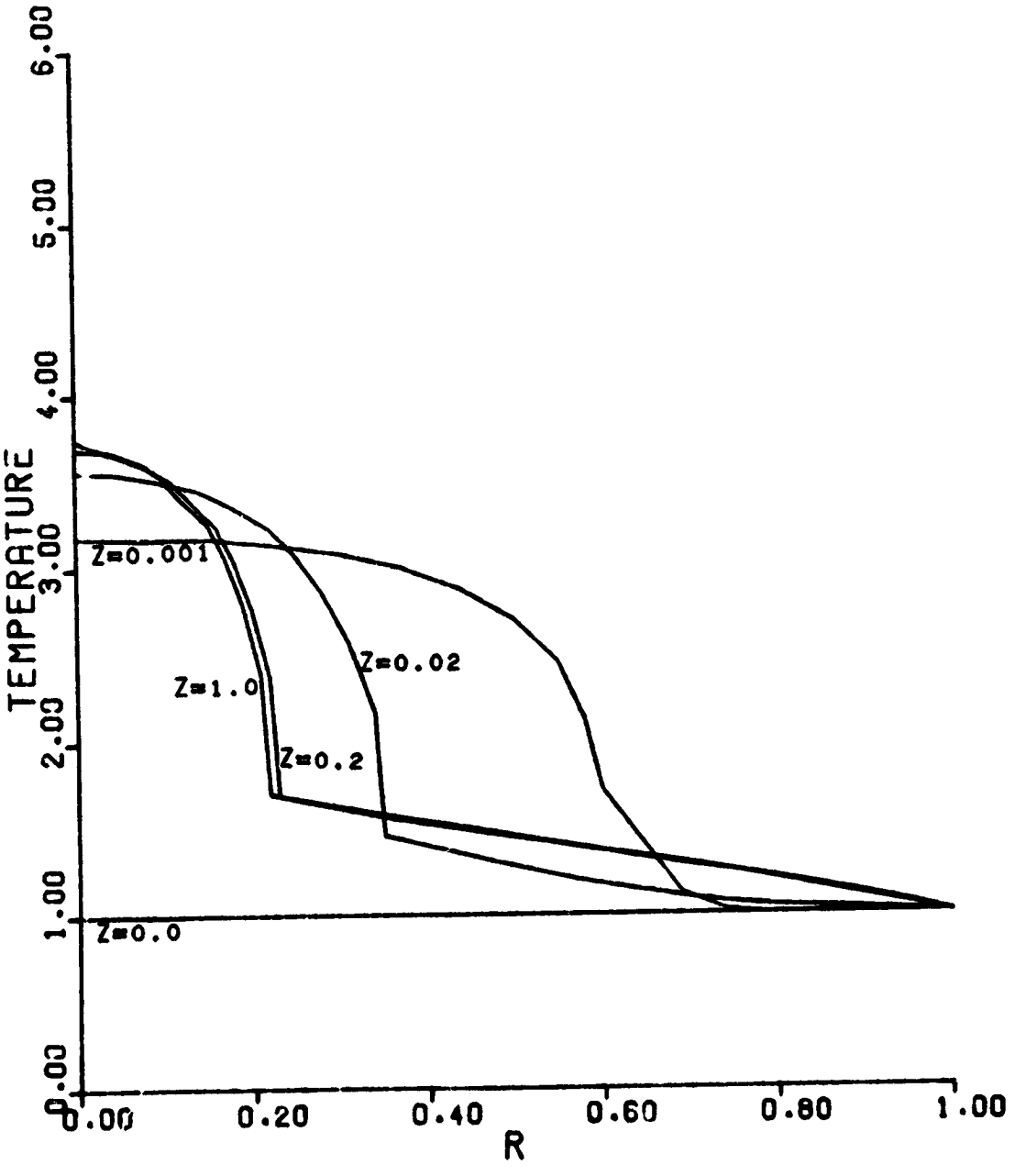

Figure 7. Temperature Profiles - Constant Generation per Unit Mass Case - Parameter Set No. 2

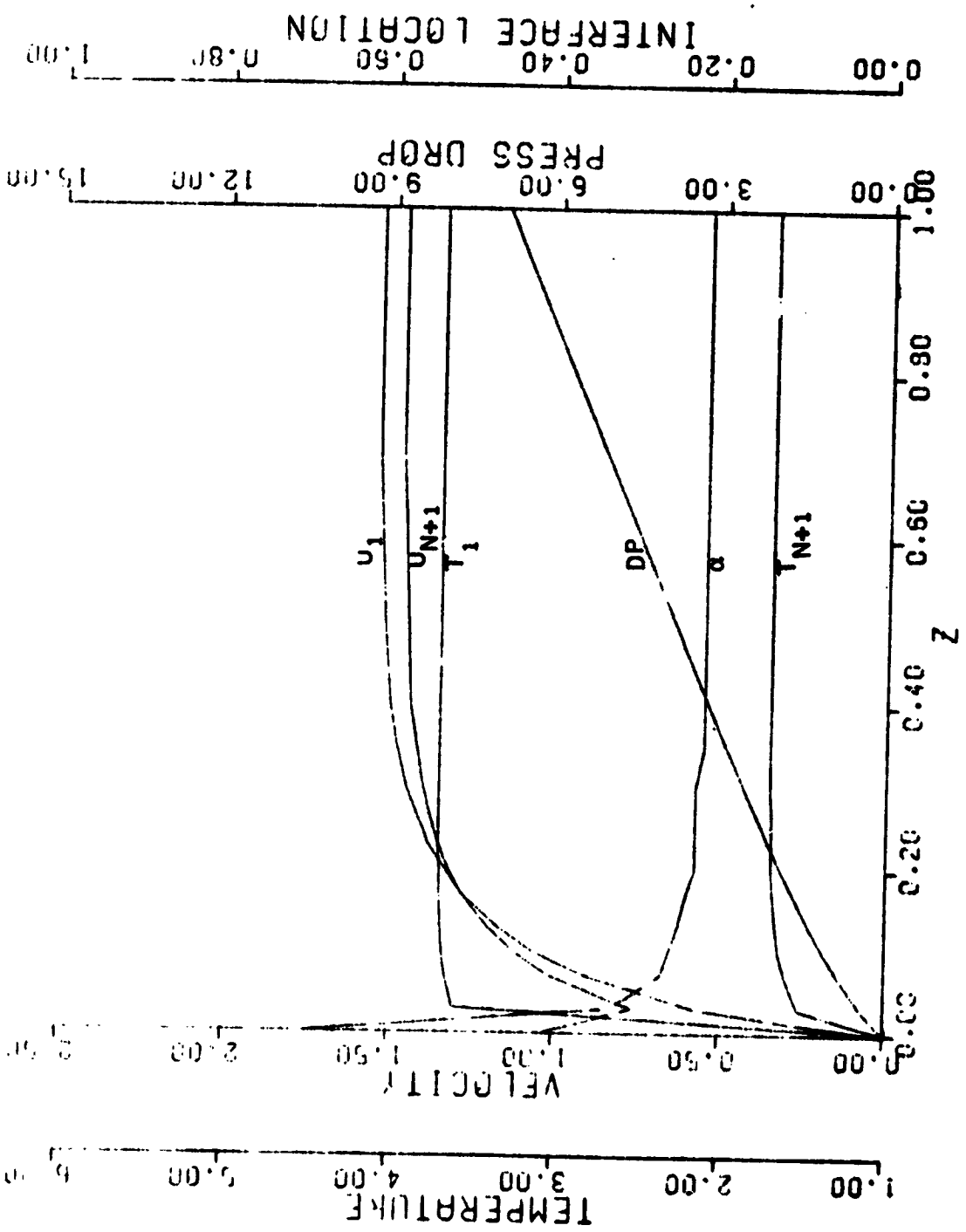

Figure 8. Axial Development of Central and Interfacial Axial Velocities and Temperatures, Pressure Drop and Location of Interface - Constant Generation per Unit Mass Case - Parameter Set No. 2

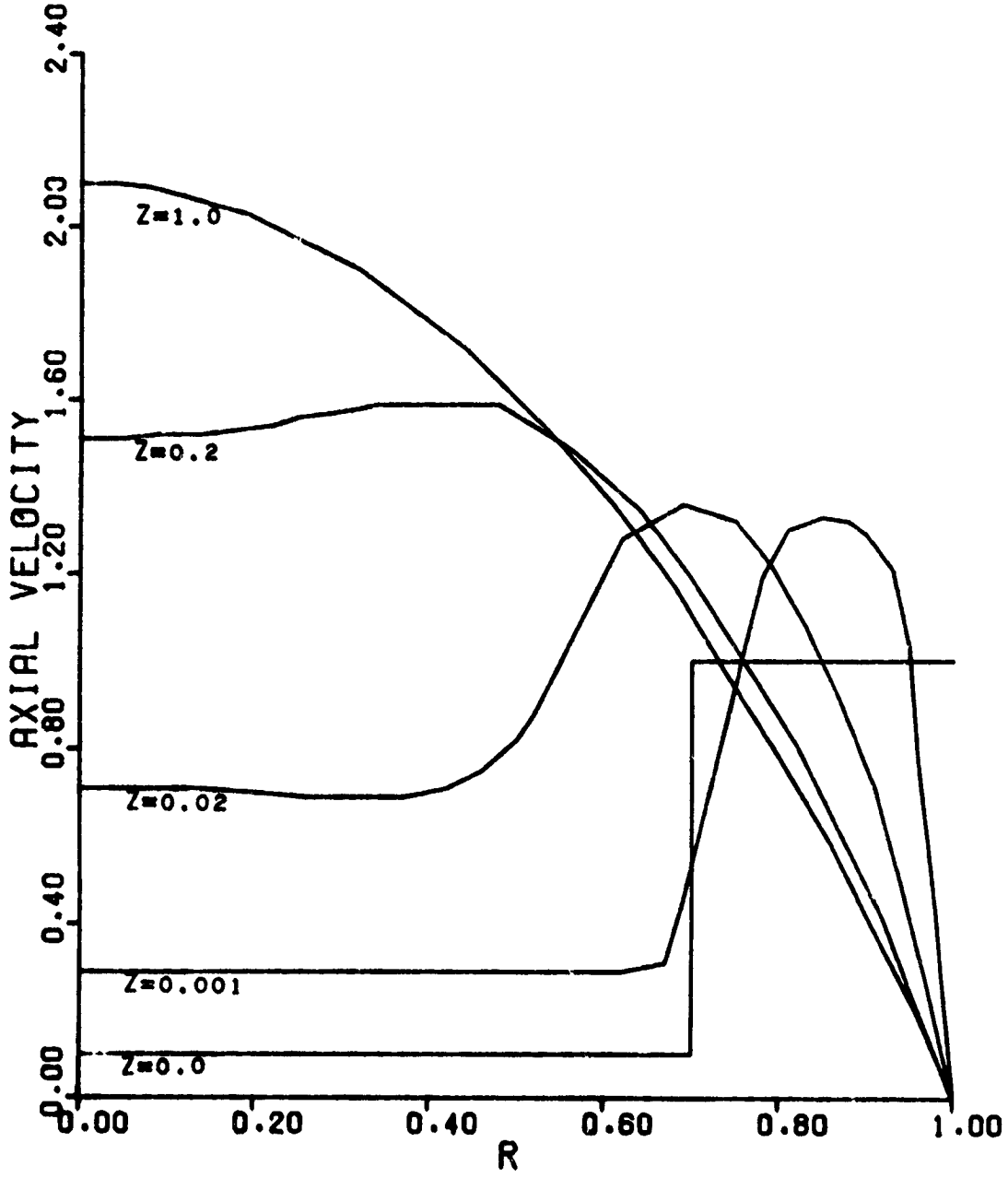

Figure 9. Axial Velocity Profiles - Constant Generation per Unit Mass Case - Parameter Set No. 3

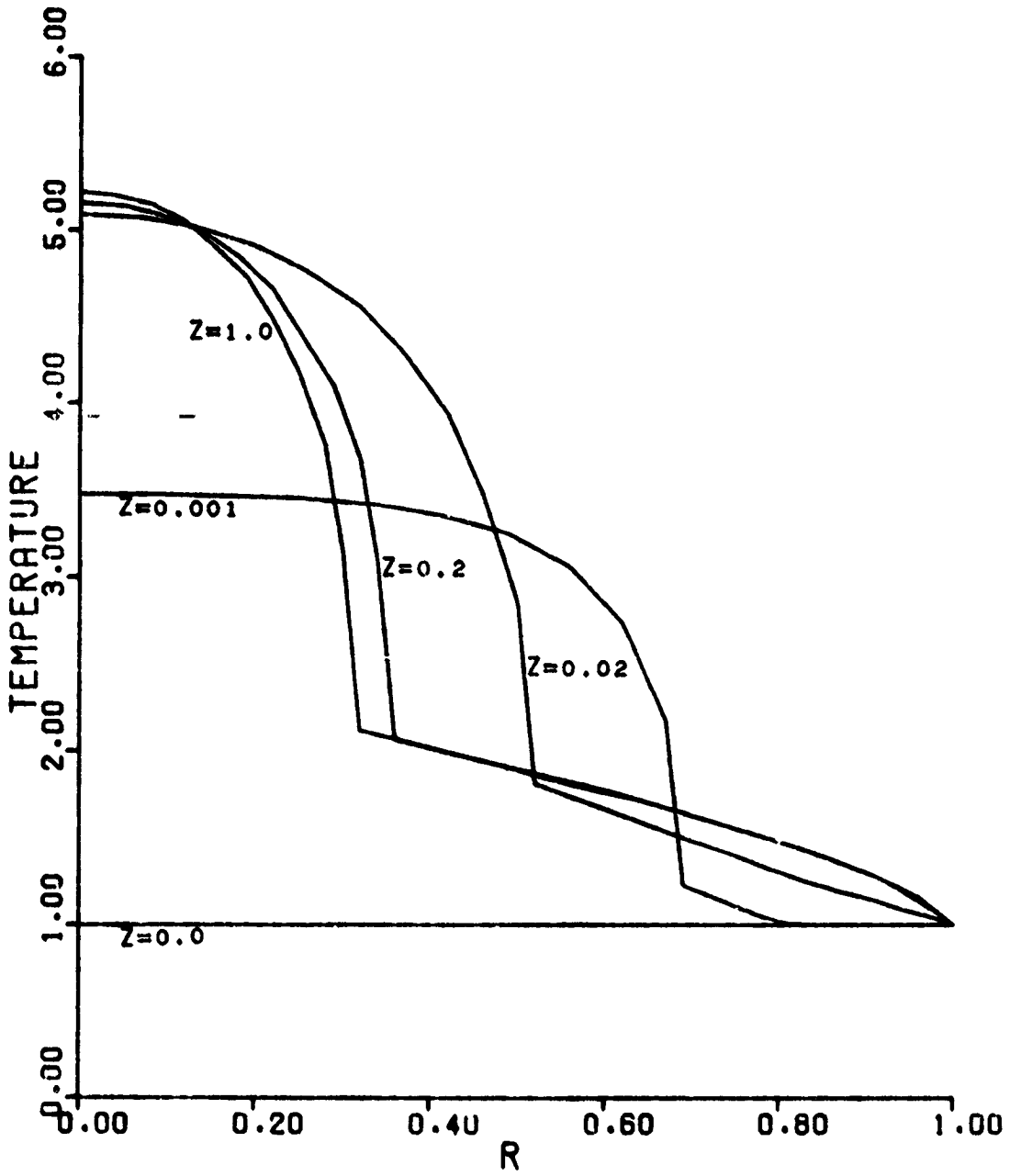

Figure 10. Temperature Profiles - Constant Generation per Unit Mass Case - Parameter Set No. 3

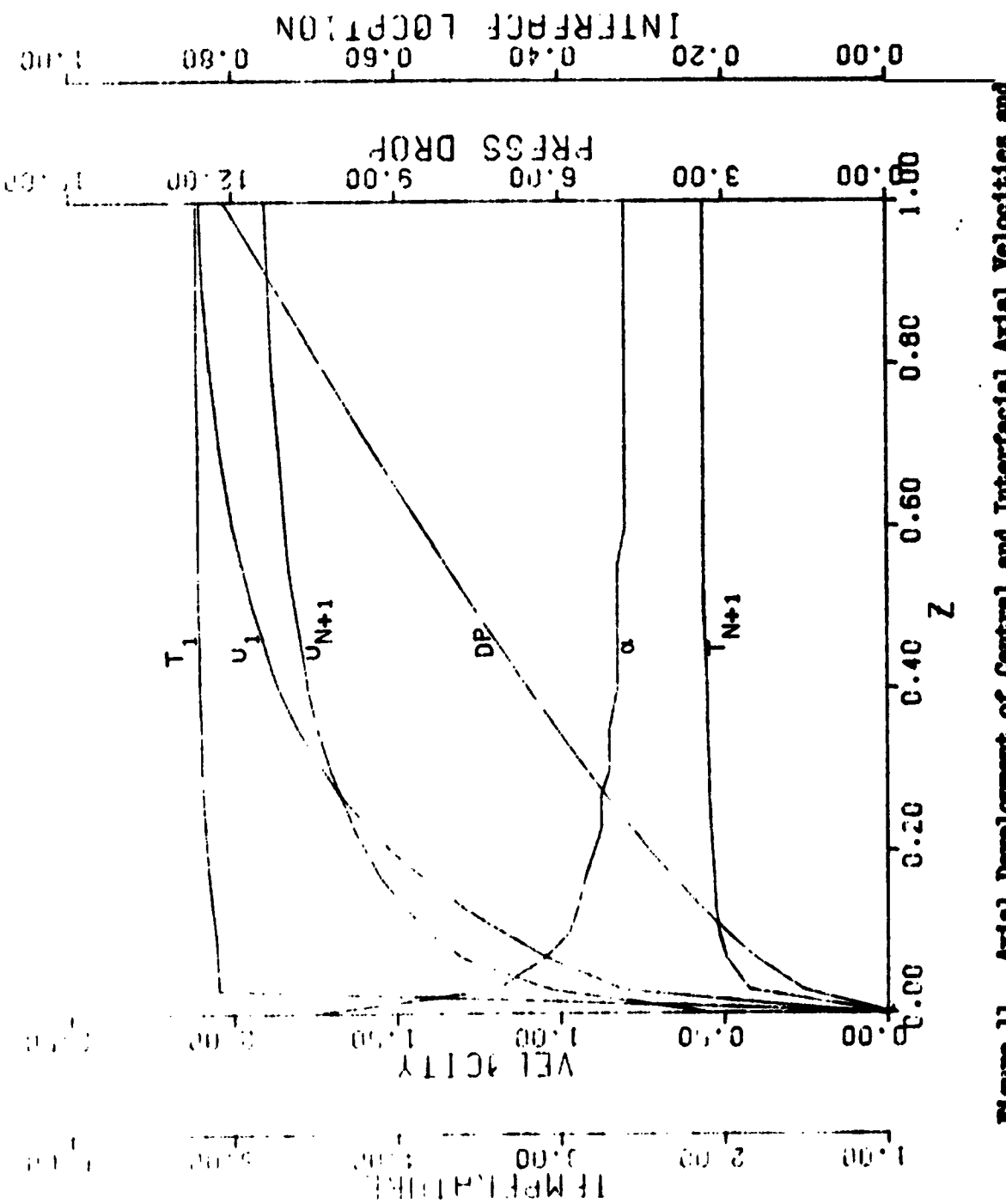

Figure 11. Axial Development of Central and Interfacial Axial Velocities and Temperatures, Pressure Drop and Location of Interface - Constant Generation per Unit Mass Case - Parameter Set No. 3

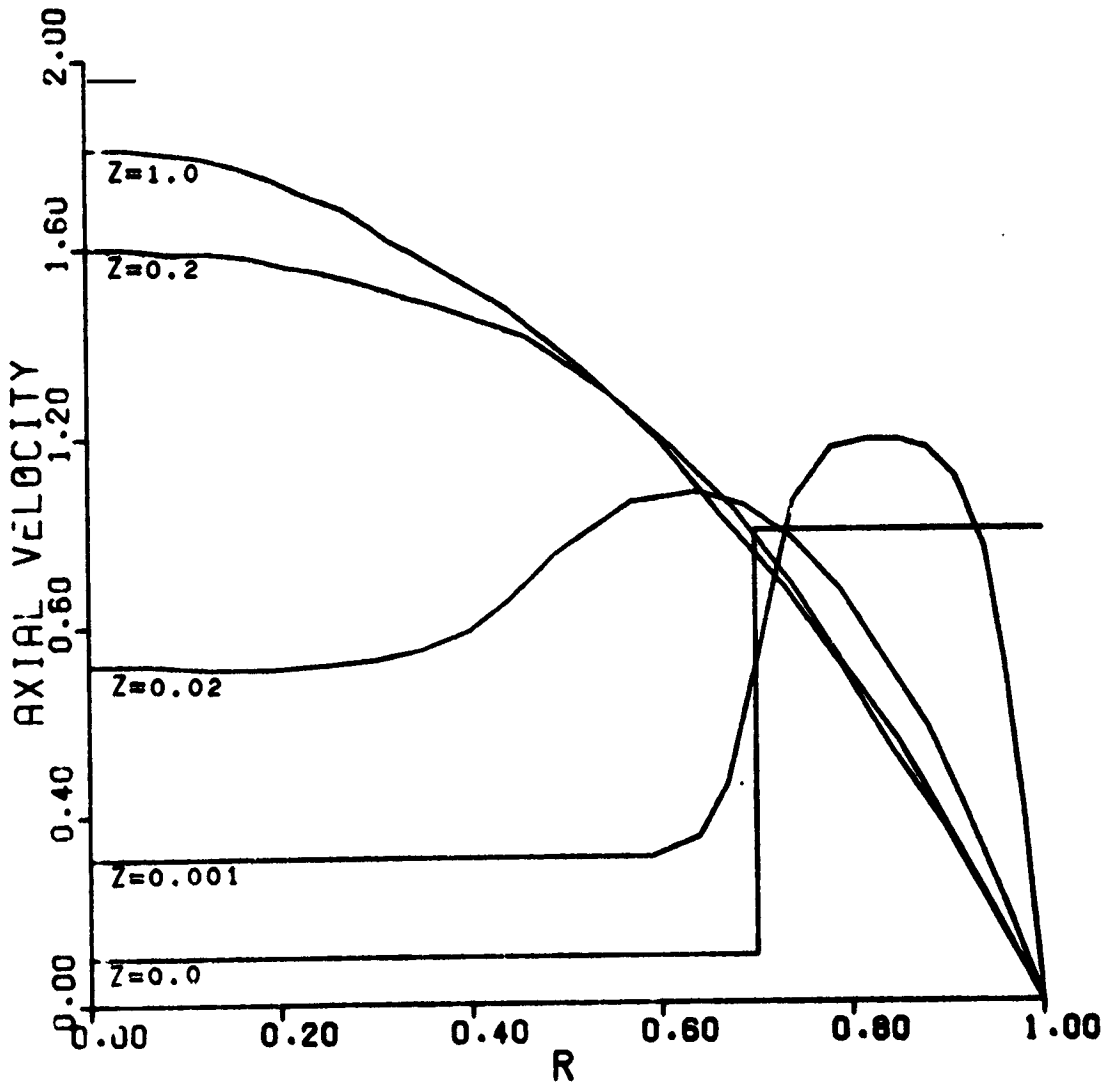

Figure 12. Axial Velocity Profiles - Constant Generation per Unit Mass Case - Parameter Set No. 4

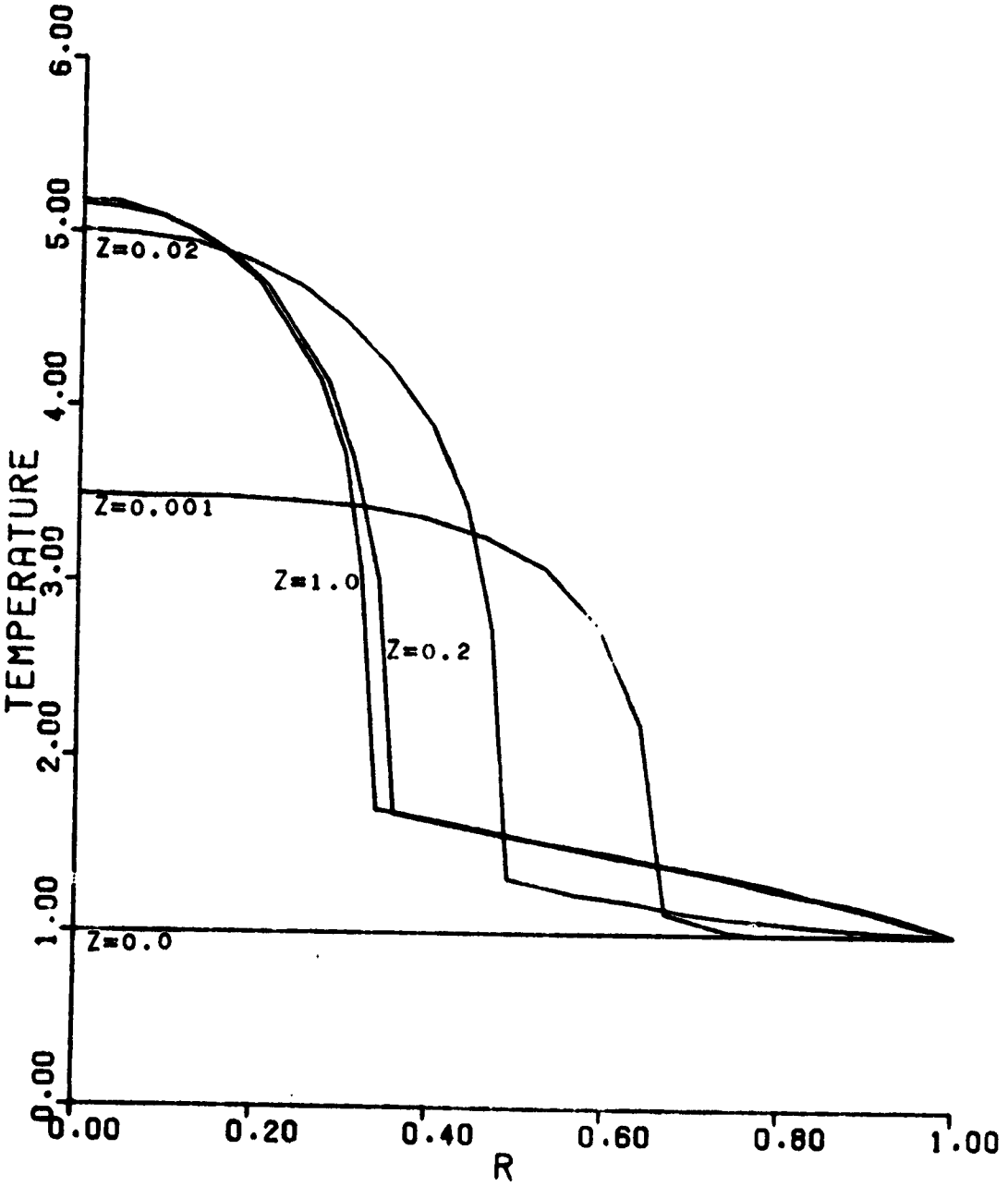

Figure 13. Temperature Profiles - Constant Generation per Unit Mass Case - Parameter Set No. 4

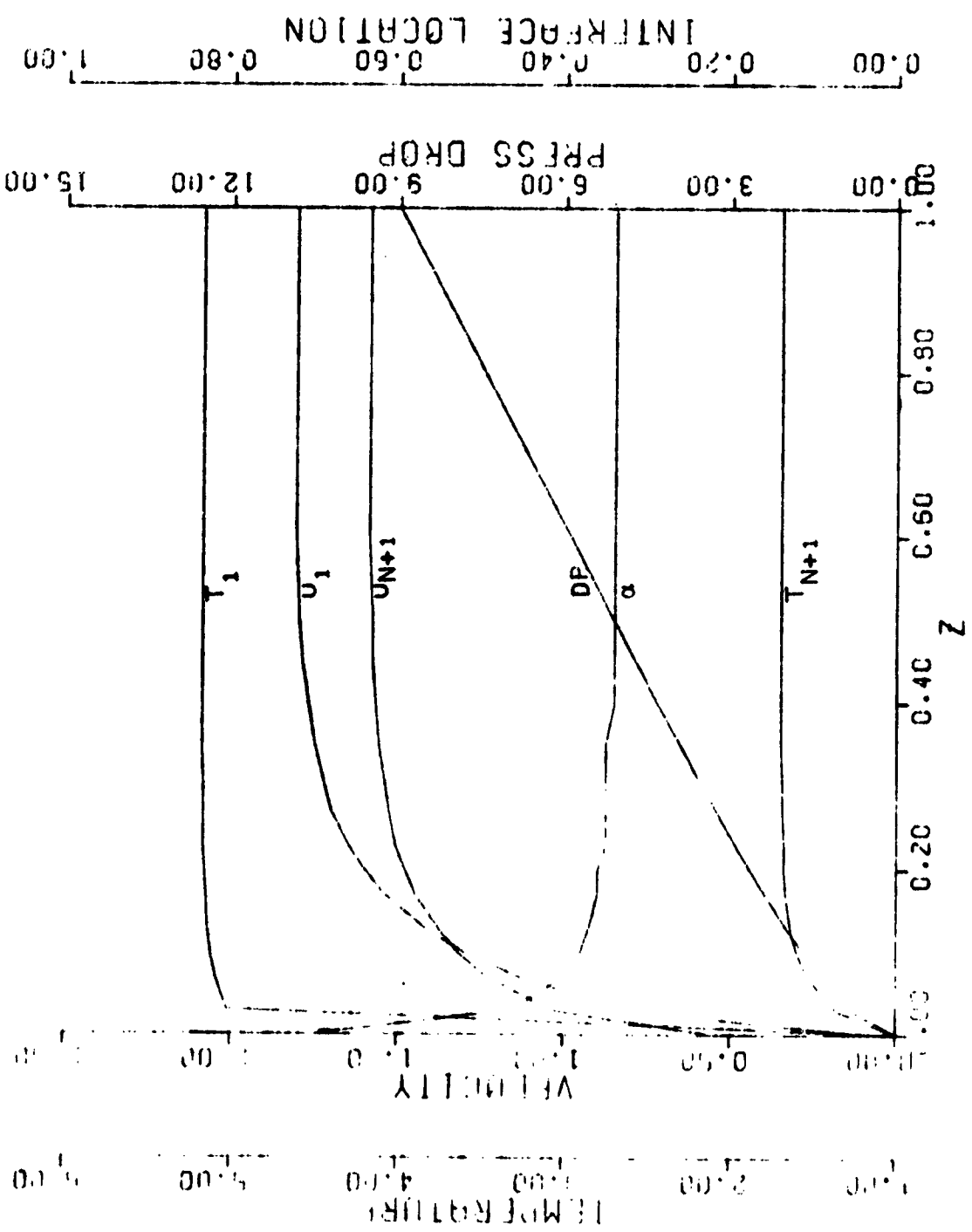

Figure 14. Axial Development of Central and Interfacial Axial Velocities and Temperatures, Pressure Drop and Location of Interface - Constant Generation per Unit Mass Case - Parameter Set No. 4

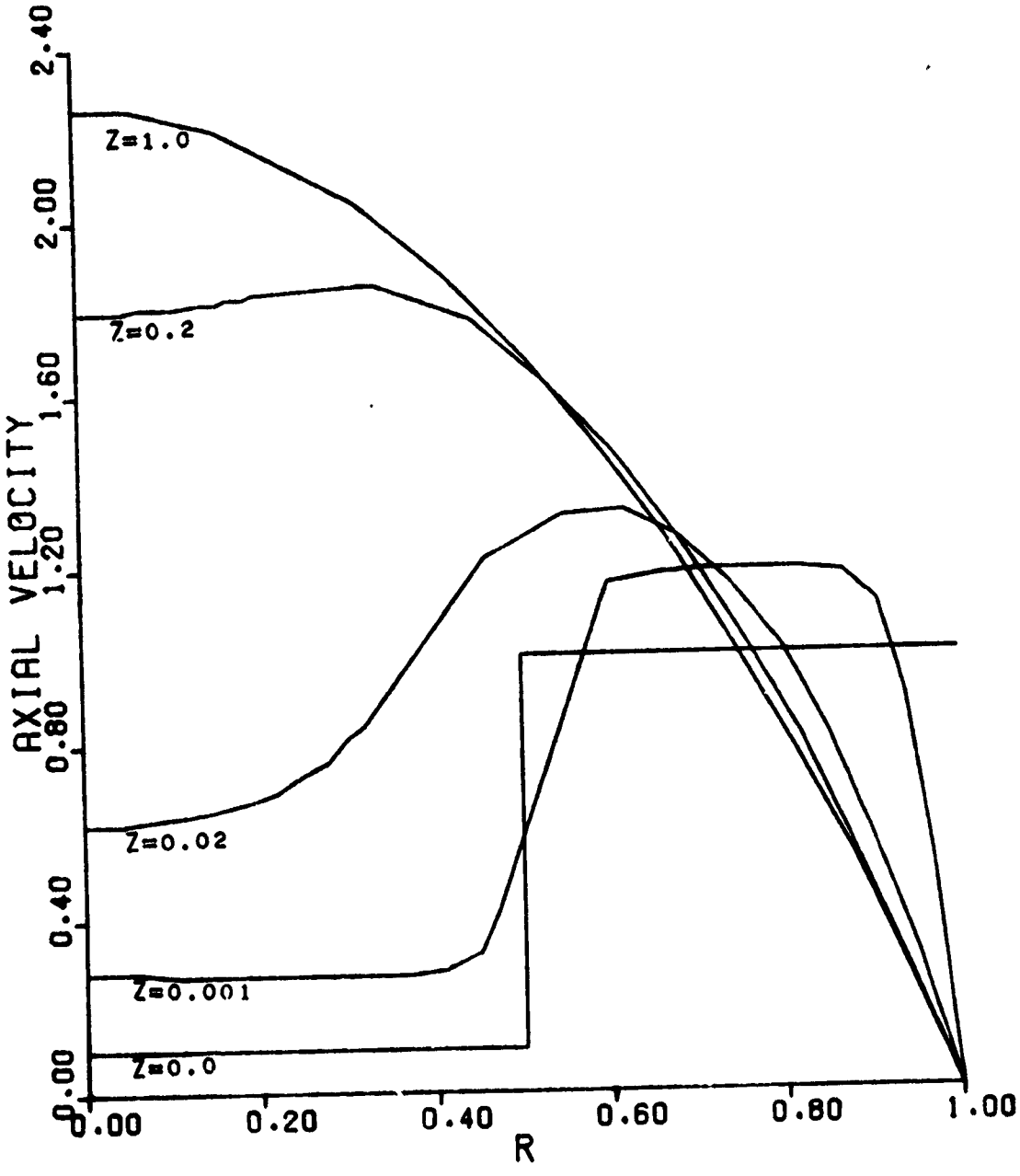

Figure 15. Axial Velocity Profiles - Constant Generation per Unit Mass Case - Parameter Set No. 5

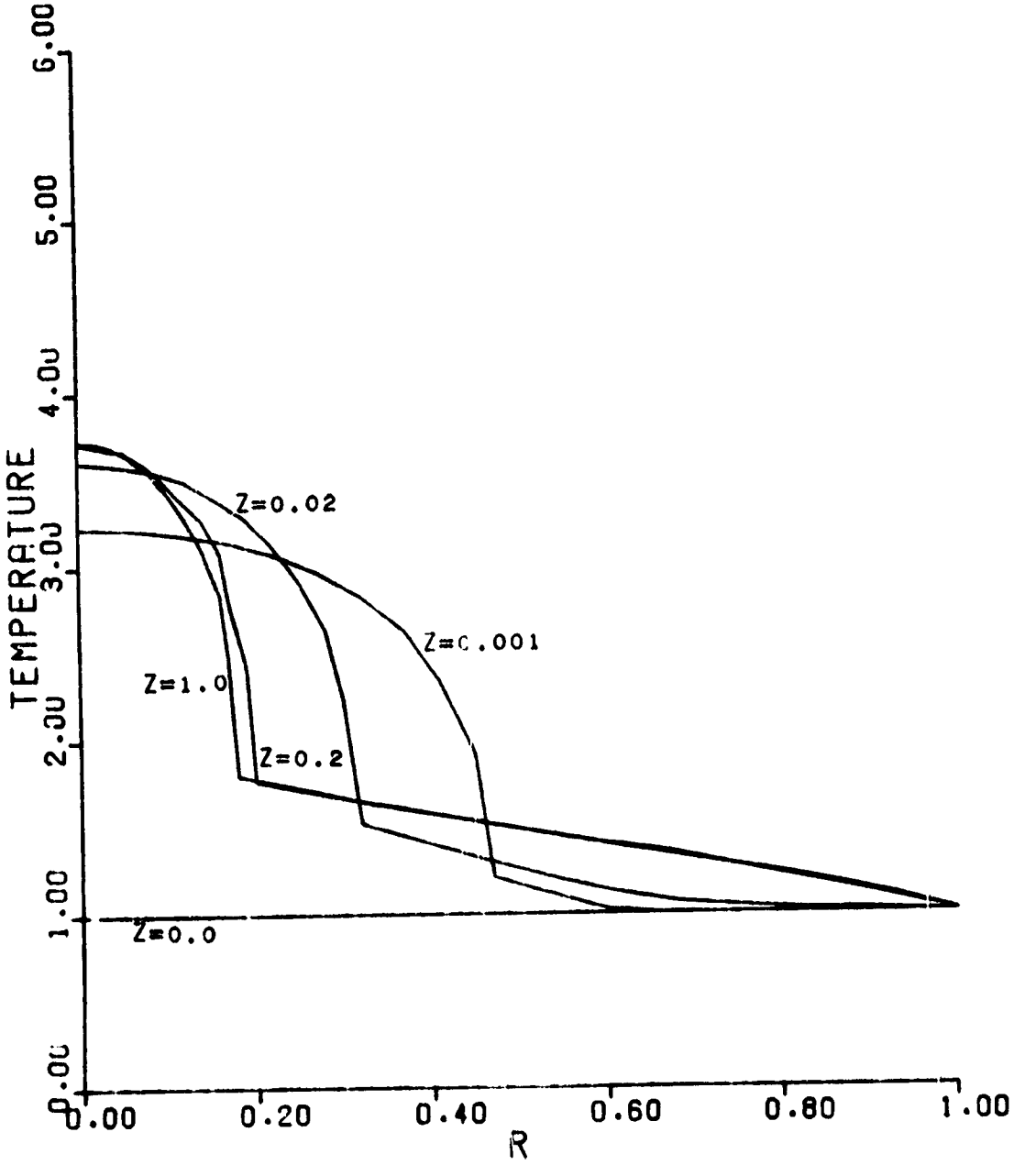

Figure 16. Temperature Profiles - Constant Generation per Unit Mass Case - Parameter Set No. 5

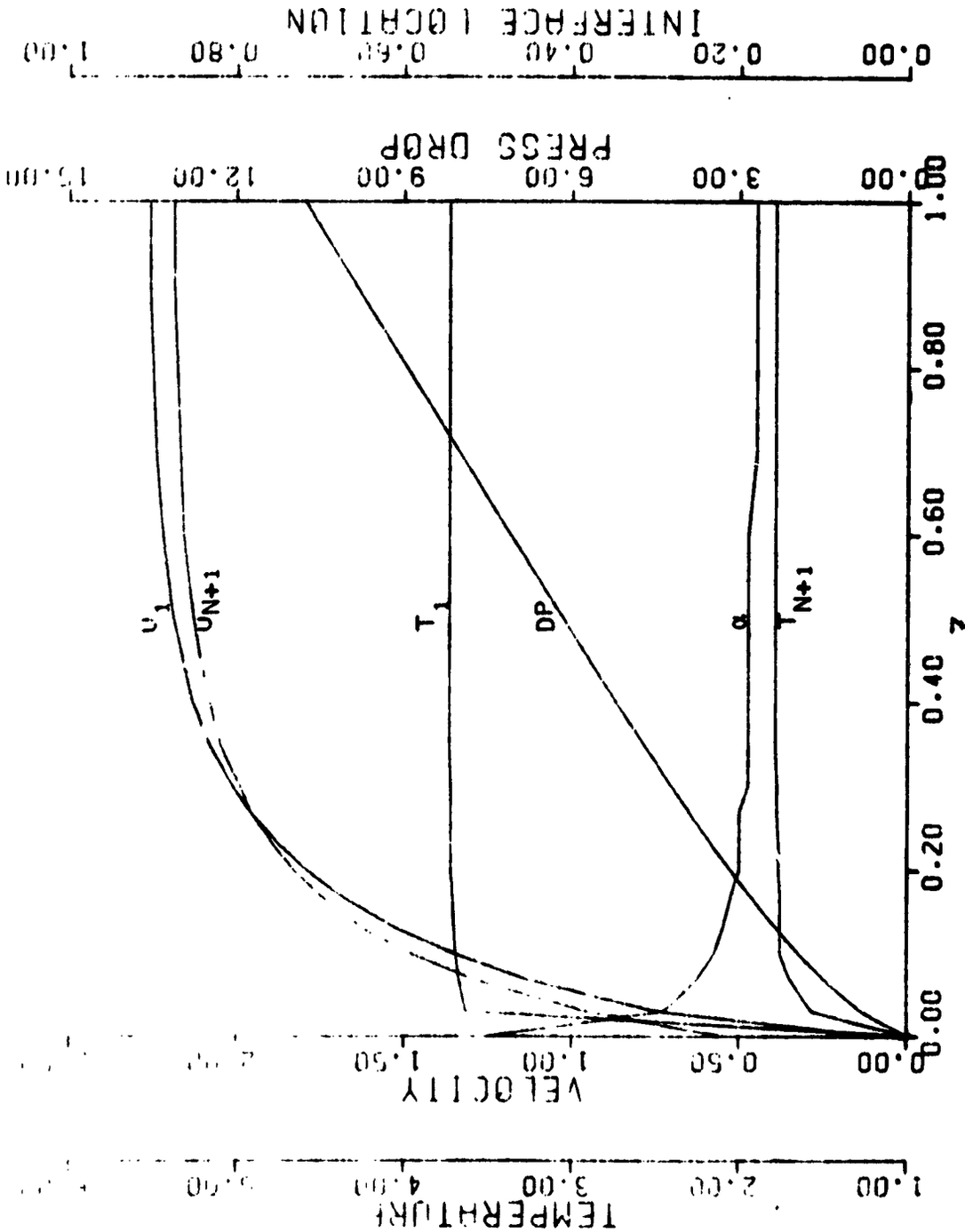

Figure 17. Axial Development of Central and Interfacial Axial Velocities and Temperatures, Pressure Drop and Location of Interface – Constant Generation per Unit Mass Case – Parameter Set No. 5

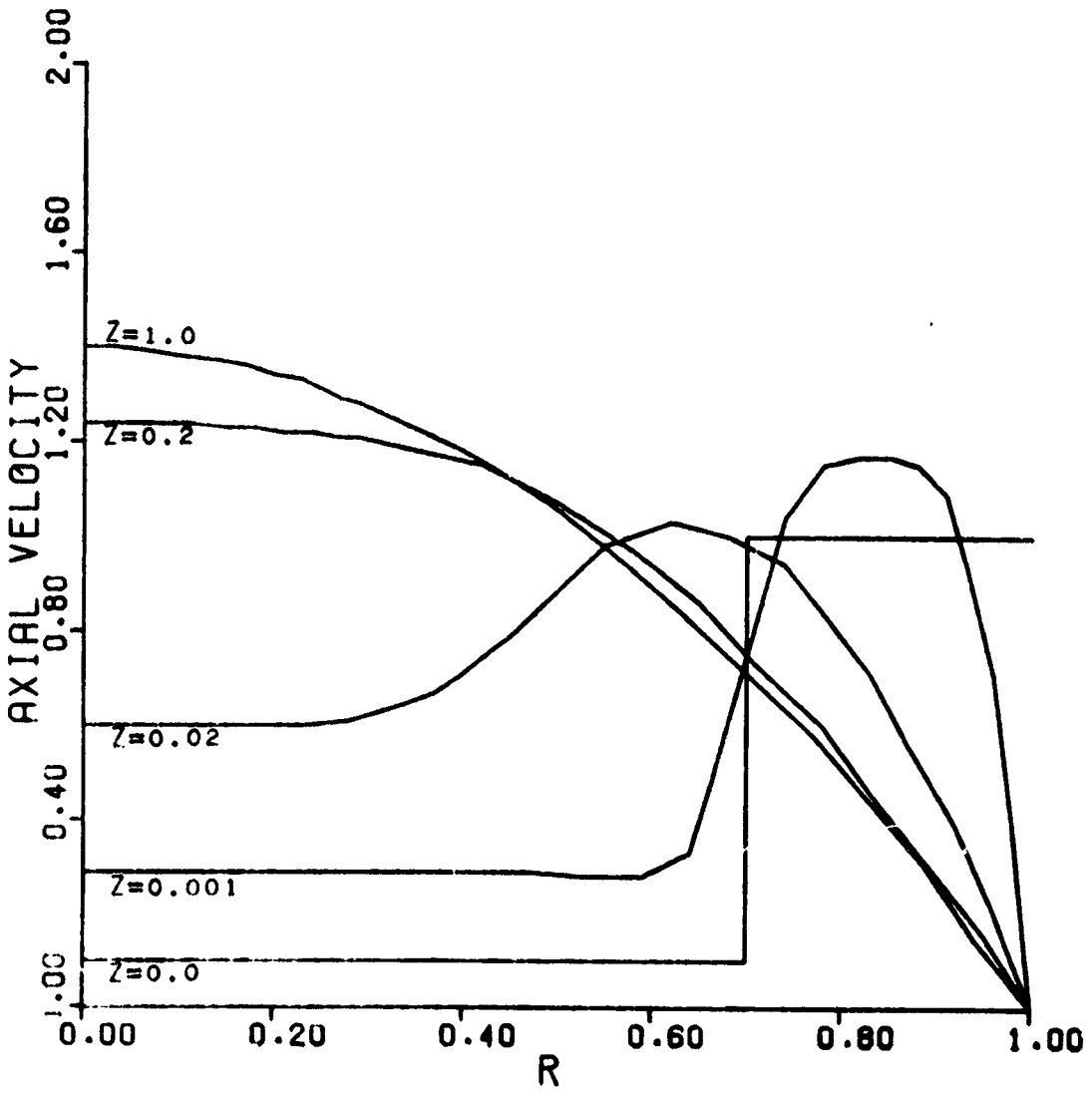

Figure 16. Axial Velocity Profiles - Constant Generation per Unit Volume Case

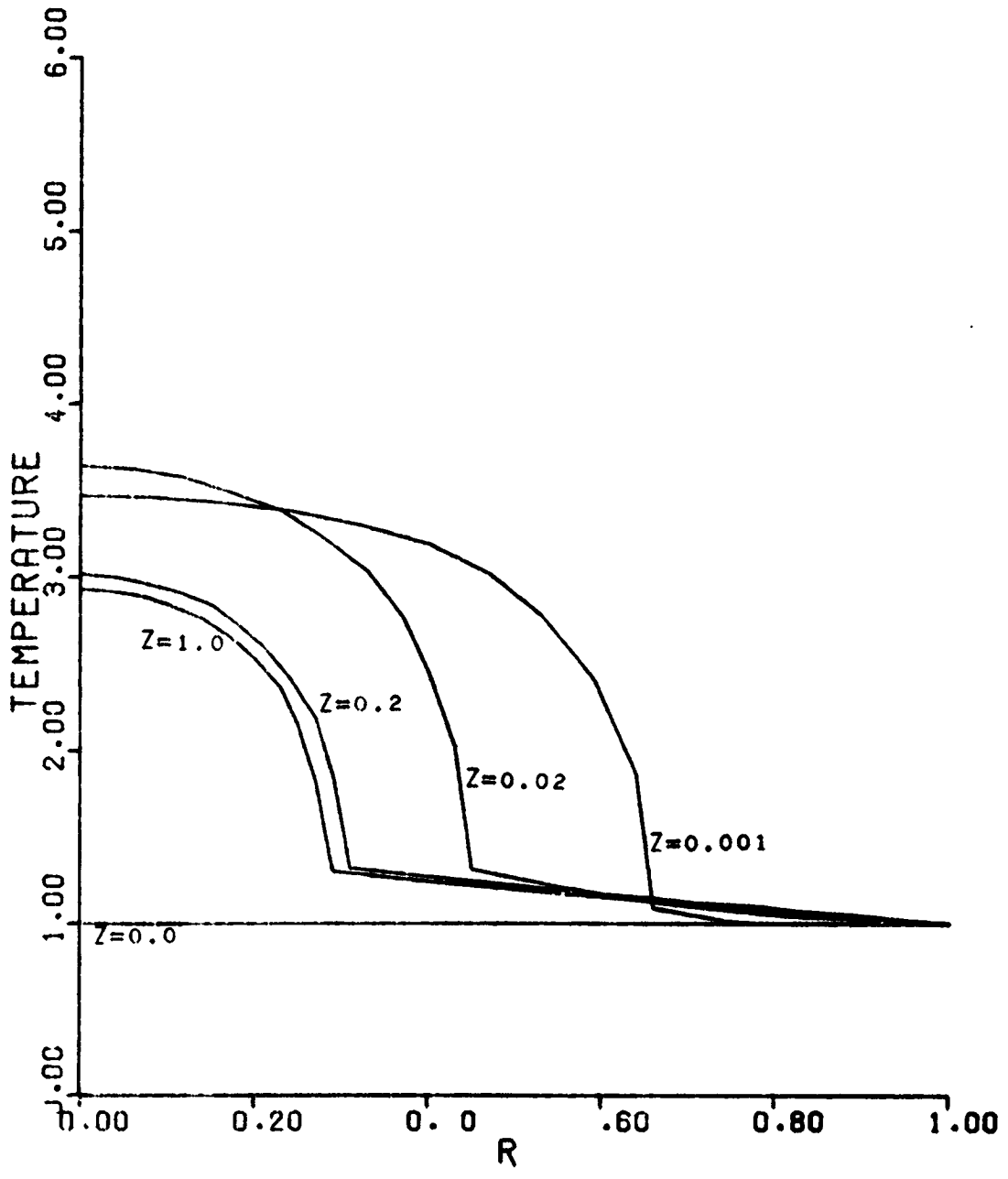

Figure 1[illegible]. Temperature Profiles - Constant Generation per Unit Volume Case

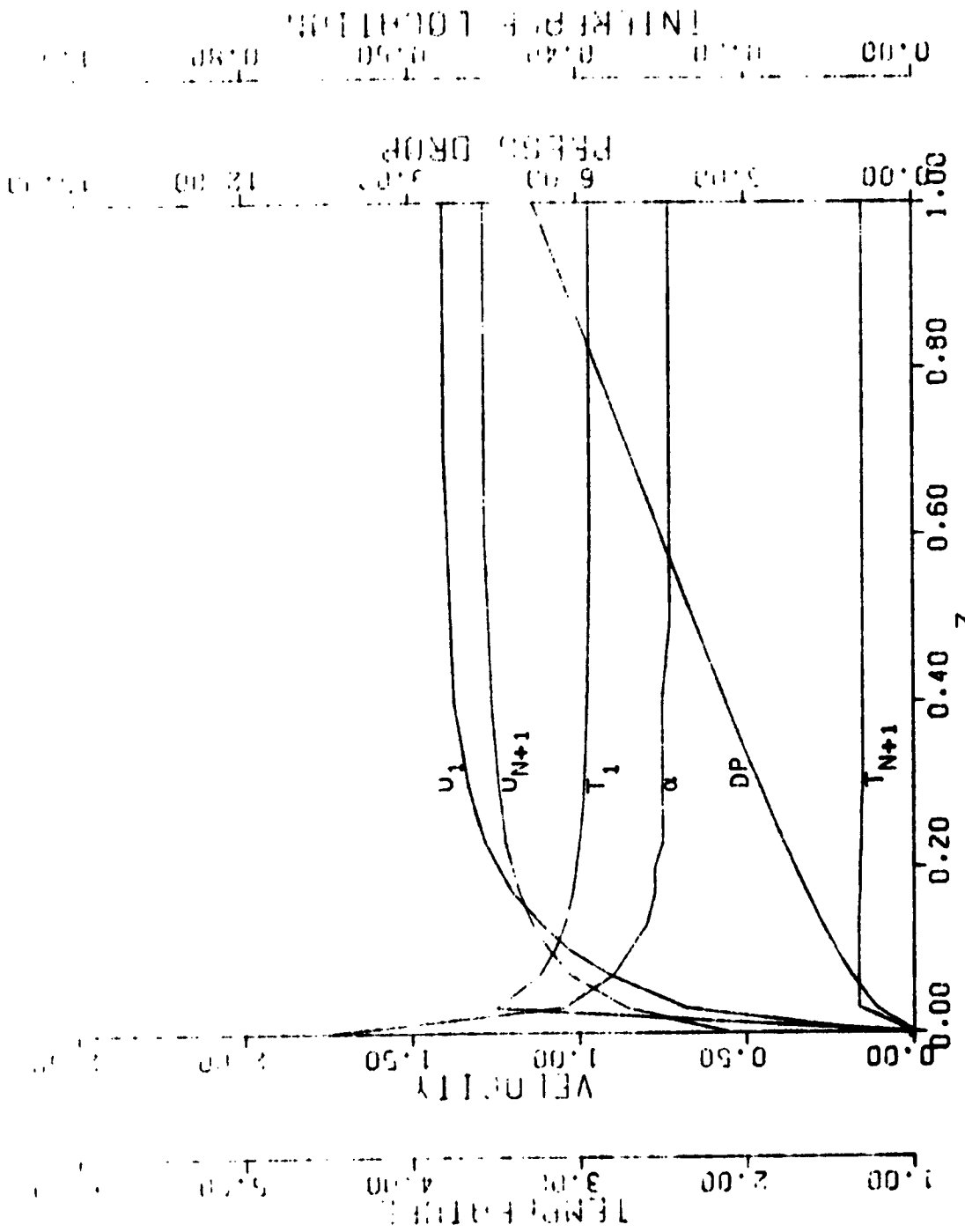

Figure 20. Axial Development of Central and Interfacial Axial Velocities and Temperatures, Pressure Drop and Location of Interface - Constant Generation per Unit Volume Case

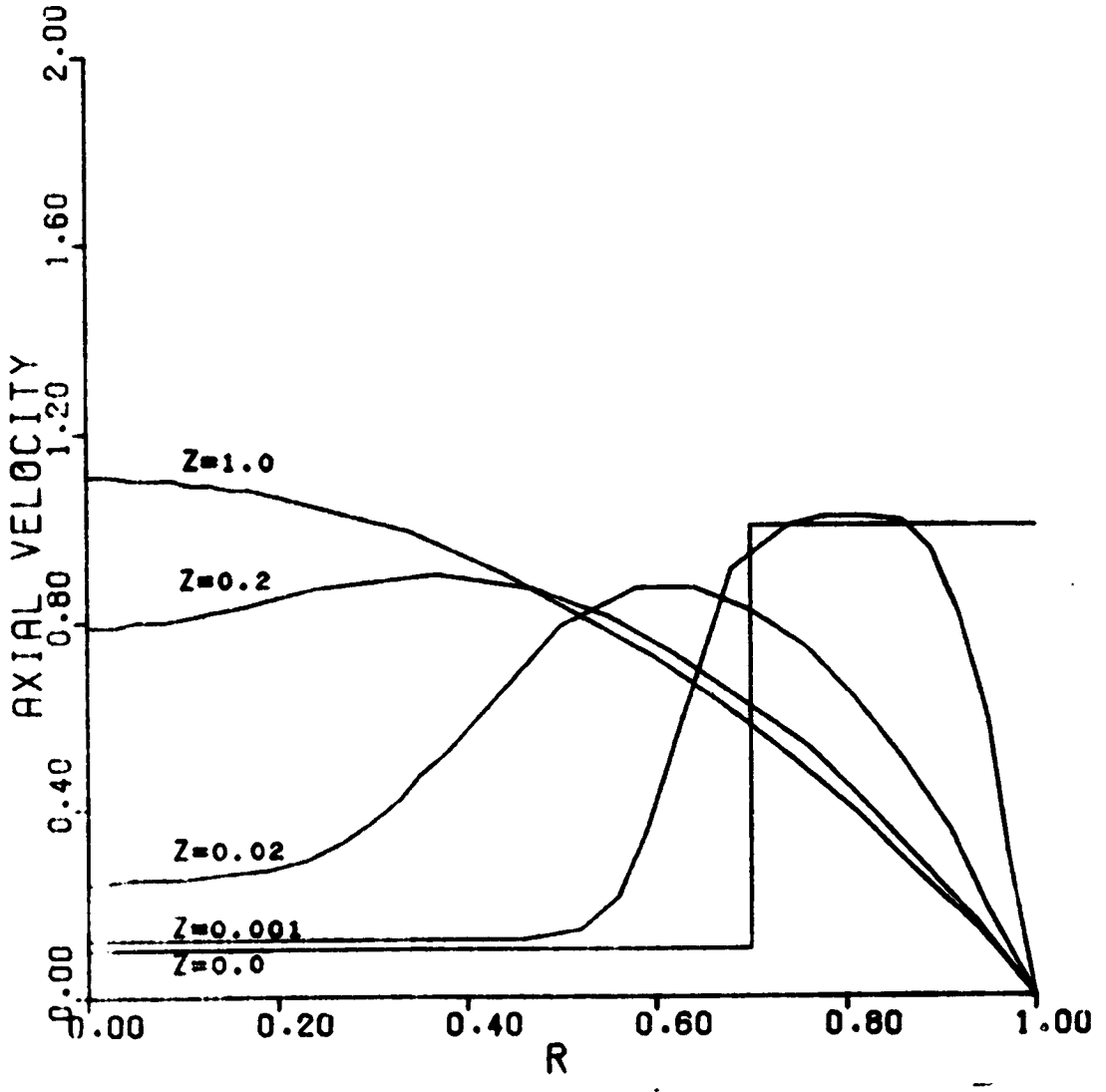

Figure 21. Axial Velocity Profiles - Zero Generation Case

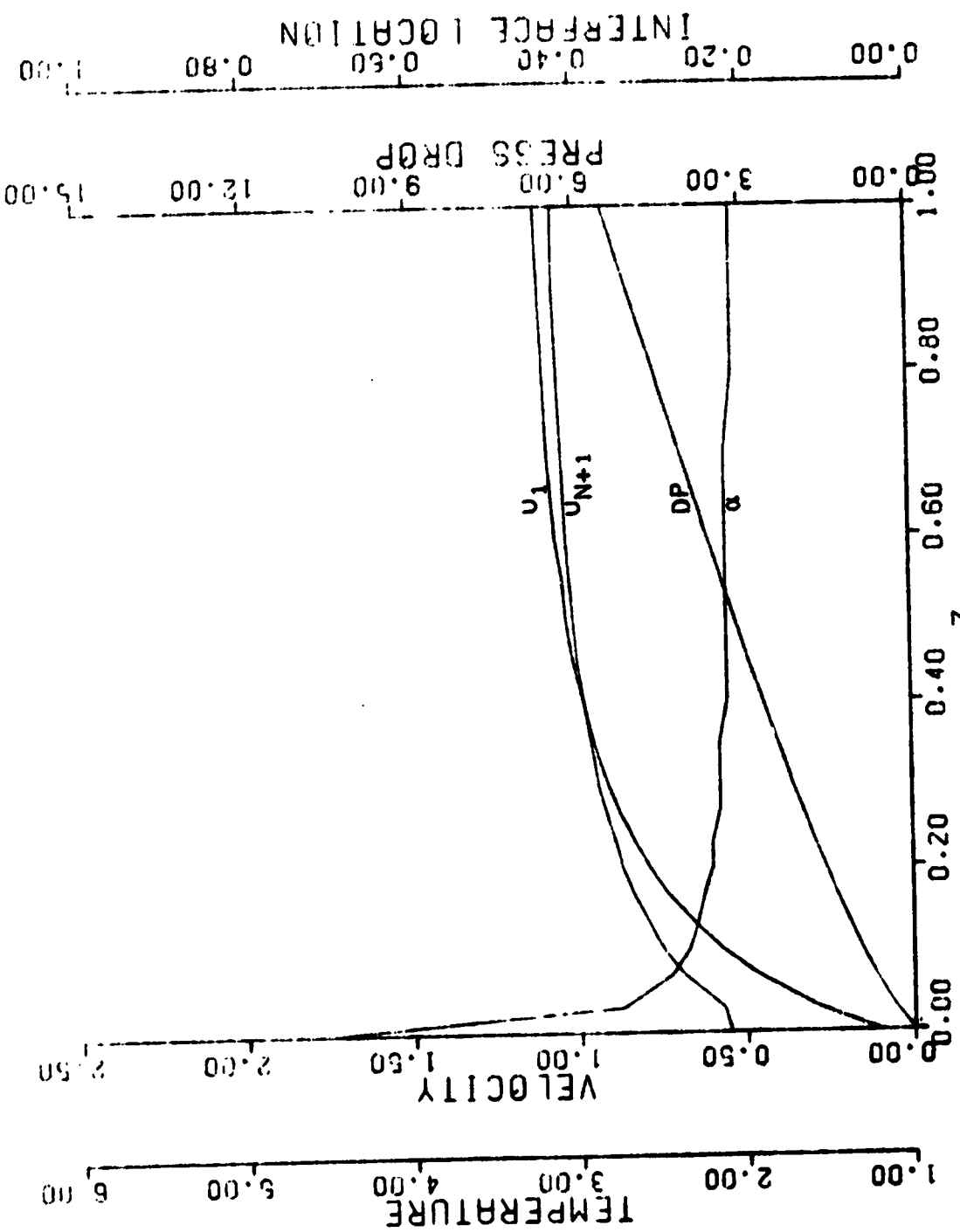

Figure 22. Axial Development of Central and Interfacial Axial Velocities and Temperatures, Pressure Drop and Location of Interface - Zero Generation Case

A total of seven runs were made to study the effect of various parameters on the flow field. For the first five runs, the generation term was chosen as constant per unit mass of fluid. The parameter variations for the first five runs are listed in Table 2. The sixth and seventh runs were made to study the effects of different forms of generation terms. For the sixth run generation term was chosen as constant per unit volume. Coaxial entrance flow without heat generation was simulated by the seventh run.

Table 2. Parameters for Constant Generation Per Unit Mass Case

Set No.	Parameter which is Varied	Value
1	Base	-
2	u_R	0.05
3	ρ_R	20
4	k	0.005
5	α	0.5

Before discussing the results obtained, it is necessary to explain the shape of the initial profiles chosen.

Initial Profiles

Flat initial profiles were chosen for simplicity in calculation. Even though a singularity exists where the inner stream meets the outer stream, this flow would be more stable than two parabolic profiles meeting at the inlet of the reactor.

There has been published experimental data which indicate that a back flow region is formed at an outer to inner stream velocity ratio of 26 for heterogeneous jets with a density ratio of 4^{16}. Since the nature of the parabolic governing equations is such that they cannot handle flow situations where there is a substantial radial variation of pressure which will eventually lead to the axial or primary flow velocity component becoming negative, a value of 10 is chosen for the outer to inner stream velocity ratio. This ensures physical stability in the computational scheme, since it limits the size of the radial pressure gradient to a negligible fraction of the axial pressure gradient.

Validation of Results

There are no known experimental data for the laminar confined coaxial entrance flow problem with or without heat generation. Therefore, checking the validity of the results by direct comparison is not possible. However, verification was attempted by simulating the classical isothermal, laminar, Newtonian flow in a tube entrance region for a uniform entrance velocity. Computed velocity profiles, entrance lengths and pressure gradients are in excellent agreement with those reported in published literature. Details of this comparison are described in Appendix B. Even though this proof of validity is not conclusive since it is inferred from simulating a special case, it provides a partial check of the method used.

Discussion of Results

The developing axial velocity profiles and temperature profiles are shown in Figures 3, 4, 6, 7, 9, 10, 12, 13, 15, 16, 18, 19 and 21. Figures 5, 8, 11, 14, 17, 20 and 22 show the axial development of center line and interfacial axial velocity and temperature, interface location and pressure drop. All the results reported were generated using a 22 point ζ grid with 11 points in each fluid. The explicit method finite difference scheme was used up to $z = 0.03$ and the implicit method was used thereon until $z = 1.0$. The convergence of the solution of finite difference equations to the solution of partial differential equations was proved by comparing the results obtained for run No. 1 of constant generation per unit mass case using a 42 point ζ grid, with those obtained using a 22 point ζ grid. The results match within 1% accuracy.

The axial velocity profile plots indicate that in all cases the flow exhibits the same type of behavior. Close to the entrance, the faster moving outer stream transfers some of its momentum to the inner stream, thus accelerating it. Also, the effect of the outer stream coming in contact with the wall, which forces the velocity of fluid at the wall to be zero, is manifested by a peak in the outer stream axial velocity to satisfy continuity. The maximum observed in the axial velocity keeps traveling towards the center line as the flow develops axially, and in all cases it is seen that at $z = 1.0$ the velocity profiles are parabolic.

The results show that the inner stream shrinks as it travels through the tube. This can be explained simply in the case of zero heat generation. The outer stream continuously transfers some of its momentum to the inner stream, thus accelerating it. The inner stream must contract in radius to satisfy continuity. This happens until the flow is fully developed.

The internal generation of heat in the inner stream raises the fluid temperature. Since the specific volume of the fluid is proportional to the temperature, the value of the center line velocity is further enhanced. This again could result in a shrinking-while-expanding inner stream. A reasonably accurate prediction as to whether the inner stream is going to expand or shrink in radius can be made from the value of the ratio of the product of average density and average axial velocity at any z to that at z = 0 of the inner stream. The inner stream will shrink or expand if the ratio is greater or less than unity, respectively. All the runs reported showed a shrinking inner stream. Attempts to obtain values of parameters necessary to generate an expanding inner stream were abandoned due to severe numerical difficulties. It is felt that full Navier-Stokes equations are necessary to describe such a flow situation.

The profiles generated and flow features are in good qualitative agreement with those reported using inviscid flow analysis[22].

Effects of Flow Parameters

Figures 5, 8, 11, 14, 17, 20 and 23 present the effects of the following flow parameters on flow variables:

1. Magnitude and type of generation term,

2. u_R ratio of inner to outer stream initial entrance velocities,

3. ρ_R ratio of inner to outer stream initial entrance densities,

4. K ratio of inner to outer stream thermal conductivities, and

5. α, dimensionless inner stream radius.

Figures 5, 20 and 23 show the effects of magnitude and type of generation term on the flow variables. With no generation, values of center line velocity u_1 and interfacial axial velocity u_{N+1} reach values of 1.11 and 1.06 respectively, at z = 1.0. The inner stream has a diameter α of .21 and the pressure drop DP has a value of 5.47. With the same flow parameter values, but different generation terms, there is a significant increase in the values of all variables just described. In the first case where the inner stream generates heat at a constant rate per unit mass, u_1, u_{N+1}, center line temperature T_1, interfacial temperature T_{N+1}, α and DP attain values of 1.84, 1.66, 4.39, 1.81, .31 and 9.04, respectively, at z = 1.0, compared to 1.4, 1.28, 2.93, 1.3, .29 and 6.78 respectively, in the second case where the fluid is assumed to generate heat at a constant rate per unit volume. Values in the second case are lower

than those in the first case due to the smaller amount of heat generated. If the inner stream is expanding it is expected to result in an increase in all values. A comparison of values of product of average density and average axial velocity explains why the diameter of the inner stream is larger in the first case compared to the second case. It is also interesting to note that the inner fluid temperatures reach a maximum near the entrance for the second case and gradually become smaller as the flow develops. This is completely opposite to the behavior in the first case. A close look at the phenomenon explains this behavior. Initially, the inner stream occupies a large area and as it goes down the conduit it starts to shrink in size and hence the amount of heat generated decreases. Since the fluid cannot generate enough heat to compensate for heat transferred to the outer fluid, thereby sustaining the initial temperatures, the temperatures start falling off. Similar behavior is expected to be seen in the first case also, if the magnitude of generation term is not as large.

The effect of change of other parameters is only reported for the constant generation per unit mass case. A similar study was also made for the constant generation per unit volume case, but the results are not reported since no new information was obtained.

By decreasing the value of u_R to 0.05, the final values of u_1, u_{N+1}, T_1, T_{N+1}, α and DP decreased to 1.54, 1.47, 3.7, 1.7, .22 and 6.98, respectively. This is due to the decrease

in total initial momentum and amount of heat generating fluid. The opposite reason explains the increase in the values of u_1, u_{N+1}, T_1, T_{N+1}, α and DP to 2.1, 1.9, 5.22, 2.12, .32 and 12.15 resulting from an increase in the value of ρ_R to 20. A decrease in the value of K reduces the amount of heat transferred from inner stream to outer stream, resulting in a hotter inner stream and a colder outer stream. This leads to smaller u_1, u_{N+1} and DP values, and a larger value of α. The temperature profiles exhibit steeper gradients in this case. A reduction in the amount of inner fluid entering the tube (i.e., smaller value of α) results in a faster moving inner stream (due to increased total initial momentum) with smaller temperatures (due to lesser heat generation).

A comparison with the fully developed profiles was not made since the flow does not seem to have been fully developed at $z = 1.0$.

CHAPTER VI

CONCLUSIONS AND RECOMMENDATIONS

The original contributions of this thesis are a model describing transport mechanisms in the entrance region of the gas-core nuclear reactor, and a ζ transformation which makes possible the use of a protean coordinate system for confined flows.

The results obtained in this thesis using the laminar flow model show that the rapidly accelerating, heat generating inner stream actually shrinks in radius as it expands axially. This conclusion is in opposition to that assumed in previous analyses of the flow region downstream of the entrance region.

Since the attempts to obtain an expanding inner stream by varying the basic system parameters were not successful, it is recommended that full Navier-Stokes equations be solved to gain better understanding of the complex entrance flow problem.

The value of ζ transformation as an efficient method to solve confined flows should be further explored.

APPENDIX A

ζ TRANSFORMATION

Finite difference schemes using grids with uniform spacing are the simplest and the most convenient for programming. However, such schemes are not satisfactory for use in problems with boundary layers. The numerical solution could have gross errors even in the stream core, if the number of points is not great enough to resolve the boundary layer. The use of enough grid points to resolve the boundary layer makes the computational time unacceptably large. This problem can be alleviated by introducing an irregular net with smaller spacing near the boundary in such a way that the order of magnitude of numerical error is the same throughout the flow field. One choice is to use grids with discontinuously varying resolutions. However, there are two disadvantages to this method: 1) it is necessary to interpolate values of variables or their derivatives at intermediate points, and weak numerical instabilities usually arise at the boundary between the large and small grid size, and 2) this method cannot give very small grid intervals without greatly increasing the computational time. Another possibility is to vary the grid intervals continuously, avoiding the necessity of intermediate interpolations. This can be done by defining a stretched coordinate ζ

$$\psi = \psi(\zeta)$$

such that the grid intervals $\Delta\zeta$ are constant while the $\Delta\psi$ varies appropriately. $\psi(\zeta)$ should have the following properties:

1. $\frac{d\psi}{d\zeta}$ should be finite over the whole interval and such that there are no singularities in the region of interest. If $\frac{d\psi}{d\zeta}$ becomes infinite at some point, then the mapping $\psi = \psi(\zeta)$ will yield poor resolution near that point, which cannot be improved by increasing the number of points, since

$$\Delta \psi \approx \frac{d\psi}{d\zeta} \cdot \Delta\zeta$$

2. $\frac{d\psi}{d\zeta} = 0$ at $\psi = \psi_w$. This will insure a high resolution near $\psi = \psi_w$. Elsewhere, $\frac{d\psi}{d\zeta}$ should be different from zero.

An error analysis based on Taylor series expansion suggests the convenience of choosing a function $\psi = P_n(\zeta)$, where P_n is a polynomial of degree greater than one; also, P_n should be the lowest order polynomial such that good resolution is maintained at $\psi = 0$.

It is also convenient to choose ζ such that:

1. Symmetry with respect to $\zeta = 0$ is restored, and
2. ζ coincides with r when the flow is fully developed.

These requirements strongly suggest an inverse Von Mises transformation with fully developed axial velocity replacing axial velocity at any point. For flow of an incompressible fluid through a conduit, this yields

$$\frac{d\psi}{d\zeta} = 2(1-\zeta^2)\,\zeta.$$

Solving this differential equation with the boundary condition $\zeta = 0$ at $\psi = 0$ the following relationship between ψ and ζ is obtained:

$$\psi = \zeta^2 - \frac{1}{2}\zeta^4$$

It can be shown that this transformation satisfies all the above mentioned requirements. The advantages of the ζ transformation are best understood by observing the development of nonuniformly spaced r grids (resulting from uniformly spaced ζ grids) along the flow. Near the entrance, where the gradients are very severe, very small grid sizes are maintained close to the wall. As the flow develops, the gradients become less severe and r grids become more or less uniform, thus ensuring errors of the same order of magnitude in the computational scheme everywhere in the r direction. This also results in a progressive reduction of average error in the r direction along the flow.

A scale factor L is required to map the region of interest $0 \leq r \leq 1$ into $0 \leq \zeta \leq 1$, in the case of coaxial flow of two incompressible fluids. The value of L can be shown to be:

$$L = \frac{\int_0^{\alpha} u_{11}\rho_{11} r dr + \int_{\alpha}^{1} u_{21}\rho_{21} r dr}{2 \int_0^1 (1-r^2)\, r dr}$$

It is also convenient to use the same stretch factor for the coaxial flow of compressible fluids.

APPENDIX B

APPENDIX B

ENTRANCE FLOW IN A TUBE

The results of an analysis on the steady, laminar, incompressible, isothermal, Newtonian entrance flow through a tube for a uniform entrance velocity were obtained using the implicit numerical scheme described in Chapter IV and by specifying that:

a) properties and entrance velocities and temperatures of both fluids are the same, and

b) the heat generation rate is zero.

The only modification in the numerical scheme is that the pressure drop was calculated using a macroscopic momentum balance. Results were obtained using a 12 point ζ grid. Even though this is a very coarse grid, the results are in good agreement with values obtained by other sources.

The developing velocity profiles are shown in Figure B-1. For comparison purposes, values of dimensionless excess pressure drop C defined as

$$-2\,\Delta P = 16z + C$$

and entrance length defined as the dimensionless axial position at which the center line velocity reached 99% of its fully developed value, are listed in Table B-1.

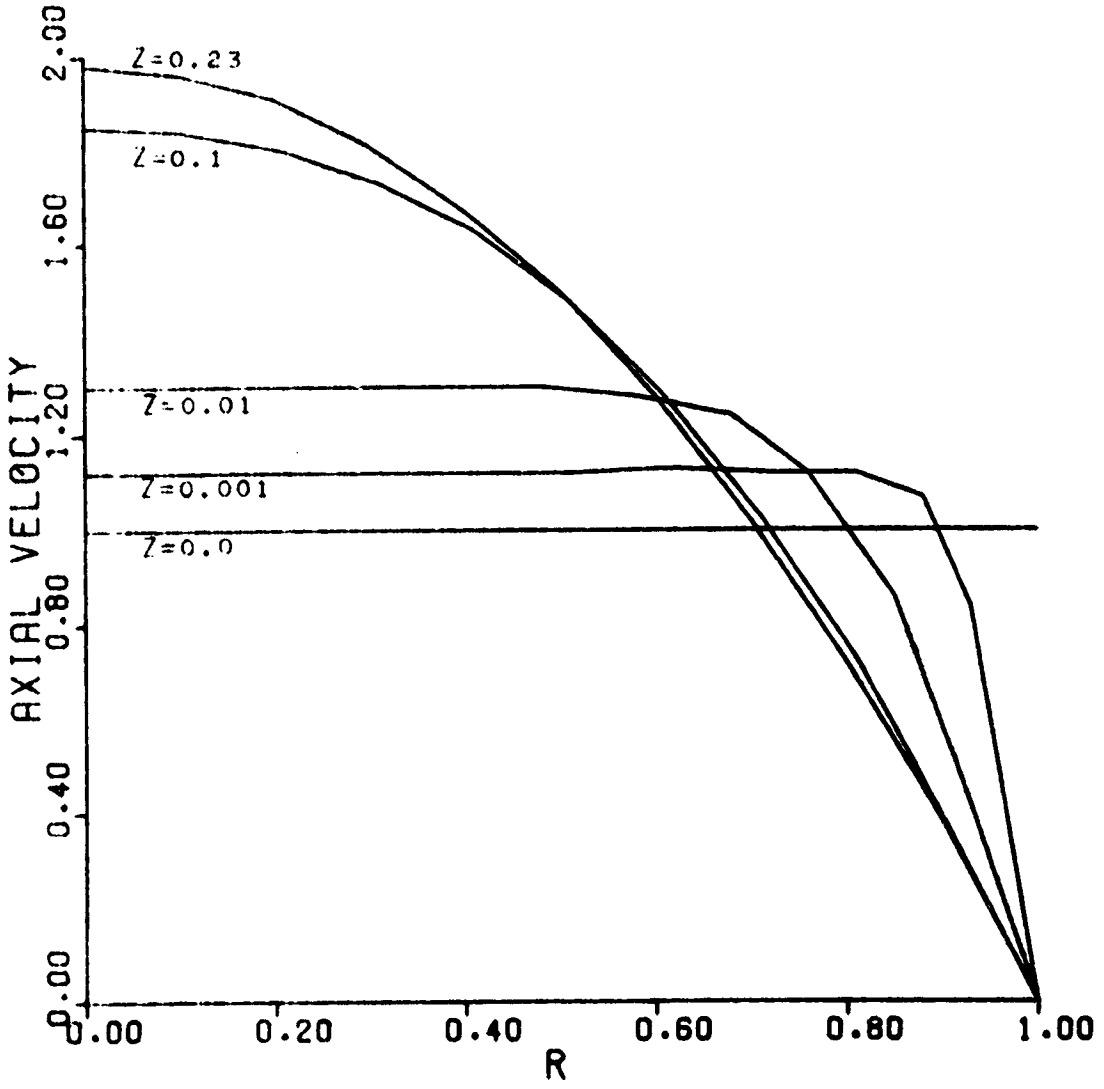

Figure B-1. Axial Velocity Profiles - Entrance Flow in a Tube

Table B-1. Values of C and Reduced Entrance Lengths

Source	C	Entrance Length
This study	1.24	0.23
Campbell and Slattery[1]	1.18	0.24
Christiansen and Lemmon[3]	1.33	0.24
Collins and Schowalter[4]	1.33	0.24
Langhaar[11]	1.28	0.23
Hornbeck[9]	1.28	0.23
Trentas[21]	1.18	0.23

The accuracy of the results could further be improved by increasing the number of grids in the numerical method.

BIBLIOGRAPHY

1. Campbell, W. D. and J. C. Slattery. March 1963. Flow in the Entrance of a Tube. Trans. of the ASME, Journal of Basic Engineering, pp. 41-46.

2. Cess, R. D. 1964. The Interaction of Thermal Radiation with Conduction and Convection Heat Transfer. Advances in Heat Transfer, Vol. 1, pp. 1-50.

3. Christiansen, E. B. and H. E. Lemmon. 1965. Entrance Region Flow. AIChE Journal, Vol. 11, No. 6, pp. 995-999.

4. Collins, M. and W. R. Schowalter. Nov. 1963. Behavior of Non-Newtonian Fluids in the Entry Region of a Pipe. AIChE Journal, Vol. 9, No. 6, pp. 804-809.

5. Dealy, J. M. 1965. A Neglected Effect in Entrance Flow Analyses. AIChE Journal, Vol. 11, No. 4, p. 745.

6. Donovan, L. F. and C. A. Todd. 1968. Computer Program for Calculating Isothermal, Turbulent Jet Mixing of Two Gases. NASA TN D-4378.

7. Ghia, K. N., T. P. Torda and Z. Lavan. 1969. Laminar Mixing of Heterogeneous Axisymmetric Coaxial Confined Jets. AIAA Journal, Vol. 7, No. 11, pp. 2072-2078.

8. Hellums, J. D. 1966. On a Neglected Effect in Entrance Flow Analyses. AIChE Journal, Vol. 12, No. 1, pp. 197-198.

9. Hornbeck, R. W. 1964. Laminar Flow in the Entrance Region of a Pipe. Applied Scientific Research, Vol. 13, Section A, No. 2-3, pp. 224-232.

10. Kascak, A. F. 1967. Estimates of Local and Average Fuel Temperatures in a Gaseous Nuclear Rocket Engine. NASA TN D-4164.

11. Langhaar, H. L. June 1942. Steady Flow in the Transition Length of a Straight Tube. Journal of Applied Mechanics, pp. A55-A58.

12. Ragsdale, R. G. and F. E. Rom. 1967. Gas-Core Reactor Work at NASA Lewis. NASA TM X-52309.

13. Ragsdale, R. G. and H. Weinstein. Aug. 1962. On the Hydrodynamics of a Coaxial Flow Gaseous Reactor. Proceedings ARS/ANS/IAS Nuclear Propulsion Conference, TID 7653, Part 1, pp. 82-88.

14. Richtmyer, R. D. and K. W. Morton. 1967. Difference Methods for Initial-Value Problems. Interscience Publishers, New York, 2nd ed., Chapter 8.

15. Rom, F. E. 1969. Comments on the Feasibility of Developing Gas Core Nuclear Reactors. NASA TM X-52644.

16. Rozenman, T. and H. Weinstein. Dec. 1972. Recirculation Patterns in the Initial Region of Coaxial Jets. Trans. of the ASME, Journal of Applied Mechanics, pp. 891-896.

17. Schlichting, H. 1960. Boundary Layer Theory. McGraw-Hill, New York, 4th ed., p. 168.

18. Shavit, G. 1970. Analytical and Experimental Investigations of Laminar Mixing of Homogeneous and Heterogeneous Jets in a Confining Tube. Ph.D. Thesis, Illinois Institute of Technology.

19. Sparrow, E. M., S. H. Lin and T. S. Lundgren. March 1964. Flow Development in the Hydrodynamic Entrance Region of Tubes and Ducts. The Physics of Fluids, Vol. 7, No. 3, pp. 338-347.

20. Van Dyke, M. 1970. Entry Flow in a Channel. J. Fluid Mech., Vol. 44, Part 4, pp. 813-823.

21. Vrentas, J. S., J. L. Duda and K. G. Bargeron. Sept. 1966. Effect of Axial Diffusion of Vorticity on Flow Development in Circular Conduits: Part I. Numerical Solutions. AIChE Journal, Vol. 12, No. 5, pp. 837-844.

22. Weinstein, H., B. G. K. Murty and R. W. Porter. November 1971. An Analysis of the Flow Field Near the Fuel Injection Location in a Gas Core Reactor. 2nd Symposium on Uranium Plasmas: Research and Applications. AIAA/ANS/Georgia Inst. of Tech./NASA, pp. 214-220.

23. Weinstein, H. and R. G. Ragsdale. 1960. A Coaxial Flow Reactor - A Gaseous Nuclear-Rocket Concept. Preprint 1518-60, American Rocket Society, Inc.

24. Weinstein, H. and C. A. Todd. 1964. Analysis of Mixing of Coaxial Streams of Dissimilar Fluids Including Energy-Generation Terms. NASA TN D-2123.

APPENDIX: Publications of Grant Sponsored Work

Contractor Reports

1. 'Analytical Investigation of the Mixing of Two Parallel Streams of Dissimilar Fluids", R.L. Baker and H. Weinstein, CR-956.
2. "Experimental Investigation of the Mixing of Two Parallel Streams of Dissimilar Fluids", R.L. Baker and H. Weinstein, CR-957
3. "Calculation of Stability of Shear Flow with Density Gradient and Viscosity", R.L. Baker and H. Weinstein, CR-958.
4. "Turbulence in the Mixing Region Between Coaxial Streams", T. Zawacki and H. Weinstein, CR-959.
5. "Turbulent Correlations in a Coaxial Flow of Dissimilar Fluids", G. D'Souza, A. Montealegre and H. Weinstein, CR-960.
6. "Evaluation of Turbulence Correlations in Coaxial Flow of Dissimilar Fluids", A. Montealegre, G. D'Souza and H. Weinstein, CR-961.
7. "Numerical Investigation of Coaxial Unsteady Laminar Incompressible Boundary Layer Flows", U. Agarwal and T.P. Torda, CR-908.
8. "The Effect of Free Stream Turbulence on Coaxial Mixing", R. Kulik, J.J. Leithem, and H. Weinstein, CR-1336.
9. "Turbulence in the Mixing Region between Ducted Coaxial Streams", J. Leithem, R. Kulik and H. Weinstein, CR-1335.

10. "Laminar Mixing of Heterogeneous Axisymmetric Coaxial Confined Jets", K. Ghia, T.P. Torda and Z. Lavan, NASA CR-72480.

11. "Analytical Investigation of Incompressible Turbulent Swirling Flow in Stationary Ducts", A. Rochino and Z. Lavan, CR-1169.

12. "Flow in a Two-Dimensional Channel with a Rectangular Cavity", U. Mehta and Z. Lavan, CR-1245.

13. "Experimental Investigation of Recirculation Patterns in the Initial Region of Coaxial Jets", T. Rozenman and H. Weinstein, CR-1595.

14. "Turbulent Mixing of Heterogeneous Axisymmetric Coaxial Confined Jets", K. Ghia, T.P. Torda and Z. Lavan, CR-1615.

Journal Papers Published or Submitted

1. "Laminar Mixing of Heterogeneous Axisymmetric Coaxial Confined Jets", by K.N. Ghia, T.P. Torda and Z. Lavan, AIAA Journal, 7, 2072 (1969).

2. "Analytical Investigations of Incompressible Turbulent Swirling Flow in Stationary Ducts", A. Rochino and Z. Lavan, J. Applied Mechanics, 36, 151 (1969).

3. "Flow in a Two Dimensional Channel with a Rectangular Cavity", U. Mehta and Z. Lavan, J. Applied Mechanics, 36, 897 (1969).

4. "The Mixing of Parallel Streams of Dissimilar Fluids", Analytical, R.L. Baker, L.N. Tao and H. Weinstein,

J. Applied Mech., 38, 301 (1971).

5. "The Mixing of Parallel Streams of Dissimilar Fluids", An Experimental Investigation, R.L. Baker and H. Weinstein, J. Applied Mech., 38, 310 (1971).

6. "Turbulence Measurements in a Ducted Coaxial Flow", R.A. Kulik, J.J. Leithem and H. Weinstein, AIAA Journal, 8, (1970).

7. "The Temperature Distribution in an Infinite Medium Resulting From a Line Source of Finite Duration", A. Montealegre and H. Weinstein, Int. J. of Heat and Mass Transfer, 14, 998 (1971).

8. "The Temperature Distribution in an Infinite Medium Resulting from a Plane Source of Finite Duration", A. Montealegre and H. Weinstein, Ibid., 15, 161, (1972).

9. "The Mixing of Monogeneous Coaxial Streams", A. Montealegre and H. Weinstein, Israel J. Tech., 9, 141 (1971).

10. "Separation and Flow Reversal in Swirling Flows in Circular Ducts", Z. Lavan, H. Nielsen and A.A. Fejer, The Physics of Fluids, 12, 1747 (1969).

11. "Recirculation Patterns in Confined Laminar Jet Mixing", Z. Lavan and G. Shavit, Israel J. Tech., 9, 51 (1971).

12. "Recirculation Patterns in the Initial Region of Coaxial Jets", T. Rozenman and H. Weinstein, J. Applied Mech., 39, 891, (1972).

13. "An Analysis of the Flow Field Near the Fuel Injection Location in a Gas Core Reactor", H. Weinstein, B.G.K. Murty and R.W. Porter, Proceedings of the 2nd Symposium on Uranium Plasmas: Research and Applications, Atlanta, Georgia, Nov. 15-17, 1971.

14. "Experimental Investigation of Recirculating Cells, N.R. Wa. kis, H. M. Nagib and Z. Lavan, AIAA Journal, 10, 1204 (1972).

15. "Numerical Solutions of Driven Vortices of a Binary Fluid in Cylindrical Geometries," Y. Shin and Z. Lavan, to be submitted to J. App. Mech.